Multi-material 3D Printing of Bioinspired Mechanical Structures

A THESIS SUBMITTED TO THE UNIVERSITY OF PORTSMOUTH

FOR THE DEGREE OF DOCTOR OF PHILOSOPHY

MARCH 2019

BY

Marco Curto

SCHOOL OF MECHANICAL DESIGN AND ENGINEERING

UNIVERSITY OF PORTSMOUTH

ANGLESEA BUILDING, ANGLESEA ROAD, PORTSMOUTH PO1 3DJ

Declaration

Whilst registered as a candidate for the above degree, I have not been registered for any other research award. The results and conclusions embodied in this dissertation are the work of the named candidate and have not been submitted for any other academic award.

Marco Curto

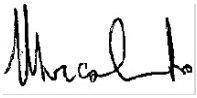

~ 45000 words

Acknowledgements

This thesis is the result of all the effort and passion put into three years for my PhD project, which has been supported and contributed to by numerous people. I would like to start by thanking the University of Portsmouth for welcoming me and being my second home for the entire period. All the days spent in these walls helped develop my professional career and provided me with a clear and exciting idea about the future. Here I had the chance to find brilliant minds, from different cultures, joined together in a beautiful place of learning and evolution. Here I had the chance to first meet my supervisors and mentors who have been my guides and travel companions. I want to say thanks to Professor Asa H. Barber who always supported and motivated me to become a systematic researcher that looks for the right questions before looking for the right answers. I want to say thanks to Dr. Tozzi for his motivation and inspiration to push always no matter what. Thank you to Dr. Bucchi for all time he listened to me and for being my closest confidant. Moreover, I would like to thank Dr. Pani, for being my "fourth" supervisor, a friend, an older brother with whom sharing games was fun and constructive.

I wish to thank Our Head of the School Dr. Lynsey Plockyn, Dr. Tineke Fitch and our Dean of the Faculty of Technology Professor Djamel Ait-Boudaoud, for the support and availability demonstrated during my difficult moments, confirming the University of Portsmouth as a University where no one stands alone.

I would like to thank Dr. Mariana Dothceva and Dr. Krassimir Dotchev. Thank you to Dr. Sarinova for always being present and for inviting me to her seminars. Thanks to Dr. Jurgita Zekonyte for transferring knowledge about nanoindentation, thanks to Mr. Colin Lupton (The Navy) aka the practical encyclopedia man, to Dr Alex Kao, the man who sees though things. Thank you, Rob "Bon giorno Bonasera" for the smiles and jokes. Thanks to Dr. Stephanie Giet for the support given during the last period of my thesis and for sharing knowledge in matter of metal 3D printing and laser sintering.

I would like to thank 3D Systems for creating such an amazing and complex 3D printer whose difficulties and challenges, every now and then during this path, made me think

out of the box, letting me work out difficult situations, coming up with several ideas and inventions for the upcoming future. Every cloud has a silver lining.

The work in this PhD thesis is also supported by lots of close friends. Thank are given for useful discussion with Dr. Barrie Dunn who always gave me a third point perspective over a good coffee. My group of friends from Room 2.09, the university hostel, which put me in contact with a lot of friends from different cultures. Thanks to Hayder (Hayderone) for his loyalty, thanks to Marta (Martina) for her passion, Ahmed for his elegance, Katerina for her freshness, Tim (Timmy) for his firmness, Roxane for her kindness, to Saul (Saulito), Samuel (Big Daddy) and all the other guys for having shown their smiles at least once throughout this period.

Among the outsiders I would like to thank Alberto Sensini (Albertone), my electrospun friend. I would like to thank My ControlMad friends who made of me, an Engineer who makes pretty things and not just only boring things as Engineers usually do.

I would like to thank my beloved Melissa for being such an amazing girlfriend and soul mate, for believing in me and being my personal cheerleader.

Thanks to George Roinas (my brother from another mother) and Hivar. Thanks to Julia, Betsie, Luke, Irene, Sean, Livia, Rosie (The family who adopted me in the UK). Thanks to Alexandra from Tomorrow Land, Maria, Fabio and Federica for their friendship.

I would like to thank Darren and Ian for their kindness and humility.

Thank you to my mom and my dad who are the first and the second beat of my heart. Thanks to all my family for giving me such a beautiful life, for the love and strength they give me, and always being with me, despite decisions which took us apart. There is no distance I won't walk to see you.

Finally, I would like to thank music for making of my wailing soul a travelling soul

To my niece and nephews Sara, Francesco, Alessandro, Gregorio.

Talent hits a target no one else can hit.
Genius hits a target no one else can see.
(Arthur Schopenhauer)

Abstract

Change has long assisted nature to build strong creatures. Species adapt every day obeying to the rule of withstanding loads. Inputs are gathered to grow hard and soft tissues where needed, saving life and preventing waste. Mimicking the same stunning mechanical performances is a hard challenge for man-made products obtained with top down processes. The aim of this project was to develop digital workflows for the generation of biologically inspired composites. The fabrication of hybrid composites inspired by tough biological materials such as nacre and compact bone were provided by the assembly of hard and soft phases through a multi-material 3D Printing (MM3DP) technique known as Multijet printing technology (MJP). To start, a systematic experimentation was conducted to quantify the mechanical properties of MJP base materials as well as the mechanical interplay between such multiple materials in a composites design. A workflow based on high contrast x-ray tomography (XCT) imaging data was then proposed to provide virtual models of less and more remodelled cortical bone. Mechanical properties of the cortical bone samples as well as the 3D printed replica were evaluated using acoustic measurements. Physical output show an elastic modulus almost ten times smaller (approximately 4 GPa) than the native bone (approximately 32 GPa), with the potential to tune the elastic modulus of the 3D printed replica depending on the employed manufacturing materials. The realization of controllable bioinspired 3D designs, represented the second goal of this project, in alternative to the extraction of key features from imaging data. Two workflows based on Generative Design (GD) were proposed to fluently draw and fabricate bioinspired compact bone and nacre. A parameterized version of the typical lamellar organization

was presented for the first time to mimic compact bone and to supply a tool for the generation of a 3D crack blunting model. A further interactive workflow was proposed to produce a two-phase material inspired by nacre providing for a mechano-mimetic structure that dissipate energy via cracks delocalization, thus avoiding catastrophic failures. Results from tensile testing show increasing stress transfer from matrix to reinforcement by varying the diameter of the platelets from 2 to 9 mm. The resulting structures presented a volume fraction of the reinforcement that ranged from 54% to 69%, enough to absorb 20% energy than the stiffer base materials when subjected to dynamic loading. Finally, a semi-automated XCT based workflow was proposed to cover the absence of a volumetric metrology tool destined to multi-material AM when photo curable materials similar in density coexist.

Keywords**:** Bioinspired, Composites, Parametric, Additive Manufacturing, X-ray

Publications and personal development

Grants and awards

£500 awarded during the Fourth annual FortisNet meeting to support the short collaborative project "*Tangible bone cells for outreach and teaching"* between the University of Southampton, University of Portsmouth and the startup 3D 4U-MAN, Southampton, 2019.

Best two minutes presentation, Fourth annual FortisNet, Southampton, 2019.

Best Poster presentation presented to the Innovation and technology conference, University of Portsmouth, 2017.

Italian national winner, SME assembly conference – European Enterprise Promotion Awards, Tallin, 2017.

Publications generated from this thesis

R. Parwani, M. Curto, A. P. Kao, P. J. Rowley, M. Pani, G. Tozzi, A. H. Barber, "*Morphological and Mechanical Biomimetic Bone Structures*," ACS Biomater. Sci. Eng., vol. 3, no. 11, pp. 2761–2767, 2017.

M. Curto, M. Pani, G. Tozzi, A. H. Barber, R. Parwani, "*4D printing biomimetic tissues structures using correlative approaches*" In : Orthopaedic Proceedings: A Supplement to The Bone and Joint Journal. 99, SUPP 1, p. 32-32, 2017.

M. Curto, A. P. Kao, G. W. Blunn, G. Tozzi, A. H. Barber, "*Generative design and 3D printing of tough biomimetic compact bone.*" **In preparation to be submitted to the journal "Virtual and Physical Prototyping"**

M. Curto, A. P. Kao, M. Pani, A. Bucchi, G, Tozzi, A. H. Barber, *"X-ray tomography evaluations of failure in additive manufactured biomimetic structures"* **In preparation to be submitted to the journal "Virtual and Physical Prototyping"**

Bioinspiration related outputs

M. Fantini, M. Curto, and F. De Crescenzio, "*A method to design biomimetic scaffolds for bone tissue engineering based on Voronoi lattices*," Virtual Phys. Prototyp., vol. 11, no. 2, pp. 77–90, 2016.

M. Fantini and M. Curto, "*Interactive design and manufacturing of a Voronoi-based biomimetic bone scaffold for morphological characterization*," Int. J. Interact. Des. Manuf., pp. 1–12, 2017.

M. Fantini, M. Curto, and F. De Crescenzio, "*TPMS for interactive modelling of trabecular scaffolds for bone tissue engineering*," Lect. Notes Mech. Eng., pp. 425–435, 2017.

Other outputs

M. Palanca, L. Cristofolini, E. Dall'Ara, M. Curto, F. Innocente, V. Danesi, G. Tozzi, "*Digital volume correlation can be used to estimate local strains in natural and augmented vertebrae: An organ-level study*," J. Biomech., vol. 49, no. 16, pp. 3882–3890, 2016.

G. Tozzi, E. Dall'Ara, M. Palanca, M. Curto, F. Innocente, and L. Cristofolini, "*Strain uncertainties from two digital volume correlation approaches in prophylactically augmented vertebrae: Local analysis on bone and cement-bone microstructures*," J. Mech. Behav. Biomed. Mater., vol. 67, pp. 117–126, 2017.

International conferences

23rd Congress of the European Society of Biomechanics, Seville, 2017

- Podium presentation "*3D printing of composites structures directly from x-ray tomography*"
- Flash presentation and poster "*Direct metal laser sintering of a Voronoi-based biomimetic bone scaffold for bone tissue engineering*"

Tomography for scientific advancement (ToSca), Portsmouth, 2017

- Podium presentation "*X-ray tomography evaluations of failure in additive manufactured biomimetic structures* "
- Poster presentation "*Manufacturing of a Voronoi-based biomimetic bone scaffold by means of Direct Metal Laser Sintering*"
- Image Competition "*CT scanning of a synthetic 3D printed trabecular bone scaffold*" – selected to be exposed during the conference.

In-house conferences

Innovation and technology conference, University of Portsmouth, 2017.

- Poster and three minute thesis competition: *Multi-material 3D printing of bioinspired mechanical structures*

Faculty research conference, University of Portsmouth, 2018.

- Three minute thesis competition: *Biomimetic Nacre: parametric design and assembly of engineering polymers via multi-material 3D printing*

Presented workshops and seminars

Tomography for scientific advancement (ToSca), Portsmouth, 2017

- Workshop title " From x-ray to 3D printing "

SMDE research seminar, Portsmouth 2019

- Seminar title "Multi-material 3D printing of bioispired mechanical structures"

Table of Contents

Chapter 1. Introduction to biologically inspired materials

1.1 Motivation of the study

Creatures from any kingdom whether they are plants, animals or human, need to withstand mechanical loading in order to survive. The environment in which each species developed over a billion years can be compared to a black box where multiple inputs have and are still contributing to species adaptation in terms of mechanical design, remodelling and evolution. Remarkable mechanical properties can be found in biological materials where mechanical resistance mechanisms such as abrasion, impact, fatigue and tolerance to crack propagation are solved using minimum material volumes and exploiting elements available locally.

Biological materials are widely accepted as being compositionally composites [1], made of soft and, in some cases, hard phases assembled and precisely distributed over different length-scales [2] [3]. Here, a biopolymer binding phase acts as matrix, whereas mineral features produced by bio-mineralization or harder polymeric phases act as reinforcement. Structural design, hierarchy, materials distribution and mechanical control is critically described through biological DNA information within creatures. Such an approach provides lightweight materials that are constructed from sustainable resources, which is currently a particularly important societal challenge.

The efficiency of a biological material or composite lies in fulfilling complex requirements depending on the living system and structural optimization due to environmental conditions. Optimization fundamentally requires design occurring at different levels or scales where several processes act from the atomic level (of basic

single building blocks) to the functional level (of the final "material system"). The range of length scales considered gives rise to the concept of *architectured* and *hierarchically* organised systems. Architecture denotes the control of material composition and shape, whereas hierarchy indicates the range of length scales over which architecture occurs. This thesis will use these terms interchangeably. Cortical bone and nacre are excellent examples of a hierarchically organised biological material so that their architectures can achieve outstanding toughness under compressive and tensile load conditions [4] [5]. Fish scales, shark and human teeth are examples of evolved structures organised to oppose wear and abrasion [6] [7] [8]. Wood, palm and bamboo are particularly efficient in bending and resistant to buckling [9].

From a structural point of view, mechanical functions of biological composites are strictly related to the stress transfer from matrix to reinforcement. Here, geometries and shapes are parameterised and dimensioned in relation to the mechanical properties of base constituent materials. In this way, the matrix and reinforcement interplay allows the activation of mechanisms responsible for enhancing mechanical performances of biological materials rather than being made of monolithic materials, as usually occurs in engineering. For instance, nano-dimensional fibres and platelets provide cortical bone with one of the best load-bearing and crack stopper architectures known and nacres shell particularly tolerant to flaws [10] [11].

Hence, the benefit in understanding how biological composites were structured for specific mechanical functions is to provide patterns for the next generation man-made composites. In this way mechanical engineering has the opportunity to widen its boundaries in learning from natural design, embracing a multidisciplinary approach often referred to as *bioinspired*.

No general approaches have been developed to replicating biological architectures so far. Despite different systematic theoretical and experimental attempts can be found in literature, many procedural conflicts are still looking for better solutions to design and technology transfer. In general, geometrical key-features and parameters can be gauged from biology thanks to medical imaging or microscopy, then processed, often modelled and replicated in a Computer Aided Design (CAD) environment (Figure 1.1).

Figure 1.1. Workflow approach to manufacturing bio-inspired structures.

Difficulties arise when the information is transferred between the various operations of the workflow in Figure 1.1. Current approaches are lacking in terms of both CAD design and manufacturing strategies meant for hybrid replication. Technology is consequently missing many advantages of bio-inspiration because of:

- Big data handling
- Absence in materials manufacturing control at the small scales

The processing of data has a considerable impact on the entire workflow process in terms of computational costs. On the one hand, the supply of volumetric information, such as High-Resolution X-ray Computed Tomography (XCT) technology, needs to preserve fidelity and consistency of the biological architectures of interest that are to be subsequently replicated via 3D Printing or Additive Manufacturing (AM). On the other hand, literature lacks in material manufacturing control at very small lengths since only

recently manufacturing devices such as MJP and MM3DP in general, are available on the market. Several questions concerning the adopted technologies need to be satisfied especially when it comes to cutting edge strategies using techniques that are integrated together in the workflow of Figure 1.1.

Once limits of manufacturing techniques are highlighted, design strategies can be attempted, compatible with manufacturing capabilities and application of the final object. The resulting materials will offer new combination of low weight, stiffness and toughness allowing the customization of the solution to a particular case when it's needed. Perhaps the most important method of providing information is through imaging techniques but the correlation with suitable manufacturing processes is a critical challenge.

1.2 Aim of thesis

A bioinspired approach requires reliable ways to transfer technology from biology to adequate manufacturing processes. Therefore, the main goal of this PhD is to correlate the latest technologies, from imaging to manufacturing, aiming to transfer structural concepts and mechanical strategies from biology to engineering.

The aims of the project can be therefore summarised as follow:

1. Exploring the basis of bioinspiration, focusing on the main strategies and key features adopted by nature to control and enhance performances of biological materials.
2. Understand the capability of multi-material 3D printing to realize the forms and resultant mechanical properties that mimic those found in nature.

3. Identify and describe physical challenges related to multi-material 3D printing when accuracy and precision of composites manufacturing approaches length scales comparable to the biological ones through metrology. XCT is explored as a metrology tool for ascertaining MM3DP accuracy.
4. Develop robust workflows that enable the transfer of imaging data arising from XCT through a CAD design and towards a physical output.

The achievement of the previous aims will represent the background necessary to support and find 3D printing solutions destined to several disciplines and field of applications such as defence, aerospace, automotive, ballistic, tissue engineering

Critically, the specific aim of the thesis is to investigate and find possible pathways to produce MM3DP bioinspired tough structures. Therefore main objectives can be resumed and listed below:

- Description of the compact bone using an XCT image based workflow to duplicate via MM3DP mineralised and less mineralised features considered to be at the base of the compact bone toughening mechanisms.
- Realization of a controllable and customizable lamellar design, suitable for MM3DP, to mimic the composite structure of the compact bone which toughening mechanism is related to cracks blunting and cracks opening when failure is occurring at organ level.
- Realization of a controllable brick and mortar design to mimic the toughening mechanism of nacre due to the mechanical interplay at the interface between hard and soft phases organization.

- Realization of a semi-automated network for multi-material 3D printing to give volumetric insight about the interplay of matrix and reinforcement phases simultaneously 3D printed

1.3 Thesis overview

Chapter 1 represents the general introduction which was indeed the aforementioned discussed. Chapter 2 will review the basic background and knowledge that are related to biological composites, bioinspiration, composites theories and 3D printing technologies emphasizing biological architectures of interest found in a diverse set of samples of nacre and cortical bone. In Chapter 3, physical and digital investigations of MM3DP are presented defining dimensional boundaries to which bioinspired architectures produced via additive manufacturing are constrained. Chapter 4 proposes two different approaches to replicate cortical bone features: firstly directly 3D printing from XCT scanned samples of bovine cortical bone with structural variations and, secondly, attempting a 3D parametric CAD design approach to replicate cortical bone key features. Chapter 5 is focussed on the development of a hybrid composite inspired by nacre. The design is developed adopting 3D parametric tools such as algorithm modelling based on the mechanical properties of the available 3D printing materials. Quasi-static and dynamic mechanical tests are coupled to optical imaging and x-ray micro tomography investigation of the 3D printed output to verify mechanical functions found in nacre. Finally, composites theories are used to predict elastic material properties of the resulting 3D printed composites to answer the following research questions:

1. Can we reproduce a mechanical interplay within different phases of a hybrid composite material, similar to its biological counterparts?
2. Which are the limits of Multijet 3D printing technology in reproducing features that approach biological dimensions and length scales.
3. Which opportunities XCT microscopy offers to supply accurate volumetric information about Multijet 3D printed assemblies?

Chapter 6 will summarize the main conclusions from this work highlighting criticisms and advantages of employed techniques to replicate biological architectured materials, as well as suggested future works.

Chapter 2. Biological structures and architectured materials

2.1 Introduction

Bio-inspiration represents a novel field of study where multiple disciplines are used to replicate a natural system. This replication can be broad and includes metabolic and mechanical functions, architectural and structural strategies to fabricate adaptable composites. Transferring knowledge from nature to exploit in an engineered system usually deals with chemical, physical and structural compromises over different length scales of design and manufacturing. From a structural standpoint, material science finds nature appealing for its ability to meet contradictory mechanical properties such as toughness and stiffness, strength and flexibility, hardness and stiffness through hierarchical assembly of a range of materials. Hence a biological structure in an engineering sense is a composite made of different materials produced using biological processes and, thus, results in what is defined here as a biological composite. Most often, organic and inorganic materials are organized within a biological structure to produce an optimized function that complies with species adaptation and survival.

This chapter aims to review the relevant literature concerning bio-inspiration, initially examining biological materials and architectures within living creatures. Mechanical theories are then reviewed to explain the functions found in biological structures. Finally, 3D printing technologies are reviewed as a method potentially able to replicate the structural and mechanical functions of a biological composite system.

2.2 Biological structures

Biological composites and usual engineering materials can be grouped together under the concept of *architectured materials* [12]. From an engineering point of view an architectured material is an object, made of organised matter that responds to external stimuli to absolve certain functions. The way in which material is organised and combined with other materials provides their functions and effectiveness. For example, the ability of a material to float in a fluid depends on its density relatively to the fluid. The conductivity of a material is associated with its electrical resistivity and, ultimately, the atomic organization within the material that opposes electric current flow. Critically, the functionality of a desired object cannot rely only on materials properties but must also consider its geometry and architecture. The limitation of an architectured material can be sometimes overcome by varying the shape and scale of components, or coupling different components together to obtain better performances.

Both engineering and nature are adept at creating functional components sometimes achieving the same result, such as a particular mechanical property, but adopt different design strategies. Structures made of cork and steel can both float in water but steel requires appropriate processing to become a sufficiently hollow structure to float. Optimization is a critical step that defines the 'best' design strategy to achieve the required function. So the selection of cork for buoyancy is a more optimized low energy design strategy compared to the more energy intensive route of processing steel to achieve the same floating structure. It is up to scientists of different background, whether they are chemists, mechanical, electrical or process engineers cooperating towards new structural designs and improvements over micro- and macro-structures functioning.

Structure provides the framework for the distribution of materials and is demonstrated here across a range of length scales. A generic architectured material can be schematically represented in Figure 2.1. At the lowest level of the nanoscale, atoms form the material that can then progress towards microstructures. Architectured materials will use a variety of different materials, resulting in hybrid composition, with their properties causing potential gradients of functions. The resultant superstructure at the largest length scale in typically engineered systems has properties that are controlled by the composition and at the smaller length scales.

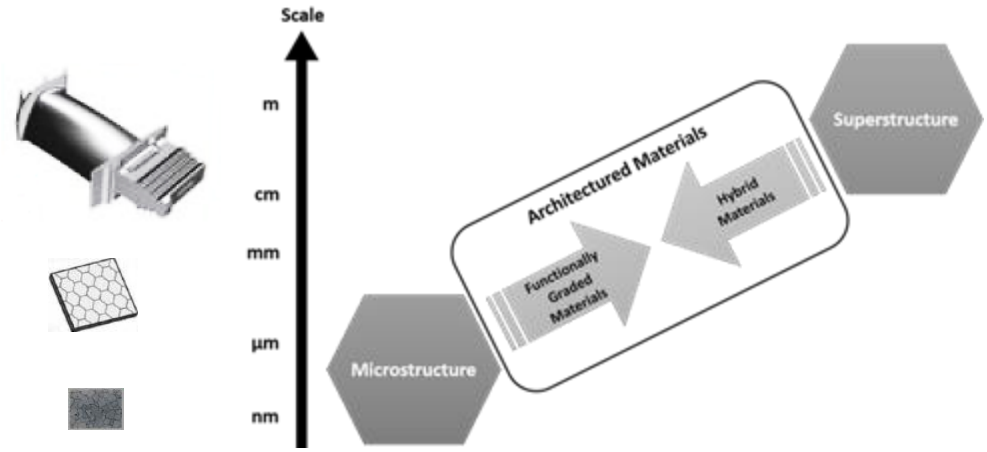

Figure 2.1. Schematic showing the relationship between multiple length scales, the potential for functional grading and the use of multiple materials to produce hybrid materials [12] [13].

2.3 Man-made versus biology

A rope is an example of architectured material as described in Figure 2.2. The rope function is well defined and must be of relatively high strength to resist failure under axial loading. The architecture exploits an organization of fibres that are twisted

together, as shown in Figure 2.2. These fibres are typically natural, polymeric (such as nylon) or steel [14]. Strength and flexibility are defined by the materials of the fibres as well as the braiding and the angle of organization between the fibres. Further functionality such as electrical conduction is achievable notably by using steel fibres in preference to natural or polymeric fibres. Additional hybrid materials can be exploited by using coatings to insulate the electrically conducting fibres from external environment. Thus, a relatively simple function can be extended towards multiple functionalities and performance through varying a number of parameters.

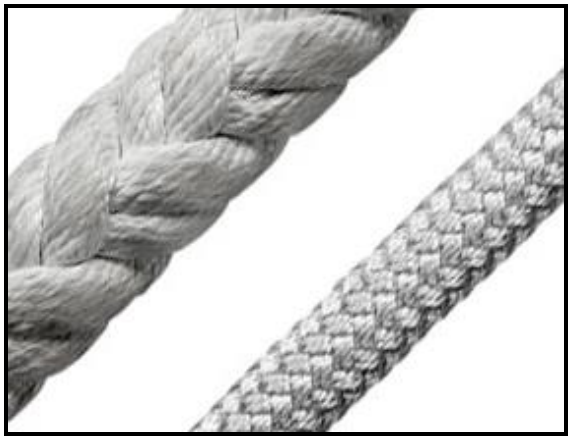

Figure 2.2. Two ropes are presented above as an example of an architectural materials. Mechanical properties under uniaxial loading depend on constitutive fibre thickness, material and braiding.

Nature extensively uses design strategies that employ architectured materials to fulfil desired requirement, often with a restricted set of elements. While biological processes are quite different to manufacturing techniques used in engineering, the resultant structures highlight similarities in both approaches. Indeed, the effectiveness of nature to provide optimized function is a strong motivation to engineering application.

An example of a material used extensively in nature and organized for mechanical function is collagen. Collagen is considered here because of its versatility, adopted by biological composites over different length scales and used in several tissues and organs [15], in order to achieve structural integrity as well as a remarkable range of mechanical properties depending on the functionality of the final formed tissue. Collagen constitutes the principal load-bearing component within biological structures not because of the intrinsic strength, but for being the principal load-bearing component found within blood vessels, tendons, bone, muscles and many other anatomical locations [16]. At the molecular level, collagen has a triple helix structure made strands which composition varies according to the biological tissue they belong to. Collagen differs among biological tissues relying on twenty types of amino acidic configurations, organised into fibre-forming collagen systems at the microscopic hierarchical level called a collagen fibril. Fibrils aggregate into fibres that are ubiquitous in biological organisms. Collagen molecules affect the final shape and mechanical properties of fibrils, which show different striations depending on the constitutive collagen chains that are directional and staggered in periodical patterns to allow molecular bonding. Anisotropy of the resulting tissues depends on the formed hierarchical fibre network dimensions that can vary from one-dimensional patterns (i.e. the fibres are all aligned along the loading axis) within tendon and ligaments, whereas two-dimensional or more complex patterns can be found in more compliant tissues such as skin and blood vessels. Mechanical properties of collagen such as elastic modulus, maximum strain and maximum strength are of the order of 1-1.5 GPa, 10-20% and 70-150 MPa, respectively but can vary more both in the resultant tissue, due to the organization of the fibre units, as well as notably molecular variations specifically due to crosslinks between molecules from aging [17].

A comparison can be made between the rope and tendon to consider the mechanical functions from similarly ordered man-made and biological hierarchical architectures. Tendon passively regulates muscle force that is transmitted to the bone and provides stability during body motion. Effectively this requires tendon to resist failure in tension in a similar manner to a rope. However, specific mechanical functions vary according to the loading conditions provided from the anatomical location. Fingers are stabilised by tendons, for example, while writing whereas others tendons behave as springs during physical activities allowing muscles to generate higher forces. The mechanics of tendon shows initial low stiffness to allow a flexible range of movement at low loading but then this increases towards high stiffness at larger displacements to resist excessive deformation that may cause damage [18].

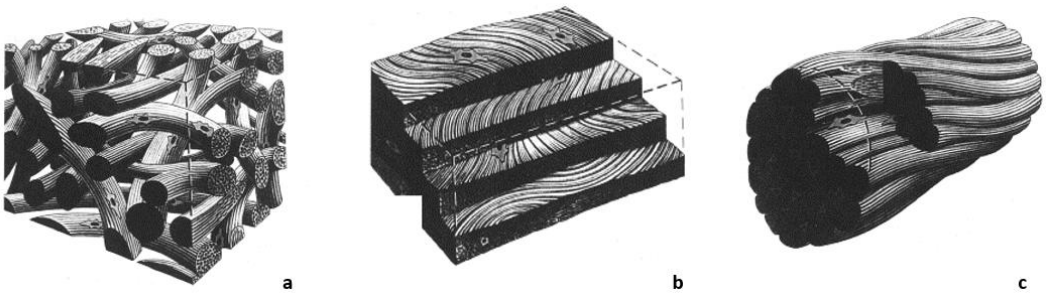

Figure 2.3. Schematic showing three types of arrangement of collagen fibres. a) a random organization of fibres in dense connective tissue, (b) sheets of fibres formed in ligaments, (c) aligned fibres found in 'rope-like' tendons [19].

The hierarchy in tendon is critical in defining the resultant mechanical function that is required at the anatomical location. Indeed, connective tissues achieve mechanical performance through the assembly of natural polymer macromolecules into collagen fibres existing at micron length scales, which then form a number of differing

specialised architectures [20]. Figure 2.3 shows a variety of collagen fibre architectures representative of tendon as well as complex organizations that are found in other anatomical locations requiring dense connective tissue as well as ligaments. Despite ligament and tendons are structured in a very similar way the effects of their mechanical behaviour is different because of the specialised function in musculoskeletal systems [18]. Particularly, the tendon triggers joint movement during muscle contraction transferring the load from muscle to bone whereas the ligament aims to stabilise joint movements stiffening trough torsional and tensional loading actions, bridging bone to bone systems. Although a critical difference in their structural composition is pointed out in Figure 2.3b and 2.3c both tendon and ligament are made of parallel aligned collagen fibres to accomplish their mechanical function. The reason why the tendon is shaped as a rope is to withstand to frequent superior tensile forces generated from muscles, absorbing impulsive activation while maintaining flexibility to prevent muscles failures. The ligament is recruited to avoid joints dislocation and injuries showing restricted elongation within the physiologic region after which they become rigid. Tendon and ligament activities have been extensively investigated through mechanical tensile tests, appropriate to verify their mechanical behaviour because coincident with their mechanical biological functions. Examples of typical tendon or ligament force-elongation (a) and stress-strain (b) curves are displayed in Figure 2.4 to provide a typical collagenous tissue mechanical behaviour. In particular, the stress-strain plot considers nominal stress (σ) and strain (ε %), respectively defined as the applied force divided by the nominal area of the specimen, the first, and the difference between stretched length and initial length of the ligament divided by its initial length, the second.

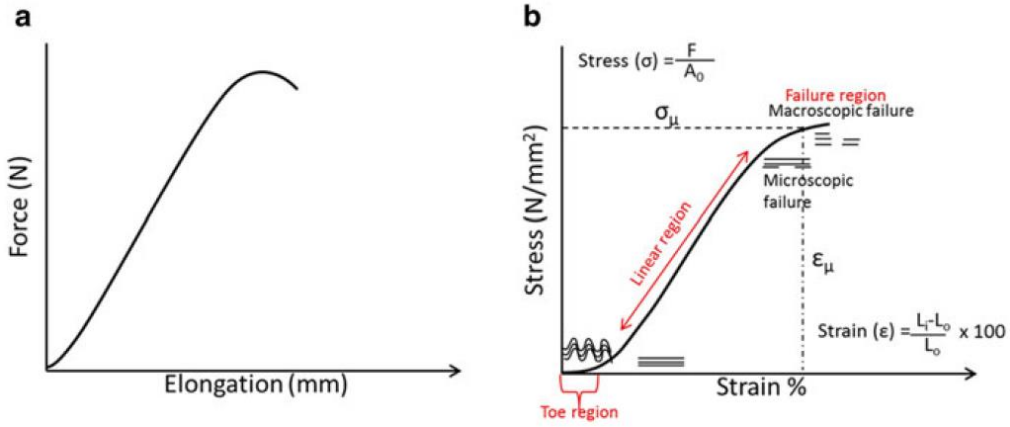

Figure 2.4. A sketch of two graphs, (a) force-elongation and (b) stress-strain curves of ligament tested to failure [21].

Three regions highlighted in red constitute a nonlinear mechanical behaviour of the tendon/ligament: 1) compliant response to low applied loads (toe regions), 2) rapidly switching after the elongation to a stiffer behaviour (linear region) reflecting the collagen fibre resistance, 3) transition from unstressed to aligned configuration until the failure of the tendon occurs. It is important to mention that ligament and tendon stress-strain curves can differ despite both architectures use collagen fibre units that have consistent mechanica properties, but have organizations that vary and continue to vary under mechanical loading. For example, the ligament flavum, adept at controlling spine motion, stretches within the physiologic range from 5 to 50 per cent in strain, failing when loaded beyond its physiologic range typically about 70 % of stretch. Thus, the variability in the use of collagen fibres in tendon highlight control through architecture and hierarchy to produce structures of varying mechanical function [17] [18] [20] [21].

2.4 Biological design mechanical performance

Biological materials have been developed with the aim of combining relatively weak constituents into remarkably mechanically efficient structures [22]. Nature is adept at satisfying vital functions assembling a restricted number of primary constituents such as biopolymers, minerals, ions and crosslinking agents. This basic building blocks can be assembled over several length scales and growing up functional systems in compliance to a so called bottom up approach. From a mechanical standpoint, the building blocks are not distinct and are taken from the local environment that the organism inhabits. The assembly of these chemical elements from the local environment is additionally limited in terms of the manufacturing processes as high energy routes, such as elevated temperature or significant electric current, are avoided in any biological system. Despite nature lacking such processing variables used for metals, polymers and ceramics, resultant materials and structures are comparable in efficiency to engineering materials [23]. The benefit of biology is the ability to produce structural systems that have considerable complexity due to the bottom up approach that is lacking currently in engineering. Furthermore, environmental conditions apply physical and resultant biochemical inputs that cause tissues to respond and adapt to these environmental conditions. A consequence is the adaptability of a living system to the surrounding environment due to an intrinsic customized design that remodels and heals itself to survive.

Most of the materials present in nature are accepted as self-assembled composites grown in a bottom up fashion by nature [24], made of a soft matrix (bulk) combined with high aspect ratio reinforcement parts (fibres). The density and distribution of a single element whether it be collagen, keratin, lignin, is a result of an evolutionary

processes so that certain basic engineering concepts, such as stiffness, viscoelasticity, strength and toughness can simultaneously cooperate in the same biological structure [25]. As previously discussed, collagen, for example, is an example of a ubiquitous protein that differentiates over twenty configurations within human body. The collagen differentiation allows soft and hard tissues to contribute simultaneously to different mechanical functions and activation mechanisms in human physiology. Arrangements of collagen vary in length from a few Ångstroms where tropocollagen macromolecules self-assemble into fibrils, which aggregate into fibres and further into fascicles. The collagen then produces large scale anatomical features including whole tendon, ligament, bone, skin, blood vessel, muscle, cartilage and cornea [26]. The mechanical performances of these collagenous structures are shown in Figure 2.5 and highlight how the single material of collagen can use hierarchical organization to provide a wide range of mechanical function [27].

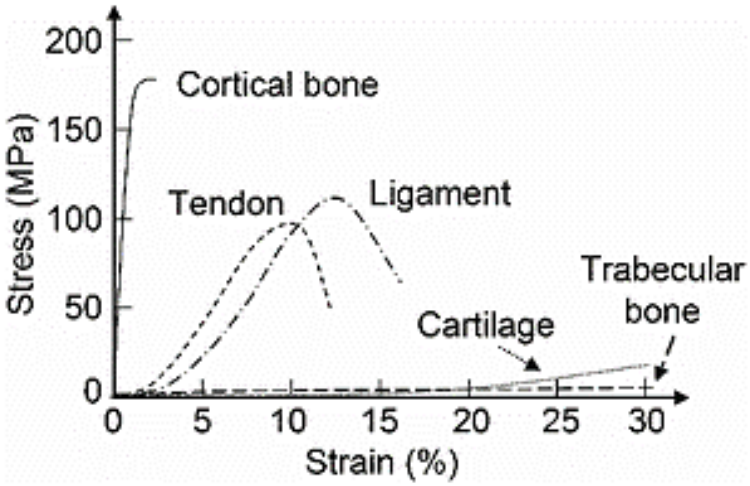

Figure 2.5. The mechanical performance of a range of collagen structures found in the human body [28].

A comparison between biological materials and engineering materials is now carried out in order to highlight the potential advantage of biological design. Intrinsic materials properties are typically described by density, ρ, Young's modulus, E, strength, σ_u, and toughness, J_c. Comparing performance between biological and engineering materials can be done using these intrinsic properties. For example, the Young's modulus of elasticity is similar for collagen fibres and polyethylene; Hydroxyapatite formed in bone is similar to engineering ceramics and lignin hemicellulose matrix in trees has a similar stiffness to many epoxy plastics. Such use of intrinsic material properties is beneficial in highlighting distinct mechanical benefits of biological materials. Cellulose fibres found in trees and plants have a density ρ six time smaller than mild steel (7.9 Mg m^{-3}), but have a strength comparable to steel. The elastic modulus of cellulose is half that of steel but, again, the considerably smaller density of cellulose compared to steel highlights efficient specific properties. The highly ordered molecular organization in cellulose provided bioinspiration, following liquid-crystal strategies, in the production of Kevlar [29]. Kevlar in the form of fibres is a high performing and lightweight material used both in textiles as well as reinforcement in polymer composites. The highly oriented molecular structure makes Kevlar the stiffest (200 GPa) and strongest (4 GPa) engineering plastic, with properties exceeding many metals and their alloys. A way to directly compare materials of different nature was developed first by Wainwright in order to describe and compare the energy absorption capacity $U = \sigma_f^2 / 2E$ of both engineering and biological materials plotting strength against elastic modulus (Figure 2.6). Figure 2.6 uses a logarithmic scale to ensure that a wide range of materials can be evaluated on a single plot. Materials belonging to the same family (i.e. various shells) are grouped in clusters, whereas

comparable materials such as keratin, chitin and steel are included in-between dashed lines.

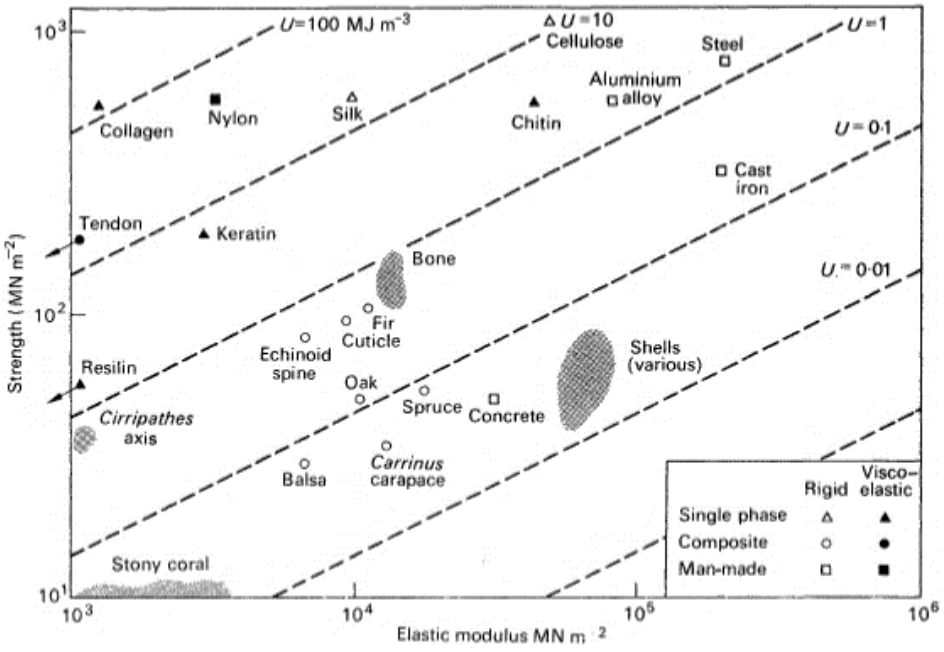

Figure 2.6. An example of a material property chart for both engineering and natural materials showing strength plotted against elastic modulus. The guidelines group in between materials with comparable energy absorption capacity [29].

Dashed lines have a meaning and are representative of a 'so called' *performance index*. In the case of Figure 2.6 the slopes are representative of the aforementioned materials energy absorption U according to a logarithmic scale that ranges from 0.001 to 100 MJ m^{-3}. A higher value indicates better satisfaction of a material in fulfilling a specific task [1]. $U = \sigma_f^2 / 2E$ is not the only performance index to refer to when choosing a material to be employed for particular needs. Figure 2.7 shows an up to date materials chart that plots Elastic Modulus against Density. The graph compares *shaped* materials according to three ratios representative for a particular mode of load: E/ρ, $E^{1/2}/\rho$, $E^{1/3}/\rho$, which represent a material in tension, beam in flexure and plate in flexure, respectively.

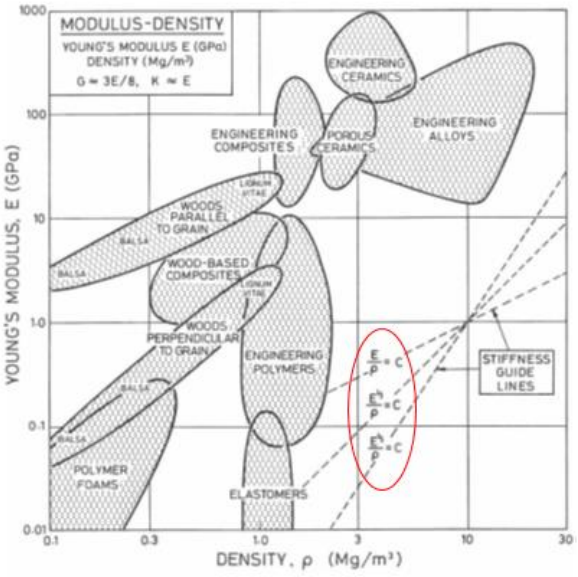

Figure 2.7. Material property chart for engineering materials. Highlighted in red the material indices onto their respective trendline [30].

In practise, biologically developed materials prone to certain mechanical activities and explains why the overall material system grows according to a certain shape. Palms and bamboo, in example, belong to the family of natural cellular materials, which are mostly anisotropic, with high volume fraction of voids and oriented fibres [30]. Palms are comparable to beams designed to comply bending, gaining with high deflections to reduce the drift of the wind on the fringes that align in a stream line shape. Checking on the graph shown in Figure 2.7 and drawing a line parallel to the $E^{1/2}/\rho$ (beam in flexure) in correspondence of *woods parallel to grain* and *wood-based composites* clusters, we can deduce that beams made of these materials perform better that engineering alloys beams because of the lighter weight of wood that provides the same stiffness as an engineering alloy.

2.5 Bioduplication versus biomimicry

The efficiency of biological materials in terms of distribution and mechanical control is critically described through biological information held within DNA. Two of the most prevalent and heavily researched biological composites that highlight a critically effective links between organizational information and mechanical function through the use of a complex system is cortical bone and nacre. Cortical bone and nacre are hierarchically organised into mineralised composites so that their architectures can achieve outstanding toughness under tensile loading conditions [31] [32]. Other biological composites include fish scales, shark and human teeth that are evolved structures organised to oppose wear and abrasion [6] [7] [33]. From a nano-structural point of view, mechanical functions are due to stress transferring from matrix to fibres ensured by nano-dimensional design parameters. It is over nano- and micro-dimensions that for instance, fibre/platelet aspect ratio makes the difference in limpet tooth to be one of the best load-bearing resistant architecture known [34] and nacreous shell particularly tolerant to flaws [11]. Understanding the structures of a biological organism can lead to two approaches towards improved systems. The first is bioduplication and is essentially a direct copying of the materials, processes and organizations that are used to produce a biological composite. For example, using hierarchical constituents to provide nano-composites for better performance at the organ level is effective in healthcare applications [7] [35]. Bio-mimicking is about replicating macro-blocks interactions of a certain functional system. Bioduplication is perhaps limited as the constraints in biology, such as using a low energy processing process and access to a limited number of elements, seldom are met. Conversely, biomimicry requires an understanding of a biological composite and, through this understanding, development

of a structure with enhanced mechanical properties relative to the constituent materials through incorporation of identified key features in manufacturing techniques. The field of bioinspiration is also known as biological inspired design [31] and is a relatively young field of study embracing the practical use of mechanisms and functions of biological science with mechanical engineering and the design of composites. Bioinspiration has a historical basis including the design of flying machines through consideration of bird mechanics by Leonardo Da Vinci [36]. Such an approach to flight is relevant today. For example birds with wings of low aspect ratio are inspiring models of drag reducers [37]. Materials science aims to develop hybrid structures inspired by nature oriented to specific applications, where building blocks combine their respective contrasting mechanical properties in one functional material system. Controlling structural key features, at any level, is essential for achieving the desired set of properties.

Biological composites are ubiquitous and widely accepted as optimised structures in terms of mechanical function and the assemblies of inorganic (hard) and organic (soft), permit to achieve plenty of different mechanical functions. Bioinspiration relies on synthetizing biological materials and alternating hard and soft building blocks over different length scales. Especially at nano and micro-metre length scales, the presence of complex architectures can achieve mechanical behaviours by far exceeding the mechanical properties of their primitive constituents [38] [39]. Thus, retrieving key features and parameters from biological composites is the first step towards the design of tough and strong architecture materials. Bone, sea creatures and turtle shells are particularly prevalent in the biomimetic literature [40] [41] [42] [43] [44] [45] due to how biology puts together contradictory requirements so that the resulting architectural

design is sufficiently stiff and tough to support a load or to resist crack propagation. Insights into the biological biocomposite constituents at sub micrometre length scale, are necessary if a reliable replica of activation mechanisms is meant to be designed, and specific examples of structures produced by biology within this group constitute an inspiration for this work. From automotive to aerospace, from ballistic to medical fields, industry is relying on AM and its freedom in prototyping parts and components according to targeted mechanical function, more often dealing with biocompatibility. However, virtual 3D geometries with almost arbitrary shape and complexity, can be grown adding material where needed [46] overcoming limits of classical manufacturing such as mould jetting and CNC machining, common techniques already used in the past to reproduce bio-architectures [47]. AM instead, follows the same approach of nature shaping objects in a bottom up fashion, from sub-millimetre scale of the building blocks of which tissues are made of, scaling up to entire system level. Nowadays hybrid materials can typically reach length scale of the micron range, but the smaller the dimension of the particles the harder becomes distributing the reinforcement according to desired pathways. Nanoparticles are commonly used for bioinspired composites where engineered constituents rival similarly small constituents, respectively contributing for a target mechanical function. For example, platelet-reinforced films were fabricated in order to reproduce synthetic nacre relying on a sequential deposition of inorganic alumina platelets and organic chitosan polymer [48]. A colloidal-based technique was employed to assembly inorganic building blocks in an oriented two-dimensional structure. Limits related to the composite inorganic inclusion were reported. In fact, the process used for this study restricted platelet volume fractions of more than 20 vol%, due to consequential platelets misalignments and voids incorporation within the film. Freeze casting techniques were employed to form porous

ceramics, complex in shape and architectures. Ceramic were filled afterwards with relatively soft organic phase of Poly (methyl methacrilate) PMMA used as non-load-bearing lubricant. The maximum alumina contents related to this technique were of the order of 20 vol% with control on the reinforcement particles dimensions but no control on the reinforcement geometrical shape [49].

2.6 Biological design of nacre and bone

The previous sections detailed a number of biological structures that use materials available to biology organised to give a range of effective mechanical properties. Bone and nacre are perhaps the most heavily researched biological structures in terms of medical importance and efficient toughness, respectively. This section provides details of bone and nacre as well as general biomineralization processes that cause the formation of composite structures.

Biomineralization is firstly considered here as a process by which organisms form minerals within bone, nacre as well as most other high performance biological composite structures. The term biomineral refers not only to a mineral produced by organisms, but also to the fact that almost all of these mineralised products are biological tissues including both mineral and organic components [50]. Biomineralization is the principle by which most of living creatures evolved, whether they are vertebrate or invertebrate, improving their mechanical resistance during activities such as rasping, piercing and crushing [22]. The energy absorption of the composite is defined as the amount of mechanical energy absorbed per unit volume when the composite is deformed up to failure [43]. The key of both structural toughness

and resistance to cracking of biological composites can be found not only in the hierarchical arrangements of their biological tissues but also by the dimension of the primary constituents, generally at the nanometre length scale. Human bone, mollusc shells and limpet tooth provide excellent and reliable examples of toughening mechanisms confirming the important interaction between soft and hard materials composite primary constituents [31] [34] [51] [52]. Single man-made materials such as steels, aluminium and alloys are frequently chosen in structural engineering for their large toughness so that they can absorb a given impact energy or carry a load without failing. As opposed to metals, biological materials, ceramics and polymeric materials do not individually exhibit the same unique combination of properties. Biology exploits solutions by assembling combinations of components resulting in exceptionally efficient hybrid materials. The effectiveness of material combinations result in many biological structures outperforming engineering materials properties, such as the strain energy per unit of mass being higher in spider silk than steel or rubber [30]. Most of mineralised tissues have a staggered arrangement so that the resulting structure is organised in overlapped mineral components, transferring loads via shear stresses through the polymer matrix-platelets interfaces [53]. Toughness is critical here, so that crack emanating from initial defects in the shell can be resisted, effectively making the material damage tolerant [47]. The nacreous layer of shell uses a high volume fraction (95%) of ceramic (aragonite) platelets and a thin layer of protein and polysaccharide resulting in a non-brittle material, characterized by a work of fracture 3000 times greater than that of pure ceramic [54].

Biological composites that are strong as well as tough are can be described by by the bone where the above discussed collagenous fibrils structure is reinforced by

hydroxyapatite platelets. Studies about protein-mineral interfaces and toughness deriving from structural orientation effects, have been carried out attempting to understand the mechanical performance of this impressive wear resistant and load bearing structure [25] [51]. Other notable example of strong biological composites are found in the teeth of limpets. Limpets have developed methods for scraping algae adhered to the rock during feeding activities. Protruding its tongue (Radula) from the mouth, it employs robust teeth for mechanically rasping across the rock surface. The limpet tooth is an impressive example of discontinuous fibre-reinforced (Goethite) polymer (Chitin) composite, easily comparable with man-made composite designs such as carbon fibre in an epoxy matrix [34]. The strategy of nature to create structures that pierce, inject or crush in both vertebrate and invertebrate species usually involves biomineralization and is therefore fairly ubiquitous.

2.6.1 The structure of nacre

Molluscs started the design process of the protective hard shells 545 million years ago giving the birth to 60,000 species different in sizes and structural organization depending on the hosting environment [11]. The shells of molluscs can be classified as a structural mineralised material developed to resist impacts. Hierarchically organised, the protective hard shell is mainly composed at macro-scale by two layers: a nacreous layer in the inside covered by a hard calcite layer (Figure 2.8).

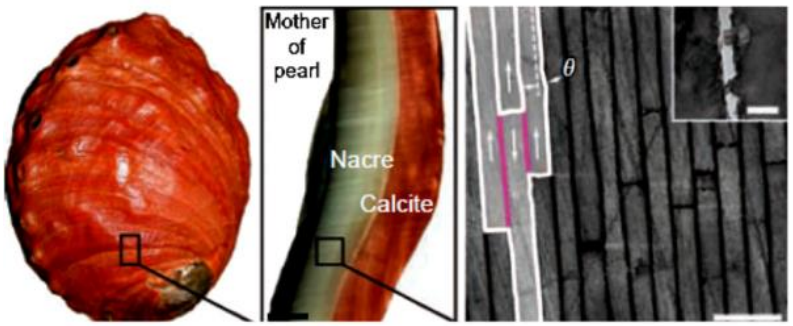

Figure 2.8. Hierarchical structure of Abalone nacre exhibiting two-level crossed lamellar micro-architectures [55].

The mechanical properties of nacre have been studied extensively [56]. This two-layers armour system attracted the curiosity of scientists interested in biomineralized models to be considered for novel design concepts of artificial materials [22]. Nacre especially has been inspiring engineers and material scientists because of its ability in dissipating mechanical energy through inelastic dissipation and cracks deflection. The importance of nacre and its structured micro-design is advantageous since the predators store strain energy that is released, such as through an impact, in order to fracture the nacreous structure [21] [57]. The resultant composite is tough, damage tolerant and ensures protection of molluscs from predators and hydrostatic pressures [10]. The toughness of nacre has been consistently noted as comparable and, in some cases, better than engineering high performance analogues. Therefore, nacre has been attracting the attention of the material science community due to its intrinsic toughening mechanisms responsible of improvement in impact resistant performance over its main constituents, dissipating energy and preventing crack catastrophic propagation [22] [29].

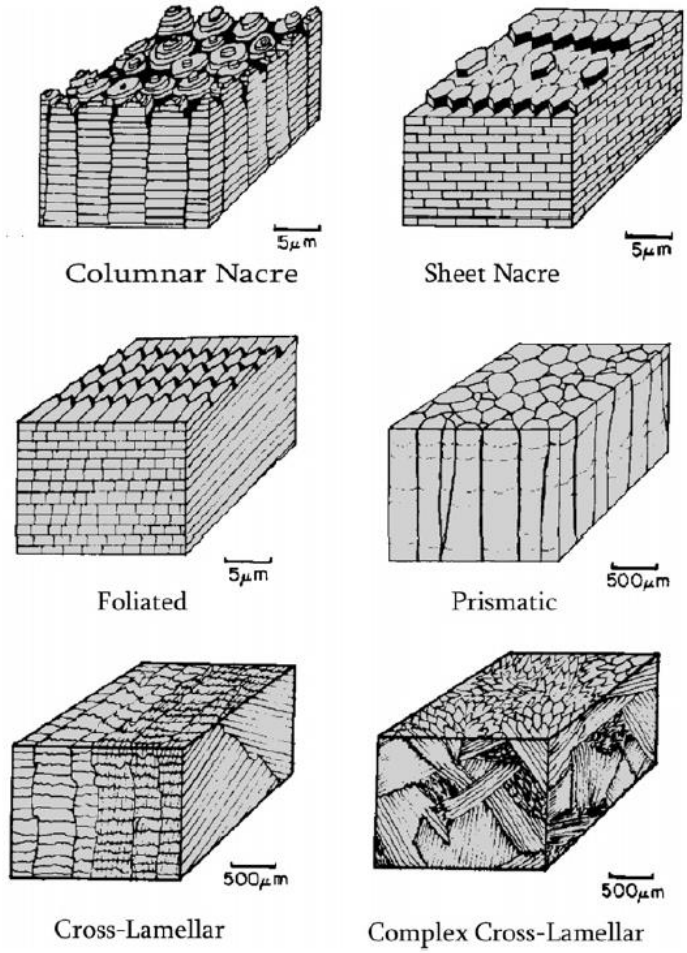

Figure 2.9. Various mollusks shell architectures all of them showing a mineral content of at least 95% [58].

The nacre opposes to a catastrophic failure by stopping cracks due to polygonal aragonite tablets embedded in a thin polymeric bulk. The platelets can be staggered in different fashions depending on the variety of shell structures (Figure 2.9). Mineral content represents the 95% in weight of the nacre and can be interlaced in prismatic, foliated, columnar, cross-lamellar, homogeneous and many other designs. In most of the cases, the mineral lamellae are adhered together by the 5% remaining part of the biocomposite made of protein [25], without which, high toughness and cracks stopping mechanisms would not be possible to take place. Shells mechanical properties can vary according to the different mollusc families. It had been revealed how the elastic

modulus and strength range over 20 different species from 40 to 70 GPa and from 20 to 120 MPa, respectively [59].

Mechanical testing conducted on a variety of bivalves, gastropods and cephalopods have shown stress-strain curves generally made of an elastic region that anticipates a plastic behaviour before nacre fails under tension. Furthermore, the effect of the hydration can influence the mechanical properties such as strength, elastic modulus and work to fracture [15] (Figure 2.10). The elastic modulus can reach values of approximately 60 - 70 GPa depending on the dry or wet condition of the sample and the strength varies from 60 MPa of a not nacreous shell to 120 MPa of the shell colled "Turbo" [37] [60] [61] [10].

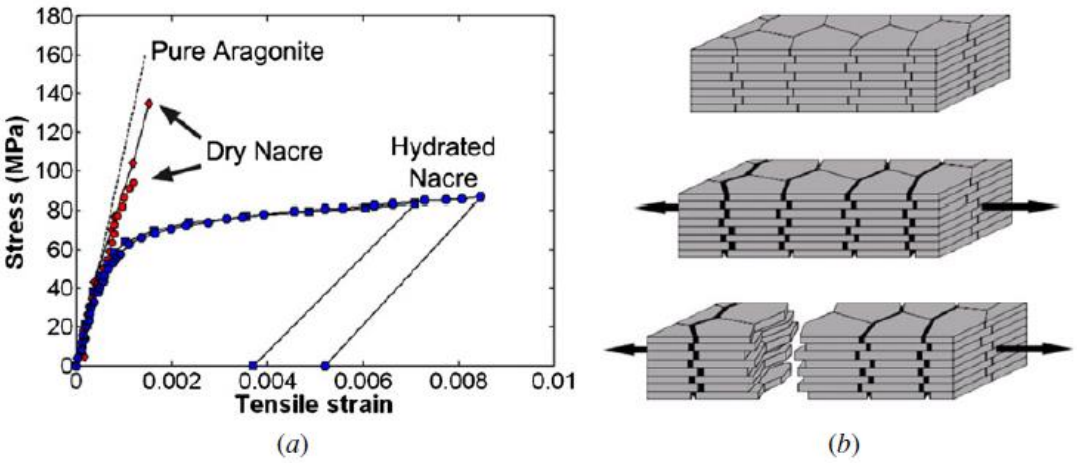

Figure 2.10. (a) Stress-strain curve of pure aragonite, dry nacre and hydrated nacre in tension. (b)Tablet sliding mechanism at microscale justifying the relatively large strain in the case of the hydrated nacre [47].

Interestingly, the work to fracture can be 3000 time higher if compared to monolithic calcium carbonate and it can rise up to 1240 J/m^2 for a wet nacre sample to be compared with the approximately 350-450 J/m^2 if the test is conducted in dry

conditions [62]. Standard four-point bending had shown nacre toughness values of 8±3 MPa accompanied by a fracture strength of 185±20 MPa [63].

At the micro-level, the distribution of the nacreous hard and soft building blocks is meant to be parameterized in such a way that the mineral platelets can carry most of the tensile load, meanwhile the protein bulk transfers the load between the hard phases via shear. According to a previous study [17] the integrity of the composite together with its toughening properties is related to a complex fracture path driven in between the platelets that should pull-out platelets instead of fracturing them, increasing the fracture surface area of the entire structure. The high stiffness of the bio-composite is related to the high aspect ratio of the hard platelets, which compensates the low elastic modulus of the protein bulk. Under load, the mechanism by which a crack propagates in the mortar layers after a linear elastic region, is verified only with an increase in force. The explanation can be found in the crack driving force that is not increasing with the crack length when propagating within the interface. Therefore, the failure mechanism is characterized by a massive energy dissipation pointed out by stress strain curves in which decreasing peaks are indicators of cracks deflections propagating in the next interfaces.

It is unclear, how the fracture energy required to break the shell of nacre is several orders of magnitude higher than that of the mineral constituents, despite their stiffness is quite similar [61]. Overall mechanical properties of a structure can be described by hardness measurements but no information concerning nano-scale interaction of the building block contribution rise from this kind of experiment. The brick and mortar structural organization of nacre is interesting because the aragonite reinforcement bricks vary around a few hundred nanometres, ensuring integrity and

optimized strength of the composite structure. A convincing design of the mineral platelets was considered with possible flaw inclusion attributable to protein molecules [11]. Starting from this statement, a hypothesis about a fracture strength optimization mechanism has been postulated so that brick components are constrained to the nano-scale. When the mineral size exceeds this length scale a failure by stress concentration at the crack tip is possible. As a result, this optimized design generates a mineral phase able to sustain large tensile stress without fracture, cooperating with the protein layer in an interfacial system that sustains the shear stress without failure [17] [54] [63] .

2.6.2 The structure of bone

Bone is a specialized connective tissue consisting of various different components highly organised across different length scales. The skeletal structure is made of bones which are dynamic. In most cases bones are vascularised, able to rapidly mobilize mineral stores, changing shape and continuously remodel according to the metabolic demand. Like any other connective tissue, bony material is mostly characterized by an extracellular matrix that confers rigidity and mechanical strength to the organ, consequently to mineralization processes. The calcified tissues within bone must satisfy two separate functions: physiological function that includes calcium storage to control the metabolic balance (homeostasis) and mechanical function to withstand loads, hence allowing movements as well as protecting internal organs.

Thus, bone tissue has to be rigid to avoid an excessive deformation and strong for dissipating energy from shocks. According to other biological systems, several components populate the bone hierarchy. Particularly, bone is the result of a summation

of phases, architectured on at least 5 hierarchical levels: *whole bone*, *architecture*, *tissue*, *lamellar*, and *ultrastructure* level (Figure 2.11). Each level depends on the lower levels to provide function and structural support, despite mechanical properties are not constant in each structural reference frame [64].

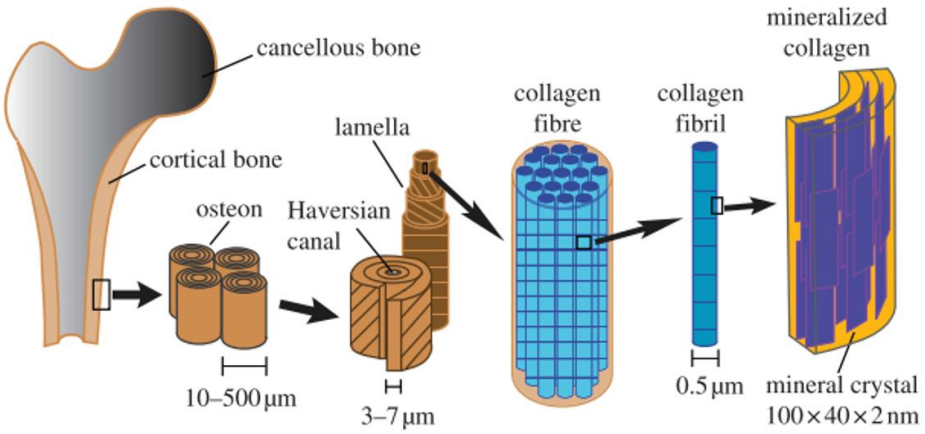

Figure 2.11. Representation of the hierarchical structure of bone. In particular the reported example refers to a femur that is a load-bearing biological material [65].

Primary and secondary ossification (known synonymously as osteogenesis) [26] [66] [67] are the two main stages of bone formation, mainly involving three cellular activities: the chondrocytes producing cartilage for ossification in early stage, the osteoblasts secreting collagen to form bone organic matrix that then differentiate into osteocytes embedded in bone tissue and the osteoclasts that dissolve and absorb old bone tissue for remodelling [68]. An example of growth process of long bone is shown in Figure 2.12 [66] [69] [70]. A "woven" bone microstructure is formed during this rapid and unorganised mineralization in which the mineral component does not form in close association with the collagen and no regulated structures are formed [71]. The

bone material produced during this process is called primary bone, which is usually found to exist shortly in the early development stage.

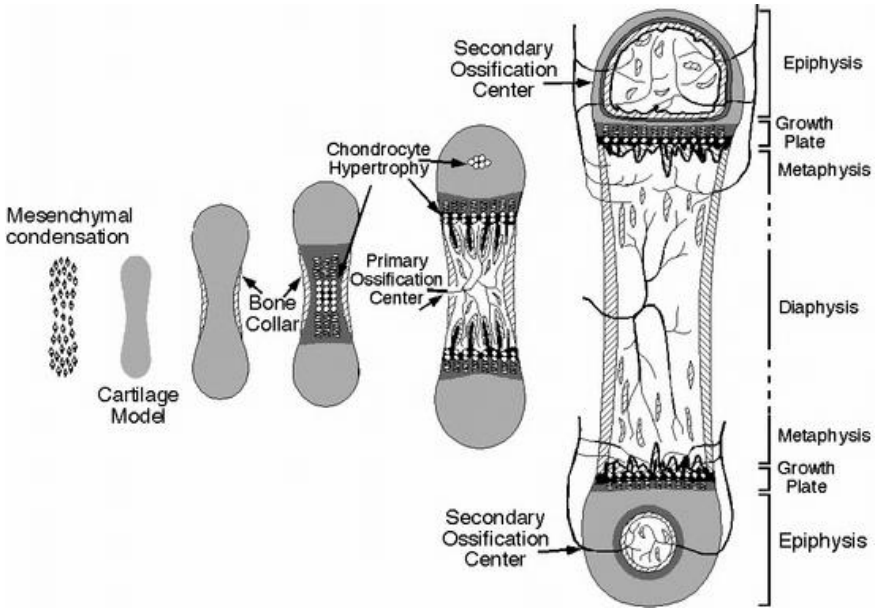

Figure 2.12. Schematic diagram showing the stages of endochondral ossification [72].

The primary bone can be also found in later development stages when skeleton is healing from trauma. The initiation of secondary ossification occurs at each end of long bones where the mesenchyme and blood vessels are developed in a similar process to primary ossification. The changes in the primary bone material structure, referred to as bone remodelling, form bone material called secondary bone [73]. The shape of whole bone is therefore defined by the activities of osteoclasts and osteoblasts. As their main constituent, bone tissue supports a fleshy structure that harbours the bone marrow. Within the medullar cavity of long bones and the interstices of cancellous bone, blood cells are formed. Bones come in a variety of shapes and have a complex internal and

external structure. Bones are lightweight, strong and hard, able to fulfil many other functions such as acid-base balance, detoxification and sound transduction.

One step below the global or organ level of the bone is the *architecture* level where microstructures are contained and distributed over the micro length scale and serves to provide mechanical stability to the entire structure of bone. The two distinct architectural regions (75÷300 μm) are *trabecular* bone, generally occurring at the ends of long bones, and *cortical* bone in the concentric shaft of long bones [64] [68] (Figure 2.13).

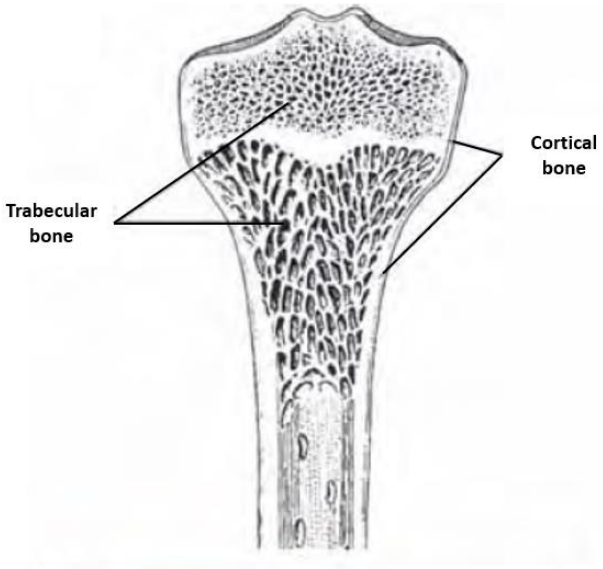

Figure 2.13. Longitudinal section of a femur showing the combination of trabecular and cortical bone architectures [15].

The proportion of these two architectural forms differs depending on where they are located into the skeleton. Cortical bone is almost solid, being only 10% porous, and can be divided into different subgroups: long bones (femur and tibia), short bones (wrist and ankle), and flat bones (skull vault and irregular bones). On the other end, trabecular bone presents a higher porosity, 50–90%, making its modulus and ultimate compressive

strength around 20 times inferior than that of cortical bone. Trabecular bone is arranged in a sponge-like form, with a honeycomb of branching plates and rods of various sizes called "*trabeculae*". Trabecular bone is found in metaphysis of long bones, covered by cortical bone and also in the vertebral bodies [66] [67]. Morphological factors such as trabecular thickness, density, and bone surface to bone volume ratio, which can analysed from imaging techniques, are related to the organ mechanical strength [74].

A central feature of compact bone is the cylindrical shape of the osteons parallel to the bone long direction. The osteons are formed during remodelling of primary bone into secondary bone and are initiated by osteoclasts removing primary bone material. Such dissolution forms channels that are subsequently filled by osteoblasts. Other smaller capillary-like features (canaliculi) are also built into the structures and connect trapped osteoblasts, referred to as osteocytes. These tubular structures are also called Haversian systems named after John Havers who discovered the *lamellae* structure in 1691 [75]. Primary bone is mostly formed of primary osteon whereas the most common structures found in mature bones are secondary osteons containing high concentration of calcium phosphate crystals, reason why they are stiffer and stronger than the extracellular matrix existing in between [35] [75] [76]. Apparently, this mechanical mismatch between different phases of the compact bone appears to control toughening at large length scales (i.e. hundreds of micrometres) [77]. When a bone fracture initiates, the osteons provide a source of toughening that arises during crack growth. Hence, osteons are not inherently tough but control the propagation of cracks in bone, known as shield toughening. The crack path within compact bone is driven along brittle hyper-mineralised interfaces called cement lines [78] [79] [80] between osteons and bone matrix.

Secondary osteons coupled with the cemented lines reveals a very dense system, oriented in accordance to the long axis of the bone. A high osteons density results in a high micro-crack density concentrating on the cemented lines that explains why bone it's easy to brake but not to split. The presence of hydroxyapatite affects the stiffness of the bone, which can be mitigated thanks to molecular stretching of the collagen fibrils responsible of the enduring large plastic strain without failing in a brittle fashion. The absorbed plastic energy during a crack propagation allows to stops the spreading of the fracture and it has been identified as the main toughening strategy for the bone whom uses recoverable bonds among fibrils [43].

Despite toughening mechanisms preventing bones fractures, every year, thousands of surgical treatments are performed in order to repair or completely substitute, where possible, bony and other biological tissues affected by degenerative diseases [81] [82]. Patients with these kind of illnesses experience extensive waiting for a donor that could replace, in a short time, the damaged organ [83] [84] [85]. Furthermore, since a number of disease states and conditions exist compromising the mechanical integrity of bone, healthcare requires an effective replacement material that is able to provide suitable mechanical and biological function [86] [87] [88]. The lack of biological alternates, related to conventional surgical treatments such as autografts, allografts and xenografts led the way to innovative solutions [89] [90]. Broadly, such solutions are referred to as tissue engineering (TE) [91] and tend to bridge multiple disciplines including molecular biology, biomaterials, biomechanics and recently, design and architecture knowledge [92]. A number of routes are employed in TE, but mainly towards biological approaches where cells are included within an engineered scaffold, typically a porous material structure, which promotes cell adhesion,

proliferation and differentiation. Thus, the scaffold controls the biological processes to produce mimetic tissue.

An alternative to bioduplication is the biomimicry approach that uses parametric designs to generate the organizations found in bone or, indeed, any biological composite. Parametric design has been widely applied to the field of bone tissue engineering in order to produce customised scaffolds for trabecular bone tissue. The parameterization can occur in multiple ways, especially in the case of trabecular bone, which is supported by a large variety of libraries developed through CAD-based software. In this sense, polyhedral shapes or cells are generally considered for their practicability to be assembled in both regular [93] or heterogeneous[94] matrices. On one hand, the current state of the art seems to be represented by parametric equations able to generate 3D mathematical surfaces called isosurfaces, which visualization and manipulation can be performed in three, four, five and six dimensions [41] as in the case of regular scaffolds. On the other hand, Voronoi diagrams have been proposed to overcome limits related to the scarce natural appearance of the former category doubling the permeability and the level of biomimicry of the bone substitutes [94].

Bone is an important example of mineralized tissue demonstrating considerable mechanical performance, including resistance to compression and relatively high toughness [1], using hard mineral apatite and a range of softer materials mostly consisting of collagen. Bone substitutes typically follows two pathways where architectured biomaterials allow bone regeneration [95] or engineering structures at organ level replace significant volumes of the whole bone [96]. Additive layer manufacturing, commonly referred to as 3D printing (3DP), shows significant potential in reproducing the complexity required for replacing large bone volumes, especially due to the more recent availability of multi-jetting technology to facilitate the

production of composite structures [42]. Several works have been already introduced to the field of bioinspiration highlighting the use of 3DP where different materials are put together in one single print. The aim was to reproduce bony biological via material jetting technology topologies including a rotated bone-like geometry [97] [98] [99] avoiding problems related to multipart assembly over small length scales, typical of classic subtractive manufacturing. Inputs coming from computed aided design (CAD) are then translated in standard tessellation language (STL) embracing either simple controllable parametric algorithms to generate hard or soft phases. The challenge of accurately reproduce volume fractions above 90% of hard material within a softer matrix material still remains. Research in the field has indicated a broader approach that allows a mimetic hard−soft material composite with functionality that tends toward that of the host biological structure [98].

2.7 Composites and their mechanical advantages

The theory of composite mechanics has been established for synthetic composites and it is therefore relevant to describe the mechanical performance of biological structures. The constitutions and hierarchy of a biological structure is classified depending on the reinforcement as:

- Fibre Reinforced Composites
- Laminar Composites
- Particulate Composites

Fibre reinforcements are commonly due to their high strength and mechanical performance strongly related to the orientation of the fibres, therefore to structural

anisotropy. The resulting mechanical behaviour is always defined by the material properties of the constituents but even more from the shape, orientation, length and overlapping disposition of the fibres that exhibit the greatest strength along their longitudinal direction [100]. Toughness can be described as a material resistance mechanism that enables dissipation of stresses avoiding material fracture. The performance of biological hybrid materials can be expressed in terms of toughness and it is assessable considering architectures failure mechanisms at nano and micro-level, mostly activated by crack development and relative deflection into weaker regions of the composites. Different explanations of toughening phenomena have been developed leading to a theory also known as intrinsic-extrinsic damage conflict [10]. Intrinsic toughening is more related to plasticity associated with dislocation motion in crystalline materials, opposing to both crack initiation and propagation. Extrinsic mechanisms are only effective in resisting crack growth involving processes such as crack bridging by means of fibres or a ductile phase into composites. Generally, intrinsic damage mechanisms act at the crack tip and are defined by material behaviour to characterize the crack advance, whereas the extrinsic mechanism acts around the crack tip and is influenced by the structural organization of materials. This cooperative mechanism is at the base of the mechanical behaviour of biological structures, which are defined as damage-tolerant materials [63]. An organic framework made of collagen fibrils plays a crucial role in determining the mechanical properties of the bone and antlers of deer. This nano-template composed by fibrils with diameters ranging around less than a millimetre, allows the intra-fibrillar mineralization of carbonated apatite crystals providing a fibre composite modelled system made of collagen reinforced with minerals [101]. The result is a mechanical behaviour in which the presence of mineral phases, increases the fibre local yield, improving their stiffness.

Comparisons to synthetic short fibre composites help to describe the mechanical behaviour of biological structures, for example, expressing the elastic modulus dependence on orientation and fibre length. Furthermore, fibre reinforcement efficiency seems to be attributable to a critical fibre length [51], where stresses can be transferred efficiently from matrix to fibre resulting in fracture of the reinforcement during an external loading.

Hybrid structured materials, inspired by biological composites such as nacre shell, bone tissues and limpet tooth, could be described by fibre reinforced composite theories so far developed. The hierarchy by which both biological and bioinspired synthetic composites are organised, with a focus on the mismatching mechanical properties belonging to different but interacting material system regions, may be linked to short fibre composite theories. This permits to find insights about multi-material 3D printing hard and soft materials interaction in bio mimicking toughening mechanisms. Indeed, despite their simplicity, composites theories matrix such as Voigt and Reuss describing long fibres embedded in a soft matrix seldom find practical application in man-made hybrid materials. Nevertheless, it is important defining concepts related to the case of fully aligned long fibre composites. The reason is to define upper and lower boundaries on the elastic modulus of a composite where assumptions of uniform strain (Voigt) [102] and uniform stress (Reuss) [103] are required when the load is axially applied to the composite system. This implies load transfer via shear stress from stiff fibre embedded in a softer matrix, passing through the interface in between.

2.7.1 Long fibre composites: Voigt versus Reuss

The case of a simple long fibre composite where aligned continuous fibres are embedded in a softer matrix is depicted in Figure 2.14. The deformation mechanism to which the material system is subjected, when a force F is applied, depends on the force orientation respect to the fibre, plus the interaction between the different regions composing the system.

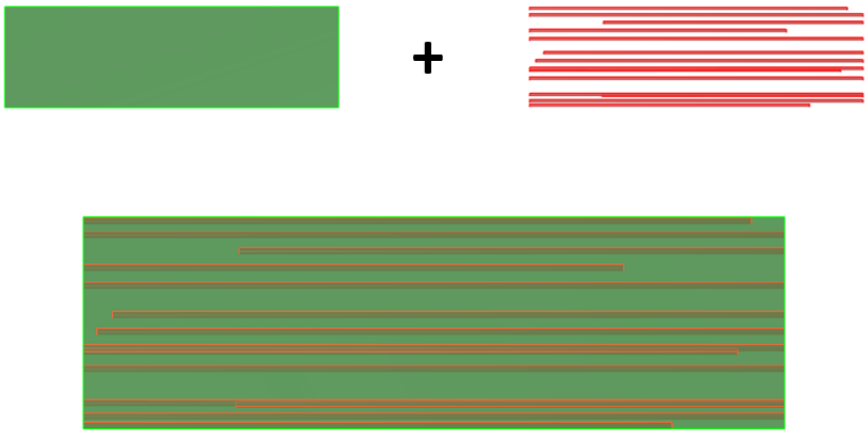

Figure 2.14. Schematic of a composite material assembly made of a soft bulky matrix (in green) and long fibre (in red).

Assuming the fibres and the matrix made of elastic polymeric materials, with the fibres being the stiffer phase, the overall deformation of the composite is determined by the alignment of the resulting tensile stress due to the applied force in relation to the reinforcement orientation and volume fraction (V_f).

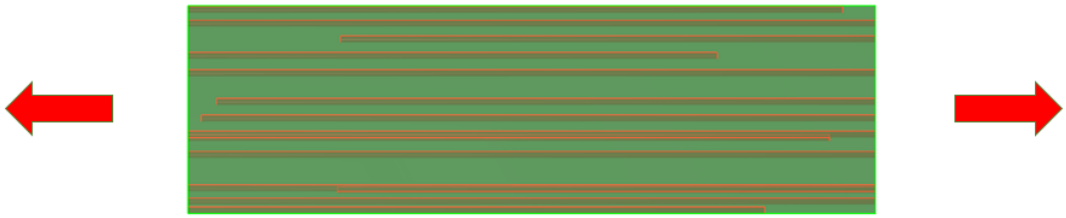

Figure 2.15. Representation of a tensile force applied to the long fibre composite according to the reinforcement direction as assumed by the Voigt model.

If the acting force F is applied according to the fibre direction as shown in Figure 2.15, the overall load F is partitioned between the matrix and the reinforcement, with the latter carrying the larger stress because stiffer and axially prone to bear larger stress which is further transmitted via shear by the matrix. Hence, a matching tensile strain between matrix and fibre can be assumed, defining a condition of *iso-strain* [102] also referred as *Voigt* model or *rule of mixture*:

$$E_c = h\,E_f + 1 - h\,E_m \quad \text{with} \quad h = \frac{V_f}{Vf + Vm} \qquad \textit{Equation (2.1)}$$

The equation above is taking into account materials volume fractions (V_x) and elastic moduli (E_x). In particular, V_f and V_m weight the contribution of fibre and the matrix elastic moduli to the overall elastic moduli of the composite E_c. Matrix and fibre superimpose their contribution to the overall composite elastic moduli which is driven by the fibre volume fraction. The acting load can be otherwise transversely applied to the reinforcement as shown in Figure 2.16, affecting the strength of the overall system which will result in a much lower elastic modulus.

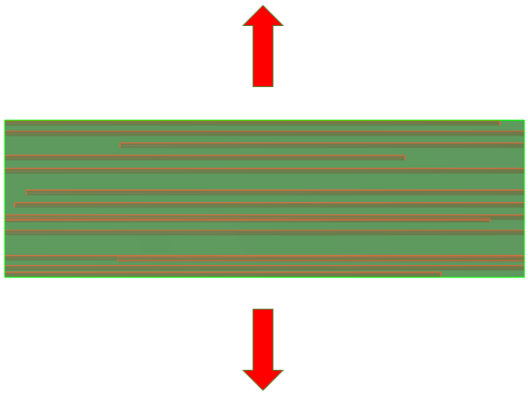

Figure 2.16. Representation of a tensile force applied to a long fibre composite transversely to the reinforcement direction as assumed by Reuss model.

Compared to the previous case, the composite phases are in a condition of iso-stress [103] and no shear is transmitted from the matrix to the fibres. This is the case of the *inverse rule of mixture* also called *Reuss* model, representing the stiffness lower bound of the composite:

$$E_c = \frac{1}{\frac{h}{E_f} + \frac{1-h}{Em}} \qquad \textit{Equation (2.2)}$$

2.7.2 Short fibre composites

Short fibre composites theories are more realistic compared to the more simplistic cases of iso-strain or iso-stress. In reality, most of the reinforcement's materials cannot easily processed to reach very long dimension when embedded into the matrix. Therefore, fibres are generally shorter than expected (Figure 2.17).

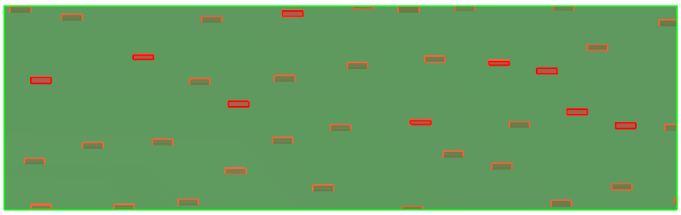

Figure 2.17. Schematic of a composite material assembly made of a matrix (in green) and short fibre (in red).

The consequence of a load applied to a composite where the reinforcement has a shorter average length compared to fibres running through the matrix, regards mostly the way in which the shear is transmitted from matrix to fibres. Especially for the case of iso-strain, the stress decreases at the fibres ends implying a strain mismatch between reinforcement and matrix which should be stronger than in the long fibre case. Therefore, the Voigt model is not valid. Among the models developed to describe the interaction between short fibres and matrix useful to quantify how the stress varies while the fibres dimension shortens, Kelly-Tyson represents a first simple analytical attempt to derive interfacial relationships [104]. It assumes a constant interfacial shear stress spread on a rigid fibre embedded in a plastic matrix (Figure 2.18)

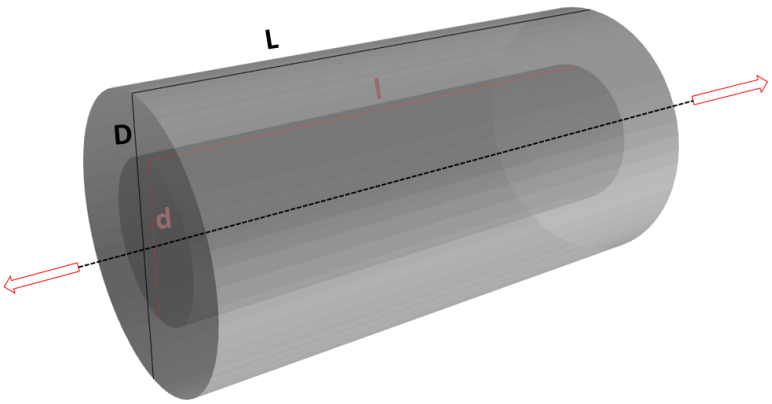

Figure 2.18. Representation of the Kelly-*Tyson model. The volume of interest is represented by the matrix (light grey) and an embedded fibre (dark grey).*

The red arrows represent a load applied according to the fibre orientation. Figure 2.19 shows a simplified region of the discontinuous fibre composite where a cylindrical fibre is embedded into the bulky matrix. The fibre is long l and thick d whereas the matrix is long L and thick D.

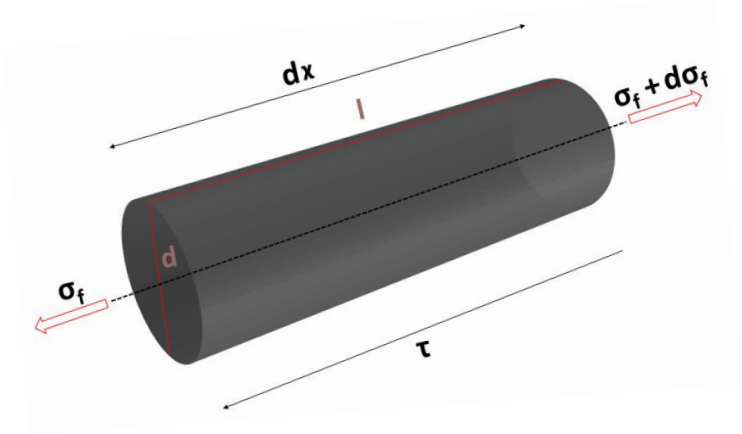

Figure 2.19. Equilibrium on infinitesimal segment of fibre subjected to external load.

$$\sum F_x = (\sigma_f + d\sigma_f)\left(\frac{\pi d^2}{4}\right) - \sigma_f\left(\frac{\pi d^2}{4}\right) - \tau\,(\pi d)\,dx = 0 \qquad \textit{Equation (2.3)}$$

By solving the equation above it can be pointed out that:

$$\frac{d\sigma_f}{dx} = \frac{4\tau}{d} \qquad \textit{Equation (2.4)}$$

Hence, the fibre stress is:

$$\sigma_f = \frac{4\tau}{d}\,x \qquad \textit{Equation (2.5)}$$

A practical explanation of the above stress analysis model is shown in Figure 2.20 where a fibre embedded into a matrix is subject to axial load. The matrix transmits shear

stress to the fibre through the interface, which is balanced by the tensile stress that gradually grows inside the fibre. The mechanism is balanced since the shear stress in the interface is maximum at the fibre ends and zero at the centre. The opposite can be said for the stress that grows into the fibre, which reaches the maxim value at the fibre centre and it is almost zero at the fibre ends. The higher the adhesion between fibres and matrix the higher the stress that grows along the fibre length. If the fibre is long enough the maximum tensile stress is reached at a certain distance x and the fibre will break in several fragments but never under a certain dimension coinciding with a fibre critical length l_c.

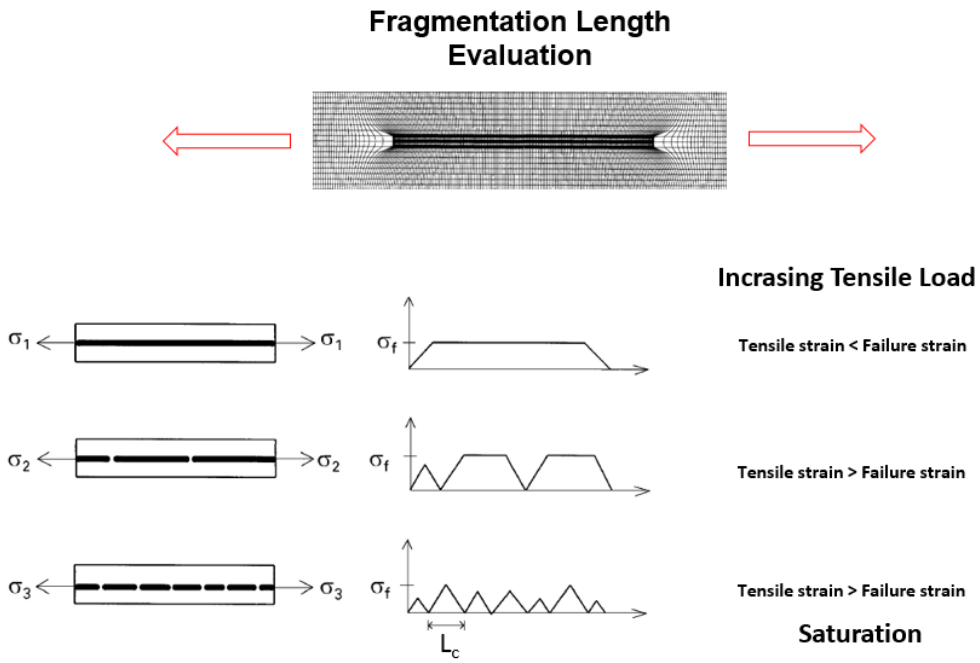

Figure 2.20. Schematic representation of a reinforcement fibre fragmentation [105] .

The fibre critical length can be expressed as follow:

$$\frac{L_c}{\mathrm{d}} = \frac{\sigma_f}{2\tau} \qquad \textit{Equation (2.6)}$$

A set of empirical equations that allow to describe the micromechanics properties of a composite material has been proposed by Halpin and Tsai [106] [107]. The assumptions for this model are the same as the ones given for the rule of mixture and it was derived from the work of Hermans [108] [109] who first developed the first generalised model for a composite with continuous aligned fibres.

$$\frac{P}{P_m} = \frac{1+\xi\,\eta\,\nu_f}{1-\xi\,\eta\,\nu_f} \qquad \text{with} \qquad \eta = \frac{(P_f/P_m)-1}{(P_f/P_m)+1} \qquad \textit{Equations (2.7)}$$

P represent a generic modulus of a composite such as longitudinal or transverse modulus, in the case of particulate composites, P_f and P_m are the moduli of the fibres and matrix, and ξ is a parameter that depends on the matrix Poisson ratio. Halpin Tsai equations can be used in the case of short discontinuous fibre, oriented according to the applied load, showing good accuracy at low fibre volume fraction but under predict some stiffness at high volume fractions.

Halpin and Tsai noted that ξ should be fall positive reducing to the inverse rule of mixture for the lower boundary and to the rule of mixture for the second boundary thus:

$$\frac{1}{P} = \frac{\nu_f}{P_f} + \frac{\nu_m}{P_m} \qquad \text{and} \qquad P = P_f\,\nu_f + P_m\,\nu_m \qquad \textit{Equations (2.8)}$$

Further studies were conducted to correlate ξ to the geometry of the reinforcement in the prediction of the longitudinal modulus of short fibres composites. The best results were achieved for $\xi = 2$ *(l/d)* in comparison to 2-D finite element methods investigation.

Among the micromechanics models for short-fibre composites the shear lag methods were the first developed and widely used to evaluate the behaviour of broken fibres near the end in continuous-fibre composite. They are famous for their physical simplicity and they find the first development in the Cox [110] shear lag analysis who was the first to examine continuous fibre multi material composites. Classic shear lag models only predict the longitudinal modulus giving the basis for the already mentioned model developed by Kelly. From shear lag model the stiffness can be predicted as:

$$E_c = \left[V_f\, E_f \left[1 - \frac{\tanh(ns)}{ns}\right] + \left(1 - V_f\right)E_m\right] \qquad \textit{Equations (2.9)}$$

Where s is the aspect ratio (*l/d*), *l* is the average fibre length, d is the diameter of the fibre and n is as follows:

$$n = \left[\frac{2E_m}{E_f\,(1+V_m)\ln(1/V_f)}\right] \qquad \textit{Equation (2.10)}$$

2.8 3D Printing

Nowadays hybrid materials can typically reach length scale in the micron range, but the smaller the dimension of the particles, the harder becomes distributing the reinforcement according to desired patterns. Currently, transfer of information and concepts from biology to engineering is still at early stages of development. Additive Manufacturing (AM) and three-dimensional 3DP printing are now providing the possibility to create complex topologies with resolutions approaching the nano-composition [111] [112] [113]. A wide range of different materials can be manufactured according to different processes, from micro- to meter-scale extruding, curing, binding and sintering polymers, ceramics, organics and biomaterials. Advantages are currently under evaluation aiming at understanding technology drawback and possible improvements and developments [114] [115] [116]. However, virtual 3D geometries with almost arbitrary shape and complexity, can be produced adding material where needed[117], overcoming limits of classical manufacturing such as mould jetting and CNC machining [47] [45] [118]. AM instead, follows the same approach of nature shaping objects in a bottom up fashion. Multi-materials printers are fostering additive processes into industries are popular for the ability to combine different materials attempting to transfer activation mechanisms from biological to engineering composites. Manufacturing can rely on Computed Aided Design (CAD) coupled to algorithm modelling and imaging technologies to exploit the complexities enabled by 3DP using multiple materials. Algorithm modelling and 3DP are now providing the possibility to create complex topologies with resolutions approaching several length scales [111] [112] [119] [120]. In this regard, algorithm modelling is capable to speed up the design stage to replace user intervention, whereas imaging supplies guidelines

to assembly hard and soft materials simply extracted automatically from the image to the CAD [94].

Several kinds of 3D Printing exist but most can be placed into one of three distinct categories [118] [121]. Firstly, there are printers that form object layers extruding a semi-liquid material from a computer-controlled print head nozzle. Secondly, there are printers that use photo polymerization to selectively solidify a liquid with a laser beam or either light source. And finally, there are devices that 3D print by adhering particles of powder to achieve some form of granular materials binding. The aim of this section is to give an overview on all 3D printing methods, starting with material extrusion, and progressing to explain photopolymerization process and granular materials binding.

Thermoplastic extrusion 3D printers (3DP) are widely used to produce concept models that allow users to handle their creations before conventional manufacturing may take place [122]. The technology can produce functional prototypes of objects to be checked before conventional manufacturing starts. It is also used in the creation of the patterns, moulds, dies and jigs that are required to tool up a manufacturing facility in order to create objects via conventional means. The operational principle of thermoplastic extrusion is based on a spool of build material referred to as ‘filament’ that is slowly fed to a print head, heated in a specific temperature range (melting temperature). Depending on the specific material the machine is designed to extrude. The high temperature (typically 230 °C but depends on the material used) melts the filament, which is then extruded through a fine nozzle and flattened slightly by the print head on its way out. Initially, molten filament is deposited directly onto a smooth, flat, horizontal surface known as the build platform. Here the filament very rapidly cools

and sticks, with the print head moving in a 2D space to trace out the first layer of the object being printed. Once the first layer of the object has been traced out, the build platform lowers very slightly and the next layer of thermoplastic is deposited on top of it. The process will be repeated until a complete plastic object has been printed. Different build materials can be used at the same time, allowing to mix several different thermoplastics, even if most thermoplastic extrusion 3D printers can currently only manufacture objects in one material (Figure 2.21).

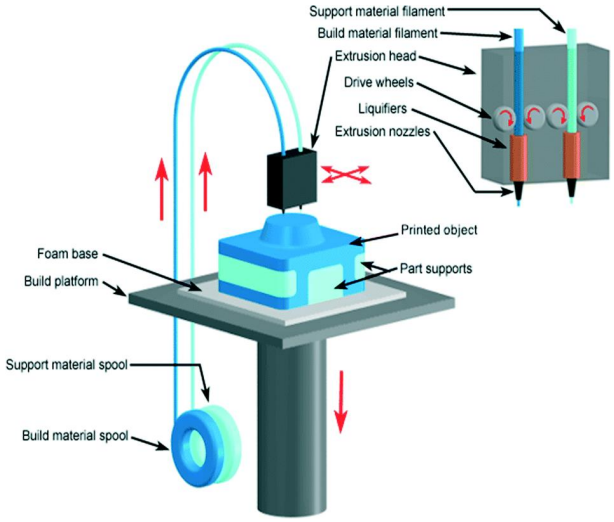

Figure 2.21. In the picture a schematic related to the thermoplastic extrusion is presented. Both build and support materials are driven from their respective spool to the nozzles to be melted and extruded onto the building platform [123].

Photopolymerization is based on the selective solidification of materials called photopolymers, which harden when exposed to an ultraviolet (UV) laser or similar controlled light source [118]. The first 3D printing technology to be invented was called "stereo lithography" known as SLA and used the photopolymerization process [124]. This apparatus uses a computer-controlled laser beam to build a 3D object within a tank of liquid photopolymer. As in material extrusion, the object is created on a build platform, which in this instance is made of perforated metal. Initially, the platform is

positioned just under the surface of the photopolymer in the tank. A UV laser beam then traces out the shape of the first object layer on the surface of the liquid. This causes it to set solid (Figure 2.22). And the build platform than lowers just a little. More liquid photopolymer then naturally flows over the top of the first object layer and the next object layer is traced out and set solid by the laser.

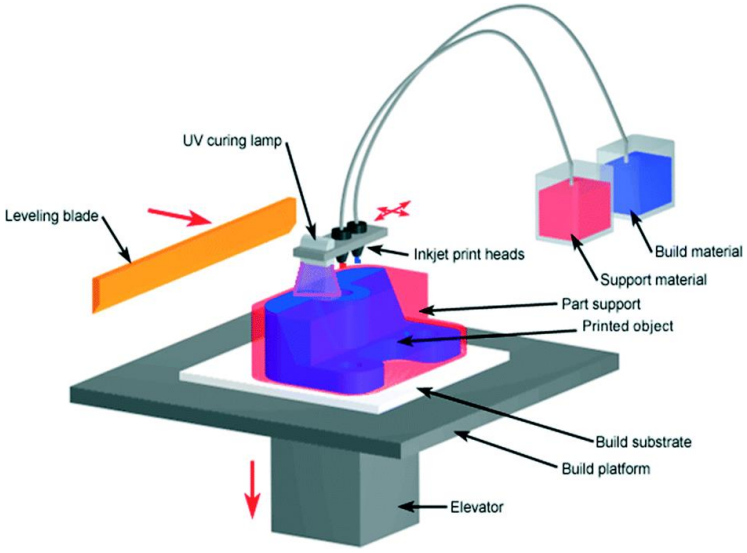

Figure 2.22. The figure provides an illustration of the stereolitographic 3D printing method. As in material extrusion, the object is created on a build platform. A UV laser beam then traces out the shapes of the first object layer on the surface of the liquid. This causes it to solidify (cure) and the build platform then lowers just a little [123].

Granular material binding [125] refers to a wide range of technologies. The working principle is based on 3D print objects by selective sticking together the granules of successive layers of very fine powder that can be made from many different materials such as plastic, metals, and ceramics. Powders can be used in two distinct ways: printers use a print head to spray a glue or binder on to the build material, printers use some kind of laser to partially or completely fuse the powder granules together. The build process of the binder jetting technologies starts when a layer of powder is laid on a build platform termed power bed. This is usually achieved by raising the base of an

adjacent powder reservoir and using a roller to push the powder so raised out across the powder bed.

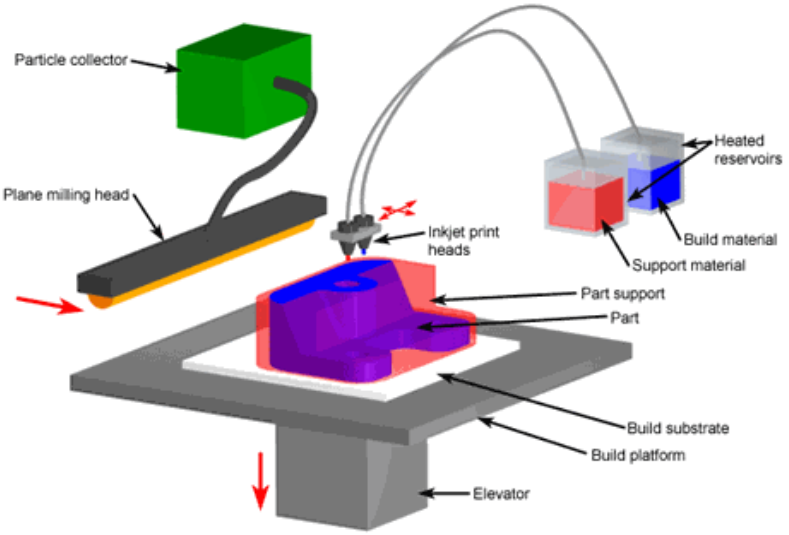

Figure 2.23. Diagram illustrating the whole binder jetting technology process. The object is created from two materials which are a powder based material and a liquid binder. The printing head of the 3D printer moves along x and y axes, shaping objects layer by layer alternately [123].

A multi-nozzle inkjet print head then travels across the powder bed, selectively jetting a binder solution onto it in the shape of the first object layer (Figure 2.23). The powder bed is then lowered and another layer of powder is than laid down so that another layer of binder is jetted onto it. This process is repeated until the whole object has been printed. Once curing is complete, some of the latest binder jetting 3D printers automatically remove most of the loose powder from around the object using a vacuum system; permitting to recycle the powder.

The second method based on the granular material binding principle, uses the selection application of heat to bond adjacent powder granules in a process generically termed powder bed fusion [126]. The most widespread process is the selective laser sintering (SLS). The operations starts with a layer of powder rolled across a powder

bed, following which a laser beam traces out the cross-section of the first object layer. The heat from the laser sinters the powder granules, causing them to at least partially melt and fuse with adjacent granules. The powder particles can be made by different materials, from plastics to metals, ceramics, sand and wax.

2.9 Summary

Different strategies for reproducing bioinspired structures have been used in the past to duplicate and mimic tough composites such as nacre and bone. Nevertheless, the concept and the application of a bottom up approach similar the one adopted by nature is missing because challenging for several reasons. Indeed, conventional fabrication methods such as CNC machining, mould jetting, colloidal-based and freeze casting techniques mentioned in section 2.5, gave an idea of several limitations related to the control on the geometrical shape of the reinforcement fibres as well as their spatial distribution inside the whole three-dimensional domain. This thesis wants to overcome and minimise the gaps due to geometric control, adopting automated or semi-automated procedures based on algorithm modelling and MM3DP. On the one hand, algorithm modelling represents an innovative tool that aims to speed up the design process providing a family of solutions rather than a single output. On the other hand 3D printing is destined to improve materials control and distribution thanks to its ability to add single or several materials in a layer by layer fashion at very small scales. Workflows embracing both design and manufacturing techniques will give the chance to reach manageable complex designs, organic structures and materials assemblies in one single process, contrary to conventional manufacturing that always requires a manual assembly before reaching the final product.

Chapter 3. Mechanical and physical investigation of 3D printed materials

3.1 Introduction

A number of physical and digital approaches are required to develop bioinspired structures based on two biologically diverse tough composite designs of nacre and bone. So far, few strategies or procedures have been proposed to replicate biological composites, especially in the case of AM. Therefore, a reasonable starting point to develop materials' assemblies and functional bioinspired prototypes is to investigate capabilities and criticisms of the available manufacturing technology. Criticisms will identify thresholds above which hybrid materials and 3D printed composites in general can be successfully manufactured. When additive manufacturing (in the common vernacular indicated as 3D printing) is adopted for mimicking biological structures, a key point is the control of geometrical shapes in both virtual and physical environments. Indeed, features and digital designs can be exported to a 3D printer adopting pathways related to medical imaging techniques or starting afresh from on purpose designed CAD drawings. The ideal case would see a perfect replica manufactured approaching length scales found in features of biological materials. However, every manufacturing technology has practical limits that need to be explored in order to best benefit from their usage.

This chapter mainly reviews MM3DP process used throughout this research to manufacture digital designs. Mechanical performances of available 3D printable materials are then explored to validate understanding of designs and test whether mechanical performance found in bone and nacre is transferred to an engineered

composite. Imaging techniques such as optical microscopy and high-resolution x-ray computed tomography (XCT) are adopted to evaluate produced parts. This latter point specifically relates to the use of XCT as metrology tool for multi-material 3D printing purposes, widely adopted in material science to mainly investigate monolithic prints [127][128]. Furthermore, meshing procedures applied to basic 3D printed composites (made of a single fibre embedded in a matrix), are adopted to evaluate geometrical difference between design and prototypes, providing a link between digital design and physical manufacturing.

3.2 Mechanical experimental procedures of Multijet 3D printed materials

The purpose of this section is to identify and describe the mechanical properties of the base materials of a multi-jet 3D Printer (ProJet 5500X, 3D Systems, USA). Properties such as strength, Young's moduli and elongation at break are partially reported in the datasheet supplied by the manufacturer. Furthermore, full stress-strain behaviour of the materials used for 3D printing are missing, indicating a lack of understanding on how the base materials perform. Actual mechanical properties are critical for any biomimetic approach whose aim is to replicate functionalities and peculiar interplay of phases belonging to biological composites. The literature [98] suggests that materials with a stiffness ratio as high as possible should be employed for the final assembly. This can be explained by the fact that reinforcement (minerals) and matrix of biological composites (biopolymer) exhibit stiffness values that are very far from each other which are generally assumed to be of 100 GPa 0.4 GPa respectively [129]. As described in the composite mechanics section above, the interface between materials with highly

contrasting mechanical properties are found in biological composites, specifically deformable matrix (bio-polymers) and stiff minerals building blocks (platelets or fibres), is critical in defining overall mechanical performance and thus requires consideration in 3D printing technology [45].

Material jetting is an additive manufacturing process that is recognised by ISO and ASTM International standards [114] [124]. Material jetting systems are also known as drop-on-demand systems and exploit a piezoelectric ink-jet print head to precisely deposit liquid nano droplets of photo-curable materials containing a photo initiator. A photopolymerization system is coupled to the piezoelectric printing head to cure the droplets which form a solid polymer layer by layer onto the building platform also called substrate [130] [131]. In the presented work multi-material parts were manufactured with a dual jetting systems that is able to inkjet two different materials, hard and soft, at the same time. The two materials are stored into cartridges to which the printing head is connected to get the amount of materials needed for the build. An additional material is available which function as support material for free standing features. The light coming from an ultraviolet lamp activates the curing process of the photopolymer layers, each one sticking to the previous layer until the entire designed part is realised. The way in which photo curable materials are assembled layer after layer leads to challenges related to structural inhomogeneity and then structural anisotropy. Uncrossed linked materials contained in the same build lead to softer regions or potential liquid polymer that promotes causing aging, geometric variations or premature failures [132]. Validation of the 3D printing process is required but currently few standards are available or can be adopted for testing 3D printed parts. ASTM and ISO have a number of standards focused on additive manufacturing (AM)

of metals and polymers but without any specific consideration on mechanical testing [133] [134] [135]. Comparison between different AM systems is challenging especially when functionality of parts needs to be predicted. Therefore, the mechanical testing of the base materials is required here. The following sections will show how tensile and shear testing provides descriptions of the mechanical behaviour of 3D printed parts and the transfer of stresses between the differing materials manufactured together.

The ASTM D638 (Type IV) shaped dog bone sample is one standard used here, with dimensions related to the case of study presented in Figure 3.1, and is used to evaluate tensile strength, elongation at break and Young's modulus [136] of 3D printed materials.

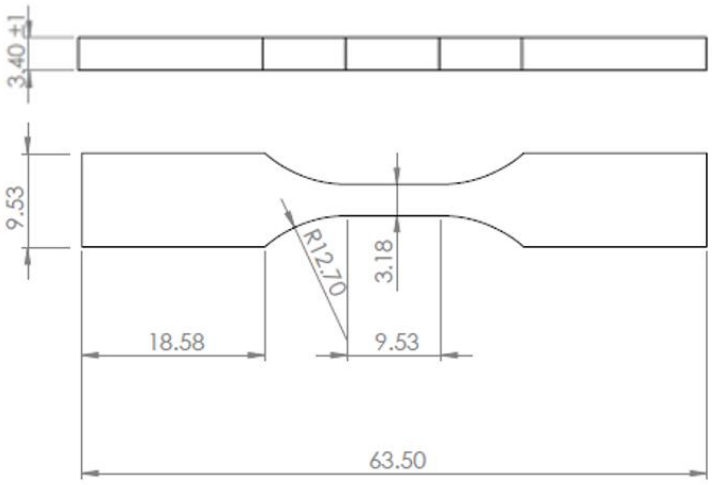

Figure 3.1. Schematic representation of the ASTM D638 Type IV tensile specimen [137].

As a starting point for the analysis of the mechanical properties, specimens were manufactured according to the materials available for use in the 3D printer, specifically from a hard or soft rubbery plastic. The upper limits can be represented by CR-WT (rigid white material or WT) and CE-BK (flexible black material or BK), which represent the stiffer and the elastomeric materials, respectively. According to the

manufacturers, custom mechanical performances can be reached by mixing BK and WT constituents blending in one single print flexible and rigid materials as architectured composites. The result is a palette of greys which mechanical properties gradually vary in-between BK and WT from flexible to rigid. This is possible thanks to the 3D printing head that contains three reservoirs in the inside, which are destined to CR-WT, CE-BK and the support material. The support material is a wax and allows for overhanging or open object parts manufacturing. The materials are delivered onto the building platform layer after layer passing through one of the destined 268 nozzles, which remain open for a certain amount of time t.

Manufacturing of biologically inspired composites of bone and nacre require understanding of the combination of hard and soft materials as well as the routes to incorporate design principles from biological composites in a 3D printed output. Materials with a stiffness ratio as high as possible [98] [138] need to employed in the attempt to approach a similar stiffness ratio as in nature. Throughout this thesis CR-WT (white rigid) and CE-BK (black flexible) will be the mostly used and mentioned 3D printing materials, named WT and BK respectively. For combined materials in between BK and WT the acronym CMX% is adopted, where X indicates base materials volume fraction. For the mentioned case of 50% vol. BK and WT material composite the acronyms will therefore be CM50% where 50 refers to the volume % of BK material. For a combined material CM70%, the volume fraction of BK material is 70%. Samples were 3D printed lying in the x-y plane first coinciding with the printing head movement (3D printing platform) and then rotated of 90° into the same plane to describe the effects of the stripes left by the nozzles while extruding materials. Schematics of dog bone samples printed out according to the two mentioned directions

are reported in Figure 3.2. The schematics indicate stripes due to the 3D printing head motion while printing. Parts are then subjected to axial testing to evaluate resultant mechanical performance and the effect of printing direction.

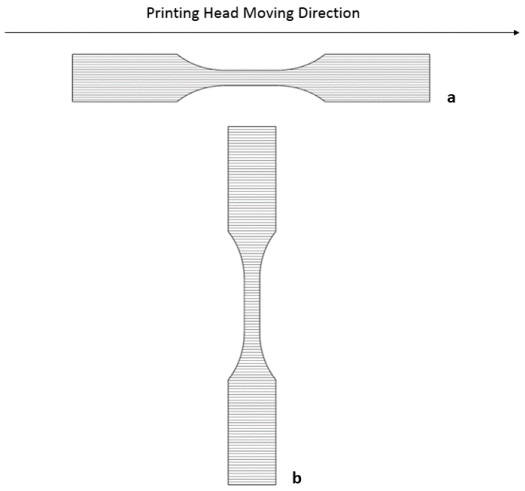

Figure 3.2. Schematic of two tensile samples 3D printed with their long edge coinciding with the printing head movement (a) and with the long edge transverse to the printing head movement (b).

Each x-y plane of material is deposited on top of another and 'builds up' along the z-axis. Final parts are reported in Figure 3.3 for representative purposes.

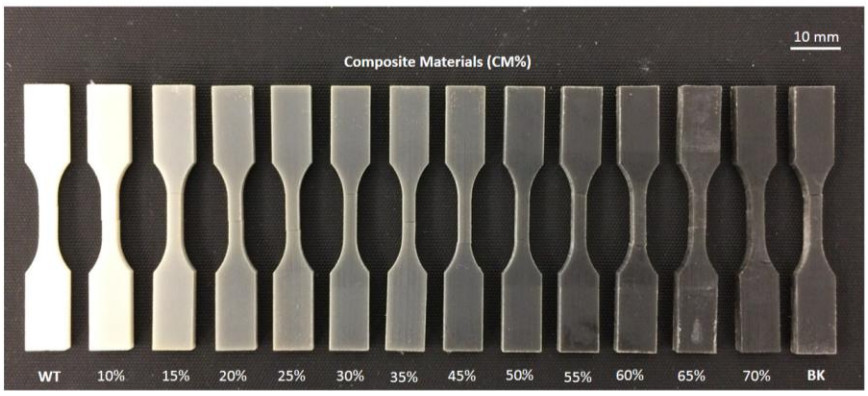

Figure 3.3. Representative dog bone specimens. Materials Constitutive relations have been retrieved for all available materials, from stiff (WT) to black (BK), applying an axial load in quasi-static conditions.

All the samples were tested under quasi-static condition to failure. These were clamped in a universal testing machine Electronforce® 3200 Series III (BOSE, UK) equipped with a load cell of 250 N (class 0.1). A testing speed of 2mm/min was applied to perform the tensile tests. Furthermore, no preload was applied due to the unknown mechanical behaviour of inkjet materials, hence giving the opportunity to observe the entire mechanical performance from zero strain

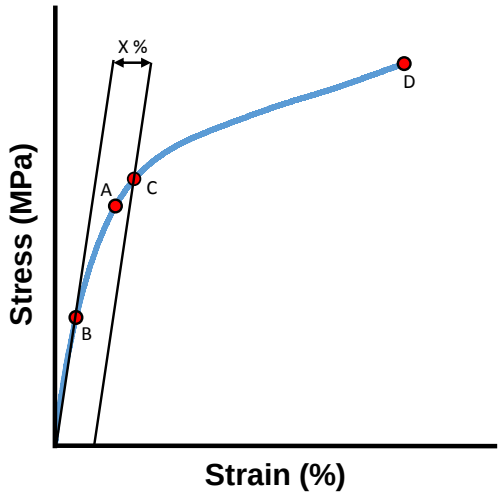

Figure 3.4. Illustration of the relevant tensile stress-strain properties evaluated during this study: A) yield strength, B) 50% yield stress, C) elastic limit, D) ultimate stregth.

Figure 3.4 shows an idealised stress-strain curve that is representative of a sample mechanically tested in tension. The initial response of the material is linear elastic until localization of the yield stress (point A). Point B is identified at 50% of the yield stress and the gradient at this point is then shifted to X % where X coincides with 5% of the total strain in the strain axis in order to find the elastic limit (point C). The evaluation of the modulus of elasticity was retrieved with a linear regression of the dataset embraced between the origin and point C. Further increases in the strain of the sample produces non-linear behaviour beyond point C until, at point D, failure of the

sample occurred. The standard used as shown in Figures 3.1 and 3.2 were sufficient to provide failure in the tensile tests as shown in Figure 3.5.

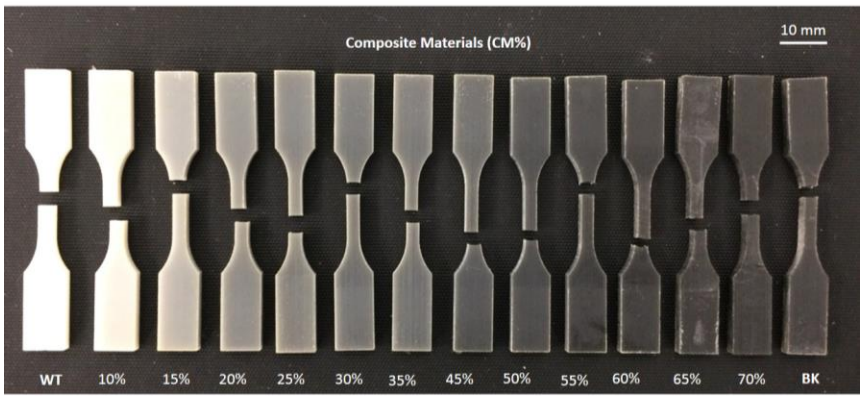

Figure 3.5. Optical image of the 3D printed base materials after tensile testing to failure.

The stress-strain behaviours of all materials are presented in Figure 3.6. Experimental results show the variation of the Young's modulus that increases according to the composition of the material. All of the stress-strain curves followed the ideal schematic behaviour shown in Figure 3.4 although the difference between points A to C are more difficult to identify with the softer materials as the stress-strain profile appears relatively flat and featureless (Figure 3.6).

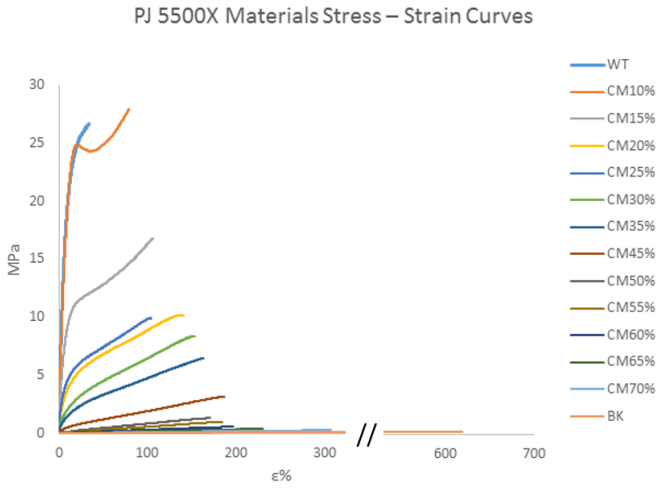

Figure 3.6. Stress strain behaviours of fourteen different CR-WT/CE-BK material ratios from ProJet 5500X.

The Young's modulus, tensile strength, elongation at break and work to failure of the 3D printer materials are shown in Table 3.1. Table 3.1 highlights the above mentioned mechanical properties retrieved applying tensile testing to two sets of samples fabricated according to the 3D printing directions shown in Figure 3.2. The Young's modulus and strength of the materials decrease as we move from the white (CM15%) to the black (CM70%) series. However, the elongation to break of the material increases as we move from the WT to the BK. These observations are consistent with the WT material being stronger and stiffer than the rubbery BK, as well as the CM greys between WT and BK material bounds.

Table 3.1. Mechanical properties of ProJet 5500X available 3D printing materials WT, BK, and WT-BK combination (CMX%) (referred ASTM standard: D638 Type I

	Long Edge coinciding with the printing head moving direction				
	Properties	**Young's Modulus (MPa)**	**Tensile Strength (MPa)**	**Elongation at Break (%)**	**Work to Failure(J/m^3)**
Longitudinal	**WT**	363.62	24.4	13.27	1.06E-03
	CM10%	298.55	20.35	39.06	6.50E-04
	CM15%	158.1	16.85	91.11	1.14E-03
	CM20%	97.3	12.44	102.98	9.01E-04
	CM25%	6.72	4.65	107.9	2.74E-04
	CM30%	6.7	4.25	108.9	2.57E-04
	CM35%	5.18	3.29	109	2.00E-04
	CM45%	1.42	1.08	81.5	7.84E-05
	CM50%	0.7	1.25	158.2	1.21E-04
	CM55%	0.45	0.83	183.95	8.44E-05
	CM60%	0.32	0.59	181.69	5.87E-05
	CM65%	0.21	0.41	192.26	4.33E-05
	CM70%	0.12	0.28	225.24	3.48E-05
	BK	0.05	0.15	270.95	2.53E-05
	Long Edge transverse to the printing head moving direction				
	Properties	**Young's Modulus (MPa)**	**Tensile Strength (MPa)**	**Elongation at Break (%)**	**Work to Failure(J/m^3)**
Transverse	**WT**	267.92	26.68	34.04	7.14E-04
	CM10%	221.42	27.93	78.94	1.84E-03
	CM15%	119.11	16.82	106.1	1.35E-03
	CM20%	41.37	10.19	138	2.45E-04
	CM25%	62.43	9.93	102.71	2.78E-04
	CM30%	24.66	8.38	151.76	1.49E-04
	CM35%	19.4	6.48	162.56	1.09E-04
	CM45%	7.85	3.17	185.99	3.31E-04
	CM50%	0.75	1.32	168.63	1.26E-04
	CM55%	0.53	0.98	180.28	9.86E-05
	CM60%	0.29	0.58	195.57	6.21E-05
	CM65%	0.17	0.39	228.63	4.98E-05
	CM70%	0.09	0.3	306.79	4.93E-05
	BK	0.03	0.24	317.41	7.78E-05

Generally, the samples manufactured with the long edge coinciding with the printing head movement produced mechanical properties that are similar to those for which long edge is transverse to the printing head movement, with the exception of increased elongation to break for the rubbery materials.

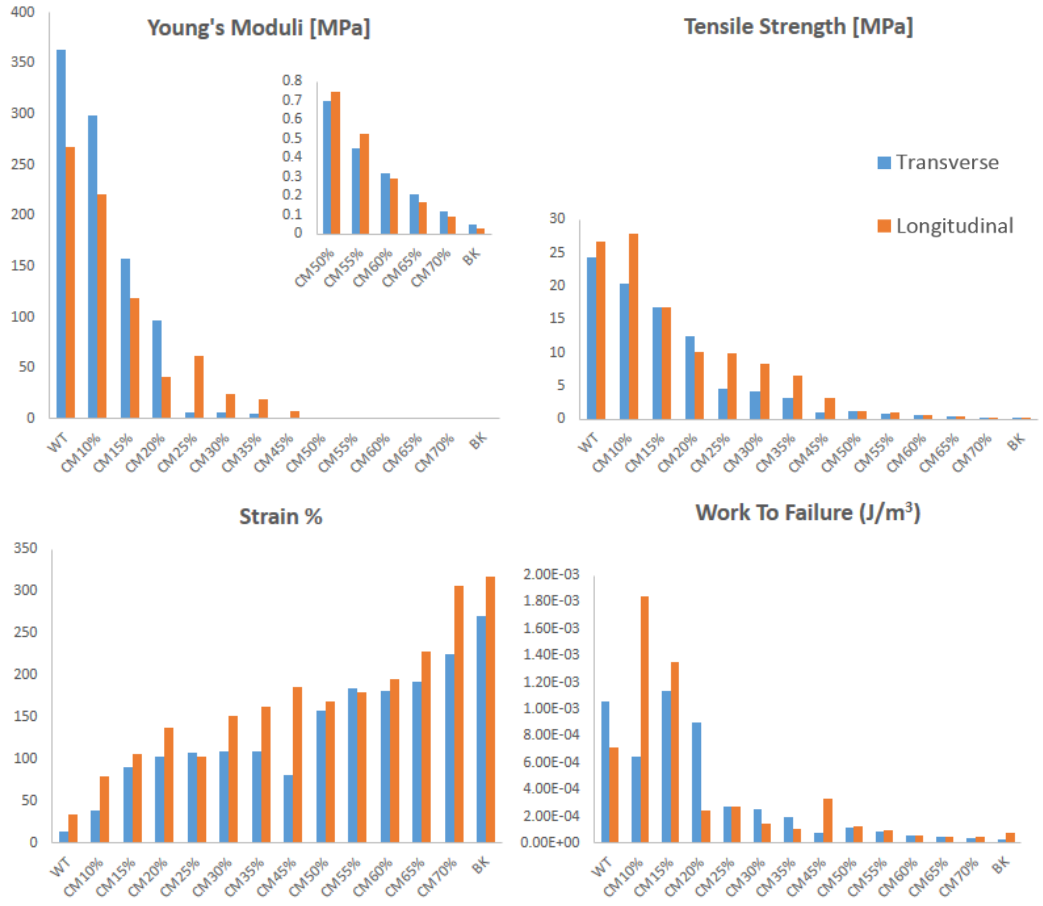

Figure 3.7. Comparison in terms of Young's moduli, tensile strength, strain % and work to failure among samples manufactured edgewise (blue) and transversely to the printing head movement (orange).

Figure 3.7 groups the tensile mechanical properties of dog bone samples produced according the different printing head movement directions. Generally, both sets show the same trends when passing from the WT material to the BK. As expected, the material composites in between WT and BK show decreasing values in terms of

elastic modulus and ultimate strength. A correlation between printing direction and mechanical behaviour of materials has been found. The samples printed out edgewise to the printing head movement are stiffer than the samples printed aout according to the 3D printing head movement, which instead appear to be stronger. Furthermore, the longitudinal samples show a higher strain % and work to failure compared to the transverse printed samples.

The use of multiple materials in biological structures requires additional understanding of the interaction between such multiple materials in a composite design. This section examines the interaction between materials through the use of a mechanical shear testing.

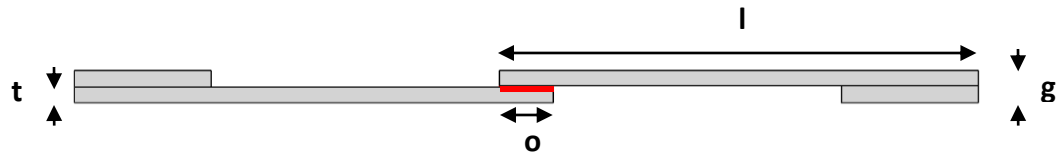

Figure 3.8. Example specifications following ASTM D1002 for creating lap-shear coupons. In the side wiew shown above l refers to the length of each specipen, t to the thickness, o the overlapping distance of the aderend and g the thickness of specimen plus gripping area.

An interaction between two materials is commonly found using the lap joint shear strength testing based on ASTM (D1002-99), which is a common standard for composites. A drawing of lap joint shear test is shown in Figure 3.8 for a side view of a test sample of two materials. The figure above depicts a double lap structure made of stiff white material, each lap of length *l*, and thickness *t* with the compliant material represented by the red line. The parameter *o* represents the overlapping distance between laps. The parameterization of o and the width of the double lap set defines the

interfacial area. The test is relatively simple so that gripping of the sample ends while testing cause shear stresses to develop at the interface until a critical force fails the adhesion in-between. To start, a fixed overlapping distance was held constant to 5 mm, varying the thickness of the compliant material between a lower and an upper thickness bound. The lower bound coincided with the resolution of the 3D printer (13 µm), whereas the upper bound of 300 µm coincided with one tenth of the lap joint thickness, assessable as distance to which the shear stress falls to a constant level. Then, the interface thickness was held fixed to the lower bound, whereas the overlapping distance was varied between 5 to 40 mm (Figure 3.9). The aim of this design variation was to select an overlap distance so that a tensile test causes interfacial failure in order to evaluate the interaction of the materials through an interfacial strength.

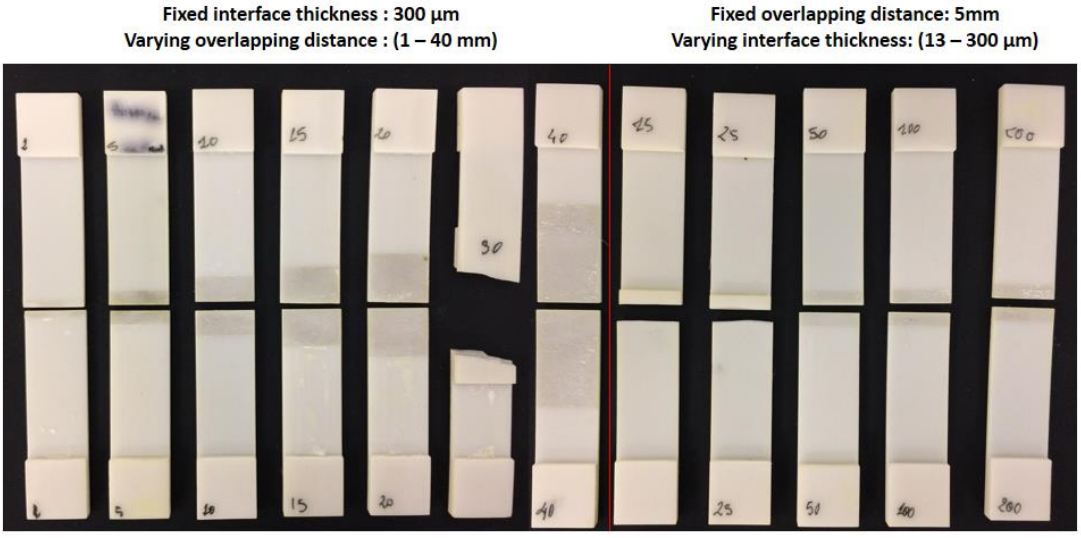

Figure 3.9. Broken samples after tensile loading test of the lap shear joints. In particular samples at the right of the red line represents the broken samples which overlapping distance was fixed to 5mm and the soft BK material in between the coupons was varied from 13µm to 300µm. Furthermore the figure shows lap joints overlapped over different lengths with a thickness held constant to 300µm on the left-hand side of the red line .

These regions are therefore indicative of interfacial failure τ. The average interfacial shear strength was calculated simply accordingly to:

$$\tau_{av=}\frac{Fmax}{A} \qquad \textit{Equation (3.1)}$$

Where F_{max} is the maximum force applied during the tensile loading experiment to cause shear failure and A is the total interfacial surface area between the black and white materials. The maximum shear strength calculated for a range of overlap lengths, with fixed interfacial thickness, and interfacial thicknesses, with a fixed overlap length, are plotted in the graphs of Figure 3.10.

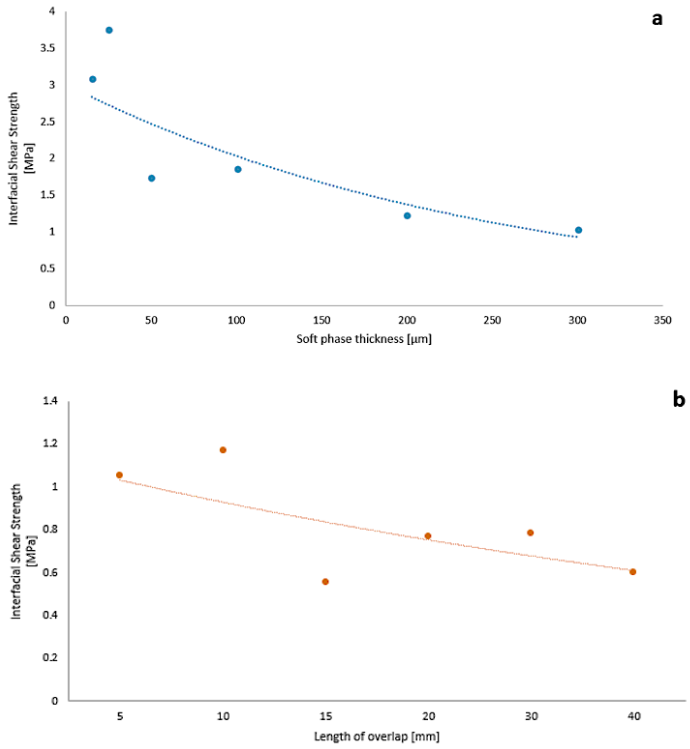

Figure 3.10. The reported plots are relative to the broken samples shown in Figure 3.9. In (a) the trend relative to the varying thickness of the soft material in between the shear lap joints when the overlap length is held constant. In this case, the interfacial shear strength decreases when the soft phase thickness increases. The orange trend (b) represent the resulting interfacial shear strength when the thickness of the material at the interface is held constant, but the overlap length between the joints of the shear sample is varied.

Figure 3.10 b shows that the shear strength generally decreases as the length of the overlap between the black and white material increases. Such an observation conforms to general composite theory for interfacial strength as described in section 2.7 of Chapter 2. Composite theory with hard reinforcements in a softer compliant material is therefore highlighted here as being relevant for the 3D printed structures of this work. Figure 3.10 indicates that the interfacial shear strength is initially relatively high at the resolution limit of the 3D printer.

An increasing interfacial thickness, essentially more BK material between the WT, is associated with a potential rapid drop in shear strength followed by a more gradual decrease as the interfacial thickness increases. This increased interface thickness may still have mixing at the boundary between the black and white but would be expected to retain a homogenous black region of lower stiffness and, hence, the lower interfacial shear strength indicated in Figure 3.11 as the interface thickness increases.

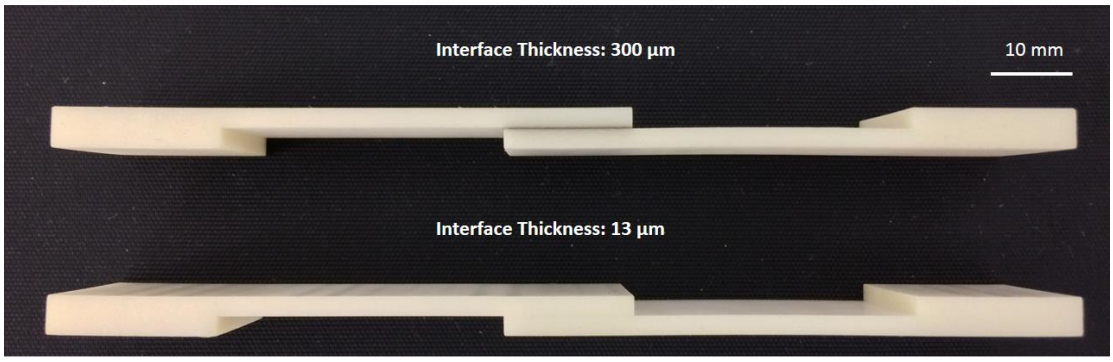

Figure 3.11. The presented picture reports two shear samples which interface thicknesses are 300µm and 13µm respectively. Especially in the case of the 13µm interface thickness, the black material dissolves within the white material contrary the larger interface thickness of 300µm where there is still mixing between black and white but the interface inner-core is still black.

3.3 Volumetric experimental procedures of Multijet printed materials assemblies

The 3D printing of structures with WT and BK materials indicates variability in mechanical performance of the resultant composite. For example, the shear strength between white and black material varies according to the dimensions of the interface length and thickness between the two. Manufacturing different phases is therefore critical in defining the mechanical efficiency of the 3D printed composites structures. This section used various microscopy techniques to characterize 3D printing formed structures. The focus falls onto 3D printed composites mainly formed by WT and BK materials. Such an approach differs from literature where, for example, the durability of 3D printing structures involves one material only. In order to describe and investigate which effects are generated when two different materials are built together one single process, six different inclusions with decreasing thickness and length were designed to be embedded in a matrix as shown in Figure 3.12.

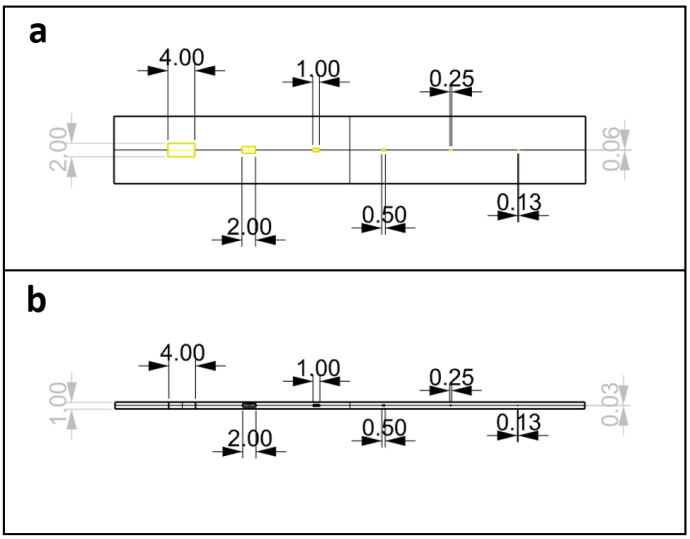

Figure 3.12. The picture propose two views of the designed composite. (a) represents a top view from which a varying length and width of the embedded fibres can be appreciated. (b) shows a side view of the composites reporting the variation in thickness of the fibres that ranges from 1 mm to 0.03 mm.

The aim of the experiment was to define a limit below which is not possible to discern an inclusion/fibre from the matrix, hence to understand not only how designed shapes are maintained after manufacturing but even to investigate if the drawn geometrical boundaries will be respected despite different materials assignments. Technically, given the little variation in density (5%) of the two base materials, an inclusion will not be identified from the matrix when the material mixing dominates over geometrical boundaries smaller than a certain dimension. According to the 3D printer manufacturer's equipment specifications, replicating geometries should be possible down to micron length scale.

Three possible outcomes are suggested below to evaluate 3D printed morphologies when attempting the fabrication of the assembly design shown in Figure 3.12:

I. 3D printed fillers are manufactured faithfully to the 3D CAD drawing, hence maintaining matrix and inclusions assigned surface boundaries. From a mechanical stand point, the interplay at the interface between different phases, could be predicted and controlled.

II. 3D printed fillers can be identified despite their boundary surfaces do not maintain the designed geometrical boundaries, hence spreading in the matrix. The interplay at the interface between different phases, could be difficult to be predicted and controlled.

III. 3D printed fillers disappear into the matrix, losing completely geometrical and mechanical consistency.

To examine durability at dry conditions, the set 3D printer accuracy was set of an ultra-high definition 13 μm (750 x 750 x 2000 Dots Per Inch (DPI)) coinciding with the highest performance of the in-house 3D printer. The design presented in Figure 3.12

was manufactured via multi material 3D printing with BK elastomeric fibres embedded in a WT rigid bulk and vice versa as shown in Figure 3.13.

Figure 3.13. An optical image is presented here to show two 3D printed material assemblies generated by the same CAD drawing. The first case was fabricated with a matrix made of WT hard material filled with BK rubbery fillers/fibres whereas the second case provide for a matrix made of BK rubbery material filled with stiff fillers/fibres. Morphologies and surface charachteristics of matrix and filled are differently manufactured depending on the WT and BK materials allocations.

Discrepancies due to the material mixing were already visible by eye observing the bigger fibres spreading or shrinking into the surrounding bulk. The effect is different for both material assemblies. According to Figure 3.13, the BK fibres seem to expand into the rigid matrix, conversely to the WT fibres that seem to shrink into the BK elastomeric matrix. Printing quality of the two material assemblies was investigated with a high precision Leica Microsystem (Switzerland).

Figure 3.14. 3D printed assemblied reported in Figure 3.13 are furtherly investigated via optical microscopy. Images of the two materials assemblies (WT-BK and BK-WT matrix-fillers) were investigated with a 25X magnification lens. The yellow rectangles were drawn in order to highlight visible fibres. It is shown that no fibres can be recognised below 1mm long fibres for both material assemblies.

Optical images were taken with a 25X magnification lens and resulting distances of the investigated geometrical shapes were verified using a 0.01 millimitre division. Figure 3.14 displays two materials assemblies where fibres shorter than 1mm are not visible, due to an excessive material mixing between black and white phases.

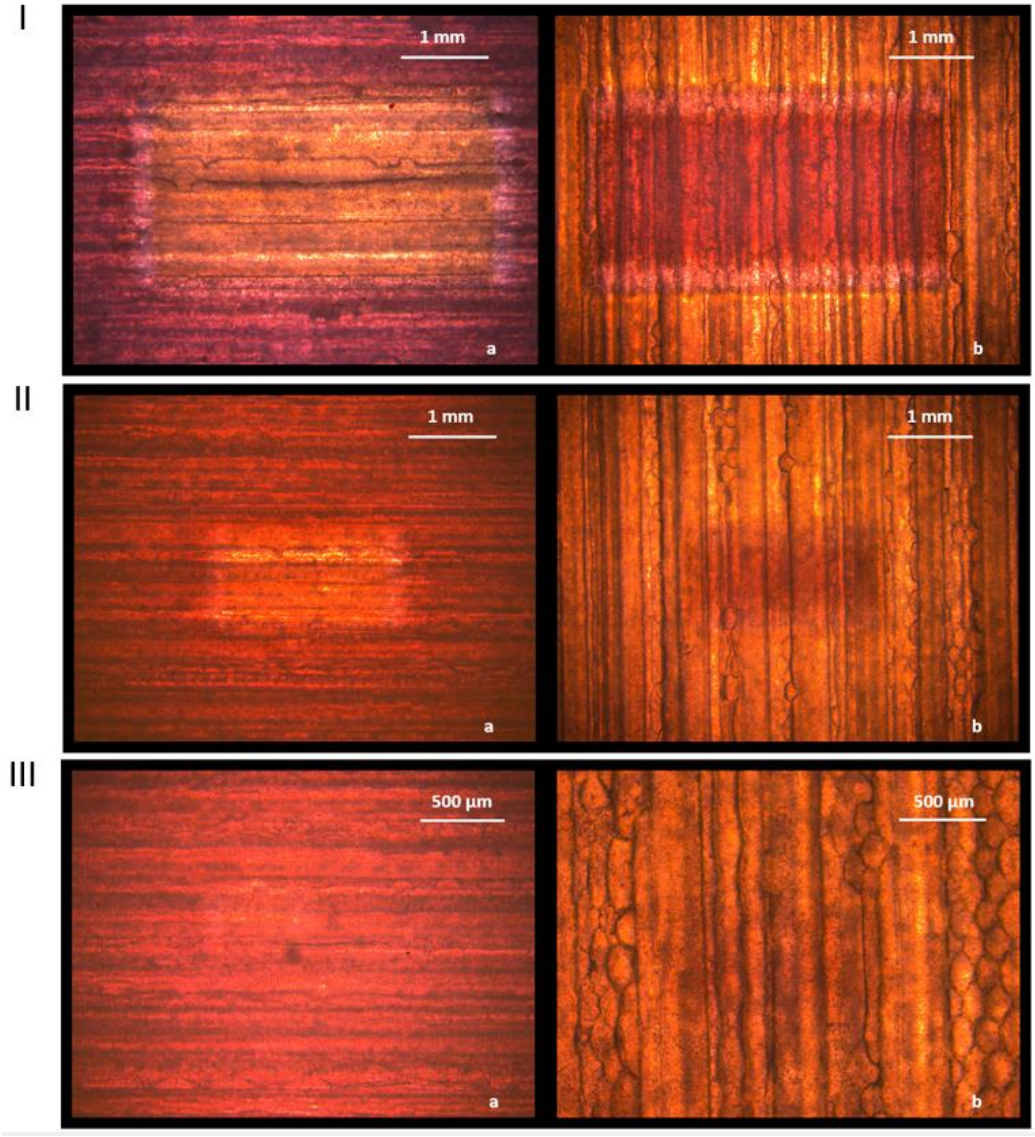

Figure 3.15. The (a) column depict the visible WT fibre into the BK material, conversely the (b) column represents the BK fibre into the WT matrix. The rows are related to the following lengths and thicknesses of the fibres: (I) 4mm-1mm, (II) 2mm-0.5mm, (III) 1mm-0.25mm.

The investigation was conducted with the same optical apparatus, but with a 50X magnification lens to verify lengths and widths accuracy of the bigger fibre that was 4 mm long, 2 mm wide and 1 mm thick. A mean length of 4.18±0.05 mm accompanied by a mean width of 2.33 ± 0.06 mm was revealed for the BK fibre embedded in the WT bulk (Figure 3.15 I-a), contrary to the case of the WT fibre embedded in the BK matrix (Figure 3.15 I-b), where a mean length of 3.90±0.06 mm accompanied by a width of 2.00 ± 0.08 mm was measured. Optical images indicate that fibres are partially reproduced following the Figure 3.12 design. In particular, fibres of 4 mm and 2 mm in length fall into the second case of the assumptions made before, where geometrical boundaries are maintained showing a strong material mixing at the interface (Figure 3.15 I-b). Fibres 2 mm long are reported in Figure 3.15 II-b, which shows how boundaries start to disappear especially when the white material is placed into the black elastomeric phase (Figure 3.15 II-b). The third case can be associated to fibre 1 mm long, 0.5 mm wide and 0.25 mm thick. Taking into account the findings above, a single fibre composite was designed in order to investigate the accuracy of the multi-material 3D printer when regular shapes are dimensioned above the previously investigated sub-millimetre scale (Figure 3.16).

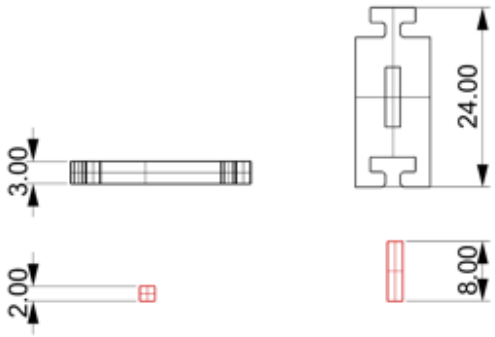

Figure 3.16. Representation of the single fibre composite. The external bulk is reported in black, the inner fibre is in red. All the dimensions are in mm.

The thickness of the fibres was doubled, as well as the length, to check if materials deposition would result in a more stable build.

Fibres dimensions are crucial when composites materials are assembled in one single print. Problems in maintaining the designed geometry of fibres can be problematic especially when BK is allocated into WT. Two different settings have been considered for the base materials allocation, as previously done for fibres varying in dimensions. Bulk and reinforcement were interchanged to generate the same geometries but with opposite materials assignments of black into white and white into black as shown in Figure 3.17.

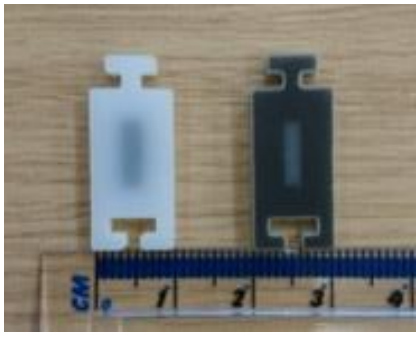

Figure 3.17. Multi-material 3D printed single fibre composites with inverted assignments of base materials.

The assumption is that for the combination of materials, when the geometrical thickness is larger than 1 mm, the manufactured sample will be closer to the digital design. A plane section of the manufactured samples was exposed using a polishing machine (Planopol, Struers) consisting of a turntable that accommodates horizontally rotating grinding foils. In this study grinding foils of 1200 micro-grains and a rotational

speed of 150 rpm were chosen in order to avoid deep scratches onto the surface, being gentle especially when the bulk material is the elastomeric one. Optical images depicting the cross-section of the fibre composites are reported in Figure 3.18.

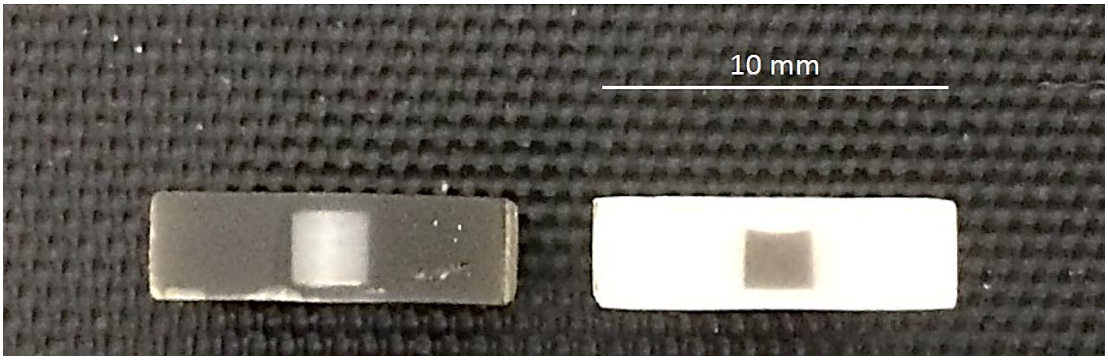

Figure 3.18. Macro optical picture of the two sectioned single fibre samples. It is noticeable how the 3D printed parts are visually different despite being generated from the same .stl file.

The contrast between the two base materials using optical microscopy is poor and led to undefined boundary edges as shown in Figure 3.19. Investigations on three different samples for each combination of materials were repeated with similar results.

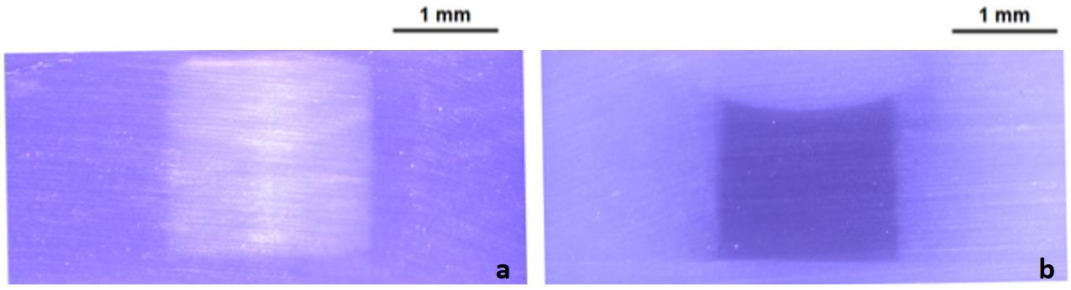

Figure 3.19. Same sections of 3D printed single fibre composite are represented in the pictures above. (a) Shows a section of the single fibre composite where the bulk is made of BK and the fibre is made of WT whereas (b) shows the same CAD geometries but with inverted materials compared to the case (a).

Linear measurements of the embedded fibres were recorded on the samples sections along x and y axes. The WT reinforcement embedded into the soft BK material shows a mean width of 1.998 ± 0.085 mm on the x axis and a mean thickness value of 2.098 ± 0.067 mm along the y axis. The BK material fibre embedded into the hard WT material showed suddenly a scarce fidelity compared to the designed shape. Indeed, a slope on the top surface of the single fibre composite was reported in all the three manufactured samples (Figure 3.20).

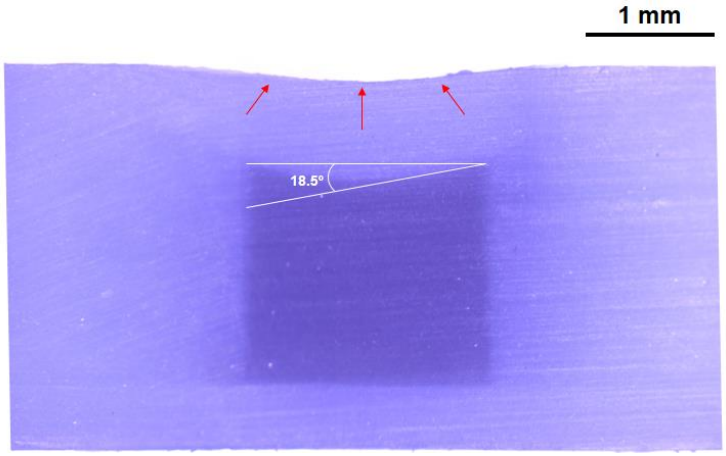

Figure 3.20. Optical image of the transversal section of an elastomeric material fibre into white stiff bulk. The inner fibre is subjected to material dispersion causing the collapse of the entire structure.

Optical investigation about the BK fibre embedded into the WT matrix revealed a width mean value of 1.874 ± 0.02 mm along x and 1.643 ± 0.044 mm along the y-axis. Critically, Figure 3.20 shows how the top surface of the sample collapses similarly the same curvature of the underneath black reinforcement fibre. The deflection was measured fitting a three points circle and tracing the angle edges respectively tangent to the arc and parallel to the top edge of the shape resulting in an angle of 18°. A shade of grey can be noticed especially along the external longitudinal edges, which flips through the centre.

Despite the setting of the 3D printer to work at the highest resolution (13 μm) the variability of the sample dimensions occurs over three orders of magnitude above this reported accuracy.

A metrology investigation is presented in this section, using higher resolution microscopy that could ideally provide 3-dimensional information comparable to that of the 3D CAD drawings manufactured via MM3DP process. XCT, which is a particularly effective 3D imaging technique with a spatial resolution that is, in principle, below the resolution of the 3D printer. XCT is not typically applied to evaluate the dimensions of multi material 3D printed samples, although there are a few examples of its application where the presence of multiple materials was due to multiple active pharmaceutical ingredients accommodated within 3D printed solid dosage forms [139], special case of interface between copper and steel to find regions of intermediate density and investigation about *in situ* alloying of molybdenum particles in titanium parts produced via laser powder bed fusion [128].

A critical aim of the evaluations here is the potential for XCT to distinguish between UV curable 3D printing base materials, hard and soft, in a 3D space. X-rays have the benefit of weakly interacting with matter, therefore allowing the x-ray probe to pass through most materials. However, this weak interacting nature of x-rays also provides challenges in distinguishing between WT and BK 3D printing materials that are of similar attenuation. This section therefore explores the capacity of XCT as a tool to investigate about morphology and surface characteristics of 3D printed assemblies, comparing through imaging techniques, additive manufacturing and 3d CAD sources in a fast and accurate way.

Image processing was performed using a semi-commercial software (MeVisLab, MeVisMedicalSolutionsAG, http://www.mevislab.de/) that allows to produce interactive networks made of blocks performing different image processing functions. Blocks are in turn made of modules or components, connected in a cascade fashion. The resulting workflow allows medical format images to be investigated in terms of scale of greys or manipulated through image filtering procedures such as segmentation and surface reconstruction. Lastly, an open source system for processing and editing 3D triangulated mesh called Meshlab was used to execute a geometric difference between the original CAD design and the triangulated surfaces representing the segmented and reconstructed regions of interest.

The schematic in Figure 3.21 shows the basic steps for the generation, acquisition and processing of the multi-material 3D printed parts. The design part considers two components, bulk and reinforcement fibre as previously described in Figure 3.16. If materials identification will be possible a comparison between designed shape and meshes resulting from the image processing will be achieved.

In the reported case of study, the difference in density between WT and BK phases is less than 5%. Distinguishing relatives' volumes can be challenging.

According to the workflow in Figure 3.21, imaging of the single fibre samples with alternated material allocations, WT into BK and BK into WT, was carried out using an XCT system (Versa 520, Carl Zeiss Ltd., USA) operating with a 70 Kv/6 W X-ray tube energy (micro ampere). Foamy material was used to support and hold in place the parts within a box confining the volume of interest within the XCT system.

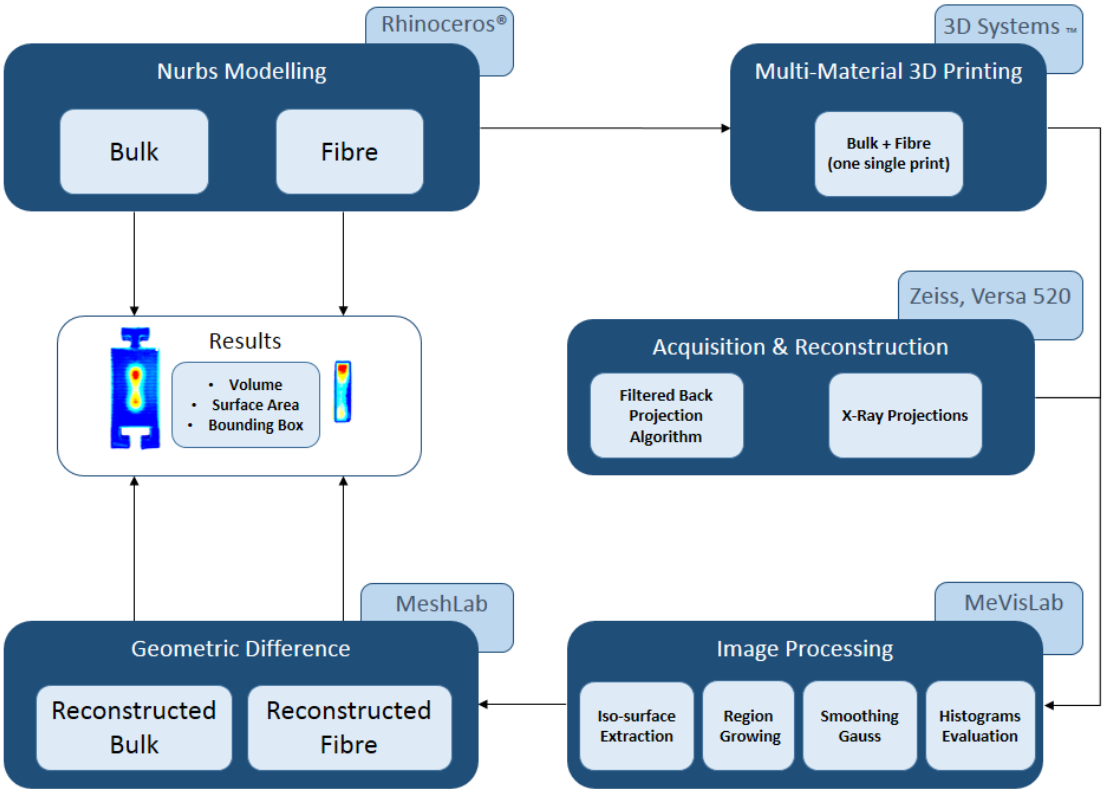

Figure 3.21. Overview of the x-ray data processing starting from the 3D modelling of the samples. Each rectangular dark blue block represents one single processing unit and corresponding software. Each light blue rectangle embedded in the dark blue ones, represent sub-operation conducted within the single processing unit.

A 29 µm isotropic voxel size was achieved from imaging samples using a total of 1018 projection across 360° of sample rotation. Each projection was collected using a 2s exposure time. The subsequent reconstruction of image datasets of the two scanned samples was performed using Scout and Scan software (Zeiss) and imaged using XM3D Viewer 1.2.8 (Zeiss). Figure 3.22 depicts a screenshot from the XM3D Viewer showing the difference between a BK into WT assembly (Figure 3.22a) and vice versa (Figure 3.22b).

The design of the experiment considered first to calibrate the segmentation process focusing on the overall shape of the composites. The different phases

composing the system matrix plus fibre were taken into account after the network calibration for consistency reasons.

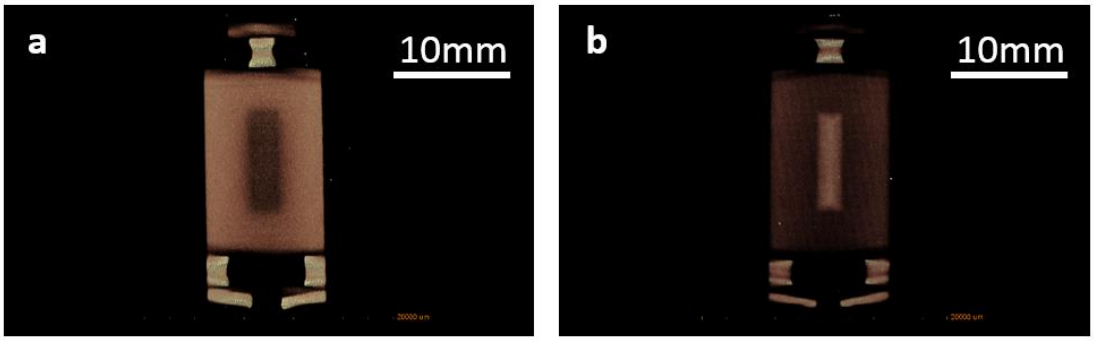

Figure 3.22. The picture shows two 3D renderings from the software Zeiss XM3D viewer. (a) Image reconstruction of the BK fibre embedded in the WT matrix. (b) Image reconstruction of the WT fibre into the BK matrix.

X-ray scans of the samples were reconstructed, exported in a .raw file format and imported in MeVisLab. MeVisLab is a stable and user-friendly semi commercial platform oriented to medical image processing and visualization. The software was chosen for the purpose of this study to define an interactive reconstruction of volumes of interest (VOIs). Indeed, an important aspect that defines the efficiency of diagnostic systems is related to the programming environments that can be very helpful especially if automatic and semi-automatic when performing imaging procedures. Diagnostic systems are popular in medical fields where algorithms help out during professional investigations and diagnosis as in the case of bioengineers, radiologists, surgeons and health professional in general. Far from the medical and biological field, there could be several research areas that can benefit from X-rays technology investigation as in the case of material composites.

Programming environments such as Matlab, strongly oriented to the development of algorithms can be sometimes very slow and inadequate for a fast

processing and visualization of large datasets coming from medical imaging systems, representing a classic bottleneck during imaging procedures. MeVisLab, instead, embraces an open source multi-platform toolkit called ITK (insights registration and segmentation toolkit) and a visualization toolkit called VTK, open source and meant to speed up medical image processing. The mentioned toolkits were originally developed by a consortium made of commercial companies and universities, then improved by researchers in performing functions to be applied on a variety of images format such as DICOM (Digital Imaging and Communications in the Medicine). In MeVisLab, image processing development can be performed on three different levels: Visual Level, Scripting Level and C++ level. The visual level is represented by a plug and play scripting where individuals image processing, visualization and interaction modules creates networks using a graphical programming approach. MeVisLab scripting level involves the user in scripting modules and component in Python and JavaScript implementing wide dynamic functionalities. C++ level allows the generation and integration of modules by using platform independent C++ libraries. The power of a programming environment such as MeVisLab compared to other programming environments devoted to algorithm development such as Matlab is that ITK and VTK libraries and relative imaging procedures can be performed assembling networks made of modules. Therefore, scripts ready to work can be easily assembled fostering the automation of image processing procedures.

The forth step in Figure 3.21 concerns the generation of a MeVisLab script that aims first to recognise how the greyscale of the imaged samples are distributed, then to apply a procedure of segmentation via region growing to discern different phases. Given the similar densities of the material used to 3D print the composite samples, a

filtering procedure based on Gauss smoothing was necessary to uniform as much as possible adjacent voxels belonging to the same phase. A calibration step performed on the overall shape of the samples was necessary to verify that the applied Gauss filtering would maintain the same volume of the original geometry. Therefore, histograms of the input images were considered to retrieve threshold values for segmenting VOIs. All the grey values belonging to air and supports, used to hold in place samples during the scans, coincided with the first histogram peak and were neglected (Figure 3.23).

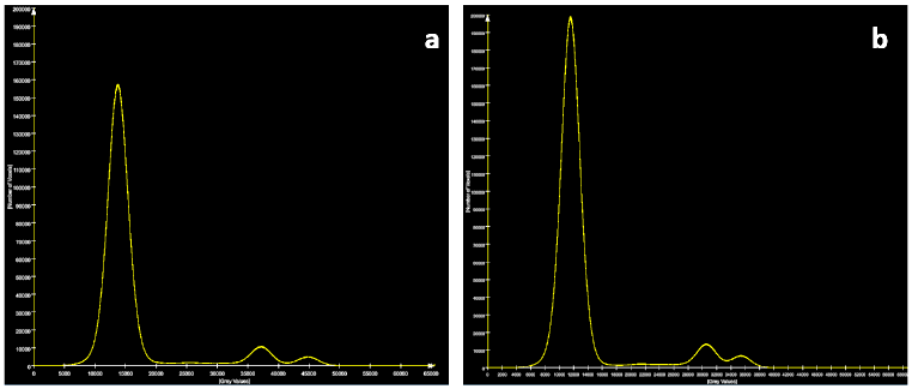

Figure 3.23. Greys scale histograms of the BK into WT (a) and the WT into BK (b) material assemblies.

The result of the first segmentation allowed to highlight three different regions shown in Figure 3.24: the box containing the sample, the matrix containing the fibre and the fibre. Especially in the case of fibre and matrix, voxels grey levels are slightly different. A yellow rectangle was used to underline where the fibre is located into the matrix of both samples BK into WT and WT into BK.

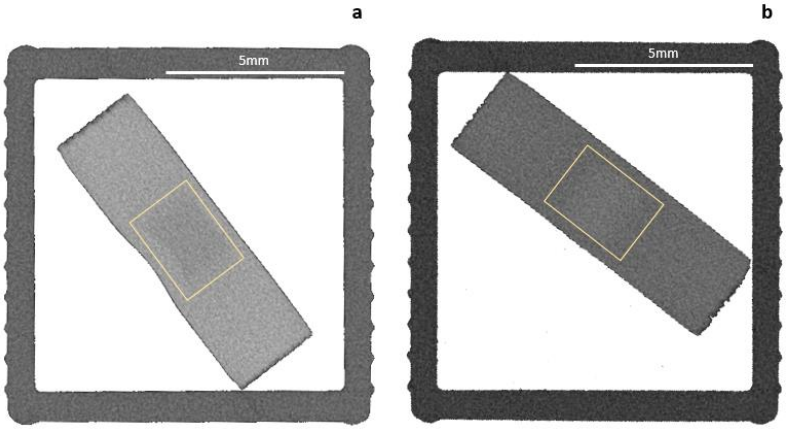

Figure 3.24. Depicted in the figure two transverse sections of the imaged samples. (a) Section of the BK fibre embedded in the WT matrix. (b) Section of the WT fibre embedded in the WT matrix. The yellow rectangles are drawn to point out the area where the fibres should be but not recognisable because of the similar light intensity; hence, material density of the WT and BK materials.

Segmenting regions with similar grey levels can be very challenging. Segmentation techniques such as thresholding, region growing, watershed segmentation, level-set segmentation, classification of clustering is commonly used in the field of medical imaging. The region growing method in particular, is a fast and basic segmentation technique that allows the separation of two or more different regions contained in the same image dataset. To accomplish the task relative to this study an operation of region growing was performed.

Despite foams used as support to hold in place the parts, as well as the air, were removed with a simple thresholding by removing the first peak appearing in Figure 3.22, the box containing the foam and the part appears because similar in density with the sample (Figure 3.25). Therefore, first aim of the region growing segmentation was to separate the sample from the box which are spatially disassembled. Then the procedure foresees the segmentation of the fibre from matrix as spatially assembled parts.

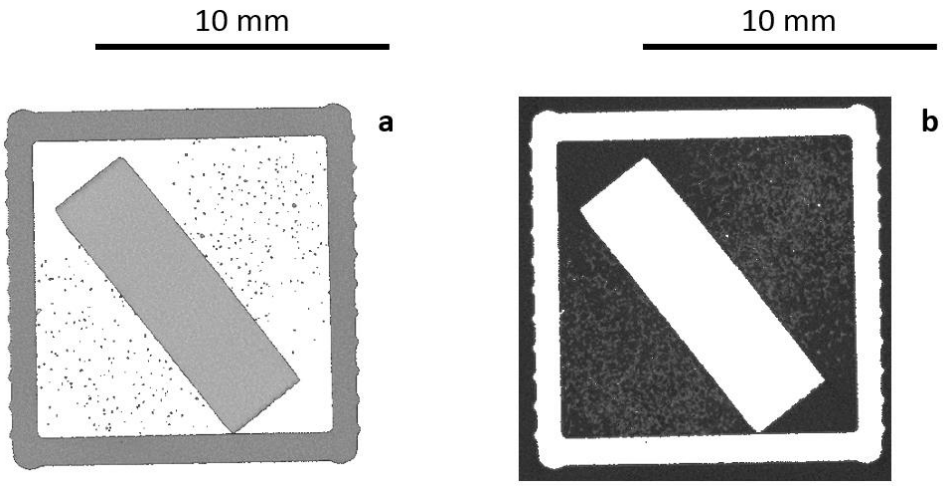

Figure 3.25. Result from the first thresholding applied to remove the background and some of the materials used to hold in place the part during XCT. (a) Segmented region of interest. (b) Removed background from the region of interest.

The region growing procedure started with the selection of a *seed* that can generally be a pixel or a voxel belonging to the considered image dataset. In our case, the investigation was performed on reconstructed XCT image, which dataset is made of 2D slices, laying in a plane transversal to the long axes of the sample. Therefore, the region is expanded from a starting seed made of pixels placed by the user within the region of interest. Neighbouring pixels were associated to the set seed building up a region in which grey values are coincident or fall in an interval defined by the user and named Threshold Interval Size [%]. To this purpose, a seed was placed within the VOI (Matrix plus fibre), adopting a threshold interval size to be decreased in a multistep procedure. The multistep procedure aimed to identify the optimum threshold to segment the material of interest only. Figure 3.26b describes how decreasing the threshold interval size the VOI is highlighted, rather than selecting the entire volume (Figure 3.26a).

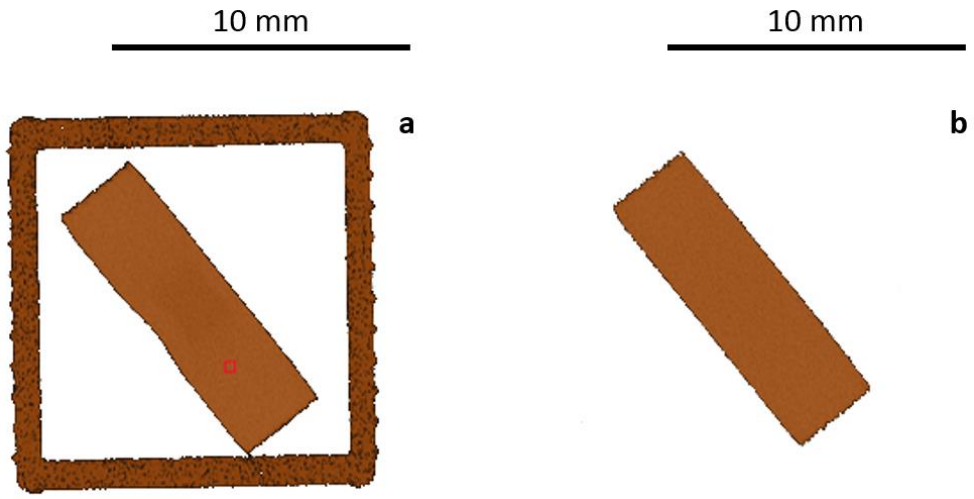

Figure 3.26. The picture shows how the region growing procedure worked on segmenting the region of interest from the box used to hold in place the parts during the XCT. (a) Starting of the region growing process. The red square indicates where the starting seed was placed to grow the region of interest according to a set threshold interval size. (b) Outcome from the segmentation process of two spatially separated objects.

Once the VOI represented by the 3D printed part had been segmented the second step of the region growing procedure aimed to separate the fibre from the matrix. The two regions are spatially assembled; therefore, the image dataset was processed applying a Gauss smoothing filtering to homogenise pixel intensity (Figure 3.27).

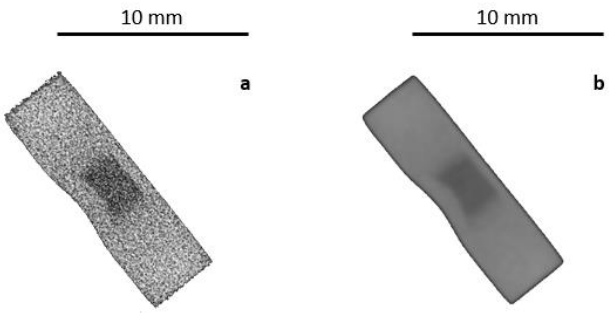

Figure 3.27. Transverse section of the imaged sample with enhanced image contrast. (a) Section of the sample taken directly from the .Raw file from XCT. (b) Same transverse section after applying gauss smoothing filtering to homogenise the two regions.

The contrast between fibre and matrix has been enhanced to facilitate the further region growing segmentation. The smoothing filtering was calibrated over the VOI shape represented by the system matrix plus fibre (Figure 3.28).

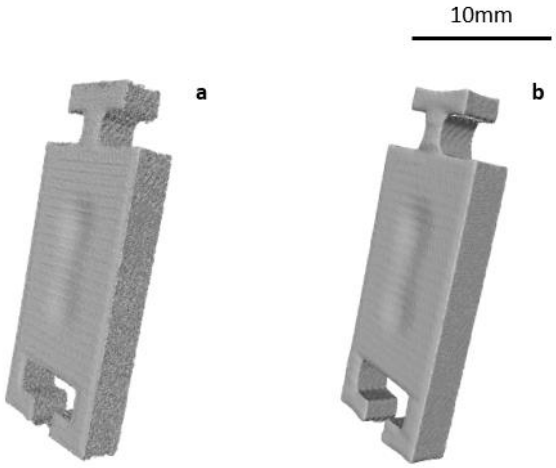

Figure 3.28. Reconstructed region of interest before (a) and after (b) gauss smoothing filtering. For the purpose of the calibration process matrix and fibre were not differentiated since interested in evaluating the global volume convergence to the ideal CAD drawing.

The volume identifying the fibre only represented the new VOI; thus, all the grey values belonging to the matrix were neglected. The starting seed was placed by the user in the VOI and a multistep procedure aimed to identify the Threshold Interval Size [%] for both BK fibre into WT matrix and vice versa (Figure 3.29).

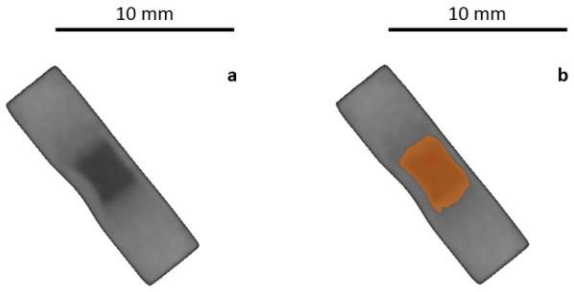

Figure 3.29. Region growing procedure applied to segment the fibre from the matrix. Differently from grey level filtered images only (a) the matrix and fibre are spatially assigned in (b).

The threshold Interval Size [%] was decreased in a multistep procedure in order to highlight a core volume comparable to the one of the designed fibre. A rendering of the fibre embedded in the volume is reported in Figure 3.30.

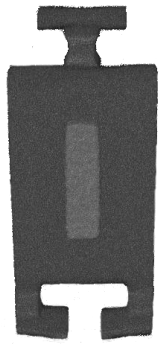

Figure 3.30. Example of a rendered assembly made of a segmented fibre (WT) surrounded by the matrix (BK).

The last step of the workflow provides a comparison between the original CAD design of the fibre-matrix assembly and the reconstructed geometries after region growing and mesh triangulation.

In order to measure how the retrieved triangulated surface differs from the original drawings we relied on a filter provided by Meshlab, an open source software. Mesh processing could be very helpful especially when the geometric difference between two 3D models gives insights about the fidelity of a manufacturing process in replicating virtual models. In the case of multi-material assemblies, objective of this study, the generated mesh comes from a reconstruction more than a simplification, due to excessive surface complexity. Nonetheless the methodology that helps to understand how well a reduced surface approximates the original one, can be converted in a tool

that describe how well a reconstructed surface approximates the original CAD drawing after manufacturing. On this purpose, Meshlab provides a sampling filter called Hausdorff Distance which is based on a digital tool also known as Metro. Metro numerically compares two triangulated meshes representing the same surface at different levels of detail. In the current study the two surfaces are represented by the ideal 3D CAD drawing and the resultant reconstructed mesh surface after imaging processing. The criteria by which Metro evaluates the difference between two meshes is to evaluate an approximation error that can be defined as the distance between corresponding sections of the meshes. Given a point p on a surface S, a distance *e (p,S)* can be defined as:

$$e\ (p,S)\ =\ \min_{p'\in\ S} d(p,p') \qquad \textit{Equation (3.2)}$$

Where *d* is the Euclidean distance between two points in E^3. The one-sided distance between two surfaces S_1 and S_2 is then defined as:

$$E\ (S1,S2)\ =\ \max_{p\in\ s_1} e(p,s_2) \qquad \textit{Equation (3.3)}$$

This definition of distance is not symmetric. There are surfaces such as $E\ (S_1,S_2) \neq E\ (S_2,S_1)$. A two-sided distance (Hausdorff distance) may be obtained by taking the maximum of $E\ (S_1,S_2)$ and $E\ (S_2,S_1)$. The MeshLab command uses a sampling approach to compute the above formula for a defined number of points over a mesh or surface S_1 and searching for each p_1 the closest point p_2 on the mesh or surface S_2. The software

reports numerical results about the computation in a box dialogue in mesh units (mm in our case). Furthermore, the filter saves in a quality field the vertex belonging to the samples mesh for the computed distance values. Hence, a red, green and blue map represent how far the sampled or reconstructed mesh is far from the original one. In our case the colour map reports blue as the minimum error and red as the maximum error found during the analysis. The image sequence in Figure 3.31 reports the application of Hausdorff distance method to a sphere. In particular, the mesh triangulated surface of the sphere was down sampled from 30k triangles, representing the best case or original mesh, to be compared with 25k triangles and 250 triangles spheres.

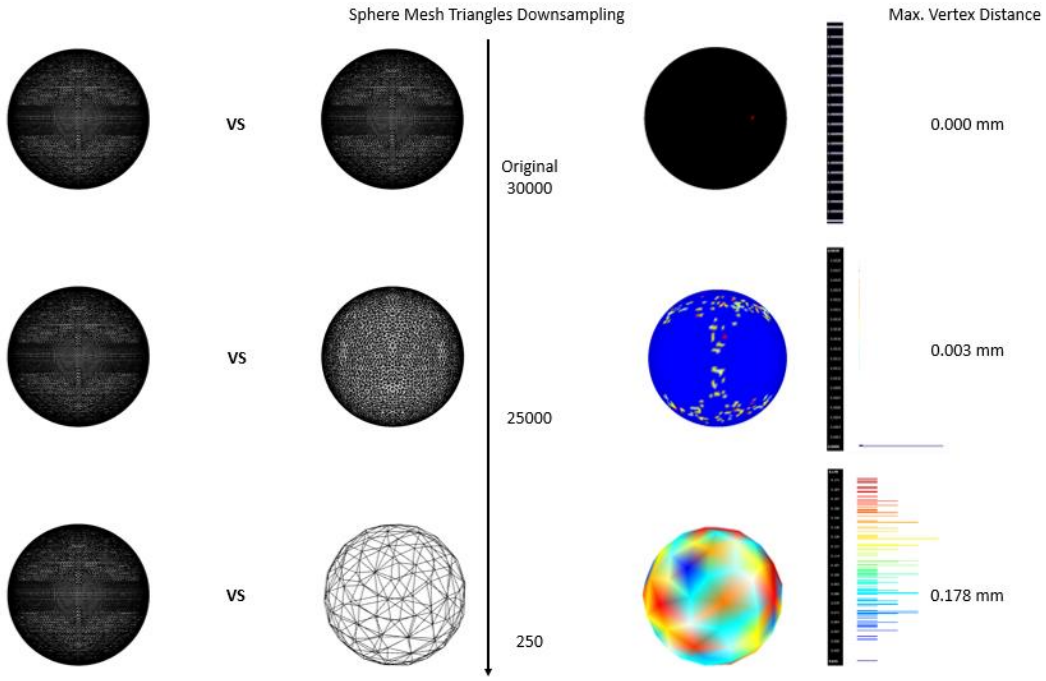

Figure 3.31. An example of the Hausdorff distance. The procedure of image difference was applied to a regular shape represented by a sphere which mesh has been decreased from 30000 triangles to 25000 and again to 250. The first spheres column depicts the best case (30000 triangle mesh), the second column contains the downsampled spheres. Results are reported on the left where spheres are coloured according to the distances between meshes. In general the blue colour represent the smaller distance value between the designed shape and the reconstructed one, whereas the red colour represents the larger distance.

The comparison between the original mesh with itself is reported in order to verify that no error occurs when the level of definition of the meshes in comparison is the same. The comparison between the best case sphere (30k triangles) and a down sampled mesh (25k triangles) reports a maximum error distance of 0.003 mm in the red coloured zones. It must be noticed that most of the out coming colour mapped mesh is blue, demonstrating the two compared meshes are similar. Finally, the best case mesh sphere was compared to the 250 triangle down sampled mesh. The colour mapped sphere highlights the larger distances between the two compared meshes in red referring to a value of 0.178 mm whereas the minimum error distance is 0.035 represented by the blue colour.

An original metrology tool applied to multi-material 3D printed composites has been investigated during this study. Two different allocation of materials, BK into WT and WT into BK, were considered to check manufacturing fidelity when fibre and matrix are mutually produced with rigid WT and flexible BK materials, but complying with the same CAD drawing.

A useful way to compare a manufactured counterpart with its CAD drawing is to refer to comparable meshes. XCT helped to produce a virtual model of the 3D printed part, showing regions very similar in density, hence difficult to be distinguished and compared.

A region growing procedure associated to a gauss smoothing image filtering was performed to precisely separate fibre from matrix. In order to stabilize the workflow avoiding geometric overestimation due to the gauss filtering, the procedure considered a region growing calibration step performed on the overall shape of the samples without taking into account the embedded fibre.

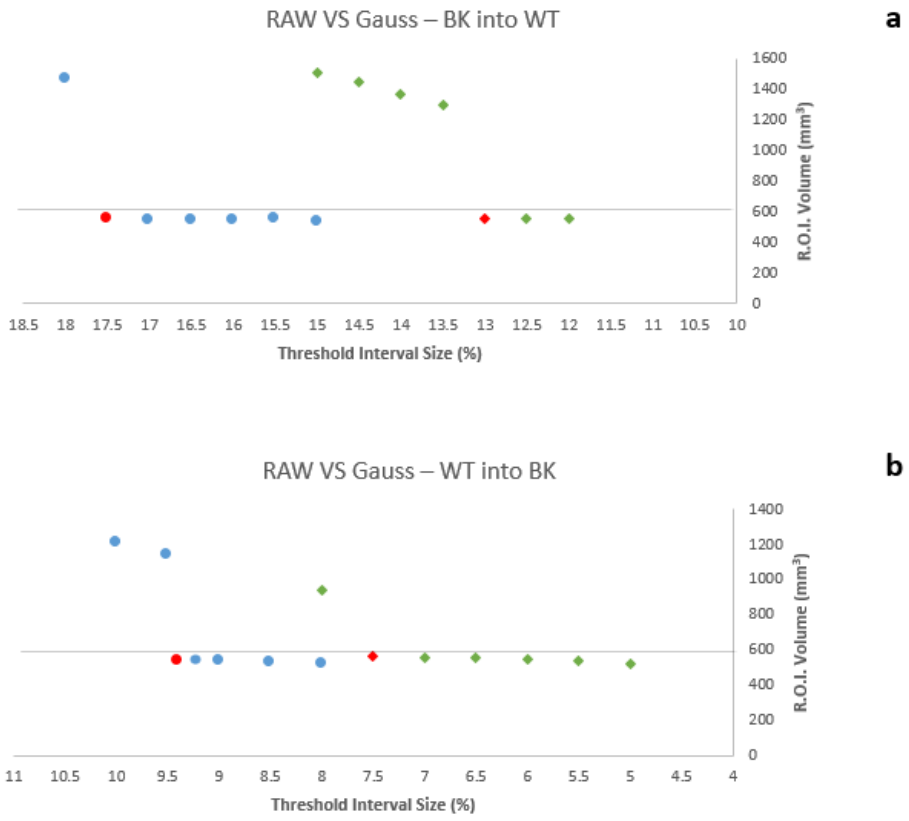

Figure 3.32. The picture shows the trend found during the multistep region growing procedure for BK into WT (a) and WT into BK (b) materials assemblies. On the x-axis the decreased Threshold interval size [%] is reported whereas the segmented volume is provided by the y-axis for each iteration step. The blue dots represent for the procedure applied to the .RAW datasets. The green rhombus draw the trends for the .Raw dataset after gauss smoothing. The red dots represent the best Threshold interval sizes for each dataset. Finally, the horizontal line traces the best case for the segmentation procedure coinciding with the ideal volume of interest from CAD drawings.

Figure 3.32 shows two graphs where the segmented volume of the original RAW dataset is compared to the segmented volume after gauss smoothing for both BK into WT (Figure 3.32a) and WT into BK (Figure 3.32b) samples. The red dots indicate the optimum threshold interval size [%] for the RAW file (blue dots) and gauss filtered image (green dots). After the red dots the VOIs volumes stabilised for both RAW and Gauss around the volume of the original CAD drawings of 600 mm^3. Optimised

threshold interval sizes [%] of 17.5% and 13% were identified for the imaged white sample RAW data set and the relative gauss smoothed version, whereas values of 9.4 % and 7.5 % were found for the black sample counterparts.

Graphs about the region growing procedure applied to separate fibre from matrix are shown in Figure 3.33 for both BK into WT and WT into BK. According to the original CAD drawing the target fibre volume was of 32 mm^3, matched into the graphs of Figure 3.33 for optimised threshold interval sizes [%] of 1.3% and 1.4% for the BK fibre into WT matrix and vice versa, respectively.

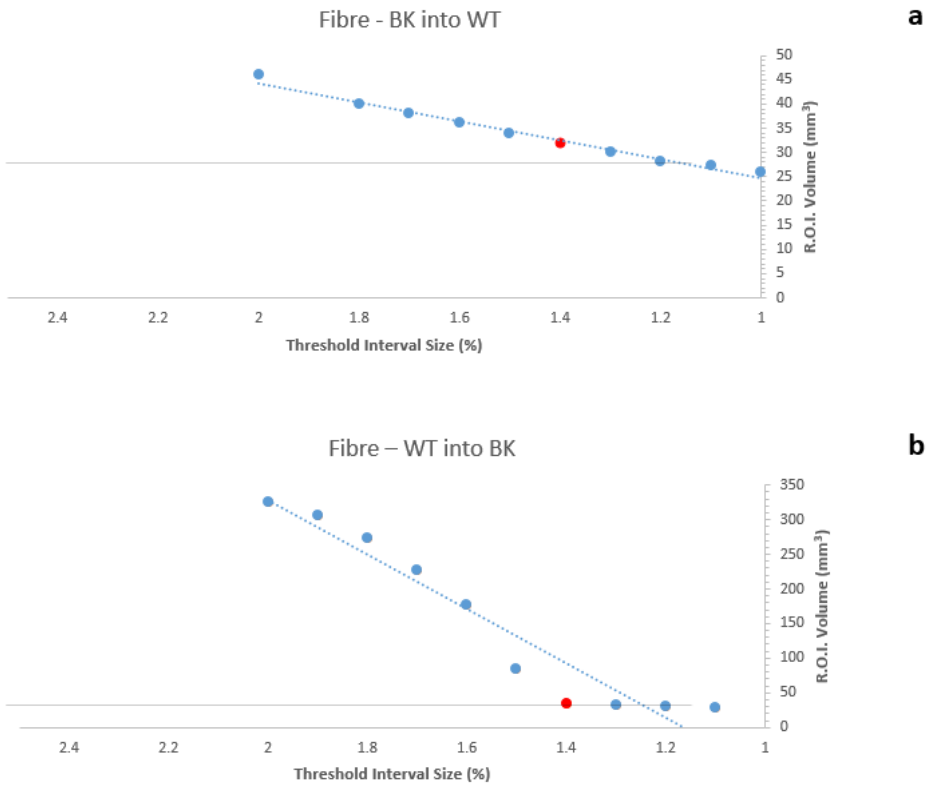

Figure 3.33. The trends for best threshold interval size [%] are depicted for the BK fibre segmentation (a), and for the WT fibre one (b).

A further investigation was carried on in CAD environment in order to give insights about the accuracy of the reconstructed ROIs in terms of linear measurements about width, length and thickness. Figure 3.34 shows drawings of the CAD shape of matrix and fibre compared to the reconstructed meshes after gauss smoothing and region growing segmentation.

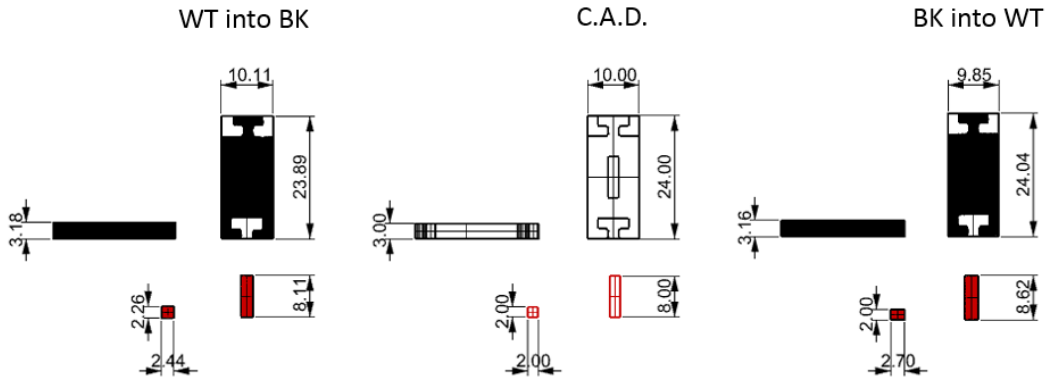

Figure 3.34. Dimensional comparison between the bulks and fibres of the segmented regions of interest. The original CAD drawing is reported in the middle. Reported on the left are the matrix and the fibre reconstructed from the region growing procedures for the WT into BK assembly as well as the region reconstructed for the BK into WT assembly on the right.

Table 3.2 presents the results of several geometrical comparisons referring to reconstructed meshes to the original CAD drawing. The analysed parameters were volume, surface area width, length and thickness for both reconstructed fibre and matrix. To have comparable measurements all considered geometries were aligned in x y and z axis and geometries bounding box volumes were retrieved. Therefore, only in the case of fibre and matrix lengths, widths and thicknesses measurements were referred to their bounding boxes since more regular in shape. Surface area and volume were evaluated again in the 3D modelling environment Rhinoceros.

Table 3.2. Reported in the table there are the original dimensions of the CAD shapes belonging to the single fibre composite (yellow column). The red and green columns report values belonging to the reconstructed single fibre composites after XCT, BK material into WT and WT into BK materials respectively.

		Digital Elaboration Rhinoceros		
		C.A.D.	BK into WT	WT into BK
Volume Part	(mm^3)	600.0	554.5	542.9
Volume Fibre	(mm^3)	32.0	30.8	31.4
Surf.Area Part	(mm^2)	669.8	635.6	637.2
Surf.Area Fibre	(mm^2)	72.0	71.2	70.8
Width Part	(mm)	10.0	9.9	10.1
Width Fibre	(mm)	2.0	2.6	2.3
Length Part	(mm)	24.0	23.9	24.0
Length Fibre	(mm)	8.0	8.6	8.1
Thick Part	(mm)	3.0	3.2	3.2
Thick Fibre	(mm)	2.0	1.9	2.2

Absolute Relative differences of considered geometrical parameters are reported in Table 3.3 and referred to the CAD drawing.

Table 3.3. The table reports the absolute relative differences between the reconstructed single fibres composite's regions (bulk and matrix) with respect to the original CAD design shapes.

Abs. Relative difference	BK into WT	WT into BK
Volume Part	7.6%	9.5%
Volume Fibre	3.6%	1.9%
Surf.Area Part	5.1%	4.9%
Surf.Area Fibre	1.1%	1.7%
Width Part	1.5%	1.1%
Width Fibre	30.5%	17.0%
Length Part	0.5%	0.2%
Length Fibre	7.7%	1.4%
Thick Part	5.3%	6.0%
Thick Fibre	5.0%	8.5%

Table 3.3 allows critical considerations of the investigated material assemblies. The volume of the whole shaped samples were coincident to the CAD model in terms of volume and surface area where the largest discrepancy was shown from the WT fibre into the BK matrix. A decrease in volume for both samples BK into WT and WT into BK of 7.6% a 9.5 % respectively, can be related to either the XCT voxel size or to the post processing chain after 3D printing. A consideration about the post processing is that 3D printed parts are washed in an oiled bath for 10 minutes, which is the time needed to wash away the support material from the builds. Since the BK material is flexible this is more incline to expand with high temperatures than the white material. Material datasheets provided by the manufacturers do not report any heat distortion temperature for the flexible material, but just only for the white rigid one that is 46°C. Safety datasheet of the support material states that the melting point temperature ranges from 55°C to 65°C, hence the post processing chain could be responsible for volume shrinking due to heat distortion. The volume of the embedded fibres are almost coincident with the original one, showing a 3.6% and 1.9% volume reduction in comparison to the original CAD drawing of the fibre. Surface area of matrix and fibre for both materials combination slightly differ from the design, showing a maximum of 5.1% surface area loss for BK into WT composite. Width, lengths and thickness of the parts and the fibre differed all for less than a 10% compared to the CAD drawing except for the fibres widths, which were fond bigger of 30% and 17% for the BK into WT and WT into BK, respectively. This can be explained referring to the 3D printing process, which used a roller in order to flatten out the printed layer according to the resolution set for the printing process. Possibly the fibre that is the core of the composite, is still partially cured by the UV light when the roller passes onto the layer, spreading the core in XY plane while pushing the fibre to spread at the interface into the matrix. This

appears to be more effective for the combination BK into WT where the black elastomeric material is the fibre. Particularly, Figure 3.20 gives an idea on how the roller could cause a collapse of the material in the middle of the geometry spreading the fibre into the matrix, increasing the width and decreasing the thickness. It is true that all the measurements taken, apart from the volume of the features and the evaluated surface area, where referred to a more regular shaped called bounding box, which is more linear and hence more comparable. To go deeper into the geometrical accuracy an idea was to retrieve contour line of the fibres as shown in Figure 3.35. In this way dimensional overestimation of width and thickness of the fibre would have been partially reduced.

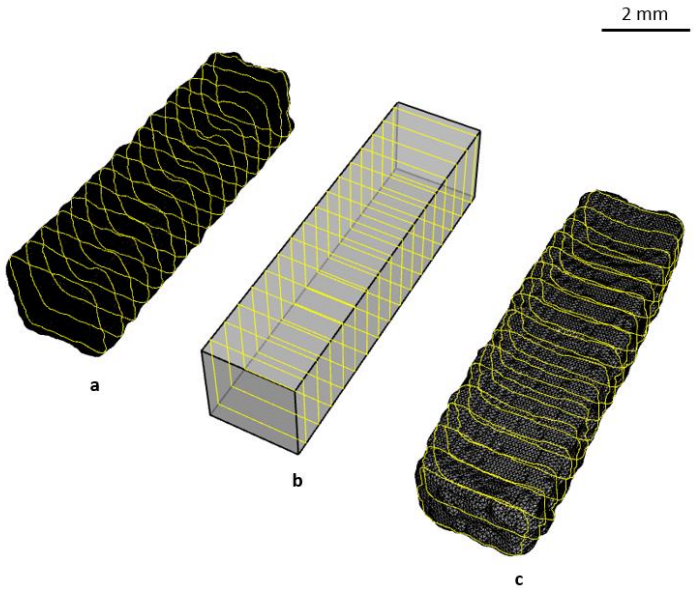

Figure 3.35. Contour section of the fibres: WT (a), CAD drawing (b) and BK (c).

Figure 3.36 shows fibres contour lines that vary in term of width and thickness according to the materials they are made of. Especially, the black fibre on the left results to be wider but with a reduced thickness if compared to the original CAD drawing.

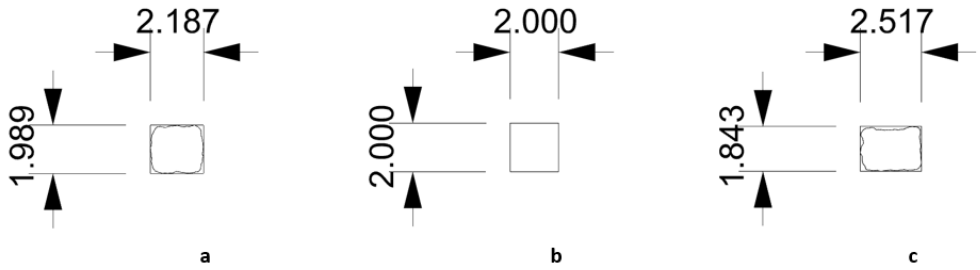

Figure 3.36. Contour sections of the fibres at comparison: (a) WT, (b) CAD drawing, (c) BK. The chosen contour sections where considered at the same level of the cut made on the samples to conduct optical investigation as shown in Figure 3.20.

A geometrical difference was evaluated according to the Hausdorff distance criteria seen previously applied for the regular shape of the Spheres.

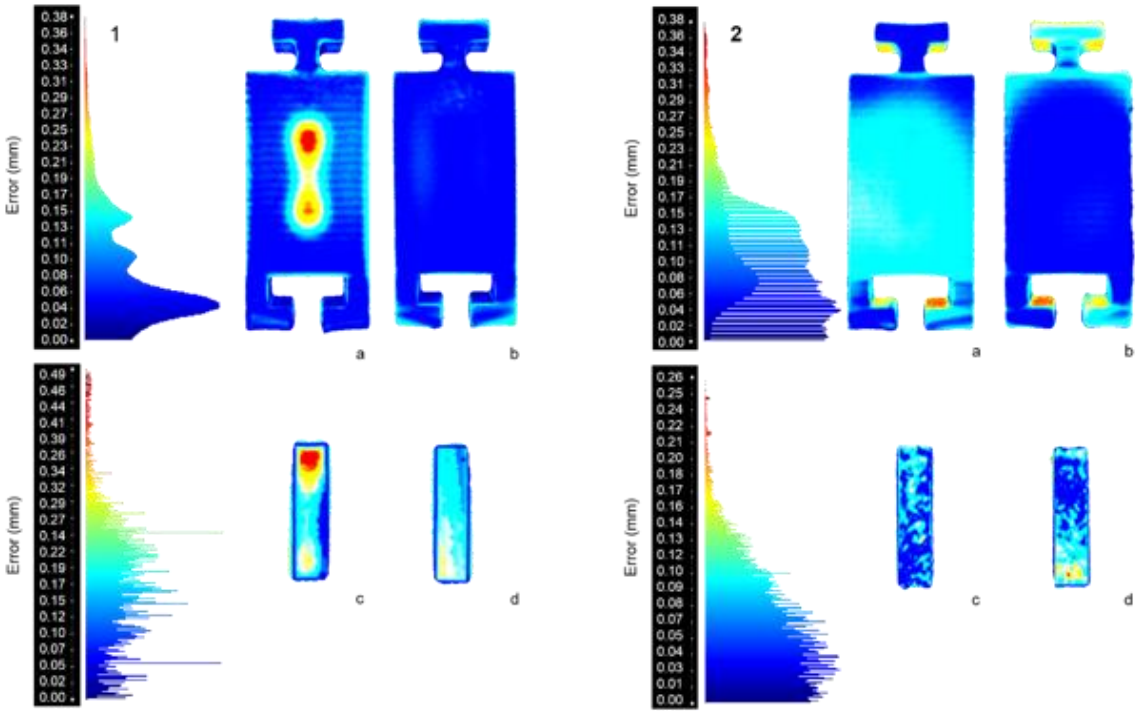

Figure 3.37. Geometrical difference applied to the reconstructed ROIs using the Hausdorff distance in Meshlab. The reconstructed geometries were compared with the respective CAD drawings. The distance range is visually reported and represented by a shade of colours that goes from blue to red accompanied by the relative numerical results.

Red and blue are the boundary colours representing distances between the meshes of 0 mm and 0.38 mm for the matrix and 0 mm to 0.49 for the fibre. On the other end the WT into BK composite showed smaller differences (Figure 3.37-2). Indeed, in this case a maximum distance of 0.38 was found in the red coloured area of the portrayed matrix, whereas a distance of 0.26 was reported for the fibre. Finally, a comparison between the reconstructed meshes of both BK into WT and WT into BK can be found in Figure 3.38. The two materials arrangements testify for a different materials deposition of the 3D printer despite the same CAD files drives the manufacturing.

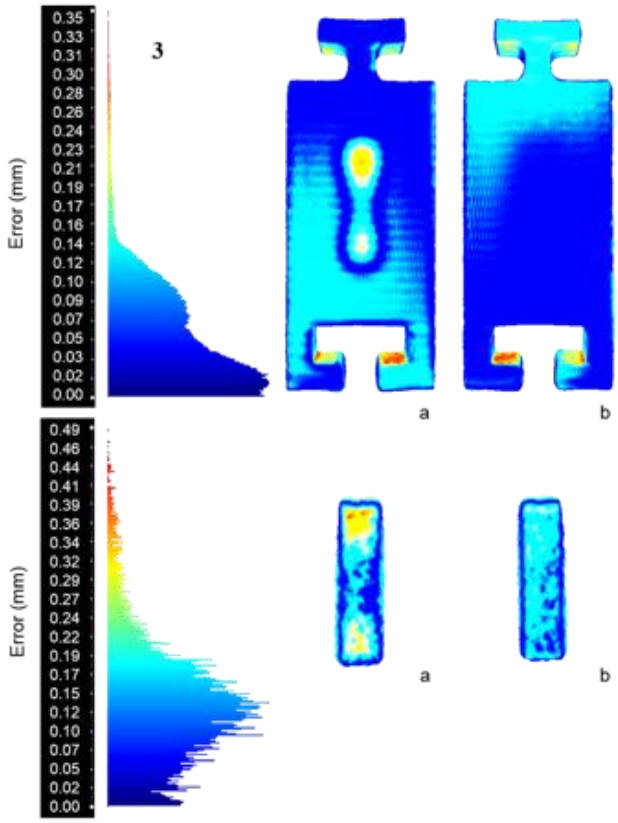

Figure 3.38. Geometrical difference applied to the reconstructed ROIs of BK into WT and WT into BK using the Hausdorff distance in Meshlab.

Chapter 4. 3D printing of biomimetic bone structures

4.1 Introduction

Bone is a complex composite structure consisting of hard and soft components distributed in three-dimensional (3D) space. The evaluation of bone organisation to produce suitable data sets that can be realised in a physical manufacturing process promises significant applications in prosthetics as well as in the wider multidisciplinary field of bioinspired composites development.

The work proposed in this chapter attempts a more engineering approach where the formed tissue is described using various techniques. 3D printing bone equivalent hybrids are therefore produced following both bioduplication and biomimicry approaches. The goal is to investigate on suitable workflows able to translate the organization and mechanical function of compact bone into a comparable engineered structure. Patient specific information is routinely provided at organ level by CT (Computed Tomography) and MRI (Magnetic Resonance Imaging). Such an image-based approach can therefore be identified as a bioduplication approach that is performed in order to reconstruct digitally the site of interest in bone, exporting the retrieved information to specific manufacturing techniques.

Scaffold design based on the repetition of a unit cell of known geometry and properties such as permeability or porosity percentage, is advantageous to predict the properties of the resulting architectured scaffold since those of the unit cell are known *a priori*. In addition, investigation to compare manufactured structures and designed counterpart gives reliable feedback to be embraced in the iterative process of custom scaffold design.

The ability to describe a biological structure using various methods, ultimately result in a digital dataset that is translated into a manufacturing process to give a physical output. Additive manufacturing (as described in section 2.8 of Chapter 2) allows sub-millimetre precision through a high degree of spatial control. Critically, high fidelity translation of the bone structure into a synthetic output can give an accurate copy of the mechanical properties of bone, providing a *mechano-mimetic* bone structure.

In this Chapter, particular attention will be given to the cortical organization of the bone, accepting the challenge of replicating a multi-material structure that is highly mineralised and vascularised, where the distribution of hard and soft phases over the 3D space plays an essential role in the development of such a dynamic system.

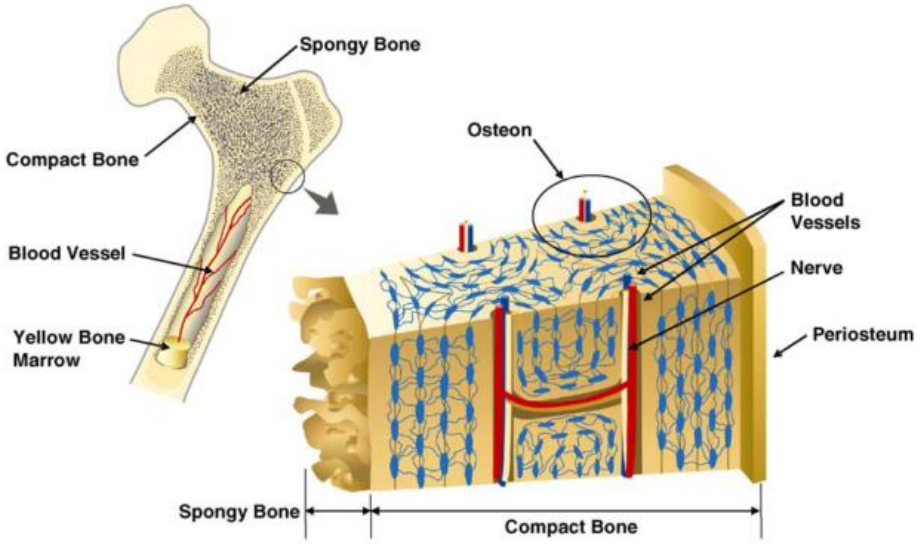

Figure 4.1. Hierarchical structure of the human cortical/compact bone [77].

The interest in replicating bony architectures is attractive for several reasons. From a mechanical point of view the main goal is to find viable pathways to manufacture tough composites inspired by nature where biological processes are adept

to create materials able to mechanically perform according to surrounding environment, inputs and different loading scenario.

What makes compact bone attractive for engineering purposes is its structural composition that demonstrates high resistance to fracture especially when micro-damages occur due to daily activities. Compact bone has a hierarchical organization that is essentially lamellar (Figure 4.1). The basic unit is represented by the osteons that can be differentiated in two types: primary and secondary. The primary osteons are the result of growth and are laid down on existing bone. Vascular canals surrounded by few *lamellae* are found within the primary osteon. Secondary osteons are found in more mature bone due to remodelling of the primary osteons. These secondary osteons represent the basic structural unit of the mature compact bone and are characterised by transvers sections that can vary from circular to ellipsoidal. Secondary osteons are bounded by cemented lines that separate a singular unit from the others as well as the lamellar bone in between units (Figure 4.2). Cement lines can be identified because of their different degree of mineralisation, roughly 85 – 90 % compared to the surrounding lamellar tissue and are meant to be responsible of toughness in bone [140].

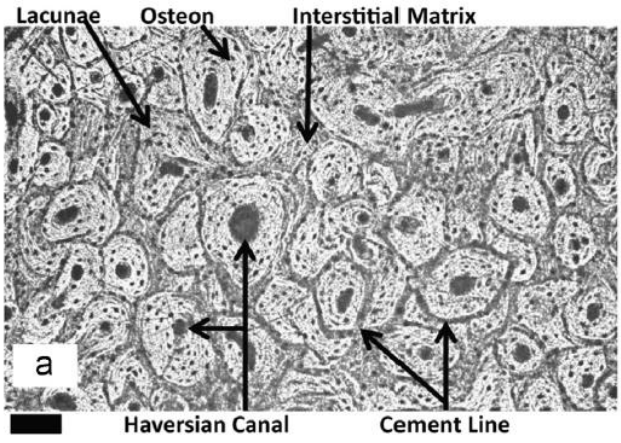

Figure 4.2. Representation of a bovine cortical bone section with emphasis on the secondary osteons composition and surrounding cemented lines [141].

This thin lines of discontinuity formed between secondary osteons and interstitial compact bone create regions of mechanical weakness, which prevent the propagation and growth of cracks in bone transversal sections [142] [80], therefore increasing static toughness and fracture properties (Figure 4.3).

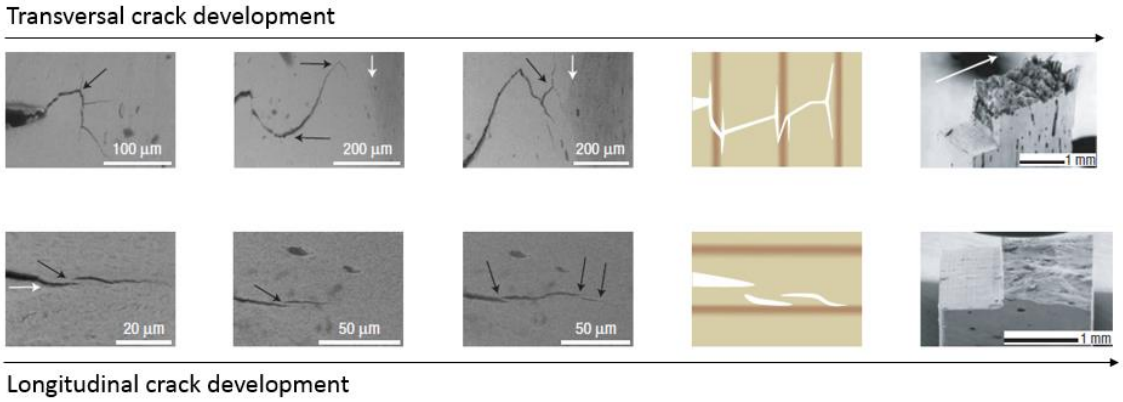

Figure 4.3. Cracks profiles revealed by ESEM fractography techniques representing toughening mechanisms in the transverse and longitudinal orientation of the bone. The schematic diagram of the crack profile is highlighted in the yellow coloured pictures: the upper crack trajectory is particularly deviated by the cemented lines that act as cemented sheaths as the crack propagates through the haversian bone [80].

The main aim of this Chapter is to establish a workflow that applies descriptive methods to compact bone, then followed by controllable 3D design and relatives' physical outputs. An overall workflow depicted in Figure 66, embraces both bioduplication and biomimetic technologies. Despite bioduplication and biomimetic are meant to be two mutually exclusive approaches, XCT represents a link for both digital techniques. Therefore, a general workflow embracing XCT, parametric design and additive manufacturing can be identified as reported in Figure 4.4. Mechanical characterisation of manufactured parts and their corresponding bone structures are included as a final

step in order to evaluate mechanical effectiveness of the biomimetic structure, which has previously been considered to test if a physical output is mechano-mimetic.

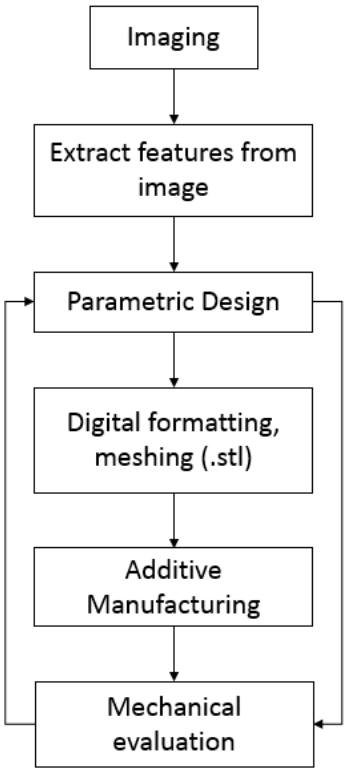

Figure 4.4. Workflow presented to produce biomimetic structures.

A number of compact bony structures are considered to evaluate the complex synergies between soft, mineralised hard tissue regions and their organization.

Although the establishment of a workflow approach from imaging to manufacturing is critical, the development of future materials is expected to embrace parametric design and algorithms, which increase freedom in generating complex shapes approaching the same level of hierarchy as their natural counterpart. Providing a workflow that considers basic parameters such as length, width and thickness of the features of interest can increase fidelity of hybrids materials composites. The realization

of controllable 3D parametric models therefore represents a secondary goal of this section to develop a simple and interactive biomimetic design framework in which any biological structure can be generated provided that features of interest are identified.

4.2 Descriptions of bone using image-based workflows

Cortical bone samples were harvested from mature bovines that were bred and slaughtered for alimentary purposes. Typical age of sacrifice in dairy cows ranges 36−48 months and this is considered as the "biological" age of the samples used in the current study. Samples from the mid-diaphysis of bovine bone femurs were cored by extracting cylinders of approximate diameters and lengths of 4 mm × 5 mm, respectively. The long axis of the cored cylinder was parallel to the long axis of the bovine bone femur. Cored samples were extracted from an extensively remodelled bovine bone region showing a significant number of secondary osteons and a less remodelled bovine bone region limiting the number of secondary osteons. Cored bone samples were wrapped in saline soaked gauze and frozen prior to imaging.

The approach taken here is to image the samples using XCT to give morphological information and identify the compositional variations of primary and secondary bone. Primary bone is produced rapidly in bovine structures but is remodelled into more ordered secondary osteonal regions. While the composition of bone is predominately hard mineral phase and softer collagen, regions of disordered bone have been shown to have relatively lower stiffness [143] whereas more ordered bone exhibits increased stiffness [144]. A workflow is therefore established as indicated in Figure 4.4 to image cortical bone samples with regions of compositional variation and then develop a virtual model of the bone, including morphological and mechanical

information, which is translated into a 3D printed composite structure of multiple materials exhibiting an organizational fidelity with the native tissue.

Imaging of bone was carried out using a 3D X-ray microscope (Versa 520, Carl Zeiss Ltd., USA) operating with a 70 kV/6 W X-ray tube energy. A 5.3 μm isotropic voxel size was achieved from imaging samples using a total of 3201 projections across 360° of sample rotation. Each projection was collected using a 6 sec exposure time. The core samples were immersed in saline during the tomography to prevent desiccation. The 2D X-ray projections from XCT were reconstructed to a 3D volume using a filtered back projection algorithm implemented in the manufacturer's software. A standard Shepp-Logan filter, Gaussian filter (0.5 strength) and beam hardening correction (strength of 0.05 for the more remodelled bone and 0.044 for the less remodelled bone) was applied to the projections. Approximately 50 slices from the top and bottom regions of the XCT datasets were disregarded due to artefacts. The resulting 3D dataset was segmented into primary and secondary bone regions by machine learning based segmentation (Weka 3.9.0, ImageJ, U. S. National Institutes of Health, Bethesda, Maryland, USA) to distinguish between the texture of primary and secondary osteons. This segmentation gave a 3D analogue of the datasets masked into binary images using image analysis software (Avizo 8, Fra.) (Figure 4.5). A thresholding excluding voxels with a scale of grey value equal to zero allowed to define the region of interest (ROI) of the datasets. An isosurface was extracted from the 3D analogue and triangulated as a mesh of polygons and volume meshes using meshing software (MeshLab v1.3.3., Ita.). Each mesh was decimated in terms of triangle number with a multistep procedure defined by a step number equal to three. A quadric edge collapse decimation algorithm with a quality threshold parameter of 0.5 and a boundary preservation weight of 5 was used to decimate the mesh to reduce data size.

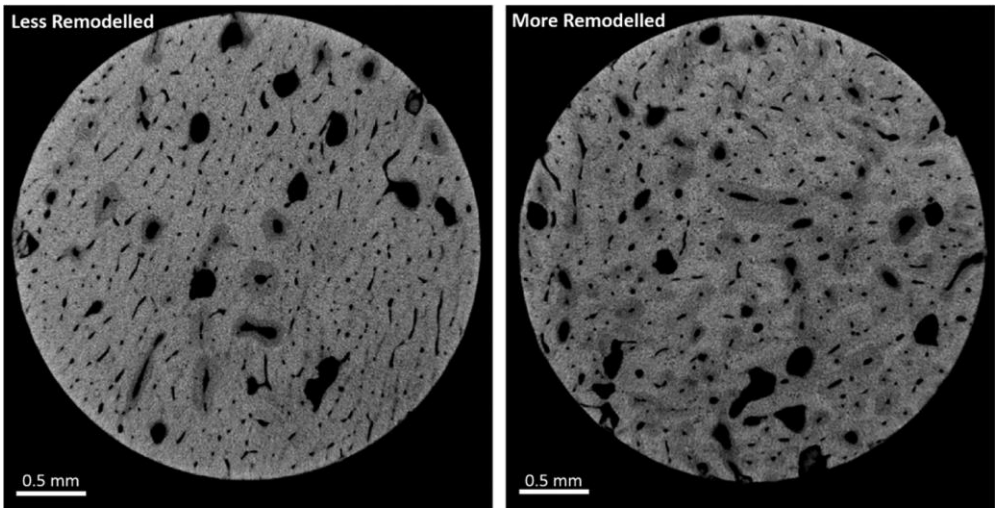

Figure 4.5. 2D virtual slices of the 3D tomography data generated from the XCT highlighting less remodelled (left) and more remodelled (right) cortical bone structure [42]. Extensive secondary osteon regions are shown around the pores of the more remodelled bone, whereas more limited numbers of secondary osteon regions are seen in the less remodelled cortical bone.

This allowed a fluent management of the meshes in the following section relative to the osteons selection and islands removal. Continuous shapes representing the osteons were selected and saved in a new .stl file in which islands parts (regions composed by a number of triangles lower than 1k) were excluded after osteon selection (Figure 4.6).

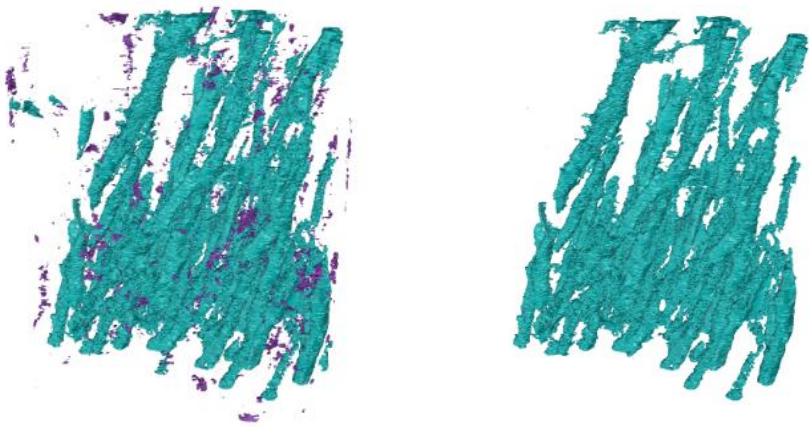

Figure 4.6. Representation of the island removal from the decimated mesh. Islands in purple in this case can be considered not belonging to the region of interest made by all the segmented secondary osteons.

4.3 Description of bone using parametric design

An approach using generative design was used as an alternative to the extraction of features from XCT to produce a CAD data set shown above. Generative design directly inputs into CAD and attempts to produce complex architectures in an easy and interactive way to speed up the creation of 3D models [145]. Currently, engineers together with designers and architects are taking advantage of powerful outputs provided by computers in 3D environments complying with the emerging field of design for additive manufacturing (DFAM). Direct tools allow the creation of architectural forms taking advantage of the intuitive interaction between user and 3D modeller. Freedom in designing complex shapes is gained, possibly made of multiple parts leading to the manufacturing of multi-material assemblies. Therefore control can be reached not only on the hierarchical disposition of material, but on its functionality [121] [146].

Until now, 3D models have been developed by polygonal meshes techniques, solid models or parametric surfaces (NURBS bi-cubic spline); the first methods are widely spread in 3D imaging as observed in the previous section 4.3.1, while many others users assemble appropriate interfaces managing geometric models through commands and routines. The absolute definition of “parametric” will be in this section significantly broadened, putting together design parameters and processes into visual algorithms exploiting a generative design (GD) approach.

Bone scaffold design, especially in the case of trabecular bone, must allow the creation of a variety of porous structures to obtain the heterogeneity of the biological tissues, controlling basic features like pore dimensions, porosity and pore interconnectivity [40]. For the cortical bone, the idea is to reproduce a parameterised

version of the lamellar structure belonging to the secondary osteons. The idea is not only to reproduce via CAD the characteristic hard and soft arrangements of osteons as appears in nature, but to couple the resulting design with trabecular architectures heading towards another level of biomimicry where two or multiple tissues contribute together to comply with structural requirements at organ level.

GD can be defined as a form finding process, meant to produce a wide range of solutions, from a few to thousand, depending on the level of complexity of the object and the controlled parameters that define the geometrical entity. Algorithms can be written starting from an ideal case and formalized in codes. The computed process is able to follow the rules in input and shapes can be therefore visualized by the user. If the output is in accordance with the ideal case, the next step is to choose an appropriate manufacturing process to realise the parts. To such extent, a tool for computer aided industrial design (CAID) called Rhinoceros (McNeal, Seattle, WA, USA) is providing means and plugins to widen free form modelling, regardless of any level of shape size and complexity. Grasshopper is a tool able to increase Rhinoceros functionalities [147] and represent a suitable instrument for engineers, architects and designers; it presents a way of thinking for design issues, a 'method' called Parametric or Associative. CAD evolved to generative design [148], where specific elements and algorithms are provided tuning geometries that can be oriented to different purposes. To the author's knowledge, several geometries have been presented so far within libraries mostly based on trabecular structures, porous and interconnected but poor in terms of morphology and natural appearance. The purpose of this section is therefore the realization of a *Generative Algorithm*, obtainable with Voronoi diagrams, proposing an easy and interactive, user-friendly method.

Computational geometry is concerned with the design and analysis of algorithms for geometrical problem [93]. Other more practically oriented areas of computer science such as computer graphics, computer aided design, robotics, pattern recognition, and operation research, give rise to the problems that inherently are geometrical. The ordinary Voronoi diagram, for a point set and its construction, have been studied extensively in both two and higher dimensions [149].

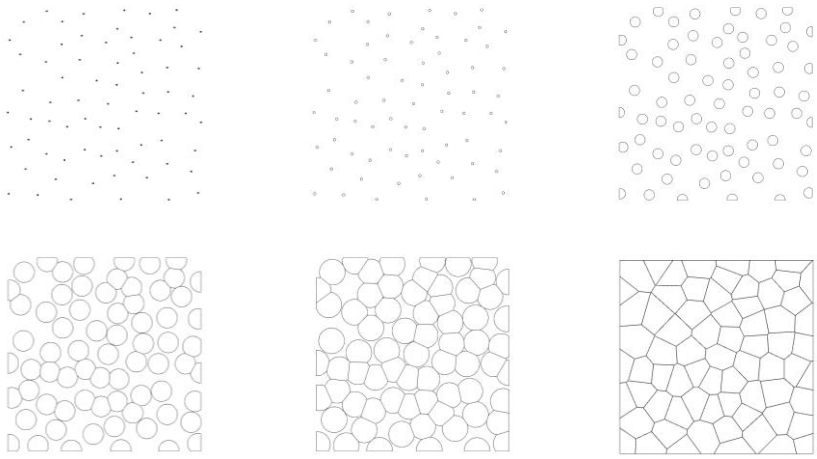

Figure 4.7. Visual representation of the formation of a Voronoi Diagram in two dimensions. Circumferences are grown from seeds to the point of colliding and forming polyedrical perimeters.

In a 2D vector space where the Voronoi diagram is modelled, points, lines and polygons are primitives. Let the finite Euclidean space contain a certain number (n) of points (with n > 1), called seeds. Around each seed a circle is drawn, with a starting radius of 0, expanding at the same rate until two circles touch so that a line or boundary is formed. The circles keep expanding until they cannot expand any further (Figure 4.7). The resulting graph is the Voronoi diagram for that set of points. The diagram is built corresponding to the areas in which each point location is closest to the seed corresponding to that area.

The mathematical equation of such a polygon V(pi) can be expressed as follows (Okabe et al. 1992):

$$V(p_i) = \{p/d(p, p_i) \leq d(p, p_j), j = i, j = 1, \ldots, n\} \quad \textit{Equation (4.1)}$$

Where:

- $p_1, \ldots, p_n$ is a set of distinct seeds located in Rd;
- $d(p, p_i)$ represents the Euclidean distance between location p and seed p_i;
- $V(p_i)$ represents the ordinary Voronoi polygon associated with seed p_i.

In 2D, Voronoi cells are separated from each other by boundaries that consist of line segments. The Voronoi cell consists of a convex polygon without holes. In Figure 4.6, an example of the 2D Voronoi diagram is shown.

In this section, a generative design workflow implementing the 3D Voronoi diagram for modelling cortical bone tissue engineering scaffolds is proposed (Figure 4.8). The aim is to automatically build a lamellar structure, starting from a set of points randomly distributed in a square regular region of interest hereafter called ROI. This process allows to obtain a multi-layered structure that corresponds to the basic unit represented by the secondary osteons, repeated into the space according to the number of seeds. The increasing number of osteons was showed [150] to be directly related to the fatigue life of bone, pertain the presence of more interstitial bone rather than secondary osteons is directly attributed to a short fatigue life. This aspect can be controlled over the design increasing the number of seeds into the region of interest (ROI), or increasing another parameter relative to the external diameter of the idealised secondary osteon.

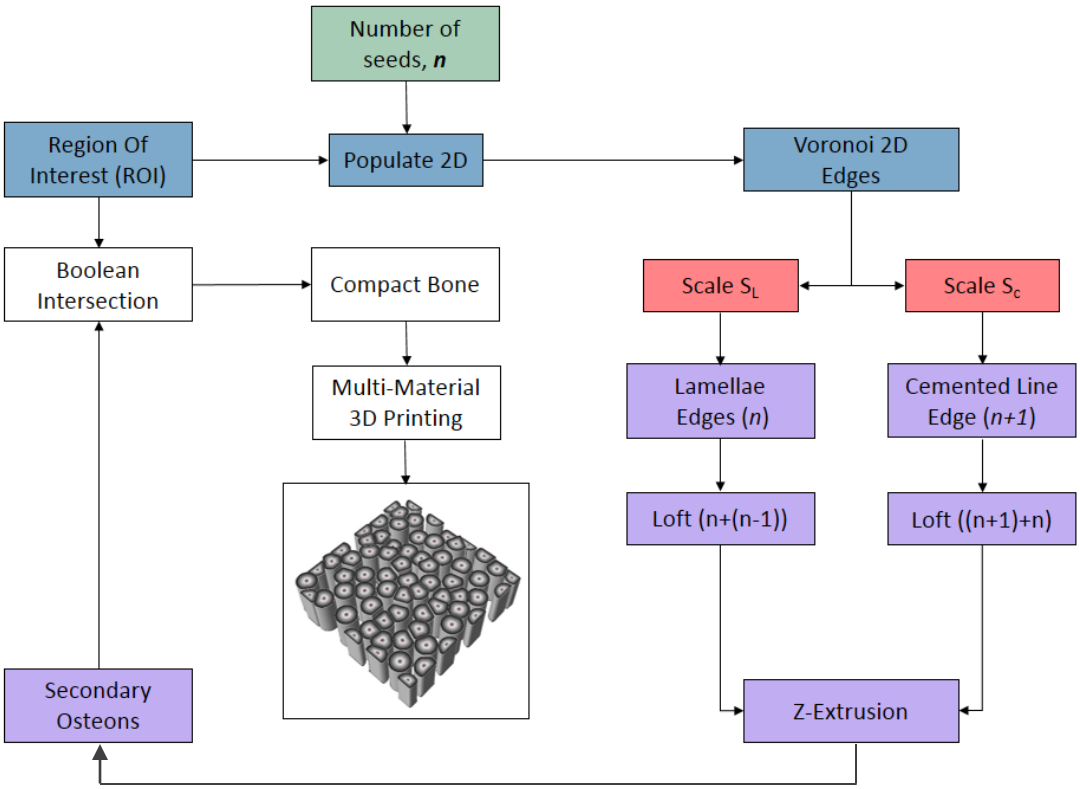

Figure 4.8. Detailed workflow for the secondary osteons scaffold generation.

The generative workflow implements a multi-lamellar structure ready to be 3D printed, starting from a dataset of five inputs: the considered ROI, that has been chosen based on a regular shape to calibrate the method, the number of seeds (n), the secondary osteon mean diameter, and two scaling factors (S_L and S_C) defining the cemented line thickness S_C and lamellae thickness S_L. The sub-circuits implemented in Grasshopper are associated into the same global graphical or visual algorithm as shown in Figure 4.9 for representative purposes.

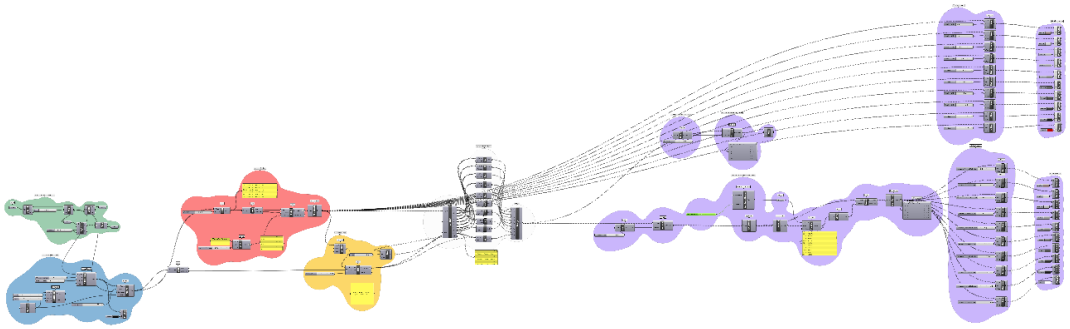

Figure 4.9. Overall generative design workflow extending over the Grasshopper canvas.The green subroutine generates the seeds distribution coinciding with the osteons centroids. The blue group, defines the region of interest that has to be filled with osteons. Any seed not included into the region of interest is excluded. The red group scales each osteon contour according to a set number (S_L and S_C). The osteon becomes a multilayered lamellar structure made of a cemented line, which represents the outern layer, and a series ofconcentric lamellae. A loft between each scaled contour is by performed by the purple subroutine which provides for a surface extrusion so that the 2D loft become a 3D hollow cylinder. Minor subroutine are the orange and white groups that act as database created to maintain ordered the geometrical shapes

The first sub-circuit works on the ROI represented from a geometry that can be regular or defined by more complex regions. The populated 2D component aims to fill the contour of interest with points randomly distributed (Populate 2D). As previously mentioned, the points are seeds from which circumferences are grown to account for cortical bone regions that can be more or less remodelled, hence, populated by secondary osteons. The points map is given as input to a component Voronoi 2D which performs the circumferences growth in accordance to set Voronoi cell diameters. The aim is to spread seeds in accordance to the desired degree of mineralization that represent the aging of a bone. Imaging of bone using XCT as shown in Figure 4.4 provides such structural variations due to age that are considered here in generative design. Each circumference is generally regular, but depends on the distances separating seeds. Irregular geometries will occur when circumferences contact one another (Figure 4.10).

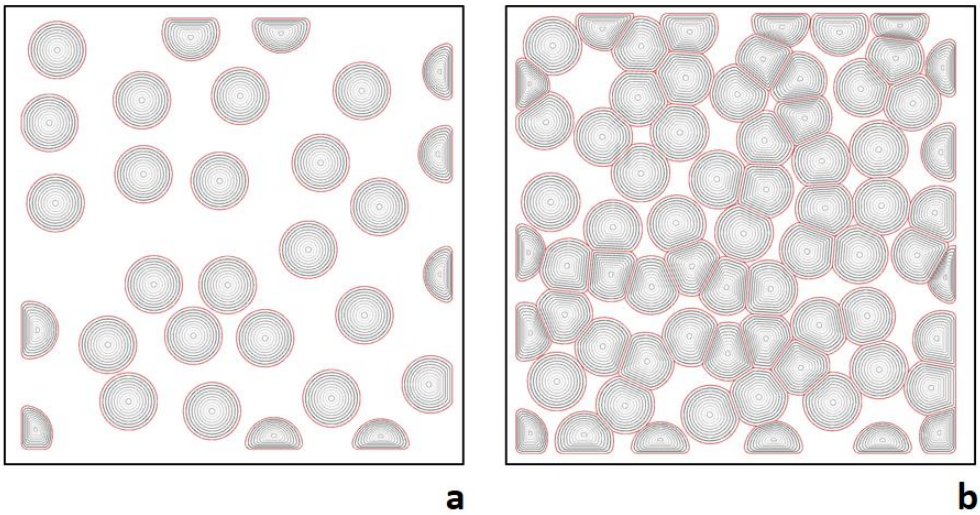

Figure 4.10. 2D CAD drawings showing secondary osteons diagrams, with a lower seeds concentration (a) in comparison with a higher seeds concentration (b). Cemented lines are colored in red whereas lamellae boundary are in black. This two cases can be representative of idealised more or less remodeled cortical bone.

Computations are then performed using two scaling factors in order to scale each boundary edge to create secondary osteons cement line, followed by a second scaling operation that creates the lamellar architectures made of concentric cylinder-like shapes. The scaling factors are chosen by the user through the number slider component, which set digits representing the thickness of both cemented lines and lamellae. The desired value can be an integer or floating number, starting from zero to the desired thickness value. The advantage of parametric design is about creating a workflow that can be implemented regardless of manufacturing technology or the specific make of a multi-material printer. However, it is important mentioning how the 3D printing materials mechanical properties vary from a technology to another as well as similar technology produced by different manufacturers using same material as in the case of photopolymers assemblies (i.e. Stratasys Polyjet VS 3D Systems Multijet). In this sense, the set value for parameterising geometrical shapes, meant to be mechanical performing in an architectured system, needs to be calibrated according to

standardised base materials mechanical tests, allowing to retrieve the best compromise between shapes, function, and builds mechanics after manufacturing.

Generative design is a conceptual, dynamic, iterative and fluent way of shaping objects. Objects dimensions can be set within the 3D environment in order to design at sub-micron length scales as well as above the meter scale. In this sense, limits related to the adopted manufacturing technology are boundary conditions necessary to the production of a bioinspired functional material.

Real cement lines represent the stiffer material contributing to cracks deviation within compact bone. The cemented line replica should be dimensioned so that the surrounding softer matrix (lamellar bone in the case of real compact bone) will not reduce cement lines mechanical consistency at the interface while manufacturing.

Afterwards, the scaled edges are lofted in order to create concentric surfaces that can be extruded into cylindrical shapes, each set per secondary osteon concentric to the respective seed point (Figure 4.11a and 4.11b). A further step can be considered by translating each secondary osteon along the Z axis as shown in Figure 4.11c.

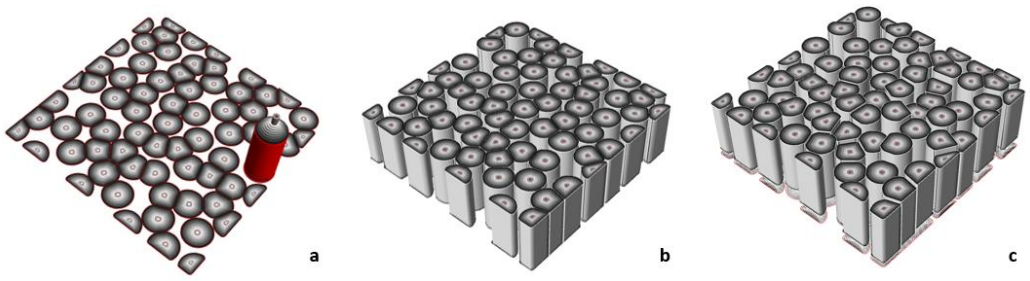

Figure 4.11. 3D CAD drawing depicting concentric surfaces to be extruded to form secondary osteons (a). All concentric surfaces are extruded to form aligned concentric cylinders (b), displaced along the Z axis to reproduce a more organic and loyal bio-design.

Finally, a solid subtraction (Boolean difference) is performed retrieving holes into the matrix where secondary osteons made of lamellae and cement lines are placed. Figure 4.12 illustrates the algorithm applied to a ROI that resembles a portion of the diaphysis from a long bone.

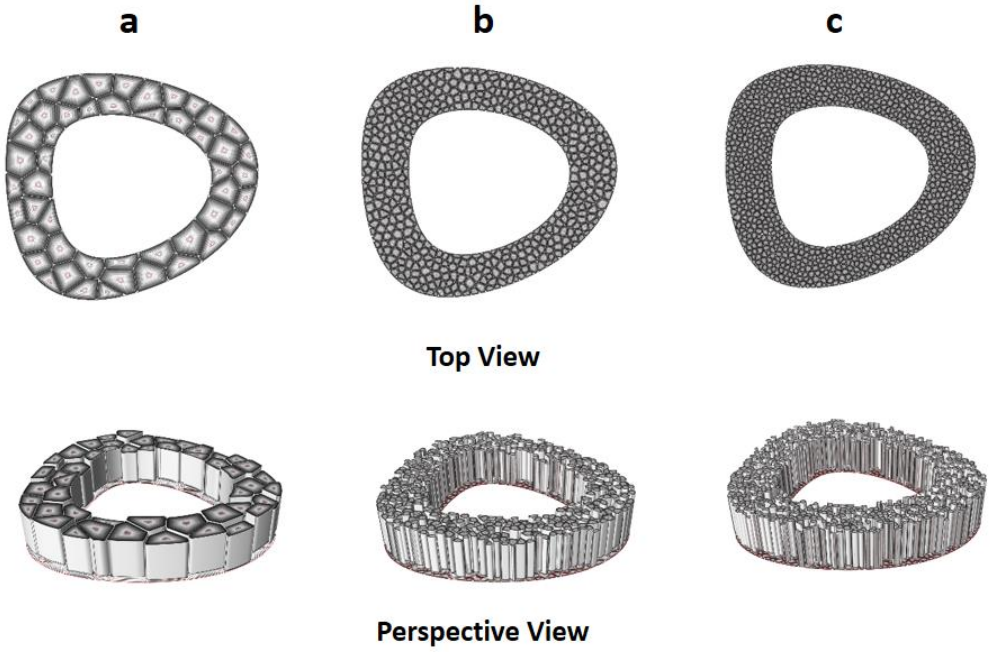

Figure 4.12. The picture shows different seeds concentrations increasing the secondary osteons density from left to right of 50, 300 and 500 seeds respectively.

4.4 Translating digital designs to manufacturing

The previous section demonstrated the use of both XCT and parametric design to produce a digital description of bone. This section progresses the workflow in Figure 4.4 that describes methodology required to produce a physical output using additive manufacturing from XCT. Indeed, mechanical evaluations of the additive manufactured

biomimetic bone samples are mandatory to allow comparisons with the corresponding mechanical behaviour of the original bone tissue.

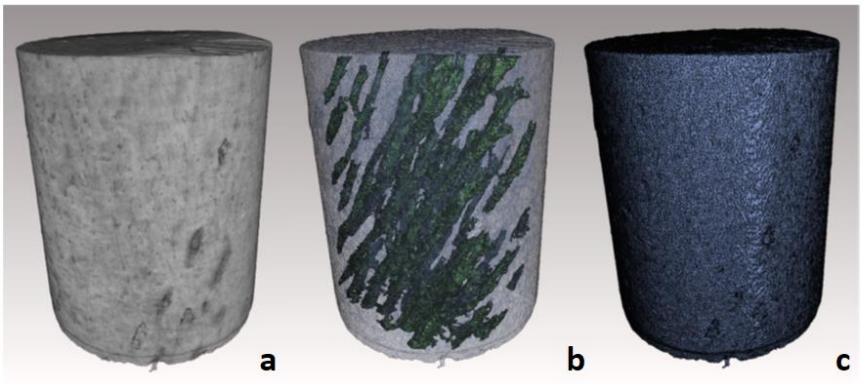

Figure 4.13. Virtual model development firstly used the X-ray tomograms (left) and resultant segmented data (middle) to distinguish the primary bone from the tubular features of the secondary osteons. Meshing (right) gave a complete model that was suitable for a physical output from 3D printing that retains compositional and morphological information.

The XCT imaging datasets shown in Figure 4.13 were selected. Meshes were imported into CAD software (Rhinoceros 5.0, Robert McNeel and Associates, USA) and scaled by ×10 to increase feature density within the 3D printed structure. Validation of the closed surface of the meshing and removal of holes and artifacts was carried out using a commercial software (NetFabb, Autodesk, UK). Finally, 3D printed samples were outputted from the CAD to a physical composite model using an inkjet-based 3D printer (ProJet 5500X, 3D Systems, USA) that allowed the additive deposition of multiple materials. The hardest material was used for the secondary bone regions WT (VisiJet CR-WT, 3D Systems, USA) and a series of increasingly softer matrix materials (VisiJet RWT-EBK 100, VisiJet RWT-EBK 250 and VisiJet RWT-EBK 500, 3D

Systems, USA) defined as CM10%, CM25% and CM50% respectively were used as the primary bone material. The materials were chosen from the range available commercially for use in this specific 3D printer. The approximate ratios of the hardest to the increasingly softer materials using the manufacturer's elastic modulus specifications are 2.7, 11, and 40, respectively. The ratio of elastic modulus for the secondary osteonal material compared to primary osteon is approximately 10, taken from literature [151], indicating a ratio of 3D printed materials comparable to those found in bone despite the absolute values being lower. The printer operated in extreme high definition mode with a 13 μm spatial resolution in the z-axis and 34 μm spatial resolution of materials deposition in the x and y-axes of the build plate plane. The long axis of the cortical bone structure was aligned along the x-axis. XCT validation of the 3D printed samples was attempted but was impossible to distinguish between the different material compositions due to similarity of X-ray attenuation across all the base materials.

4.4.1 Mechanical evaluation of 3D printed biomimetic bone structures

Mechanical properties of the cortical bone samples and 3D printed mimics were evaluated using acoustic measurements. The propagation of ultrasonic waves is an established method of measuring the elastic properties of bone as well as 3D printed trabecular bone phantoms as demonstrated recently [152]. Samples of bone and 3D printed structures were fixed between a transmitting and receiving transducer setup (Olympus V103/V153, UK). The transducers were clamped using coupling media (ShearGel, Magnaflux, USA) to the opposite ends of the samples using an approximate force of 10 N/cm^2 so that the long axis of the sample traversed between the transducers.

A 1 MHz sine pulse was generated, with a repetition frequency between 10 and 1000 Hz, at the transmitted end of the sample so that the ultrasonic pulse was detected at the receiver using an oscilloscope. The fast first arrival ultrasonic wave velocity, defined as the primary p-wave velocity V_p, and secondary s-wave velocity V_s were calculated using:

$$V_p = Lt_p^{-1} \qquad \textit{Equation (4.2)}$$

$$V_s = Lt_s^{-1} \qquad \textit{Equation (4.3)}$$

Where t_p and t_s are the p- and s-wave arrival times, and L is the length of the sample. The apparent elastic modulus E of the cortical bone is calculated from [153].

$$E = 2\rho V_s^2 \left[1 + \frac{(V_p^2 - 2V_s^2)}{2(V_p^2 - V_s^2)}\right] \qquad \textit{Equation (4.4)}$$

Where ρ is the sample density given from the volumetric methods. Complete volumes of the bovine bone were successfully imaged using XCT for both the less remodelled and more remodelled cortical bone samples. The 3D tomography data sets for less and more remodelled bone samples were used to provide a virtual model of the bone following a series of steps as shown in Figure 4.13. The 3D data was segmented to highlight the secondary osteons and then finally meshed with a range of triangular features from approximately 1.5 million for the less remodelled bone to 3 million for the more remodelled bone. The increased digital weight for the more remodelled bone compared to the less remodelled bone was due to the increased number of secondary osteon features in the mesh. The 3D printed physical output from the virtual model is

shown in Figure 4.14 for a number of samples. The 3D printing provides low-density wax material support that is observed as the lighter coloration under the darker structural material. Mechanical evaluations of the base materials used to construct the 3D printed structures of bovine-like bone are shown in Table 4.1.

Table 4.1. List of the P- And S-Wave Velocities and Corresponding Calculated Elastic Modulus Values for a Range of the 3D Printed Base Materials Used.

	p-wave velocity (m s^{-1})	s-wave velocity (m s^{-1})	Density (g cm^{-3})	Elastic Modulus (GPa)
WT	2401	1100	1.19	3.95
CM10%	2367	1073	1.22	3.85
CM25%	2269	997	1.18	3.24
CM50%	2155	921	1.15	2.71

Minimal variations of both p- and s- wave velocities between the WT and CM10% materials resulted in similar elastic modulus values of 3.95 and 3.85 GPa, respectively. A reduction of 16% in elastic modulus is observed between the CM10% and CM25% materials with a further 17% reduction in elastic modulus for the CM50% material. Elastic modulus measurements for the 3D printed structures and the corresponding less and more remodelled bone samples are shown in Table 4.2. The bone samples exhibit noticeably higher elastic moduli than the 3D printed structures and this was expected mainly due to the high elastic modulus, of the mineral phase in bone (129GPa [154]). Interestingly, the less and more remodelled cortical bone samples have similar elastic moduli.

Table 4.2. List of the P- And S-Wave Velocities and Corresponding Calculated Elastic Modulus Values for the Less and More Remodelled Cortical Bone Samples, and the Corresponding 3D Printed Composite Structures with a Range of Matrix Materials

	p-wave velocity (m s^{-1})	s-wave velocity (m s^{-1})	Density (g cm^{-3})	Elastic Modulus (GPa)
More remodelled	4591	2104	2.65	32.07
CM10% matrix	2409	1101	1.21	4
CM25% matrix	2331	1070	1.19	3.72
CM50% matrix	2290	988	1.18	3.18
Less remodelled	4808	2415	2.04	31.74
CM10% matrix	2260	1027	1.2	3.45
CM25% matrix	2194	968	1.19	3.08
CM50% matrix	2164	910	1.19	2.75

The variation of the secondary osteon composition of the less and more remodelled bone is clearly shown in Figure 4.15, with analysis of the 3D tomographs indicating volume fractions of 4 and 55%, respectively, for less and more remodelled bone. However, the volume fraction porosity of the more remodelled bone is slightly higher at 8% than the 7% for less remodelled bone. The porosity of the less and more remodelled bone samples as well as their corresponding 3D printed designs was taken from the XCT imaging data sets and calculated using volume fraction analysis (Visual SI Advanced, ORS, Can.). The more and less remodelled porosity volume fraction was found to be 7.12 and 6.63% respectively. The corresponding average volume fraction porosity from the 3D printed samples for the more and less remodelled designs was 5.47 and 4.24%, respectively. The bone samples show a slight increase in porosity from the less to more remodelled bone. The 3D printed samples show the same trend of increasing porosity moving from the less remodelled to the more remodelled bone design.

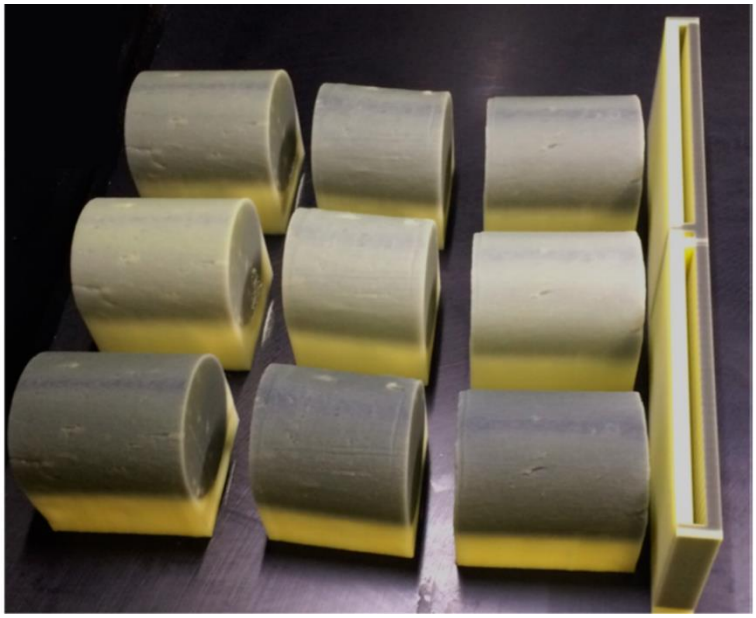

Figure 4.14. Optical image showing the 3D printing bovine bone structures from XCT data. The printed material is effectively the darker coloration whereas the wax support is the lighter region underneath the sample. Note the long axis of the bone is left to right in the image and parallel to the build plate of the 3D printer[42].

The lower porosity for the 3D printed samples compared to the bone is expected to be due to the meshing process removing small pores that are below the mesh size prior to the 3D printing. We also note that the voxel size of over 5 μm may also ignore sub-micrometre porosity in bone linked to the larger scale porosity. The increase in the stiffer secondary osteon phase of more remodelled bone is thus potentially offset by the enhanced porosity relative to the less remodelled bone. Understand the variation in the mechanical properties of the 3D printed structures was attempted by plotting the ratio of hard osteonal-like regions to softer matrix against the measured elastic modulus in Figure 4.15. A linear trend of increasing measured elastic modulus with decreasing ratio was observed for both the less and more remodelled designs. This trend is reasonable as the replacement of a soft matrix with materials of higher elastic modulus occurs when moving from the soft to the hard matrix material. The higher volume fraction of

osteonal-like material for the more remodelled bone is reflected in the higher elastic modulus of the structures using the corresponding bone design relative to the less remodelled bone design.

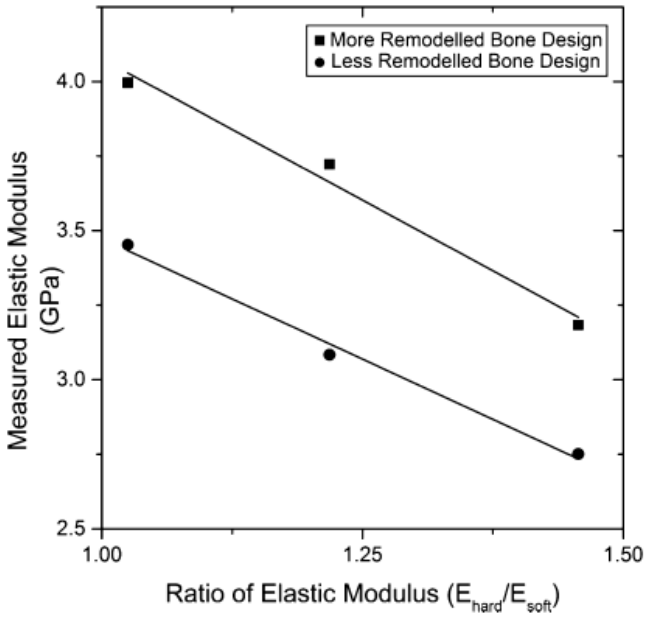

Figure 4.15. Plot of the variation in the measured elastic modulus of 3D printed structures based on less and more remodelled cortical bone design with the ratio of elastic moduli of the hard to soft materials used in these structures.

Chapter 5. 3D printing of bioinspired nacre

5.1 Introduction

Chapter 4 introduced the structure of cortical bone and efforts to replicate its architecture following both bioduplication and biomimetic approaches. High-resolution X-ray computed tomography (XCT) allowed the segmentation of hard and soft volumes, composing the organised, tough, biological architectures of compact bone. An additional approach employed CAD design and algorithm modelling to allow for an idealization of compact bone, generating a parametric controllable model able to provide a family of biomimicked solutions rather than a single output. 3D printable files were produced according to both bioduplication and biomimetic approach, despite the former demonstrated a poor control in generating a composite structure. In fact, the design control was related exclusively to the image processing and segmentation procedure used to retrieve scalable STL files to be used in the 3D printer. The CAD model instead was able to replicate the unit cells of compact bone (primary and secondary osteons) as well as the interstitial bone with multi-layered structures, where the only limit was dimensional and related to the smallest feature a multi-material 3D printer is able to reproduce. Moreover, the geometrical shapes resulted to be adaptable to an arbitrary bulky shape to be characterised with the parametric onsteonal texture.

Compact bone is a biological composite structure, which features can be easily identified and recognised with medical investigation such as XCT. However, not all the biological architectures have dimension compatible with XCT investigation. Often, images are retrieved via Scanning Electron Microsopy (SEM) providing for topological insights on key features composing the biological structures of interest. This is the case

of nacre, whose composite structure undergoes the micro-meter scale, avoiding the possibility to be investigated in a sharp way and the possibility to be directly exported as a 3D printable file from imaging. Therefore, the biomimetic approach seems to be the only affordable and reliable route to reproduce a composite structured material inspired to the tough composite of the nacreous part of some sea creature shells.

This chapter seeks to identify and replicate a nacre that is distinct from bone but provides a clear impact resistant mechanical function enhanced by toughening mechanisms. Biological hard tissues such as bone and nacre are very popular to material scientists because of their enhanced toughness that is reached adopting different hierarchical compositional strategies. Bone is more complex compared to nacre since the assembly of soft and hard phases starts from the nanoscale where the collagen fibrils are mineralised thanks to the inclusion of hydroxyapatite crystals. Moreover, the hierarchical complexity of bone is extended over several levels of organization up to the entire organ level. Contrary to bone, the structural organization of nacre starts from the micro-scale where aragonite tablets are staggered together thanks to the addition of a soft phase which turns a highly mineralised tissue to a highly mineralised tough tissue. The structure of nacre is extremely simple compare to bone nevertheless maintaining stunning cracks resistance performances. The biomimicry design criteria highlighted in Chapter 4 for the compact bone is now tested on nacre, biological shield found in the inner layer of certain sea creatures shell. Nacre is a hierarchical, biogenic layered composite material whose geometric unit is predominantly composed of rigid flat polygonal Aragonite platelets of high-volume fraction, bound together with a minor volume fraction of softer biopolymer (Figure 5.1). The resultant composite is tough, damage tolerant and ensures protection of molluscs from predators and hydrostatic

pressures [10]. The toughness of nacre has been consistently noted as comparable and, in some cases, better than engineering high performance analogues. Therefore, nacre has been attracting the attention of the material science community due to its intrinsic toughening mechanisms responsible of improvement in impact resistant performance over its main constituents, dissipating energy and preventing crack catastrophic propagation [22] [29].

The mechanical properties of nacre have been studied extensively [56]. Nacre has a similar stiffness to engineering ceramics such as alumina, but the work to fracture can rise of several orders of magnitude thanks to cohesive forces between the platelets that, organised into layers, lead to remarkable toughness 3000 times higher than calcite [155].

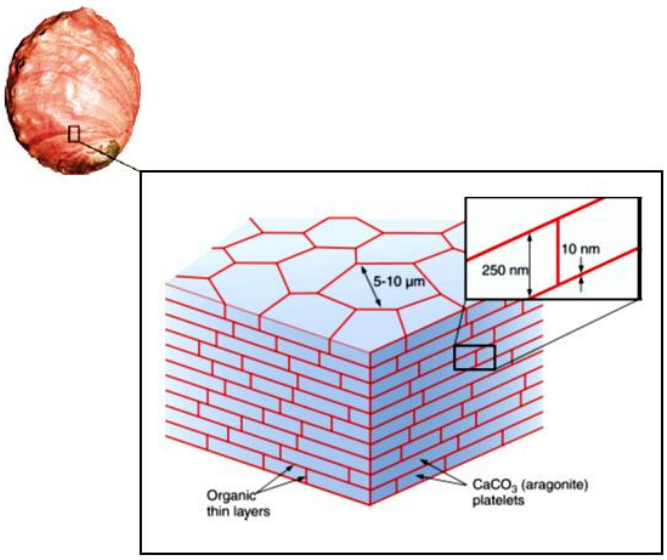

Figure 5.1. Representation of the internal nacreous organisation belonging to the nacreous layer of red abalone shell. The thin organic film in red separates the aragonite bricks [56].

Integrity and strength are ensured by building blocks parametrically designed during growth so that brittle bio-mineralised fibres are able to withstand external loads,

generating high tensile stress without fractures. A small percentage of soft bulky organic matrix at the interface between the hard plates facilitates stress transfer through shear during external loading [156]. When loaded, the failure behaviour of nacre is distinct and relies on at least micro-cracking events that propagate between the mineral platelets, failing at the interface as shown in Figure 5.2. However, the precise toughening process is contentious and additional mechanisms have been proposed to be significant in contributing to its specific toughness, including crack blunting within the nacre structure, energy absorption through plate pull-out, ligament formation and extension from biopolymer failure [157].

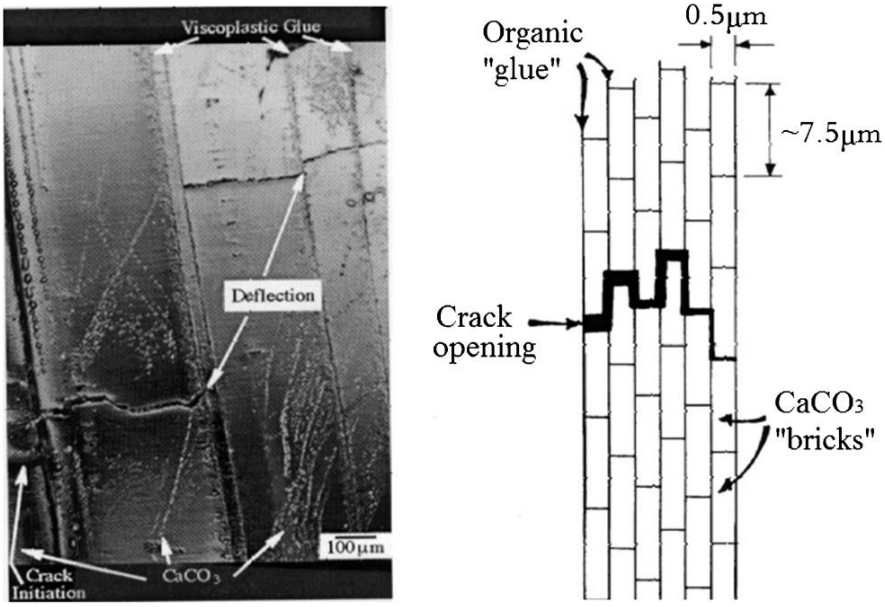

Figure 5.2. A Cross-section of the abalone shell is presented on the left showing the propagation of a crack deflected by the polymer in between the aragonite platelets. A schematic drawing is shown on the right highlighting nacre intrinsic brick and mortar arrangement [158].

Algorithm modelling and Three-Dimensional Printing (3DP) are now providing the possibility to create complex topologies with resolutions approaching several length

scales [111] [112] [119] [120]. A wide range of different materials can be manufactured according to different processes, from micro to meter-scale, extruding, curing, binding and sintering polymers, ceramics, organic materials and biomaterials. MM3DP is perhaps the most suitable manufacturing process to mimic the mechanical performance of nacre. Specifically, the combined use of hard and soft 3D printing materials, leads to complex architectures whose phases are directly assembled while printing, therefore, avoiding any additional process intended for assembling the composite phases.

This chapter therefore focuses on:

- Generating an iterative workflow meant to produce a hybrid of soft and hard phases similar to biological nacre, as input files for MM3DP.
- Suitability of the generated .stl files to be manufactured simultaneously.
- Effectiveness of combining 3D printed hard and soft materials using MM3DP to mimic cracks delocalization, at the base of toughening mechanisms in biological nacre, using standard mechanical tests such as, tensile, impact and nanoindentation tests.
- Quantitatively analyse the printing quality of the hybrid nacre using optical microscopy and XCT. Moreover, XCT is explicitly proposed as suitable metrology tool for the identification of multiple phases manufactured via Multijet multi-material 3D printing.

5.2 Material & methods

A form finding process has been proposed in order to supply a huge variety of nacre-based architectures. The resulting workflow follows the line of thought of generative design and algorithm modelling together with the biomimetic approach, already adopted in the past to produce biomimetic trabecular bone [94] as well in section 4.3 of this thesis. In the case of nacre, the proposed workflow is meant to work for MM3DP similarly to the generative compact bone of section 4.3, but differently from the trabecular bone widely printed via Direct Metal Laser Sintering (DMLS). 3D Parametric design and algorithm modelling are exploited to generate two complementary .stl files: stiff hexagonal platelets (reinforcement) embedded in a compliant polymeric matrix (bulk).

Figure 5.3 shows a schematic of the generative design used, discussed in detail below.

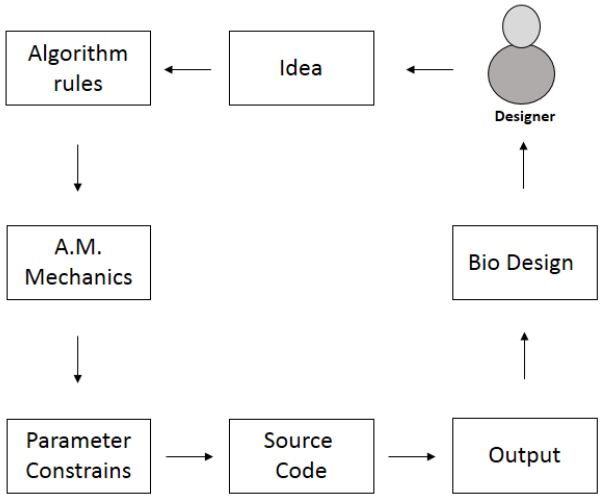

Figure 5.3. Scheme of the generative design process, adapted from[159].

The distinctive failure mode of nacre as well as the dimensioning of hard and soft phases is mostly promoted by a stiffness mismatch between reinforcement and matrix. Therefore, hybrid phases were parameterised using 3D printing materials mechanical properties, previously presented in section 3.2. Furthermore, interfacial failure between hard and soft materials shown in section 3.2.2 are also considered as critical parameter required in order to design suitable biomimetic nacre-like interface.

A commercial high-resolution multi-jetting material printer (ProJet 5500X, 3D Systems, USA) was used to produce biomimetic structures through depositing hard plastic for the platelet geometries and soft rubber materials at the interfaces between the platelets.

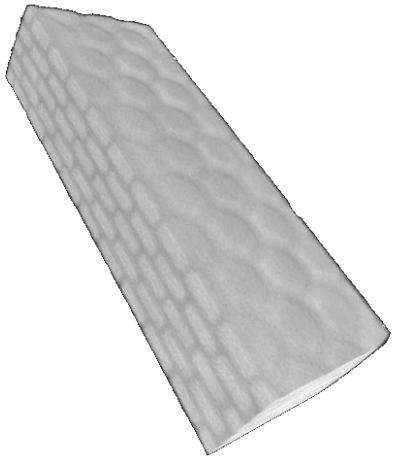

Figure 5.4. XCT reconstruction of a biomimetic nacreous structure produced from hard (bright) and soft rubber (dark) materials using additive manufacturing processes.

Mechanical testing of the resulting architectured composites was conducted to evaluate quasi-static and dynamic performances as well as to verify pull-out of the reinforcement related to the toughening mechanism of biological nacreous shell.

Subsequently, optical imaging and XCT evaluations were used to assess about fidelity of MM3DP (Figure 5.4). X-rays present a problem when imaging a 3D printed composite structure where materials with similar densities coexist. In the case of hybrid nacre, the contrast in the resulting image was maximized as the density between hard and soft materials are similar. Methods to enhance the contrast in the detected sample image included an exposure time of 2 s coincident with the XCT evaluations reported in section 3.3 and applied to a single fibre composite made of WT and BK 3D printing base materials. Therefore, the same workflow has been implemented involving operation of image filtering and segmentation such as Gauss smoothing and Region Growing. An example of contrast enhancement is show in Figure 5.5 where a single fibre composite section is showed before and after the work flow implementation.

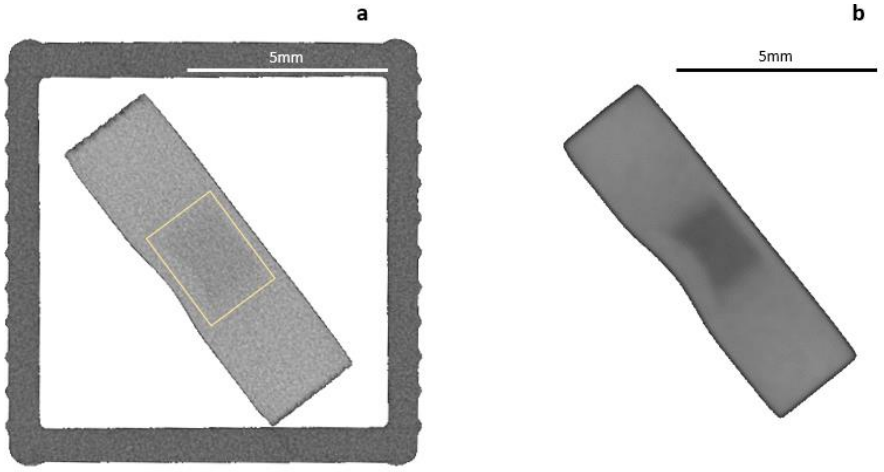

Figure 5.5. In the picture a single fibre composite is shown before (a) and after (b) image sample filtering and region growing applied to divide fibre from bulk.

5.2.1 Interactive CAD design and MM3DP of nacre

An interactive Generative Design (GD) process to reproduce a two-phase biomimetic composite inspired by nacre was attempted using a similar approach to GD of bone in

the previous chapter. The process is based on the brick and mortar structure of nacre resembling the $CaCO_3$ (Aragonite) platelets and the organic matrix (protein and polysaccharides) arrangement. The graphical algorithm editor Grasshopper, integrated with Rhinoceros 3D (Rhino) modelling tools (McNeel, Miami), is hereafter employed to control the parameterization of the hybrid nacre brick and mortar features. Grasshopper is able to work in parallel with Rhinoceros using a graphical interface, where users can build visual algorithms made of graphical objects or components. The algorithm is a set of rules and instructions iteratively applied in a step by step fashion. For representative purpose, the parametric design of a cylindrical shape is reported in Figure 5.6. The cylinder is a regular shape obtained generating a circle defined by a radius and extruded according to a vector parallel to the Z axis in the Rhino modelling environment. In this explanatory case the final cylindrical shape in output is given by the following parameters: the radius of the starting circle and the height to which the circle is intended to be extruded.

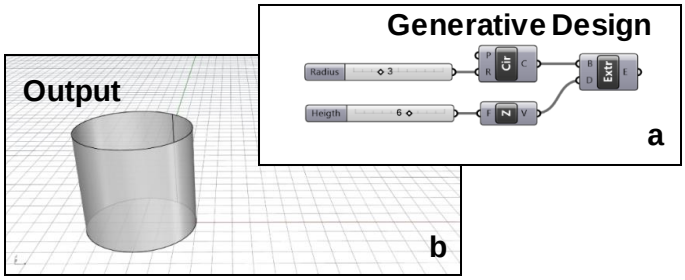

Figure 5.6. The image shows two windows, a and b, which are the Grasshopper editor and the Rhino modelling environment respectively. The output is generated by the graphical algorithm and represents a regular cylindrical geometry.

In the case of nacre, polygonal shapes are drawn to build up the structural unit to be repeated into the 3D space, distributed according to a pattern that defines the stiff reinforcement within a soft matrix. All the possible operation and commands in CAD

become part of a code able to produce a large number of objects (sometimes belonging to the same family of geometries) intended for field of materials design and manufacturing.

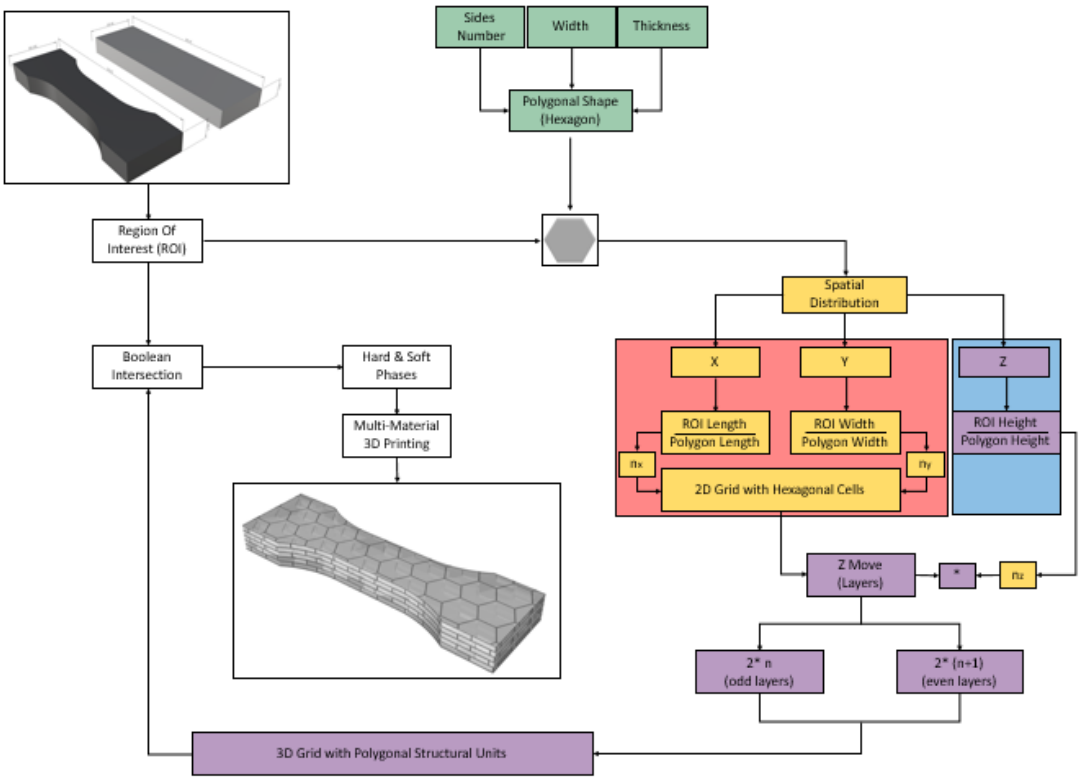

Figure 5.7. Workflow for the C.A.D. parametric nacre-like composite generation.The above schematic depicts different subroutines of the algorithm, according to different colours. The process starts taking into account the shape that has to be filled with the hard platelets texture (Region of interest ROI). The green group is the segment of the algorithm that allows to generate the cell unit. Input such as width and thickness of the plate as well as the tail sides number, are arbitrarily defined by the user.The red box togeter with the blue one evaluate ratios between the bounding box of the final component and the relatives of the cell unit created by the green group. Three numbers are given in output indicating how many time the unit cell can be repeted along x, y, z to fill the ROI. Finally the purple routine shifts each unit cell along x, y and z. The space created between platelets represents the softer phase of the hybrid composite, or the mortar phase of the brick and mortar structured composite.

A generative design work-flow is proposed below in Figure 5.7, with the aim of automatically building a hybrid nacre composites that can be fully parameterised starting from a dataset of three inputs: bulky shape, thickness and width of reinforcement.

As described in the following section, the distribution of the platelets is controlled through a series of sub-routines implemented in sub-circuits over XYZ axis, building a lattice that can vary in terms of both hard and soft volume fraction according to the desired target parameters. The work-flow above can be turned into a generative algorithm resulting in a CAD procedure cascade as shown in Figure 5.8. A coloured visual approach is shown purely for representative purposes, just to give an idea of what the global circuits and sub-circuits combination should look like. This contributes to the final 3D pattern made of plates embedded within the soft matrix.

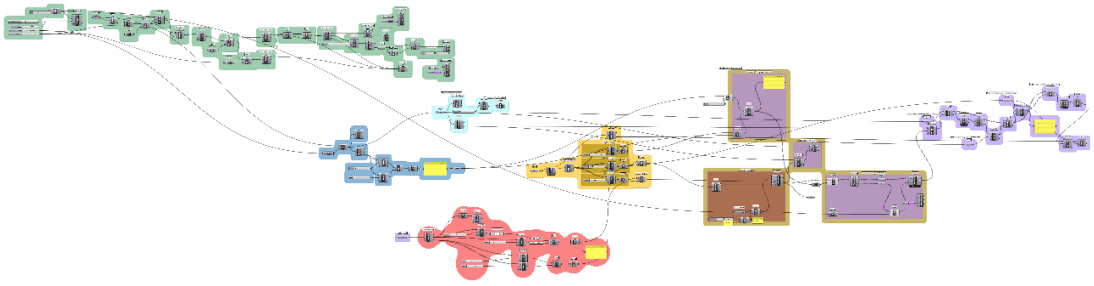

Figure 5.8. Generative design workflow converted from a generative algorithm in the Grasshopper editor canvas. All the circuits and routine described into the schematic reported in figure 83 are transformed in a visual algorithm where each component is connected to the following one recreating an automation of the conceptual CAD drawing at the base of the design.

5.2.2 Parametric design of the reinforcement

The workflow concept is described in detail below, using two different designs contributing to the final bio-mimicked structure. The first step produced the polygonal unit and is represented by the green sub-circuit (Figure 5.4-5.5). Digit inputs set the number of sides, the diameter and the thickness of the desired unit feature. A zoom in the green section of the visual algorithm is depicted in Figure 5.6a. Here, the form finding process starts from very basic primitives such as the creation of a polyline which

defines the reinforcement unit contour. The polyline, is the output of a component called Polygon available from the Grasshopper library (Figure 5.6a). The Polygon component receives four parameters in input, essentially the orientation plane, the radius and the number of segments of the desired polygon (Figure 5.6b). The polyline defines a contour that can be turned into a flat two-dimensional surface by the Grasshopper component surf, which needs to be extruded along the z axis in order to create a solid object (Figure 5.6c and 5.6d). Once the algorithm that shapes the polygonal unit has been implemented, the out coming feature varies according to the digital numbers in input. This approach represents the main advantage of a generative strategy, for which every change due to a different digit is applied to the overall design.

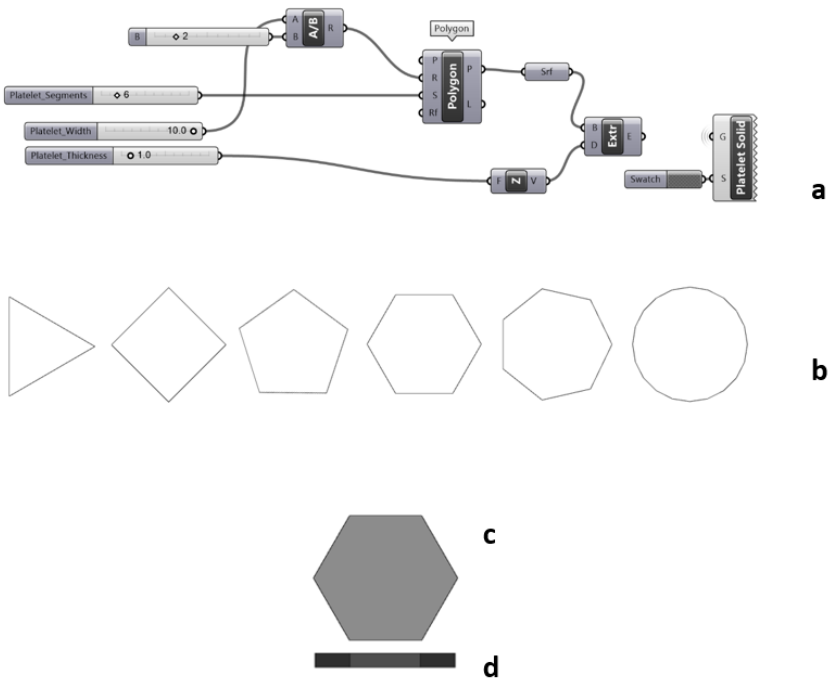

Figure 5.6. Illustrating the main steps to design the parametric platelet structural unit on which the hybrid composite is based. A hexagonal unit is therefore presented as result of a sub-routine (a) part of the green sub-circuit reported in figure 7. Digits are then set according to the desired shape defining number of segments of a polyline as shown in (b). In this case a six-fold line was produced and converted in surface (c) and extruded in a closed polysurface (d).

Thus, the reinforcement unit is repeated according to a desired pattern in the 3D space to fill up the bulk of the final component. Hexagonal platelets are obtained setting to six the slider component indicated as platelet segments in figure 5.6a. The following section defines the steps needed to systematically distribute reinforcement in a volume of interest.

5.2.3 Brick and mortar assembly parametric design

Once the structural unit of the reinforcement has been drawn, a pattern that replicates the single cell according to a three-dimensional grid inspired by the brick and mortar structure of nacre is created. The adopted strategy is to determine the platelets distribution over a single layer thanks to a two-dimensional hexagonal grid, designed by the orange sub-circuit. Then, the hard/soft assembly is carried on by the red, brown and purple sub-circuits (Figure 5.4 and 5.4), where a bounding box containing the Region of Interest (ROI) is defined as a boundary to be filled with the multi-layered reinforcement (Figure 5.7).

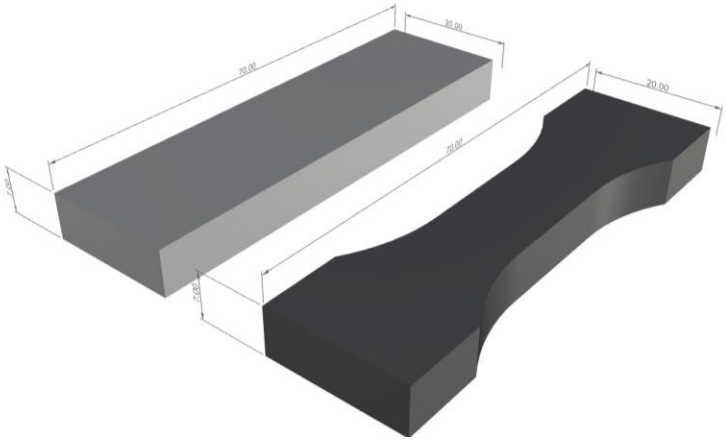

Figure 5.7. Design output for a simple box and the progression to an adapted dog bone sample. Reported measurements are in mm.

For mechanical testing purposes, a modified ‘dog bone’ standard geometry with its relative bounding box was chosen as shown in Figure 5.7. The final component represents an adapted version of the standard ASTM D638 used for the mono-material tensile results in Chapter 3.

Since the set of reinforcement fibres diameters varied from 2 to 9 mm, a dog bone shape with a wider transverse section was needed. The dog bone standard shape has been slightly changed in its dimensions to better embed platelets within the volume. The hexagonal grid that defined the first reinforcement layer is supplied by the Grasshopper library called Hexagonal grid (Figure 5.8). The hexagonal grid component receives in input an orientation plane (P) which is the base plane for the grid, a size (S) of the hexagon cells radius, a number of grid cells (Ex and Ey) in base plane x and y directions respectively (Figure 5.9).

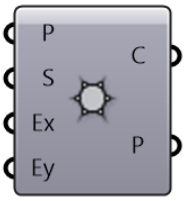

Figure 5.8. A typical Grasshopper component has input parameters represented by the dots on the left, while dots on the right represent the component output which are cells (c) or cells centroid (P). Grasshopper components work from left to right defining a cascade of actions when multiple components are join together as previously shown in Figure 5.6a.

Length, width and height of the bounding box are evaluated and divided by the corresponding dimensions of the designed platelet to obtain the number of grid cells n_x and n_y as shown in Figure 5.9a and 5.9b. The grid is repeated along the Z axis a number of times corresponding to the ratio between the height of the bounding box (box

enclosing the object which has to be characterised with the plates texture) and the height of the platelets (n_z).

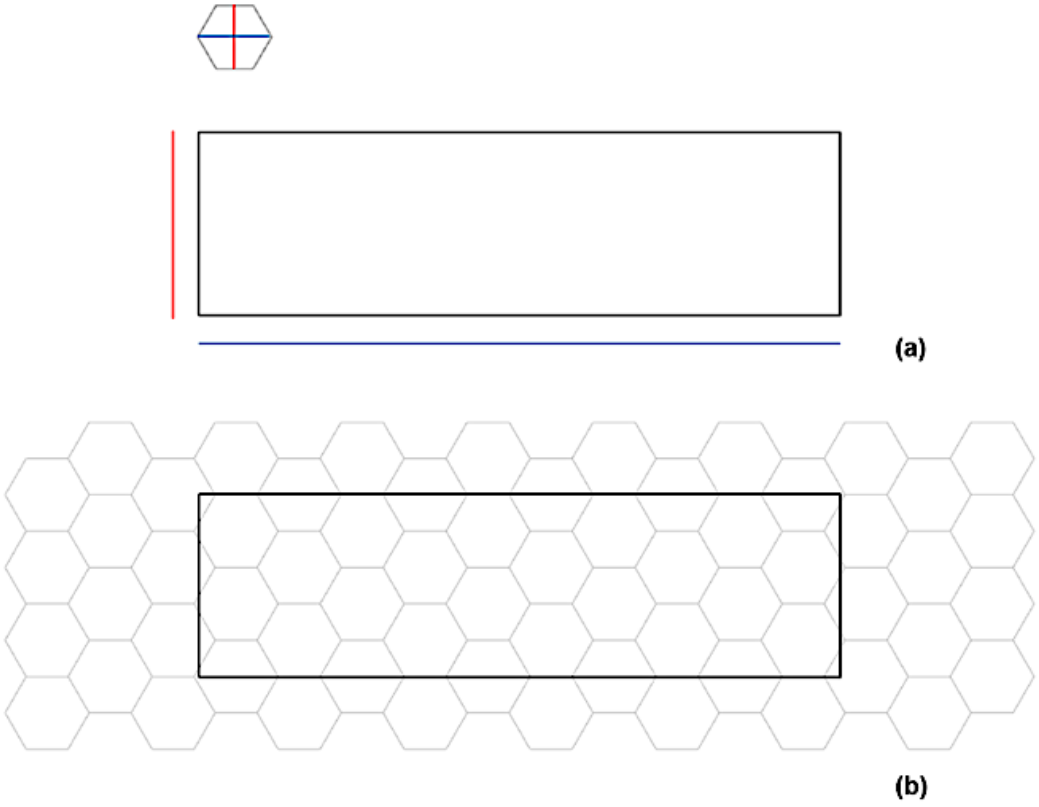

Figure 5.9. (a)Top view of the dog bone sample bounding box is reported together with the platelets. (b) The segments in red and in blue highlight widths and lengths of the base components required to produce a fit 2D hexagonal grid.

Alternate layers in a 'true-false' patterns are shifted along the X axis so that the platelets belonging to the even layers, in the workflow of Figure 5.4 indicated as 2*(n+1) and the platelets belonging to the odd layers, 2*n, are always sharing the same surface area.

Figure 5.10, highlights how the grid is shifted from a layer to another with two different colours. The red grid belongs to the odd layers whereas the blue one belongs to the even ones. The blue layer is shifted respect to the red one along the x axes of a distance coincident with the radius of the hexagonal cell unit.

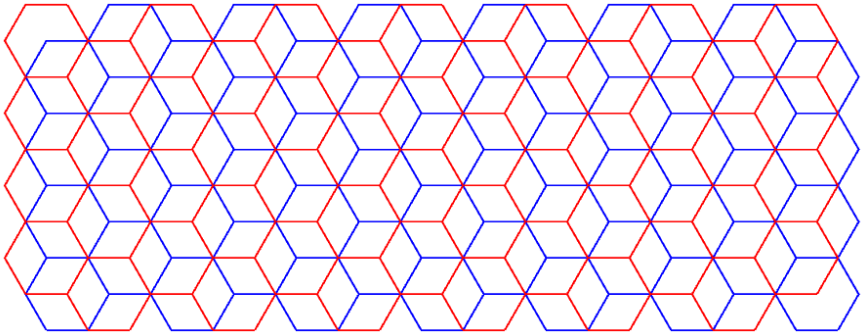

Figure 5.10. Overlapped grids from a top view, representing for the even (in red) and odd (in blue) layers. The centre of each cell coincides with three corners of the layer above or underneath. No spacing is applied in between platelets

Two offset values are introduced into the model in order to leave spaces in between platelets in the XY plane and Z direction. The thickness of the bulk material representing the polymer soft phase within the nacre can be tuned by setting the three following digits: the x and y offsets representing the size of the hexagonal cell radius, and the z axis offset representing the distance between the edges of the platelets of different layers. Figure 5.11, depicts four different cases for reinforcement settings and distribution over the 3D space.

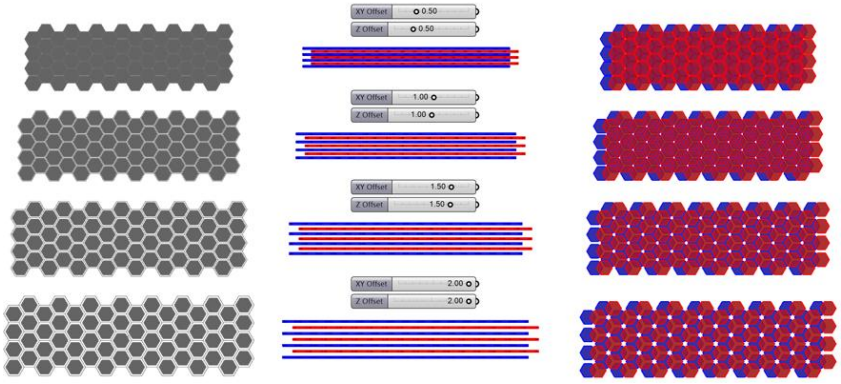

Figure 5.11. The schematic designs report the effects of the XY and Z offset values on the final multi-layered design. The space in between platelets represent the volume dedicate to the matrix of the composite defining what in the biological nacre is the polymeric phase. One single layer onto the left

side of the picture gives the idea of the platelets separation in XY, followed by the separation along Z in the middle and two layer composites (odd and even) on the right ride for offset values ranging from 0.5 to 2 mm.

The imposed numbers, set the thickness of the bulk that is the binding polymeric phase between the biological nacre platelets. Starting from 0 mm up to a given desired distance, platelets can be more or less compacted implicitly varying the volume fraction of the composite resulting in a brittle or tough composite. Finally, a non-manifold merge between the bulky component and the fibres pattern creates the two regions that, once divided, represent the hard phase of the composite and the complementary polymeric phase (Figure 5.12).

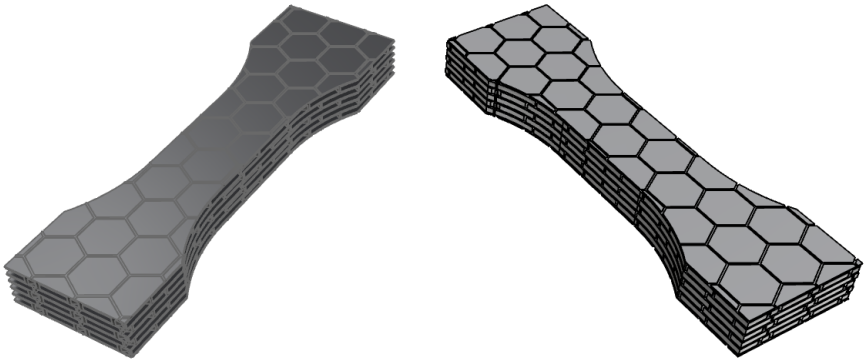

Figure 5.12. Schematic showing (left) the distribution of soft matrix material with the complementary hard counterpart made of platelets (right) from the generative design algorithm. The reported features are relative to a case of designed platelets of 1 mm thickness and 8 mm width, separated in X Y and Z by a 0.3 mm soft material.

A basic successful 3D design of nacre has been developed through generative algorithm showing the power of parametric design when a CAD environment such as Rhinoceros is coupled to the parametric platform Grasshopper. The design is free from dimensional limits given the freedom of the CAD environment to attribute an arbitrary "virtual" dimension. Moreover, no problems related to the generation of the .stl files affecting the integrity of the design, the continuity of the meshes and relative triangulation were revealed. Bulk and reinforcement phases as presented in Figure 5.12

reveal a possible output of the design workflow, ready to be given as input to MM3DP to manufacture the biomimetic composite. Additional information about the mechanics of the hybrid nacre is necessary to contextualise the use of MM3DP among the possible manufacturing techniques employed so far to realise nacre-like composites and related toughening mechanisms in one single manufacturing process.

It is worth highlighting how the following results are strictly dependent on the employed MM3DP machine as well as the set digits to parameterise the hybrid composites in accordance with the mechanical properties of the base materials. This means that the material properties can be different despite technologies being similar but produced by different manufactures. Hence a mechanical characterization of the materials to be used is strongly recommended before starting the design process.

The 3D modeller allows the user to draw shapes and geometries according to the design principles in mind. This can lead to more or less complex shapes, sometimes organic, therefore critical when it comes to the manufacturing process because of the digital weight, support material to be removed and post processing. Questions about the printability of generated files, mechanical interplay between hard and soft phases as well as the mechanical behaviour of the hybrid composite under static and dynamic loading conditions, arise from this iterative way of designing.

In the following sections insights about the mechanical performances of the nacreous biomimetic composite are presented in order to outline trends in terms of elastic modulus, strength and work to failure. Especially optical imaging of the composite points out the accuracy in manufacturing designed shapes, with a focus on the reinforcement units which carry most of the applied load under tension.

5.3 Behaviour of synthetic nacre in tension

Elastic properties of the hybrid nacre were analysed accordingly to the reported standards ASTM D638. The cross section of the tensile test specimens was slightly modified as reported in section 5.3.2 and depicted in Figure 5.13.

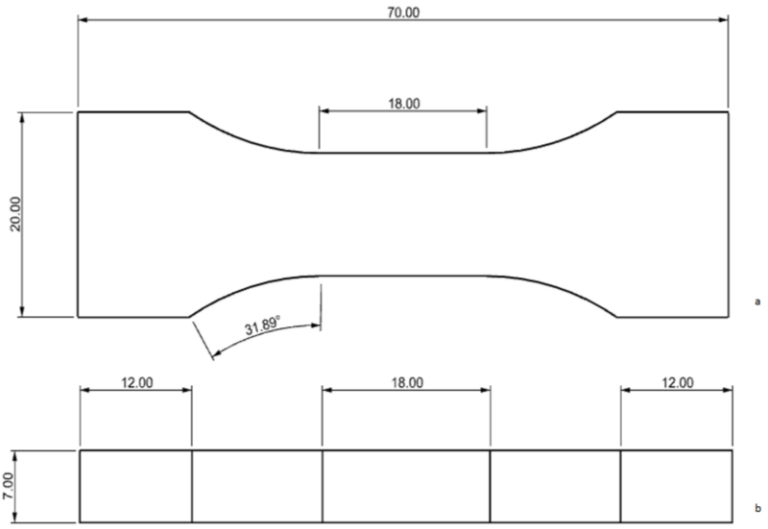

Figure 5.13. Dog bone sample designed accordingly to the ASTM D638 (Type IV) of section 3.2.1. The design has been modified to better accommodate the reinforcement fibre. Particularly, the width (a) as well as the thickness (b) have been doubled to insert multiple layers of reinforcement within the bulk. All the reported linear measurements are in mm.

A range of hybrid composites, with increasing volume fraction of the reinforcement, were obtained setting different inputs from the CAD algorithm. Physical models were obtained using an inkjet-based 3D printer (Projet 5500X, 3D Systems, USA). The process allowed the simultaneous additive deposition of two base materials VisiJet CR-WT and VisiJet CE-BK (3D Systems, USA) respectively employed to replicate the hard and soft phases of nacre. These materials will be referred from now on as material WT (hard white material) and material BK (rubbery black material). The

material cured instantly while printing. The adhesion of the two phases can be considered perfect, as strong as the one revealed during the shear test in section 3.2.2.

It is important to remark that the two base materials, WT and BK, were chosen for manufacturing the hybrid nacre because of their highly contrasting elastic modulus. Indeed, a stiffness ratio of about 1000 was reported in previous studies[98] [160], where the base materials for 3D printing should have respected as much as possible the stiffness contrast observable in biological nacre. Basic mechanical properties such as strength, elastic modulus and work to fracture of the 3D printed composites are expected to vary in accordance with the reinforcement volume fraction, highlighting if the failure mechanism of original nacre is mimicked.

Chapter 2 revealed that failure mechanics of bio-composites as well as hybrid materials are critically defined by the aspect ratio of the reinforcement units. The failure mode of composite is therefore determined by the fibres aspect ratio, which governs the effective stress transfer from the soft matrix. The aspect ratio of a fibre represents the proportion between its length and width and it is directly related to the shortest fragment that a fibre can produce when breaking when a composite is subjected to loading conditions.

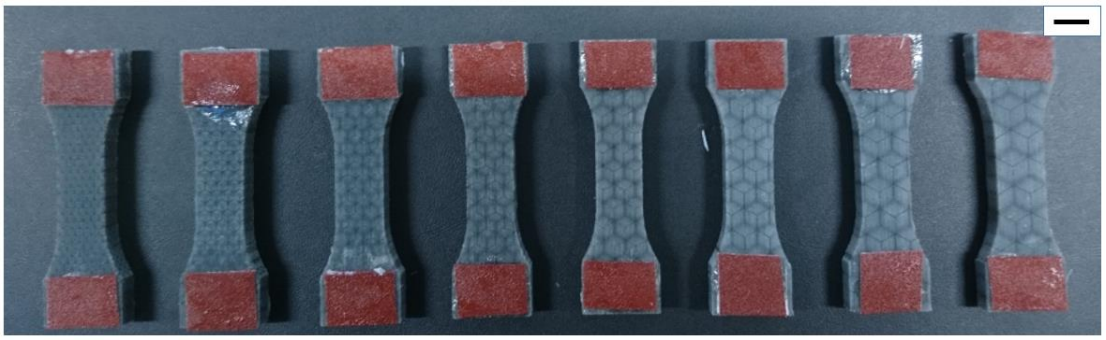

Figure 5.14. Set of samples with platelets aspect ratio varying from 2mm to 9mm, with a fixed thickness of 1mm. The scale bar on the top right is 10 mm long.

A high aspect ratio promotes stress transfer from the matrix though the fibres, maximising the probability of brittle failure of the composite. Whereas, low aspect ratio fibres promote interfacial failure where the continuous matrix yields before the platelets brake. Hence, the fibres pull-out from the softer matrix, leading to toughening mechanisms able to increase the overall toughness of the composite. For the purpose of this study, the platelet aspect ratio was varied in order to probe the pull-out mechanism within hybrid nacre when fibre aspect ratio is varied. The platelets diameter was varied from 2 to 9 mm in step of 1 mm, whereas the thickness of the plates was kept constant at 1 mm (Figure 5.14). Furthermore, two different orientations of the 3D printed parts were used to ascertain variability of the 3D printer in manufacturing composites. Indeed, the direction in which samples are printed can affect the mechanical properties of the builds, identifying a preferential printing direction.

Two sets of 3D printed hybrid nacre were successfully printed. Figure 95 shows how the first set was manufactured with the width of the samples parallel to the plane of the 3D printing platform (*in-plane*) whereas the second set was manufactured rotated of 90 degrees into the plane of the 3D printing platform (*out-of-plane*). Figure 5.15 depicts the 3D printed hybrid nacre. These multi-layered composites, vary in terms of reinforcement volume fraction, according to the diameter of the embedded platelets. The white stiff material (WT) can be distinguished from the black elastomeric material (BK) thanks to a well-defined hexagonal geometrical shape. On the other hand, the BK material is interposed in between platelets, remaining visible to the eye. From the darkest sample (2 mm diameter plates) to the brighter (9 mm diameter plates) the volume fraction of the reinforcement, evaluated as the percentage of fibre volume in

the entire volume of a fibre-reinforced composite material, varies from 53 to 63 vol%, far below the biological counterpart which reaches a 95 vol%.

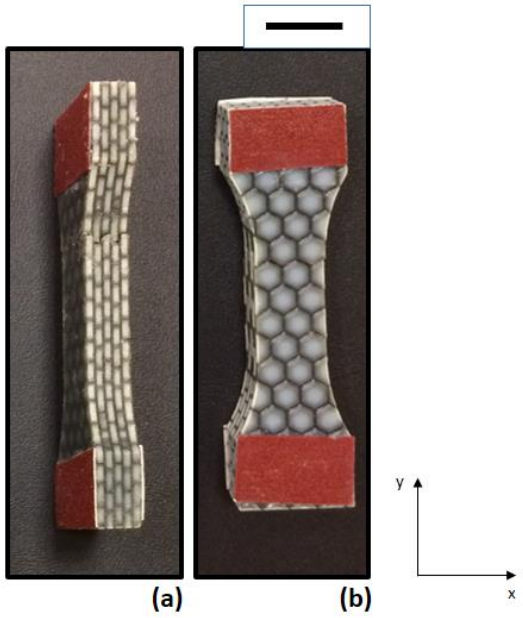

Figure 5.15. Representation of two 3D printing directions. Out-of-plane (a) and In-plane (b) 3D printing directions can produce parts with distinct mechanical properties. The reported scale bar is 1 cm long.

Mechanical tests were performed at room temperature in a Zwick/Roell Z030 Universal Testing Machine fitted with a 30 kN static load cell. Samples were fully clamped and subjected to a load of the samples at a rate of 2.0 mm/min. Sanding paper applied onto the dog bone samples' plates guaranteed a perfect adhesion avoiding dog bone sample sliding from the testing machine jaws as shown in Figure 5.15. The tablet-based hybrid structure did not incorporate any feature responsible for toughening mechanisms within biological nacre such as dovetails, mineral bridges and nano-asperities. Therefore, a simple brick and mortar structure able to define a lower bound for the entire composite interfacial hardening was adopted. Figure 5.16 is representative of the failure mode and cracks opening, developing over the entire sample volume and

testify to a principle of energy dissipation with similar mechanisms observable in biological nacre. An external load is applied to the multi-layered composite. Here a tensile stress is transferred to the fibres through an interfacial shear stress. The increasing tensile load will eventually increase the tensile strain within fibres that could fracture if the fibre tensile strain in exceeded. Under loading condition, the propagation of cracks manifested within all the 3D printed samples for both in-plane and out-of-plane 3D printing direction, eventually braking within the gauge length as shown in Figure 5.16d.

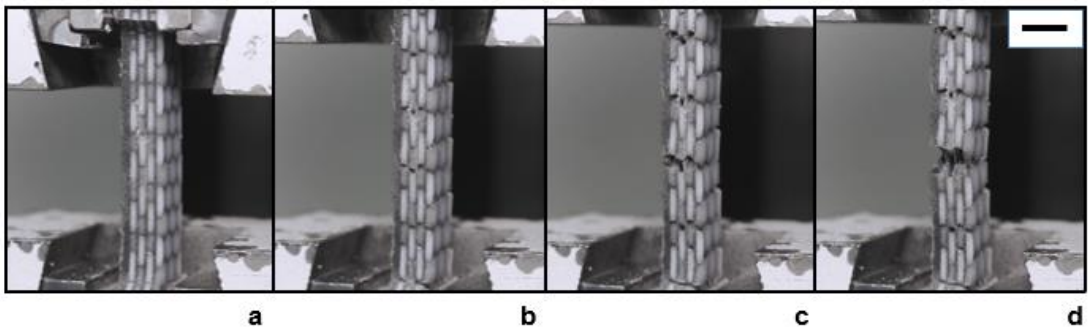

Figure 5.16. A pictures sequence showing the evolution of the cracks over the hybrid nacre structure embedded in the dog bone sample used for the tensile tests. An external load is applied to the composite (a). Cracks appear because of the matrix failure which still transmit stress to the fibre via shear stress (b). A principle of fibres pull-out begins (c), demonstrating that the shear stress transmitted to the reinforcement did not exceed the fibres tensile strain. Finally, the cracks penetrate within the structures which breaks in the gauge length for fibres pull-out (d). The reported scale bar is 7 mm long.

The image sequence reported in Figure 5.16 testifies that the black elastomeric matrix was able to transfer enough shear stress to the reinforcement without exceeding the fibre tensile strain. In other words, the fibred critical length, was not exceeded.

A visual interpretation of how cracks develop within the hybrid nacre is given in Figure 97. Here an in situ XCT study was carried out using an X-ray microscope (Xradia Versa 520. Carl Zeiss Microscopy, USA) coupled with a loading stage (CT5000 5KN, Deben UK Ltd). Figure 5.17 highlights the difference between BK

(mortar) and WT (bricks) assembly when X-ray microscopy is applied. Step-wise displacement controlled loading was performed, where a 1 mm displacement was applied and then a full tomography was acquired.

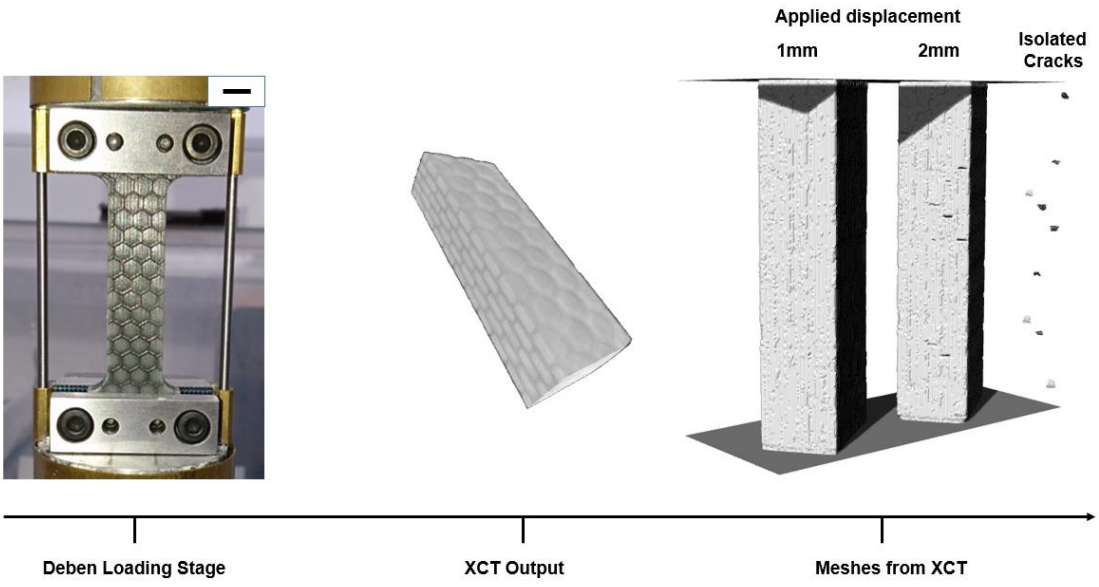

Figure 5.17. Crack development within the hybrid nacre composite when an in situ load is applied while preforming µXCT. The scale bar shown in the picture is 1cm long.

The adopted operation mode of the µXCT was of 70 kV/6 W X-ray tube energy. A 35 µm isotropic voxel size was achieved from imaging samples using a total of 1601 projections across 360° of sample rotation, with each projection exposed for 1.5 s. The 2D X-ray projections from XCT were reconstructed to a 3D volume using the Scout and Scan Reconstructor software (Zeiss) and visualized using XRM3DViewer 1.2.8 (Zeiss). Despite the visibility of the two-material assembly (Figure 5.16), fibre pull-out was not reported because the sample failed while acquiring the third applied displacement. Nevertheless, the platelets pull-out can be clearly seen in Figure 5.18. The whole in-plane 3D printed set revealed the pull-out mechanism, whereas the out-of-plane set revealed some pull-out but only for the 2 to 4mm platelets width range.

Figure 5.18. Failure and cracks opening within the nacre-like tensile sample. The picture points out the shear stress transmitted from matrix to fibre which is high enough to hold together platelets despite the enhanced pull-out. The scale bar reported is 5mm long.

Results from the tensile tests for both in-plane and out-of-plane 3D printed sets (n=8 samples per set) are shown in Figure 5.19 and 5.10 respectively. In particular, Figure 5.18 shows trends relative to the in-plane printed hybrid nacre. As observed, curves become steeper as the platelet diameter of the composites increases. This behaviour is related to the reinforcement volume fraction that rises from one sample to another according to the platelet's widths. From the 2 to 4 mm range, curves are regular and the cracks developed homogeneously within the samples. Pull-out manifested over the entire in-plane printed set, highlighted especially over the samples whose platelets width varied from 5 to 9 mm.

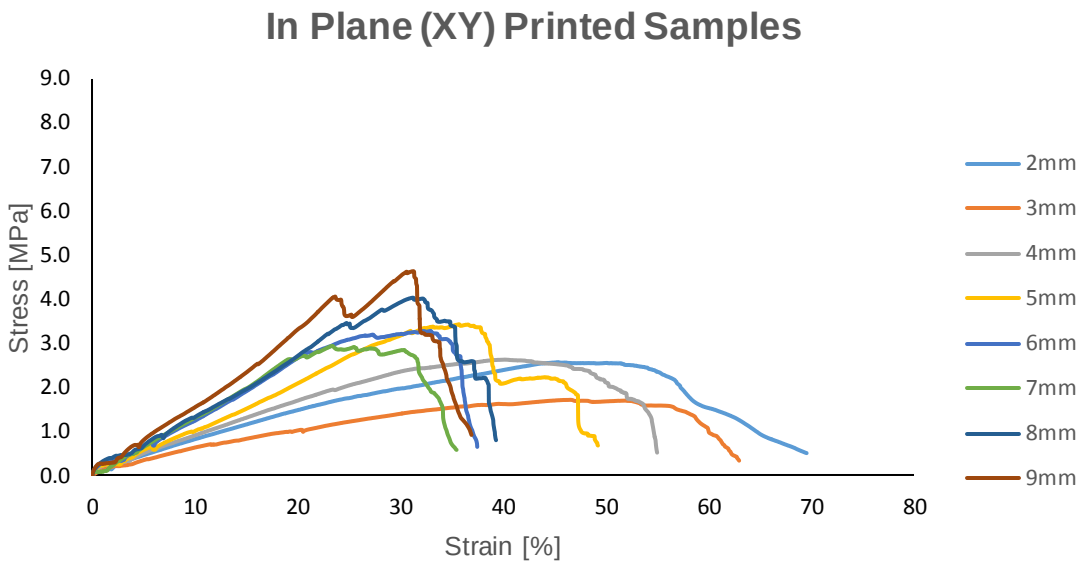

Figure 5.19. Mechanical behaviour of artificial nacre, 3D printed in an in-plane fashion. Different colours are adopted to distinguish between composites whose platelets width varied from 2 to 9 mm. Curves get steeper as the width of platelets gets larger as well as the ultimate strength. In turn the strain to failure decreases.

Here, peaks and depths manifested more within the curves as the loading cell of the testing machine could better detect the sliding of plates with a larger surface area. Overall, elastic modulus and strength of composites increased alongside with reinforcement volume fraction, contrary to the strain to fracture which decreased instead. Out-of-plane printed composites were tested and the curves are reported in Figure 5.19. These do not show any evidence of fibre pull-out, appearing linear and free from peaks and depths. Cracks propagation was delocalised over the entire set, nevertheless samples with fibre diameter smaller than 4mm presented reinforcement pull-out, hence, propagating at the interface rather than within platelets. From 4mm up to 9 mm the samples broke in a brittle fashion with cracks braking into platelets rather than being driven in-between platelets.

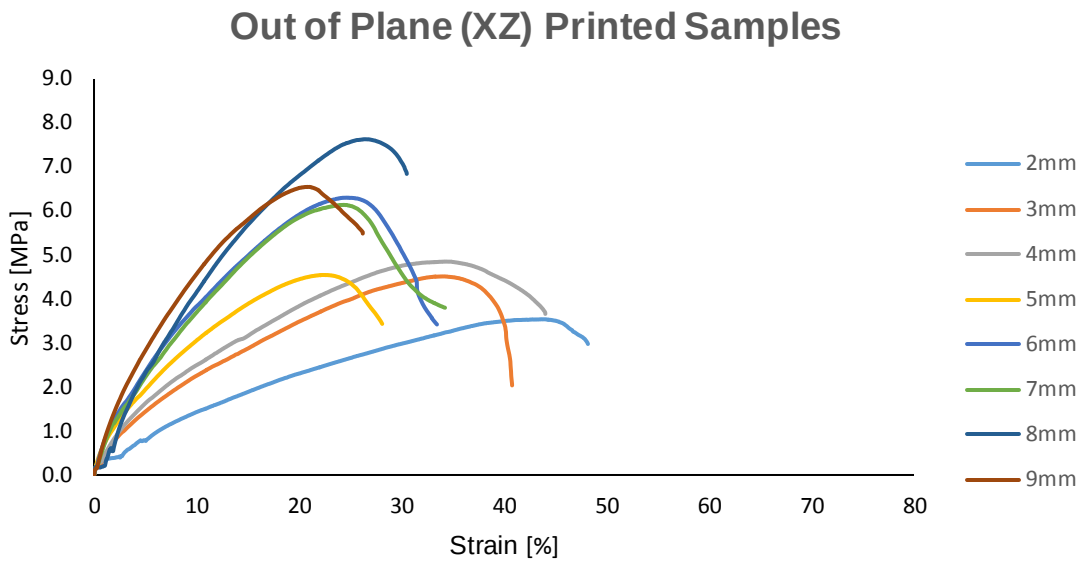

Figure 5.10. Mechanical behaviour of artificial nacre 3D printed in an out-of-plane fashion. Curves are different from the in-plane set reported in Figure 5.19, nevertheless stiffness and strength of the two 3D printing orientations increase similarly when related to the reinforcement volume fraction, whereas the work to failure decreases.

As previously seen with regards to the in-plane set, here too, elastic modulus and strength rose with the reinforcement volume fraction, contrary to the strain to failure that decreased. A comparison between in-plane and out-of-plane printed sets is presented below in order to highlight specific differences in terms of elastic modulus, strength, strain to failure and work to failure when two different 3D printing orientations are adopted.

Figure 5.11 compares the stiffness of the two set of samples, but also the stiffness among samples belonging to the same set. As predicted previously, the stiffness increases with the reinforcement volume fraction.

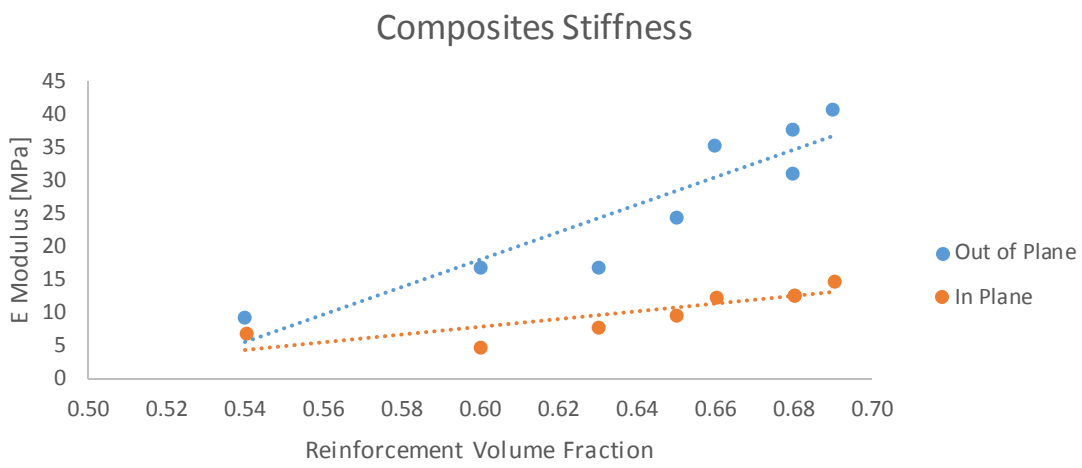

Figure 5.11. Stiffness of both In-plane and out-of-plane 3D printed composites is compared. Overall, the out-of-plane composites seems to be stiffer than the in-plane ones suggesting a stronger shear stress transfer from matrix to fibres.

Therefore, when the fibre aspect ratio is increased the stress transfer to the reinforcement also increases together with the strength and elastic modulus of the composites.

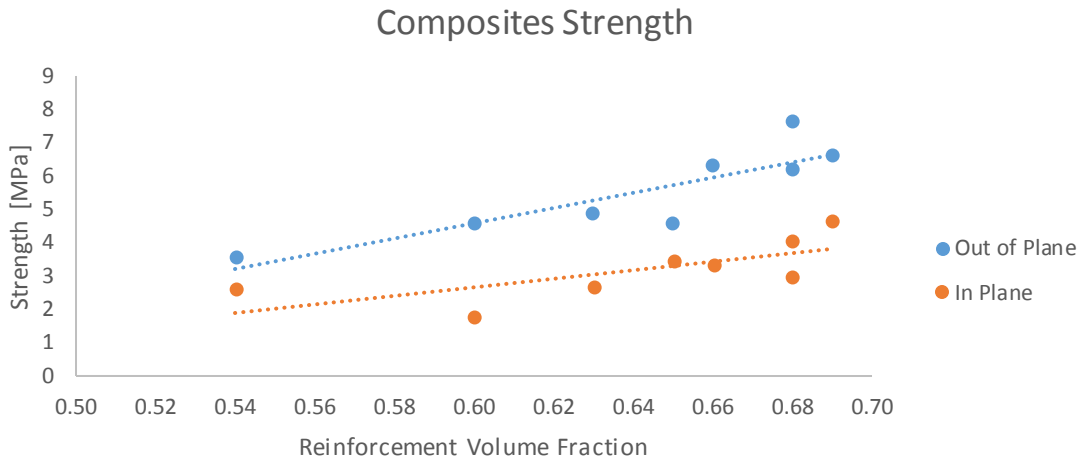

Figure 5.12. Strength dependence of the reinforcement volume fraction. Both trends are similar but out-of-plane composites show higher strength if compared to the in-plane set.

Crucially, not only appears that samples belonging to the out-of-plane set are stiffer than the in-plane set, but also that they are stronger as shown from trends in Figure 5.12.

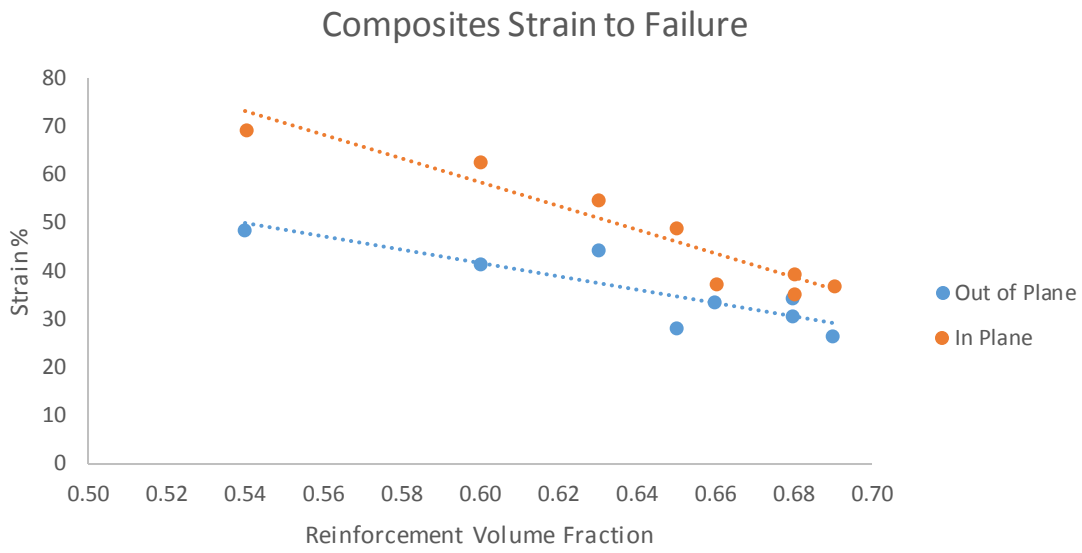

Figure 5.13. Strain dependence of the reinforcement volume fraction. Trends are coincident but, nevertheless, the in-plane 3D printed composites elongate more than the in-plane set.

Conversely, the strain to failure seemed to be larger for the in-plane printed set, reaching a peak of 70% of the gauge length with the 2 mm diameter platelets (Figure 5.13). A compelling parameter for the investigation is the work to fracture of the composites, in other words, the amount of strain energy per unit volume that the composites can absorb before fracture. A good approximation was made dividing the stress-strain curves in rectangular sections so that the area underneath stress-strain curves could be integrated.

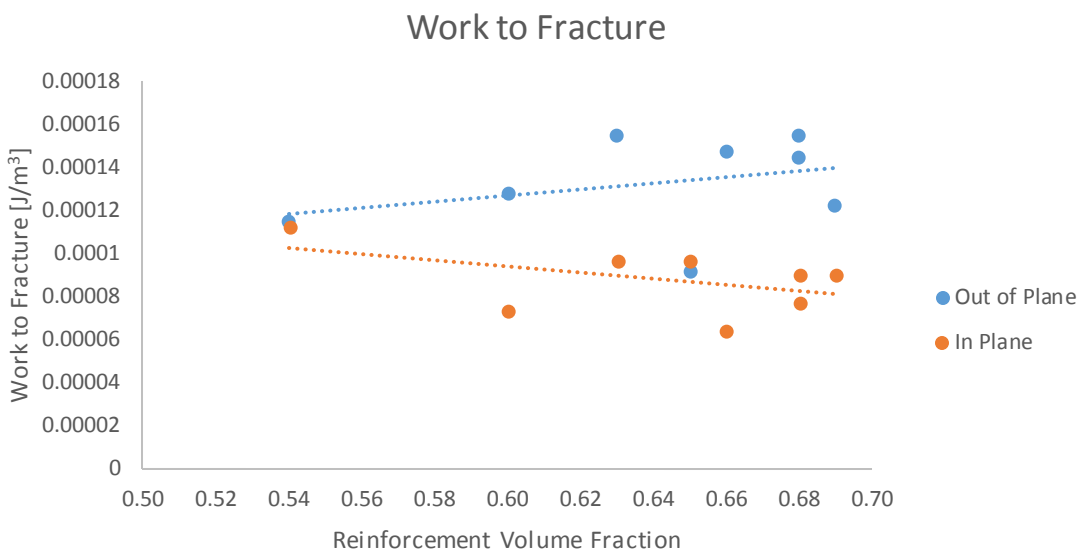

Figure 5.14. Work to fracture dependence of the reinforcement volume fraction. Here, trends are different showing a positive correlation between out-of-plane composites and volume fraction, differently from the in-plane 3D printed composites whose work to fracture decreases as the volume fraction of the reinforcement increases.

Overall, the out-of-plane composites showed better performance in terms of energy absorption, as the volume fraction of the reinforcement rose (Figure 5.14). On the other hand, although the in-plane composites work to fracture absorbed less energy, they showed a trend that is in accordance to the ideal crack path development. Thus, the smaller the platelets diameter the larger the matrix in-between platelets resulting in a longer crack propagation path. Another useful way to compare the two in-plane and out-of-plane 3D printed sets is to plot strength versus elastic modulus. Figure 5.15 shows trends at comparison stating that the out-of-plane trend is steeper than the in-plane, hence, out-of-plane 3D printed samples are able to store more elastic energy per unit volume.

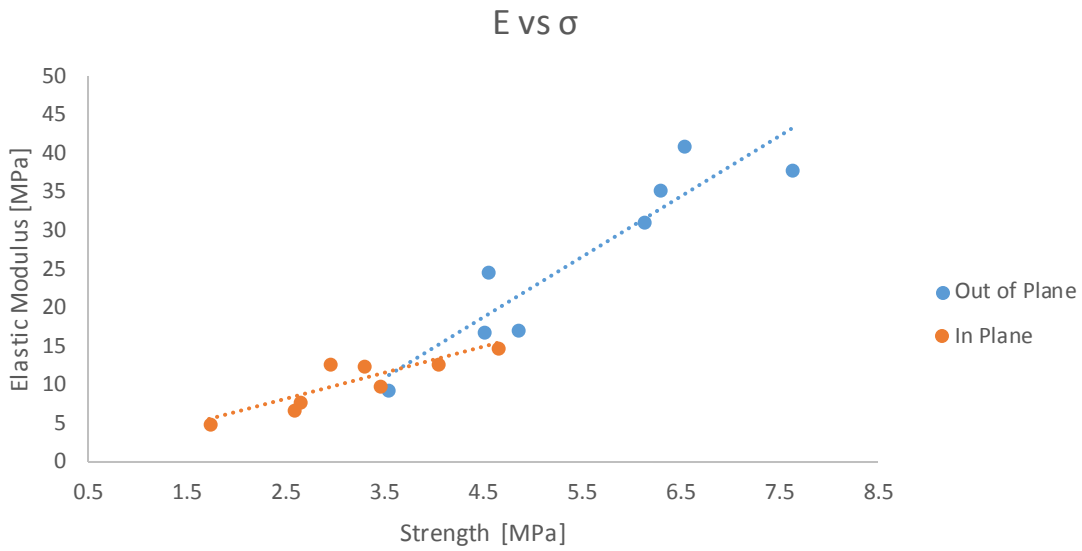

Figure 5.15. Materials property chart showing the relation between elastic modulus and strength of both out-of-plane and in-plane 3D printed composites. Materials vary widely for both parameters and mechanically important materials populate the upper right corner, where both stiffness and strength are large.

5.4 Synthetic nacre under dynamic loading

The previous section explored the mechanical properties of 3D printed nacre-like structures during relatively low, quasi-static, loading conditions. However, nacreous structures function predominantly to resist dynamic loading conditions from impact and dropped weights. Further mechanical evaluations of the 3D printed structures and their effectiveness to be tough under dynamic loading conditions are considered here. The ability of nacre in resisting impacts and tolerating defects, lies in its intrinsic and outstanding mechanical properties, due to the combination of base materials. Soft and hard phases are parametrically assembled, producing a hybrid material whose mechanical functions are superior to any of the single material phases.

The aim of this section is to test against impacts both hybrid nacre-like designs as well as base materials used to manufacture the composites. If composites overcome

the base materials in terms of energy absorption, the toughening mechanism at the base of biological nacre's toughness can be successfully mimicked by the 3D printed replica.

According to the Material Testing Standards for AM of Polymers, where the state of the art for 3D printed polymers and their applicability is widely acknowledged, ISO 179 and ASTM D6110 are mentioned as useful impact testing methods. Therefore, samples with stiff platelets (WT) embedded in an elastomeric matrix (BK) were designed and assembled in one single print starting from a boundary shape provided by the standard DIN EN ISO 179-1 [161]. Energy values for unnotched Charpy impact test were detected using a Zwick 5102 pendulum impact tester, at room temperature of 21°C. A Flatwise positioning of the 3D printed parts (Figure 5.16 b) was adopted to mimic the ideal case of a predator attacking the shell of a sea creature.

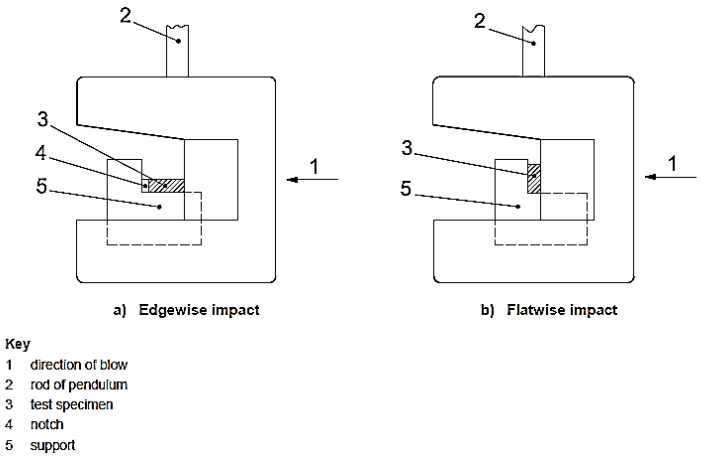

Figure 5.16. Comparison between Edgewise and Flatwise positioning of Iso 179 and ASTM D6110 sample when performing unnotched Charpy impact tests.

The specimen had building blocks of 80 mm×10 mm cross sectional area and 7 mm height placed in an edgewise direction. For each set of parameters and materials, five specimens were tested evaluating mean value and the standard deviation. In order

to investigate the influence of the reinforcement on impact strength, platelets aspect ratio was varied from 2 to 9 in accordance with Kelly's model related to the critical length of fibre. The mono-material samples of material WT were tested using a pendulum energy of 5 J differently from the samples of material BK tested with a pendulum energy of 1 J due to the varying toughness of the base materials.

Results from the unnotched impact tests carried out on both hybrid nacre 3D printed according to out-of-plane and in-plane 3D printing direction are reported in Figure 5.17.

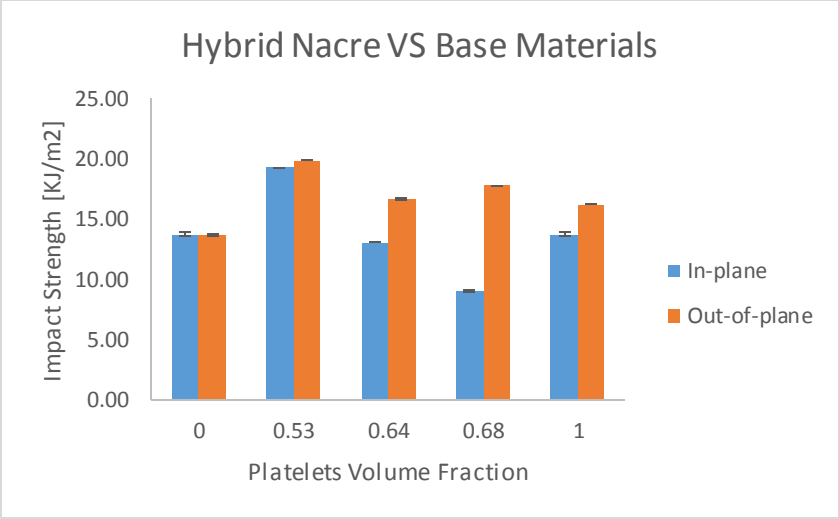

Figure 5.17. Impact strength depending on platelets volume fraction. A volume fraction of 0 and 1 is reported for the tested soft and hard material respectively. The reinforcement volume fraction can be associated to the platelets diameters, which correspond to 2 mm, 5 mm, 8 mm for volume fractions of 0.53, 0.64 and 0.68.

Mean values and standard deviation of the absorbed impact energy are shown for composites with increasing volume fraction of the reinforcement. The volume fraction of the reinforcement varied from 0.53 to 0.68 (20% range), with according platelet width of 2, 5 and 8 mm. Whereas, base materials are reported into the chart with a reinforcement volume fraction of 0 for the BK bulk material (no reinforcement) and 1

for the WT brittle material (reinforcement only). In general, the two base materials gave comparable impact results. The WT material absorbs more energy than the BK when subjected to dynamic loads. Furthermore, differences between in-plane and out-of-plane printing direction are revealed only for the WT material which absorbs more energy when samples are printed in an out-of-plane fashion. The hybrid nacre composites instead show good results when printed out-of-plane. In this case, all the volume fractions are able to exceed the impact strength of the base materials. This is not observed in the in-plane 3D printed hybrid nacre, which instead shows impact strength greater than base materials but only in the case of reinforcement volume fraction equal to 0.53 (platelets width 2 mm).

Overall, results are in accordance with tensile test results seen in section 5.4. The out-of-plane manufacturing seems to be stiffer, stronger and tougher when compared to the in-plane manufacturing fashion. Under dynamic load condition out-of-plane hybrid nacre absorbs more energy, overcoming the impact resistance of base materials. This can be explained by the impact results revealed from the WT base material which is 15% tougher when printed out-of-plane rather than in-plane. The consequential material mixing results in a stronger interface when hard and soft material are 3D printed, able to transmit more shear stress from matrix to fibres. This confirms why out-of-plane hybrid nacre showed a brittle failure when subjected to axial loads (section 5.4), restricting the cracks propagation to 4mm.

5.5 Discussion

The problem of stress transfer from matrix to fibre, generally referred to as interfacial shear strength, has received significant attention over the years. The model considered for the purpose of this study, refers to a single fibre embedded in a matrix under stress known as fragmentation test. In order to rationalize the design of reinforcement of the 3D printed nacre, a case of stiff fibre interacting with a matrix being in a plastic state was considered. Specifically, Kelly and Tyson [104] related the interfacial shear strength to a critical fibre length l_c using a force balance equation built around the single fibre.

The shear strength at the interface τ is constant and equal to the shear strength of the matrix, obtained as follow:

$$\tau_{av} = \frac{\sigma_f \, d}{2 \, l_c} \qquad \textit{Equation (5.1)}$$

The parameter d represents the fibre diameter, σ_f is the fibre strength when the fibre has a critical length l_c.

Results from lap joint shear tests (conducted in section 3.2.2 to investigate about the interaction between BK and WT base materials) suggested an average interfacial shear strength for the BK material of 1.5 [MPa]. The interaction scenario between BK and WT evaluated through the use of a mechanical shear test, was defined by an interfacial overlapping distance of 5 mm and a thickness of the compliant material of 300 μm. The result of the mechanical tensile testing on WT material supplied a σ_f value of 24.4 [MPa], whereas the considered thickness of the fibre was 1 mm according to

the optical investigation reported in Chapter 3. Rearranging, the above *Equation 5.1* gives:

$$l_c = \frac{\sigma_f \, d}{2 \, \tau_{av}} \qquad (Equation\ 5.2)$$

Replacing parameters with numbers:

$$l_c = \frac{24.4[MPa] \cdot 1[mm]}{2 \cdot 1.5\,[MPa]} = 8.1\ [\text{mm}]$$

According to the found result, the fibre aspect ratio was varied from 2 to 9, whereas the matrix interface was held constant at a thickness of 300 μm. This resulted in a reinforcement volume fraction of the biomimetic composites ranging from 53% to 65%.

Overall, the tensile tests demonstrated a correct fibres aspect ratio dimensioning especially for the case of the in-plane 3D printed set of composites for which the reinforcement pull-out took place over the entire set (Figure 5.18).

The ideal case would have seen platelets fracture for aspect ratio equal or greater than 8. This condition was verified only by the in-plane 3D printed samples (Figure 5.18b). Indeed, the applied tensile load and shear stress transmitted from matrix to fibres exceeded fibres tensile strain when the aspect ratio was greater than 8. Nevertheless, an aspect ratio pull-out threshold was presented by the out-of-plane 3D

printed set for which fibres with aspect ratio larger than 4 broke, rather than pulling-out from the matrix.

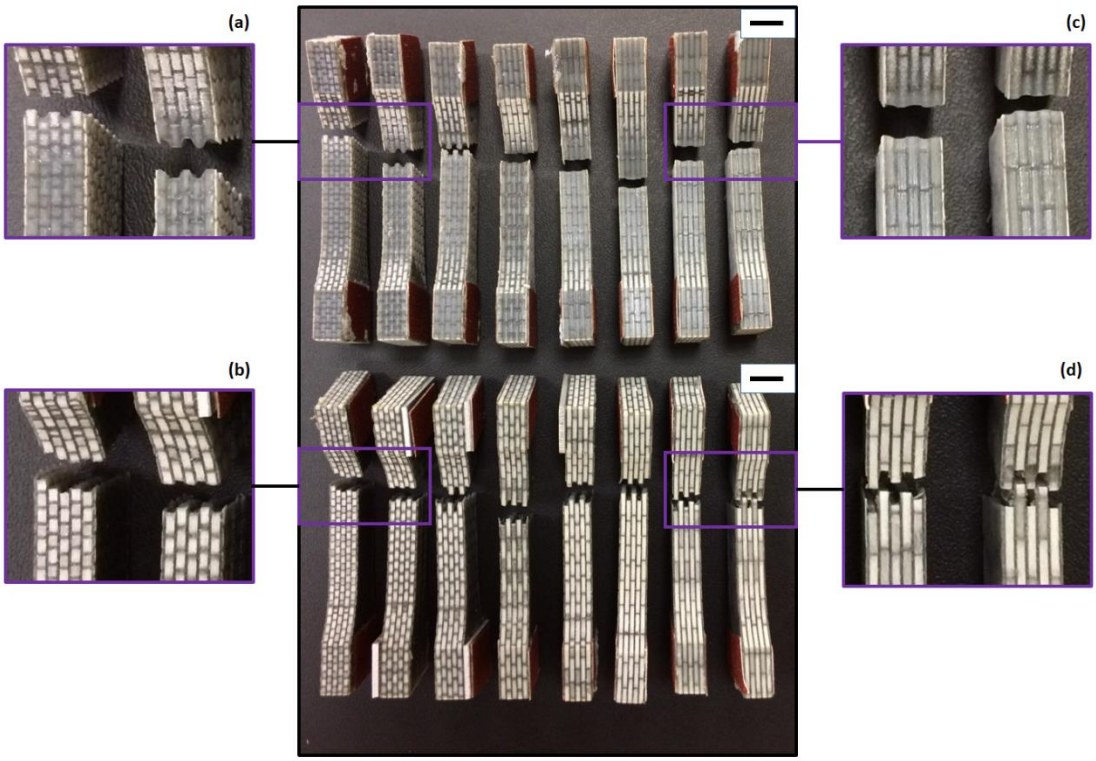

Figure 5.18. Reinforcement pull-out of both out-of-plane (up) and in-plane (down) 3D printed sets. Fibre pull-out was reported by the out-of-plane set only for composites whose fibre aspect ratio was 2,3 and 4 respectively (a) whereas, remaining samples broke in a brittle fashion as highlighted in (c). Fibre pull-out was reported over the entire in-plane set and for representative purposes reported in (b). Fibres fragmentation appeared for the in-plane samples whose fibre aspect ratio was of 8 and 9 respectively (d), confirming the prediction of Kelly's model. The scale bar on the top right is 10 mm long.

The prediction of the mechanical properties of 3D printed composites has been the main objective of material science researchers. Various models have been proposed to evaluate elastic properties of classic composites materials. Therefore, the attention is focused here on the prediction of the modulus of elasticity that is considered one of the most significant mechanical properties of materials for engineering structural design.

The elastic properties of composites materials are affected in general by a number of parameters such as, fibres geometry, orientation, volume fraction and the strength of the interfacial binding between matrix and fibres. Some of them such as Shear lag and Halpin-Tsai are fully described in section 2.7.1. Specifically, the mentioned models apply for short fibre composites, predicting longitudinal or transverse modulus of the composites in relation to the elastic moduli of matrix, reinforcement fibre as well as fibre aspect ratio and matrix Poisson ratio. Furthermore, tensile modulus (E_c) of composites has been predicted by using the Cox-Krenchel [110] model which is a modified rule of mixture. In particular, Krenchel [162] [163] introduced a fibre orientation factor and an efficiency factor related to the stress transfer from matrix to fibre. Another model proposed by Gao [11] [164] relates the stiffness of a composite to the shear modulus of the matrix.

Experimental results together with the mentioned analytical models are reported in Figure 5.19. Among the different micromechanic approaches, Gao and the Shear-lag models yield results that correlate well with the available experimental data of the in-plane 3D printed samples. In general, Krenchel and Halpin-Tsai correlate well too, nevertheless, overestimating the composites elastic modulus, contrary to Gao and the Shear Lag models, which underestimate the experimental results for different values of the reinforcement volume fraction.

With regards to the out-of-plane 3D printed composites, none of the models seemed to correlate well with the experimental data, as the in-plane experimental results did. Although for reinforcement volume fraction lower than 0.65, models show a good agreement with the out-of-plane 3D printed nacreous composite.

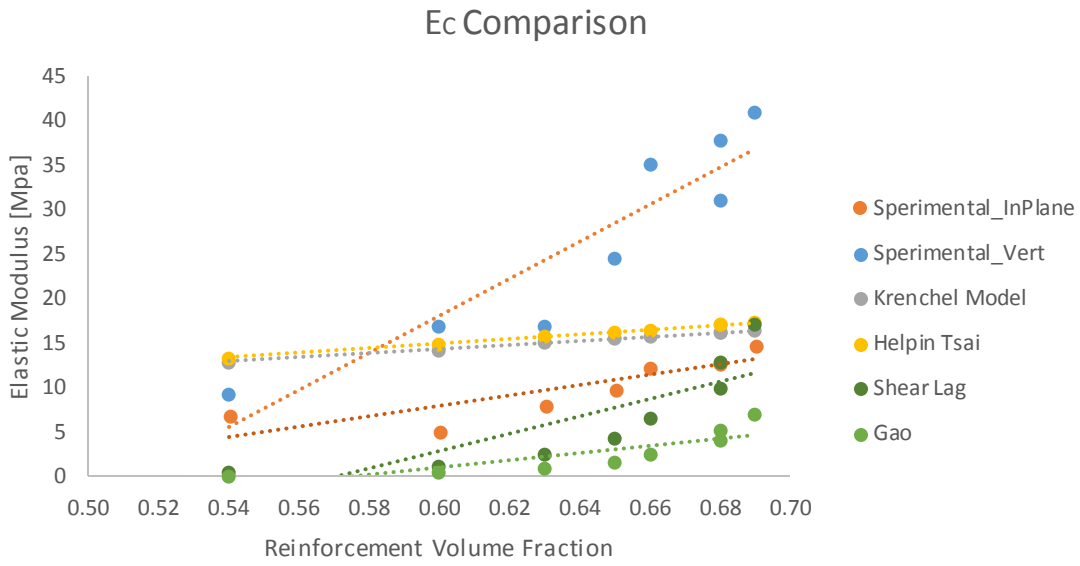

Figure 5.19. Predicted analytical and experimental results.

Optical microscopy was useful to understand how materials are deposited by the 3D printer while manufacturing, hence the quality of printing. To quantitatively analyse the printing quality of the hybrid nacre a high precision Leica Microsystem (Switzerland) was used. Optical images were taken with 25X magnification lens and the resulting platelets width and distances among platelets were investigated and verified using a 0.01 millimitre division over three different points of the 3D printed samples as shown in Figure 5.20.

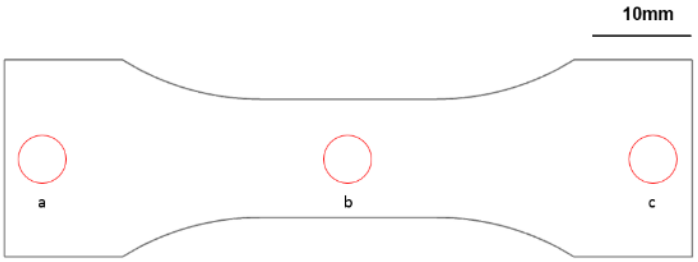

Figure 5.20. Investigated points over the 3D printed hybrid nacre sample.

For representative purpose optical images detected on samples which plates where 2 and 8 mm wide, are shown in Figure 5.21.

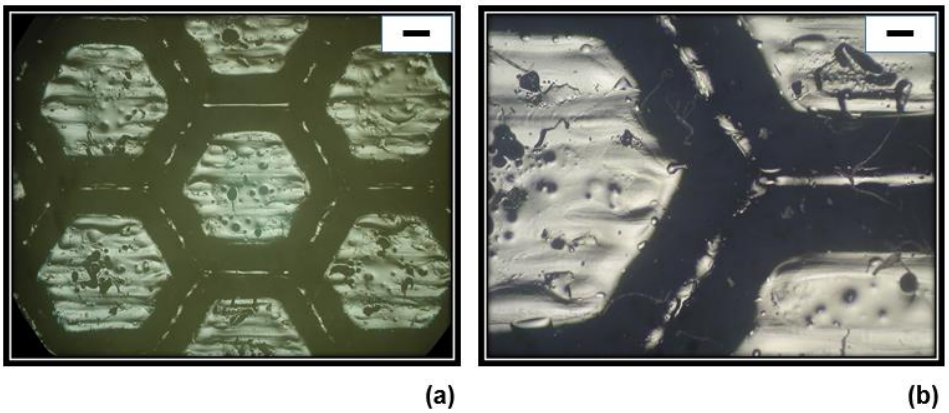

Figure 5.21. Optical images detected on 2mm (a) and 8mm (b) 3D printed Platelets. The reported scalebar is 1mm long.

In both cases in the above figure the platelets appear geometrically imperfect, presenting holes and imperfections that possibly could lead to premature failure when samples were subjected to tensile stress. Surprisingly, features similar to edges are presented between the hexagonal plates not belonging to the original CAD design. The latter feature can be possibly related to a reflection due to the light microscopy.

A quantitative analysis was carried out on each sample, detecting platelets diameters to be compared with the original design. Results are shown in Figure 5.22 where mean values and standard deviation are plotted in a bar chart. Overall, platelets' widths are in agreement with the dimension of the geometrical design they belong to (Figure 5.21), despite the build mode, hence the precision of the 3D printer being set at 13μm layer thickness. This allowed for it to build at the very highest resolution and

surface quality. Nevertheless, the printing quality highlighted in Figure 5.21 and proved to be lacking.

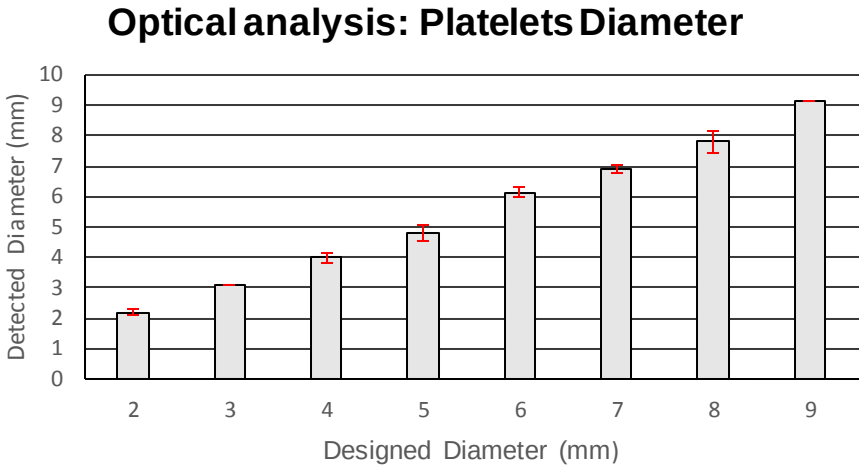

Figure 5.22. Designed diameters are plotted against the detected ones showing the deviation from the manufacturing and design specifications.

Quantitative analysis over the matrix in between platelets was conducted alongside the platelets widths measurements (Figure 5.22). The matrix thickness set while drawing in CAD was set to 300 μm. Results are depicted in the bar chart below (Figure 5.23).

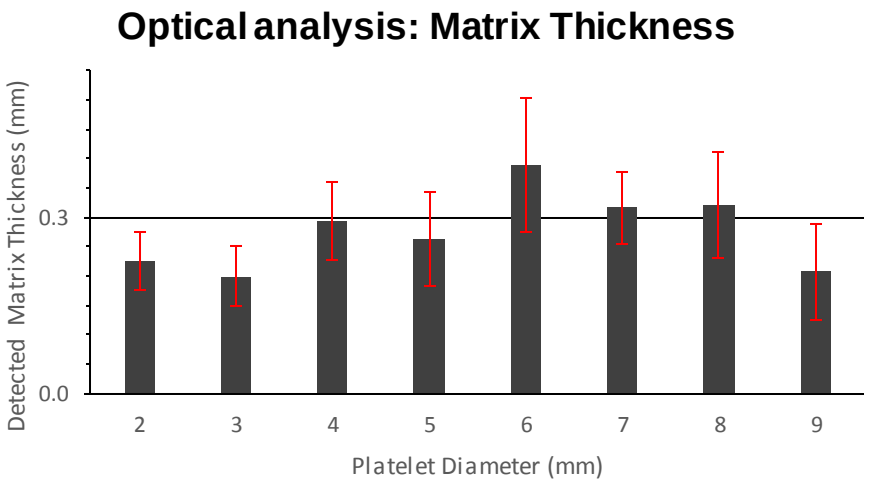

Figure 5.23. Designed matrix thickness are plotted against the detected ones showing the deviation from the manufacturing and design specifications.

5.6 Nano indentation (reduced modulus and hardness)

Nanoindentation was used in this study not only to elucidate the properties of the individual components of the proposed biomimetic nacre but even to give insights on how the hardness varies in-between the elastomeric matrix to the stiff platelets, passing through the interface in-between the two materials.

All the experiments were performed using a Nanoindenter (NanoTest 600, Micro Materials Ltd) equipped with a Berkovich indenter, at controlled environmental conditions with indentations parallel and perpendicular to the section surface (Figure 5.24-5.25). A single column containing 30 indentations points was adopted for the 3mm platelets diameter specimen instead of a single column of 100 indentation points as chosen for the specimen containing 8 mm diameter platelets. In both cases a Z offset of 100 µm was adopted in order to avoid a mutual influence of consecutive responses. The loading rate was 3 mN/s and a pre-load of 0.03 mN.

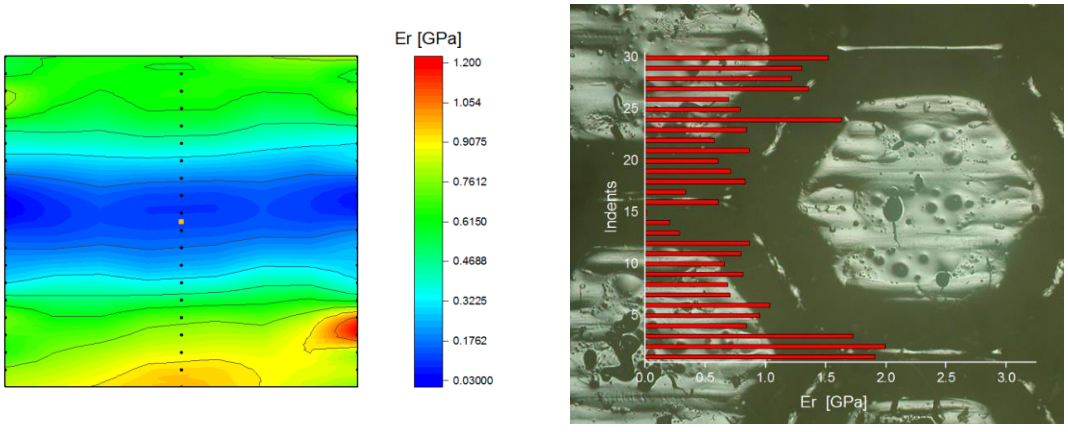

Figure 5.24. Result from nano indentation test are presented here. The reported specimen contains platelets whose diameter is 2mm wide. The reduced modulus resulting from the nano indentation test is prsented by both the colourmap and the red histogram super imposed to the optical picture.

Colour mapping is used for both investigations to highlight the reduced modulus of the composites. Results suggest that there is a gradual variation in hardness passing from the core of a platelet to another.

Furthermore, the gradual variation is followed through the interface which present values in accordance with the optical images where white is the stiffer material and black the softer one.

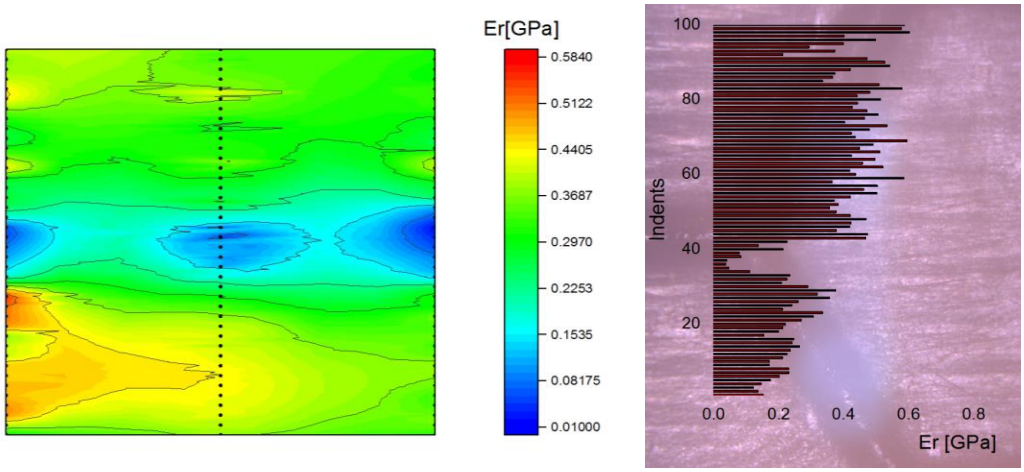

Figure 5.25. Result from nano indentation test are presented here. The reported specimen contains platelets whose diameter is 8mm wide. The reduced modulus resulting from the nano indentation test is prsented by both the colourmap and the red histogram super imposed to the optical picture.

Chapter 6. Summary and Future Developments

6.1 Conclusions

Understanding and reproducing design concepts found within biological structures presents significant opportunities in developing novel lightweight and mechanically high performing materials. Fidelity in translating mechanical function from biology to engineering is the crucial requirement for a bioinspired approach to be successful. In this work, bioduplication and biomimicry approaches brought to novel hybrid MM3DP composites inspired by bone and nacre. Nevertheless, the developed approaches are also sufficiently flexible to be applied to other biological composites. Reproducing mechanical performances in the engineered composites similar to the biological counterparts was successfully achieved and controlled through bottom up approaches that are currently unobtainable with conventional manufacturing. This work provided improvements in the much wider field of bioinspiration which is missing fluent workflows to mimic specific natural structures. The proposed procedural guidelines referred to two main branches of bioinspiration. The former, referred to as bioduplication, was limited to the detections of the XCT scanned models where the user was merely able to scale the model extracted from XCT scanning data. The second approach, namely biomimicry, was supported by CAD parametric design and GD algorithms that demonstrated to be very flexible and dynamic thanks to the establishment of conceptual association between geometries and mathematics. From this point of view, iterative parametric relationships between shape and dimensions improved the tedious process of drawing afresh features whenever changes in the design are needed.

Mechanical properties of MJP base materials as well as the interaction between such multiple materials in a composites design were investigated.

- From experimental results it has been found that elastic properties of 3D printed materials are sensibly lower than suggested by the equipment/material manufacturer. Non-elastic properties of 3D printing materials showed comparable mechanical properties to reported manufacturer values. Notably, in the case of the WT material, which represent the stiffer phase in the developed biomimetic composites, the measured modulus of elasticity reached a maximum value of 267-364 MPa (for transverse and longitudinal direction of printing respectively), against 1-1.2 GPa stated by the manufacturer.
- Tensile strength of the WT material varied between 24-27 MPa against a reported manufacturer range of 37-47 MPa. The experimentally measured elongation at break was quite similar and to the one reported by the datasheet and varying around 7-16 %. A correlation between mechanical properties of the 3D printed materials and the direction of 3D printing was reported. The mechanical properties mismatch could be attributed to the fact that the employed MJP is a beta version model still under development in terms of software, hardware settings and available materials. Therefore a trade-off between experimental results and the ideal values proposed by the manufacturer is admissible.
- Lap joint shear tests were conducted to characterise and satisfy the understanding of the mechanics at the interface of WT and BK materials. Encouraging results were found with regards to the matrix and fibres forces exchange. Dependency of the materials assemblies in relation to parameters

such as interface length and thickness was outlined in the results. Especially in the case of variable interface thickness, a rapid drop in shear strength was reviled by increasing the thickness of the soft material at the interface. This observation suggested that the mechanical interplay of the two phases can be appreciated at length scales that are 10 times greater than the set 3D printing resolution (13μm).

Imaging techniques were employed to evaluate the 3D printed geometries, specifically using optical microscopy and XCT as metrology tool in combination to optical microscopy.

- Optical microscopy showed results concerning geometrical shapes and features below the millimetre length scale.
- XCT provided volumetric insights on the manufactured assemblies above the millimetre scale, despite the similar density of the materials. This investigation was relevant in defining design boundary condition below which features are partially reproduced in respect to the original digital drawings, affecting the way in which the phases mechanically interplay.

Manufacturing 3D printed compact bone from digital design correlated to XCT was successfully achieved with a bioduplication workflow meant to transfer design from XCT to MJP.

- Variation in design was adopted considering XCT scans of less and more remodelled bone samples.
- The bioduplication approach enabled the 3D printing of composite structures from 3D image datasets. This demonstrated the versatility of bioduplication to

be applied to various biological structures as long as sufficient imaging contrast to discern morphological features and composition is presented.

- Elastic modulus of the 3D printed output allowed the selection of composite structures with a tuneable elastic modulus, demonstrating for a variability in terms of mechanical properties when combining different materials according to same 3D pathways.
- Structural differences in the 3D printed compact bone provided elastic modulus variations that were also found in the native bone samples but absolute values between the 3D printed bone and relative native bone were observed due to the lack of appropriate materials, which are currently limited in commercial 3D printing multi-material systems.
- A workflow embracing parametric design and GD allowed for a successful replica of the multi-layered osteons texture typical of the compact bone. The unit cells of compact bone (primary and secondary osteons) as well as the interstitial bone in multi-layered structures were successfully fabricated with the only limit related to the dimension of the smallest feature that the multi-material 3D printer is able to reproduce. Moreover, the geometrical shapes resulted to be adaptable to an arbitrary bulky shape to be characterised with the parametric bone texture.

A physical 3D printed nacre design was successfully manufactured adopting a biomimicry workflow.

- The high controllability of parametric modelling and GD over the hybrid nacreous design was further confirmed, giving the user the freedom to fabricate

objects that can be parameterised and customised in function to the final application.

- Kelly-Tyson composite model was used to derive the interfacial shear strength between reinforcement platelets and matrix, in relation to the mechanical properties of the employed materials. A critical fibre length l_c equal to 8 mm (fibre aspect ratio 8) was identified as dimensional parameter below which, using WT material for the reinforcement and BK for the matrix, interfacial failure between matrix and reinforcement is promoted as it happens in the real nacre to enhance energy dissipation and avoid brittle fracture of the overall material.
- In-plane and out-of-plane 3D printed nacre–like structures were fabricated and further tested under static and dynamic loading. The identified critical fibre length applied only for the in-plane set which presented pull-out within samples which fibre aspect ratio was lower than the one predicted by Kelly-Tyson.
- An enhanced stress transfer from matrix to fibres was reported in the out-of-plane 3D printed set, where the fracture of the reinforcement plates occurred within samples with an l_c equal to 4 mm. Hence, weaker interfaces that promoted toughening and enhanced biomimetic behaviour was exhibited using the in-plane 3D printing. In general, Nacre samples manufactured in-plane, exhibited less mechanical interplay in comparison to those produced out-of-plane. This could be attributed to a stronger materials bounding when composites are printed out-of-plane given the presence of both WT and BK materials in every single layer.
- Conclusion can be made regarding the hybrid nacre concerning the ability to absorb more energy than the base materials when subjected to dynamic loads.

Especially for the case out-of-plane 3D printed composites, all the volume fractions were able to exceed the impact strength of the base materials. This was not observed in the case of the in-plane 3D printed composites, for which a superior impact strength was shown only in the case of composite with a platelets width of 2 mm.

6.2 Recommendation

In the introduction of the thesis the ambition of investigating and identifying viable paths and relative workflows able to mimic biologically structures was expressed.

- Digital workflows able to duplicate and mimic biological occurring composites such as cortical bone and nacre were successfully established. This designs are meant to be applied to a number of areas such as healthcare, automotive, aerospace and defence where material scientists together with engineers from different backgrounds will benefit from fast, reliable and fluent solutions to better control and combine soft stiff materials in complex bioinspired arrangement to reach superior fracture mechanical properties.

Future works can be undertaken following two main paths: the digital side and the physical side of the project.

- Critically, the digital side could be further developed increasing the level of complexity of parametric designs for both nacre and cortical bone. Particularly, the generative design proposed for nacre could incorporate features retained responsible of the enhanced toughness of the biological composite such as:

dovetail-like features at the periphery of tablets, interlocking of nano-asperities, inter-lamellar mineral bridges.

- Detailed nanoindentation tests are needed to fully characterise the mechanical properties of single 3D printing materials as well as when mixing at the interface.
- The GD design of compact bone could be improved adding additional features such as Volkmann's canals, anatomical arrangements found in cortical bone that interconnect the Haversian canals, increasing the overall blood supply or permeability of the hybrid compact bone.
- A further step to be considered in this research is to couple both compact and trabecular parametric designs progressing from tissue to organ level to potentially replace entire bone segments or shaft in the case of long bones.

MJP has shown mechanical and spatial durability challenges, suggesting that dedicated standards are needed for both mechanical testing and metrology investigation. For example, classical ASTM and ISO standards, such in the case of tensile testing, are employed without considering that 3D printed parts are assembled layer by layer. Therefore, the final manufactured part, in most cases, results to be layered structure rather than monolithic. This point out the need of imaging techniques such as XCT to be significantly employed to quantify the amount of flaws per layer. In conclusion, there is a need to provide imaging standards to officially introduce XCT as a validation tool for 3D printed volumetric investigations. The importance of this latter point represents the ultimate link between correlating digital design to physical output from the manufacturing process.

References

[1] J. W. C. Dunlop and P. Fratzl, "Biological Composites," *Annu. Rev. Mater. Res.*, vol. 40, no. 1, pp. 1–24, 2010.

[2] P. Fratzl, J. W. C. Dunlop, R. Weinkamer, and R. S. of C. (Great Britain), *Materials Design Inspired by Nature: Function Through Inner Architecture*. Royal Society of Chemistry, 2013.

[3] S. A. Wainwright, *Mechanical Design in Organisms*. Princeton University Press, 1982.

[4] J. Rho, T. Y. Tsui, and G. M. Pharr, "Elastic properties of human cortical and trabecular lamellar bone measured by nanoindentation," vol. 18, no. 20, pp. 1325–1330, 1997.

[5] J. Rho, "Mechanical properties and the hierarchical structure of bone," vol. 20, pp. 92–102, 1998.

[6] L. Wang, J. Song, C. Ortiz, and M. C. Boyce, "Anisotropic design of a multilayered biological exoskeleton," *J. Mater. Res.*, vol. 24, no. 12, pp. 3477–3494, 2009.

[7] A. Barani, A. J. Keown, M. B. Bush, J. J. W. Lee, H. Chai, and B. R. Lawn, "Mechanics of longitudinal cracks in tooth enamel," *Acta Biomater.*, vol. 7, no. 5, pp. 2285–2292, 2011.

[8] J. Enax, A. M. Janus, D. Raabe, M. Epple, and H. Fabritius, "Acta Biomaterialia Ultrastructural organization and micromechanical properties of shark tooth enameloid q," *Acta Biomater.*, vol. 10, no. 9, pp. 3959–3968, 2014.

[9] M. F. Ashby, *Materials Selection in Mechanical Design*. Elsevier Science, 2004.

[10] R. O. Ritchie, "The conflicts between strength and toughness," *Nat. Mater.*, vol. 10, no. 11, pp. 817–822, 2011.

[11] H. Gao, B. Ji, I. L. Jager, E. Arzt, and P. Fratzl, "Materials become insensitive to flaws at nanoscale: Lessons from nature," *Proc. Natl. Acad. Sci.*, vol. 100, no. 10, pp. 5597–5600, 2003.

[12] F. Barthelat, "Architectured materials in engineering and biology: fabrication, structure, mechanics and performance," *Int. Mater. Rev.*, vol. 60, no. 8, pp. 413–430, 2015.

[13] P. Fratzl, J. Dunlop, and R. Weinkamer, "Materials Design Inspired by Nature." 2013.

[14] B. Fronzaglia, "The History of Rope," *Class. Yatch Sympoium 2006*, pp. 1–7, 2006.

[15] M. A. Meyers, P. Chen, A. Yu-, M. Lin, and Y. Seki, "Biological materials: Structure and mechanical properties," *Prog. Mater. Sci.*, vol. 53, pp. 1–206, 2008.

[16] "Biomechanics." .

[17] M. A. and C. P.-Y. Meyers, "Biological Materials Science," *Biological*. .

[18] J. H. C. Wang, "Mechanobiology of tendon," *J. Biomech.*, vol. 39, no. 9, pp. 1563–1582, 2006.

[19] M. R. Doschak and R. F. Zernicke, "Structure, function and adaptation of bone-tendon and bone-ligament complexes," *J. Musculoskelet. Neuronal Interact.*, vol. 5, no. 1, pp. 35–40, 2005.

[20] K. L. Goh, A. Listrat, and D. Béchet, "Hierarchical mechanics of connective tissues: Integrating insights from nano to macroscopic studies," *J. Biomed. Nanotechnol.*, vol. 10, no. 10, pp. 2464–2507, 2014.

[21] N. A. Peppas, *Handbook of Biomaterial Properties*, vol. 65, no. 3. 2000.

[22] F. Barthelat, "Biomimetics for next generation materials," *Philos. Trans. R. Soc. A Math. Phys. Eng. Sci.*, vol. 365, no. 1861, pp. 2907–2919, 2007.

[23] A. P. Jackson, J. F. V. Vincent, and R. M. Turner, "Comparison of nacre with

other ceramic composites," *J. Mater. Sci.*, vol. 25, no. 7, pp. 3173–3178, 1990.

[24] P. Fratzl, J. W. C. Dunlop, and R. Weinkamer, *Materials Design Inspired by Nature: Function Through Inner Architecture*, vol. 1, no. 4. Royal Society of Chemistry, 2013.

[25] F. Barthelat, "Designing nacre-like materials for simultaneous stiffness, strength and toughness: Optimum materials, composition, microstructure and size," *J. Mech. Phys. Solids*, vol. 73, pp. 22–37, 2014.

[26] C. Press and C. Press, "Bones : Structure and Mechanics . Second Edition . By John D Currey Bones : Structure and Mechanics by John D Currey Review by : Reviewed by Lance Lanyon The Quarterly Review of Biology , Vol . 78 , No . 2 (June 2003), pp . 243-244 Published by : The Un," vol. 78, no. 2, pp. 243–244, 2014.

[27] M. A. Meyers and P. Y. Chen, *Biological materials science: Biological materials, bioinspired materials, and biomaterials*. Cambridge University Press, 2014.

[28] C. M. Lewandowski, N. Co-investigator, and C. M. Lewandowski, "Physics of the Human Body," *The effects of brief mindfulness intervention on acute pain experience: An examination of individual difference*, vol. 1. pp. 1689–1699, 2015.

[29] U. G. K. Wegst and M. F. Ashby, "The mechanical efficiency of natural materials," *Philos. Mag.*, vol. 84, no. 21, pp. 2167–2181, 2004.

[30] U. G. K. Wegst and M. F. Ashby, "The mechanical efficiency of natural materials," vol. 6435, no. May, 2016.

[31] J. Rho, L. Kuhn-Spearing, and P. Zioupos, "Mechanical properties and the hierarchical structure of bone," *Med. Eng. Phys.*, vol. 20, no. 2, pp. 92–102, 2016.

[32] J. Y. Rho, T. Y. Tsui, and G. M. Pharr, "Elastic properties of osteon and trabecular bone measured by nanoindentation," *J. Biomech.*, vol. 31, no. 20, p. 21, 1998.

[33] N. Reznikov, R. Shahar, and S. Weiner, "Acta Biomaterialia Bone hierarchical structure in three dimensions q," *Acta Biomater.*, vol. 10, no. 9, pp. 3815–3826, 2014.

[34] A. H. Barber, D. Lu, and N. M. Pugno, "Extreme strength observed in limpet teeth," *J. R. Soc. Interface*, vol. 12, no. 105, pp. 0–5, 2015.

[35] S. Wainwright, W. Biggs, J. Currey, and J. Gosline, "Mechanical Design in Organisms." pp. 81–337, 1982.

[36] "Leonardo_s_Machines." .

[37] J. F. V. Vincent, O. A. Bogatyreva, N. R. Bogatyrev, A. Bowyer, and A. K. Pahl, "Biomimetics: Its practice and theory," *Journal of the Royal Society Interface*, vol. 3, no. 9. pp. 471–482, 2006.

[38] S. Kamat, X. Su, R. Ballarini, and A. H. Heuer, "Structural basis for the fracture toughness of the shell of the conch Strombus gigas," *Nature*, vol. 405, no. 6790, pp. 1036–1040, 2000.

[39] P. Fratzl and R. Weinkamer, "Nature's hierarchical materials," *Prog. Mater. Sci.*, vol. 52, no. 8, pp. 1263–1334, 2007.

[40] M. Fantini, M. Curto, and F. De Crescenzio, "A method to design biomimetic scaffolds for bone tissue engineering based on Voronoi lattices," *Virtual Phys. Prototyp.*, vol. 11, no. 2, pp. 77–90, 2016.

[41] M. Fantini, M. Curto, and F. De Crescenzio, "TPMS for interactive modelling of trabecular scaffolds for bone tissue engineering," *Lect. Notes Mech. Eng.*, pp. 425–435, 2017.

[42] R. Parwani *et al.*, "Morphological and Mechanical Biomimetic Bone Structures," *ACS Biomater. Sci. Eng.*, vol. 3, no. 11, pp. 2761–2767, 2017.

[43] H. D. Espinosa, J. E. Rim, F. Barthelat, and M. J. Buehler, "Merger of structure and material in nacre and bone - Perspectives on de novo biomimetic materials," *Progress in Materials Science*, vol. 54, no. 8. Elsevier Ltd, pp. 1059–1100, 2009.

[44] G. M. Luz and J. F. Mano, "Biomimetic design of materials and biomaterials

inspired by the structure of nacre," *Philosophical Transactions of the Royal Society A: Mathematical, Physical and Engineering Sciences*, vol. 367, no. 1893. pp. 1587–1605, 2009.

[45] G. X. Gu, I. Su, S. Sharma, J. L. Voros, Z. Qin, and M. J. Buehler, "Three-Dimensional-Printing of Bio-Inspired Composites," *J. Biomech. Eng.*, vol. 138, no. 2, p. 021006, 2016.

[46] A. M. Forster, "Materials Testing Standards for Additive Manufacturing of Polymer Materials: State of the Art and Standards Applicability," 2015.

[47] F. Barthelat, "Nacre from mollusk shells: A model for high-performance structural materials," *Bioinspiration and Biomimetics*, vol. 5, no. 3, pp. 1–8, 2010.

[48] L. J. Bonderer, A. R. Studart, and L. J. Gauckler, "Bioinspired design and assembly of platelet reinforced polymer films," *Science (80-.).*, vol. 319, no. 5866, pp. 1069–1073, 2008.

[49] M. E. Launey *et al.*, "Designing highly toughened hybrid composites through nature-inspired hierarchical complexity," *Acta Mater.*, vol. 57, no. 10, pp. 2919–2932, 2009.

[50] S. Weiner, "An Overview of Biomineralization Processes and the Problem of the Vital Effect," *Rev. Mineral. Geochemistry*, vol. 54, no. 1, pp. 1–29, 2003.

[51] D. Lu and A. H. Barber, "Optimized nanoscale composite behaviour in limpet teeth," *J. R. Soc. Interface*, vol. 9, no. 71, pp. 1318–1324, 2012.

[52] P. van der Wal, H. J. Giesen, and J. J. Videler, "Radular teeth as models for the improvement of industrial cutting devices," *Mater. Sci. Eng. C*, vol. 7, no. 2, pp. 129–142, 2000.

[53] F. Barthelat, A. K. Dastjerdi, and R. Rabiei, "An improved failure criterion for biological and engineered staggered composites," *J. R. Soc. Interface*, vol. 10, no. 79, 2013.

[54] A. P. Jackson, J. F. V Vincent, and R. M. Turner, "The Mechanical Design of

Nacre," *Proc. R. Soc. B Biol. Sci.*, vol. 234, no. 1277, pp. 415–440, 1988.

[55] H. D. Espinosa, A. L. Juster, F. J. Latourte, O. Y. Loh, D. Gregoire, and P. D. Zavattieri, "Tablet-level origin of toughening in abalone shells and translation to synthetic composite materials," *Nat. Commun.*, vol. 2, no. 1, pp. 173–179, 2011.

[56] G. Mayer, "Rigid biological systems as models for synthetic composites," *Science*, vol. 310, no. 5751. pp. 1144–1147, 2005.

[57] S. Naghieh, M. Sarker, M. Izadifar, and X. Chen, "Dispensing-based bioprinting of mechanically-functional hybrid scaffolds with vessel-like channels for tissue engineering applications – A brief review," *J. Mech. Behav. Biomed. Mater.*, vol. 78, no. September 2017, pp. 298–314, 2018.

[58] J. D. Currey and J. D. Taylor, "The mechanical behaviour of some molluscan hard tissues," *J. Zool.*, vol. 173, no. 3, pp. 395–406, 1974.

[59] "Bones." .

[60] M. E. Launey, M. J. Buehler, and R. O. Ritchie, "On the Mechanistic Origins of Toughness in Bone," *Annu. Rev. Mater. Res.*, vol. 40, no. 1, pp. 25–53, 2010.

[61] D. A. King and M. G. Wells, "Reaction Mechanism in Chemisorption Kinetics: Nitrogen on the Plane of Tungsten," *Proc. R. Soc. A Math. Phys. Eng. Sci.*, vol. 339, no. 1617, pp. 245–269, 1974.

[62] S. Mann, C. C. Perry, and J. Webb, "Structure, morphology, composition and organization of biogenic minerals in limpet teeth," *Proc. R. Soc. London - Biol. Sci.*, vol. 227, no. 1247, pp. 179–190, 1986.

[63] J. D. Currey, "Mechanical properties of mother of pearl in tension," *Proc. R. Soc. London - Biol. Sci.*, vol. 196, no. 1125, pp. 443–463, 1977.

[64] M. Liebschner, B. Bucklen, and M. Wettergreen, "Mechanical Aspects of Tissue Engineering," *Semin. Plast. Surg.*, vol. 19, no. 3, pp. 217–228, 2005.

[65] Z. Zhang, Y. W. Zhang, and H. Gao, "On optimal hierarchy of load-bearing biological materials," in *Proceedings of the Royal Society B: Biological Sciences*, 2011, vol. 278, no. 1705, pp. 519–525.

[66] H. A. Lowenstan and S. Weiner, “On Biomineralization.” 1988.

[67] &NA;, “Calcification in Biological Systems,” *Soil Science*, vol. 92. p. 217, 1961.

[68] V. I. Sikavitsas, J. S. Temenoff, and A. G. Mikos, “Biomaterials and bone mechanotransduction,” *Biomaterials*, vol. 22, no. 19, pp. 2581–2593, 2001.

[69] “Skeletal_Biomineralization_Patterns_Proc.” .

[70] O. Growth, “On Growth and Form.” pp. 1–15, 2014.

[71] D. Cameron, “The Fine structure of bone and calcified cartilage,” *Clin Orthop Relat Res.*, vol. 26. pp. 199–228, 1963.

[72] R. M. Carl T., “Histochemical localization of calcium in the fracture callus with potassium pyroantimonate. Possible role of chondrocyte mitochondrial calcium in callus calcification,” *J. Bone Joint Surg. Am.*, vol. 68, no. 5, pp. 703–15, 1986.

[73] A. Skeleton, “Principles of Human Anatomy.” .

[74] D. L. Kopperdahl and T. M. Keaveny, “Yield strain behavior of trabecular bone,” *J. Biomech.*, vol. 31, no. 7, pp. 601–608, 1998.

[75] “Osteologia_Nova_Or_Some_New_Observations.” .

[76] J. D. Currey, “The Mechanical Adaptations of Bones.” p. 294, 1984.

[77] R. K. Nalla, J. J. Kruzic, J. H. Kinney, M. Balooch, J. W. Ager, and R. O. Ritchie, “Role of microstructure in the aging-related deterioration of the toughness of human cortical bone,” *Mater. Sci. Eng. C*, vol. 26, no. 8, pp. 1251–1260, 2006.

[78] E. A. Zimmermann, M. E. Launey, H. D. Barth, and R. O. Ritchie, “Mixed-mode fracture of human cortical bone,” *Biomaterials*, vol. 30, no. 29, pp. 5877–5884, 2009.

[79] R. K. Nalla, J. S. Stölken, J. H. Kinney, and R. O. Ritchie, “Fracture in human cortical bone: Local fracture criteria and toughening mechanisms,” *J. Biomech.*, vol. 38, no. 7, pp. 1517–1525, 2005.

[80] K. J. Koester, J. W. Ager, and R. O. Ritchie, “The true toughness of human

cortical bone measured with realistically short cracks," *Nat. Mater.*, vol. 7, no. 8, pp. 672–677, 2008.

[81] F. J. O'Brien, "Biomaterials & scaffolds for tissue engineering," *Mater. Today*, vol. 14, no. 3, pp. 88–95, 2011.

[82] *The EU in the world 2018 edition*. 2018.

[83] C. J. E. Watson and J. H. Dark, "Organ transplantation: historical perspective and current practice," *Br. J. Anaesth.*, vol. 108, no. suppl 1, pp. i29–i42, 2012.

[84] R. Matesanz, "Meeting the organ shortage: Current status and strategies for improvement of organ donation," *Newsl. Transpl.*, vol. 4, no. 1, pp. 5–17, 1999.

[85] G. M. Abouna, "Organ Shortage Crisis: Problems and Possible Solutions," *Transplant. Proc.*, vol. 40, no. 1, pp. 34–38, 2008.

[86] W. Wang and K. W. K. Yeung, "Bone grafts and biomaterials substitutes for bone defect repair: A review," *Bioact. Mater.*, vol. 2, no. 4, pp. 224–247, 2017.

[87] T. Wu, S. Yu, D. Chen, and Y. Wang, "Bionic design, materials and performance of bone tissue scaffolds," *Materials (Basel).*, vol. 10, no. 10, 2017.

[88] A. R. Shrivats, M. C. McDermott, and J. O. Hollinger, "Bone tissue engineering: State of the union," *Drug Discov. Today*, vol. 19, no. 6, pp. 781–786, 2014.

[89] B. J. R. F. Bolland, K. Partridge, S. Tilley, A. M. R. New, D. G. Dunlop, and R. O. C. Oreffo, "Biological and mechanical enhancement of impacted allograft seeded with human bone marrow stromal cells: potential clinical role in impaction bone grafting.," *Regen. Med.*, vol. 1, no. 4, pp. 457–467, 2006.

[90] J. Casals, "Additive Manufacturing." pp. 1–29, 2015.

[91] U. A. Stock and J. P. Vacanti, "T ISSUE E NGINEERING : Current State and Prospects," no. 1, 2001.

[92] A. Saxena, "Tissue engineering: Present concepts and strategies," *J. Indian Assoc. Pediatr. Surg.*, vol. 10, no. 1, p. 14, 2005.

[93] W. Sun, B. Starly, J. Nam, and A. Darling, "Bio-CAD modeling and its

applications in computer-aided tissue engineering," *CAD Comput. Aided Des.*, vol. 37, no. 11, pp. 1097–1114, 2005.

[94] M. Fantini and M. Curto, "Interactive design and manufacturing of a Voronoi-based biomimetic bone scaffold for morphological characterization," *Int. J. Interact. Des. Manuf.*, pp. 1–12, 2017.

[95] G. Tozzi, A. De Mori, A. Oliveira, and M. Roldo, "Composite hydrogels for bone regeneration," *Materials (Basel).*, vol. 9, no. 4, pp. 1–24, 2016.

[96] B. H. Kapadia, R. A. Berg, J. A. Daley, J. Fritz, A. Bhave, and M. A. Mont, "Periprosthetic joint infection," *Lancet*, vol. 387, no. 10016, pp. 386–394, 2016.

[97] M. McGurk, A. A. Amis, P. Potamianos, and N. M. Goodger, "Rapid prototyping techniques for anatomical modelling in medicine," *Ann. R. Coll. Surg. Engl.*, vol. 79, no. 3, pp. 169–174, 1997.

[98] L. S. Dimas, G. H. Bratzel, I. Eylon, and M. J. Buehler, "Tough composites inspired by mineralized natural materials: Computation, 3D printing, and testing," *Adv. Funct. Mater.*, vol. 23, no. 36, pp. 4629–4638, 2013.

[99] M. J. Mitchell and M. R. King, "NIH Public Access," no. 1, pp. 1–23, 2014.

[100] "Mechanical_Behaviour_of_Engineering_Mate." .

[101] L. Ng, H. H. Hung, A. Sprunt, S. Chubinskaya, C. Ortiz, and A. Grodzinsky, "Nanomechanical properties of individual chondrocytes and their developing growth factor-stimulated pericellular matrix," *J. Biomech.*, vol. 40, no. 5, pp. 1011–1023, 2007.

[102] W. Voigt, "Ueber die Beziehung zwischen den beiden Elasticit??tsconstanten isotroper K??rper," *Ann. Phys.*, vol. 274, no. 12, pp. 573–587, 1889.

[103] A. Reuss, "Berechnung der Fließgrenze von Mischkristallen auf Grund der Plastizitätsbedingung für Einkristalle .," *ZAMM - J. Appl. Math. Mech. / Zeitschrift für Angew. Math. und Mech.*, vol. 9, no. 1, pp. 49–58, 1929.

[104] A. Kelly and W. R. Tyson, "Tensile Fibre-Reinforce11 and Metals Copper / Tuxstes," *J. Mech. Phys. Solids*, vol. 13, pp. 329–350, 1965.

[105] D. Tripathi and F. R. Jones, "Single fibre fragmentation test for assessing adhesion in fibre reinforced composites," *J. Mater. Sci.*, vol. 33, no. 1, pp. 1–16, 1998.

[106] J. C. H. Affdl and J. L. Kardos, "The Halpin-Tsai equations: A review," *Polymer Engineering & Science*, vol. 16, no. 5. pp. 344–352, 1976.

[107] E. Sciences, "(Received October 16, 2005 Accepted December 7, 2005)," vol. 34, no. 1, pp. 227–236, 2005.

[108] C. L. Tucker and E. Liang, "Stiffness predictions for unidirectional short-fiber composites: Review and evaluation," *Compos. Sci. Technol.*, vol. 59, no. 5, pp. 655–671, 1999.

[109] T. S. Chow and J. J. Hermans, "The Elastic Constants of Fiber Reinforced Materials," *J. Compos. Mater.*, vol. 3, no. 3, pp. 382–396, 1969.

[110] H. L. Cox, "The elasticity and strength of paper and other fibrous materials," *Br. J. Appl. Phys.*, vol. 3, no. 3, pp. 72–79, 1952.

[111] J. Z. Manapat, Q. Chen, P. Ye, and R. C. Advincula, "3D Printing of Polymer Nanocomposites via Stereolithography," *Macromol. Mater. Eng.*, vol. 302, no. 9, pp. 1–13, 2017.

[112] J. Z. Manapat, J. D. Mangadlao, B. D. B. Tiu, G. C. Tritchler, and R. C. Advincula, "High-Strength Stereolithographic 3D Printed Nanocomposites: Graphene Oxide Metastability," *ACS Appl. Mater. Interfaces*, vol. 9, no. 11, pp. 10085–10093, 2017.

[113] J. H. Koo, R. Ortiz, B. Ong, and H. Wu, *Polymer nanocomposites for laser additive manufacturing*. 2016.

[114] H. Yang *et al.*, "Performance evaluation of ProJet multi-material jetting 3D printer," *Virtual Phys. Prototyp.*, vol. 12, no. 1, pp. 95–103, 2017.

[115] R. Olszewski, P. Szymor, and M. Kozakiewicz, "Accuracy of three-dimensional, paper-based models generated using a low-cost, three-dimensional printer," *J. Cranio-Maxillofacial Surg.*, vol. 42, no. 8, pp. 1847–1852, 2014.

[116] E. Huotilainen *et al.*, "Inaccuracies in additive manufactured medical skull models caused by the DICOM to STL conversion process," *J. Cranio-Maxillofacial Surg.*, vol. 42, no. 5, pp. 259–265, 2014.

[117] V. Le, H. Paris, and G. Mandil, "Using additive and subtractive manufacturing technologies in a new remanufacturing strategy to produce new parts from End-of-Life parts Abstract :," *22 ème Congrès Français Mécanique CFM2015*, pp. 1–8, 2015.

[118] ASTM International, "F2792-12a - Standard Terminology for Additive Manufacturing Technologies," *Rapid Manuf. Assoc.*, pp. 10–12, 2013.

[119] B. G. Compton and J. A. Lewis, "3D-printing of lightweight cellular composites," *Adv. Mater.*, vol. 26, no. 34, pp. 5930–5935, 2014.

[120] W. Yu, H. Zhou, B. Q. Li, and S. Ding, "3D Printing of Carbon Nanotubes-Based Microsupercapacitors," *ACS Appl. Mater. Interfaces*, vol. 9, no. 5, pp. 4597–4604, 2017.

[121] S. Yang and Y. F. Zhao, "Additive manufacturing-enabled design theory and methodology: a critical review," *Int. J. Adv. Manuf. Technol.*, vol. 80, no. 1–4, pp. 327–342, 2015.

[122] J. W. Gibbs, "United States Patent Office .," no. 53971, pp. 3–5, 1866.

[123] N. Bhattacharjee, A. Urrios, S. Kang, and A. Folch, "The upcoming 3D-printing revolution in microfluidics," *Lab Chip*, vol. 16, no. 10, pp. 1720–1742, 2016.

[124] C. W. Hull and C. Arcadia, "Us4575330a," no. 19, 1984.

[125] P. E. H. T. Le, "(12) United States Patent," vol. 2, no. 12, 2008.

[126] W. E. King *et al.*, "Laser powder bed fusion additive manufacturing of metals; physics, computational, and materials challenges," *Appl. Phys. Rev.*, vol. 2, no. 4, p. 041304, 2015.

[127] A. Thompson, D. McNally, I. Maskery, and R. K. Leach, "X-ray computed tomography and additive manufacturing in medicine: a review," *Int. J. Metrol. Qual. Eng.*, vol. 8, no. May, p. 17, 2017.

[128] A. du Plessis, I. Yadroitsev, I. Yadroitsava, and S. G. Le Roux, "X-Ray Microcomputed Tomography in Additive Manufacturing: A Review of the Current Technology and Applications," *3D Print. Addit. Manuf.*, vol. 5, no. 3, pp. 227–247, 2018.

[129] S. Askarinejad and N. Rahbar, "Toughening mechanisms in bioinspired multilayered materials," *J. R. Soc. Interface*, vol. 12, no. 102, 2015.

[130] P. J. Smith and A. Morrin, "Reactive inkjet printing," *J. Mater. Chem.*, vol. 22, no. 22, pp. 10965–10970, 2012.

[131] T. Wang, R. Patel, and B. Derby, "Manufacture of 3-dimensional objects by reactive inkjet printing," *Soft Matter*, vol. 4, no. 12, pp. 2513–2518, 2008.

[132] B. Y. Ang, C. K. Chua, and Z. H. Du, "Study of trapped material in rapid prototyping parts," *Int. J. Adv. Manuf. Technol.*, vol. 16, no. 2, pp. 120–130, 2000.

[133] ASTM International, "ASTM F3122-14," 2014.

[134] ASTM International, "ASTM F3091 / F3091M-14," 2014.

[135] British Standards, "Additive manufacturing — General principles Part 3 : Main characteristics and corresponding test methods," p. 26, 2014.

[136] ASTM International, "Standard test method for tensile properties of plastics," *ASTM Int.*, vol. 08, pp. 46–58, 2003.

[137] B. Croop, "Astm d638 type iv," p. 44.

[138] L. S. Dimas and M. J. Buehler, "Modeling and additive manufacturing of bio-inspired composites with tunable fracture mechanical properties," *Soft Matter*, vol. 10, no. 25, pp. 4436–4442, 2014.

[139] D. Markl *et al.*, "Analysis of 3D Prints by X-ray Computed Microtomography and Terahertz Pulsed Imaging," *Pharm. Res.*, vol. 34, no. 5, pp. 1037–1052, 2017.

[140] M. B. Schaffler, D. B. Burr, and R. G. Frederickson, "Morphology of the

osteonal cement line in human bone," *Anat. Rec.*, vol. 217, no. 3, pp. 223–228, Aug. 2018.

[141] M. Conward and J. Samuel, "Machining characteristics of the haversian and plexiform components of bovine cortical bone," *J. Mech. Behav. Biomed. Mater.*, vol. 60, pp. 525–534, 2016.

[142] P. Frasca, R. A. Harper, and J. L. Katz, "Collagen fiber orientations in human secondary osteons.," *Acta Anat. (Basel).*, vol. 98, no. 1, pp. 1–13, 1977.

[143] J. Martínez-Reina, J. García-Rodríguez, J. Mora-Macías, J. Domínguez, and E. Reina-Romo, "Comparison of the volumetric composition of lamellar bone and the woven bone of calluses," *Proc. Inst. Mech. Eng. Part H J. Eng. Med.*, vol. 232, no. 7, pp. 682–689, 2018.

[144] J. Martínez-Reina, J. Domínguez, and J. M. García-Aznar, "Effect of porosity and mineral content on the elastic constants of cortical bone: A multiscale approach," *Biomech. Model. Mechanobiol.*, vol. 10, no. 3, pp. 309–322, 2011.

[145] J. Monedero, "Parametric design: a review and some experiences," *Autom. Constuction 9*, pp. 369–377, 2000.

[146] M. Kumke, H. Watschke, and T. Vietor, "A new methodological framework for design for additive manufacturing," *Virtual Phys. Prototyp.*, vol. 11, no. 1, pp. 3–19, 2016.

[147] A. Leitão, L. Santos, and J. Lopes, "Programming Languages for Generative Design: A Comparative Study," *Int. J. Archit. Comput.*, vol. 10, no. 1, pp. 139–162, 2012.

[148] R. Meneghello, G. Savio, R. Raffaeli, A. Cerardi, M. Turchetto, and L. Planchenstainer, "An integrated methodology for the functional design of dental prosthesis," *Int. J. Interact. Des. Manuf.*, vol. 7, no. 2, pp. 103–114, 2013.

[149] M. W. Naing, C. K. Chua, K. F. Leong, and Y. Wang, "Fabrication of customised scaffolds using computer-aided design and rapid prototyping techniques," *Rapid Prototyp. J.*, vol. 11, no. 4, pp. 249–259, 2005.

[150] F. G. Evans and M. L. Riolo, "Relations between the Fatigue Life and Histology of Adult Human Cortical Bone," *J. Bone Jt. Surg.*, vol. 52, no. 8, pp. 1579–1586, 1970.

[151] J. García-Rodríguez and J. Martínez-Reina, "Elastic properties of woven bone: effect of mineral content and collagen fibrils orientation," *Biomech. Model. Mechanobiol.*, vol. 16, no. 1, pp. 159–172, 2017.

[152] F. Mézière *et al.*, "Experimental observation of ultrasound fast and slow waves through three-dimensional printed trabecular bone phantoms," *J. Acoust. Soc. Am.*, vol. 139, no. 2, pp. EL13–EL18, 2016.

[153] R. Widmann, "International society for rock mechanics commission on rock grouting," *Int. J. Rock Mech. Min. Sci. Geomech. Abstr.*, vol. 33, no. 8, pp. 803–847, 1996.

[154] M. L. Oyen, V. L. Ferguson, A. K. Bembey, A. J. Bushby, and A. Boyde, "Composite bounds on the elastic modulus of bone," *J. Biomech.*, vol. 41, no. 11, pp. 2585–2588, 2008.

[155] F. Barthelat, "Designing nacre-like materials for simultaneous stiffness, strength and toughness: Optimum materials, composition, microstructure and size," *J. Mech. Phys. Solids*, vol. 73, pp. 22–37, 2014.

[156] I. Jäger and P. Fratzl, "Mineralized collagen fibrils: A mechanical model with a staggered arrangement of mineral particles," *Biophys. J.*, vol. 79, no. 4, pp. 1737–1746, 2000.

[157] "Biomimetics." .

[158] J. Sun and B. Bhushan, "Hierarchical structure and mechanical properties of nacre: A review," *RSC Advances*, vol. 2, no. 20. pp. 7617–7632, 2012.

[159] S. Krish, "A practical generative design method," *CAD Comput. Aided Des.*, vol. 43, no. 1, pp. 88–100, 2011.

[160] T. Swetly, J. Stampfl, G. Kempf, R. M. Hucke, M. Willing, and M. Warkentin, "Bioinspired engineering polymers by voxel-based 3D-printing,"

BioNanoMaterials, vol. 17, no. 3–4, pp. 145–157, 2016.

[161] S. C. Service, "International Standard," *Communication*, vol. 2010, pp. 1–8, 2003.

[162] H. Krenchel, *Fibre Reinforcement: Theoretical and Practical Investigations of the Elasticity and Strength of Fibre-reinforced Materials*. Akademisk forlag, 1964.

[163] G. Daniel and A. B. Thomsen, "Hemp Fibre Microstructure and Use of Fungal Defibration to Obtain Fibres for Composite Materials," *J. Nat. Fibers*, vol. 2, no. 4, pp. 19–37, 2005.

[164] H. Gao, "Application of fracture mechanics concepts to hierarchical biomechanics of bone and bone-like materials," *Int. J. Fract.*, vol. 138, no. 1–4, pp. 101–137, 2006.

Appendices

Appendix A - Basic parametric fibre design composites

The design below aims to recreate a composite material which reinforcement units are modelled as cylindrical geometrical shapes, with controllable aspect ratio. The process had been implemented in Rhinoceros 5 (McNeal, Seattle, WA, USA) with the graphical algorithm plug-in editor Grasshopper. The resulting output is a virtual composite made two phases: hard fibres embedded in a softer matrix.

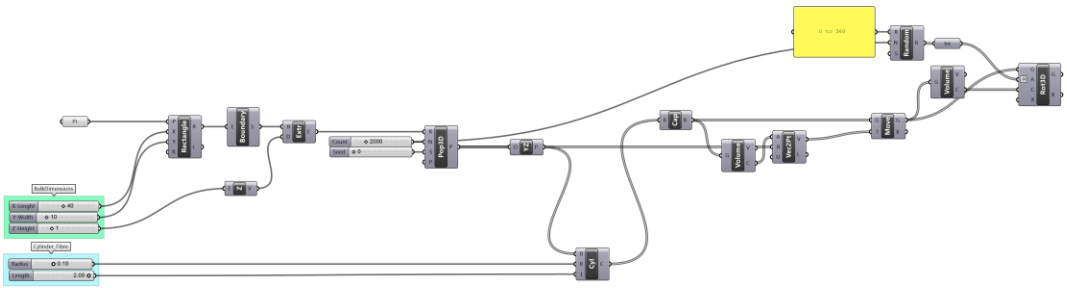

Figure A1. Schematic of the global generative algorithm.

The STL files of the two complementary phases are supplied to the 3D printer by the generative algorithm reported in Figure A1. The aspect ratio of fibres is set by two input components *number slider*, belonging to the Grasshopper library, placed at the beginning of the visual algorithm and reported in Figure A2. The given case consider an aspect ratio of 20.

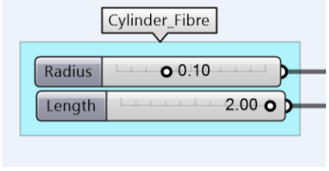

Figure A2. Input component Number Slider that generate the domain of numeric data controlling fibres aspect ratio.

Furthermore, a cylindrical shape has been selected. Nevertheless, fibres can be shaped according to different geometries: from geometrical primitives such as spheres, parallelepiped, cylinder, ellipsoid etc. to more complex shapes defined by mathematical functions drawn in the 3D environment, such as conceptual NURBS (Non-uniform rational basis spline on) on which Rhinoceros is based on. Figure A3 presents the Grasshopper subroutine made of a components cascade that allows for the creation of the bulk of the composite.

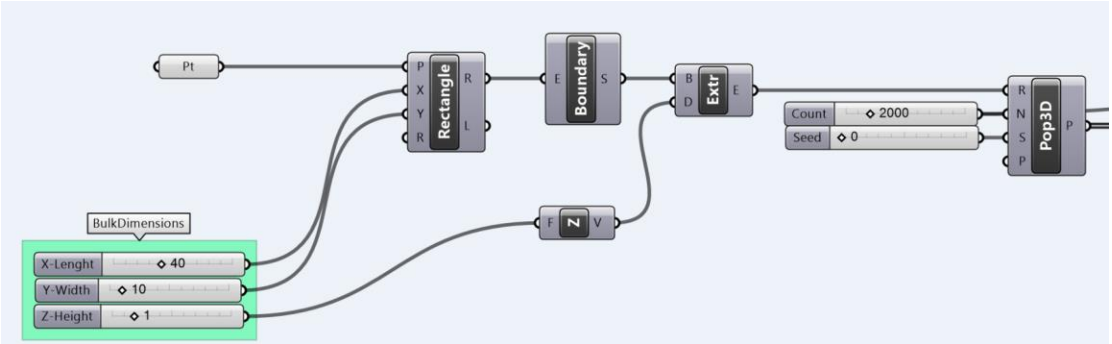

Figure A3. Zoom in of the first portion of the visual algorithm reported in Figure A1. A rectangle is created according to the set domain of numeric values. A surface is generated by the boundary edges of the rectangle and extruded to form a closed polysurface. The component populate 3D feed in anchor points on which fibres will be consequently placed.

A rectangle is drawn according to the dimensions desired by the user and set by the number *slider input* components X-length and Y-width. The rectangle is then extruded along the Z axis thanks to the *extrusion* component coupled with a *unit Z* component. In this way a vector parallel to the Z axis indicates the direction of extrusion of the rectangle, combined with the number slider which defined the modulus of extrusion. Random points are spread in order to "anchor" the designed fibre into the drawn volume. The metioned task is performed by the *Populate 3D* component (Figure A4),

which aims to spread random points inside a volume of interest (R input "Pop3D" component).

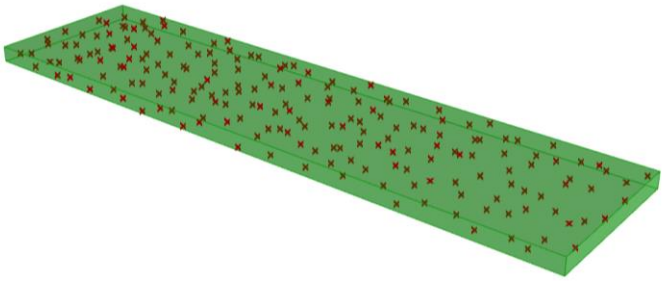

Figure A4. Random Points speaded by the Pop3D (populate 3D) component.

Fibre are placed in each point in correspondence of each fibre centroid (Figure A5).

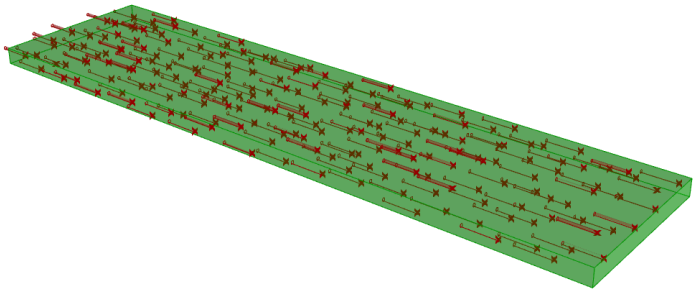

Figure A5. The cylindrical fibres are moved in correspondence of the ditributed points that will represent the fibres centroids.

In order to give a unique fibre orientation for each fibre embedded in the matrix, random values from 0 to 360 degrees were generated by the *Random* component, coupled to the *Rotate 3D* component (Figure A6). The latter takes in input an object and his axial direction, to be rotated around a center point and according to an axis vector defined by the user.

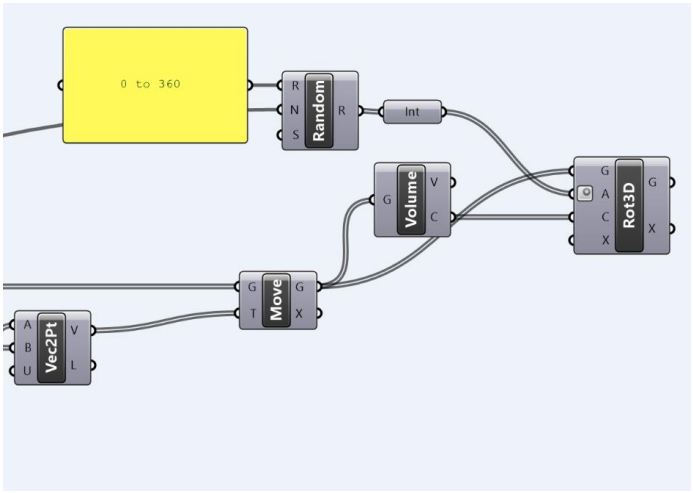

Figure A6. Zoom in of the second part of the visual algorithm reported in Figure A1. A 2points vector (Vec2Pt) component defines vectors between the cylindrical fibre centroid (unit fibre) and the random points into the volume of interest. The component Move, moves the unit fibre onto each random point distributed into the volume of interest. Finally the ratate 3D component Rot3D rotate the fibres in a random way, guided by the random generation of a domain rotation angles in radians.

The generated directions are equal in number to the fibres to be oriented. The generated output can be observed in the figure below for the given case of 200 fibre embedded in the bulk. Finally, a boolean intersection between the bulk and the fibre is performed in order to confine the fibre inside the boundary defined by the bulk, excluding every shape outside the boundary.

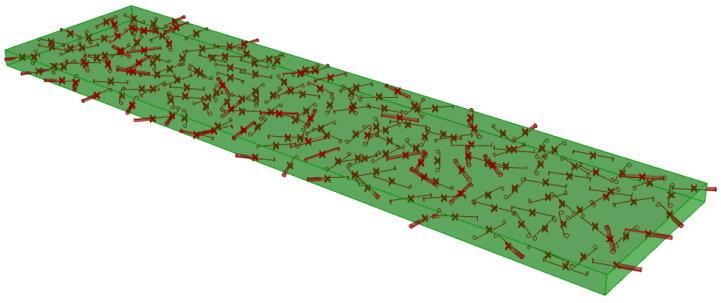

Figure A7. The cylindrical fibres rotated randomly after the generation of a domain rotation angles.

As first analysis concerning the feasibility of the study, an increasing number of fibre have been considered with a number of points ranging from 200 to 5000. Increasing renderings in terms of fibre are shown from the 3D modeller top view in the figure above.

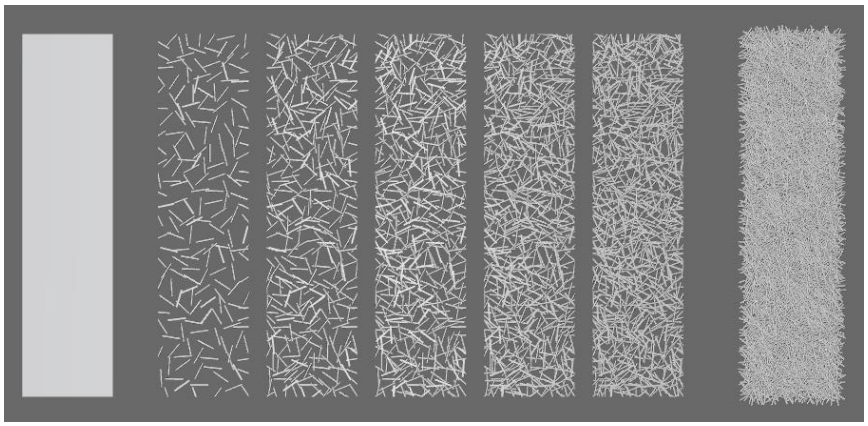

Figure A8. Schematic of the generated fibres compositesan increasing number of reinforcement fibre from 3 to 70 reinforcement vol %.

Shown below a line representing the relationship among the number of seeds or points distributed inside the bulk and the out coming fibre percentage embedded in the volume.

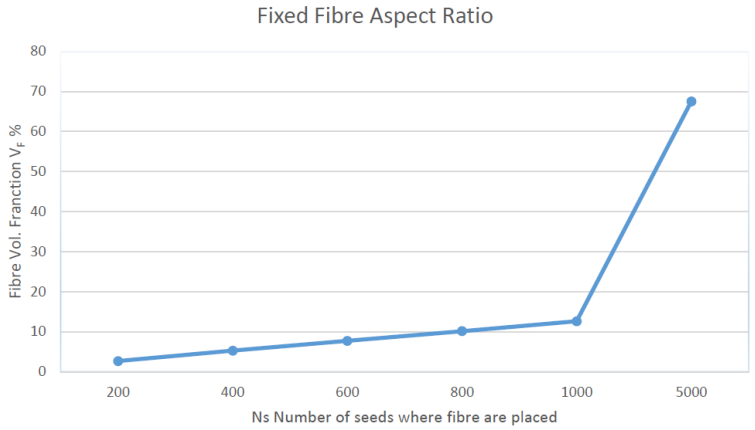

Figure A9. Effect of the number of fibers on the volume fraction of the reinforcement of the composite.

Optical images were taken with a 25X magnification lens and resulting distances of the investigated geometrical shapes were verified using a 0.01 millimitre division. Manufacturing limits are shown in Figure A10 when the fibre approache the submiter scale.

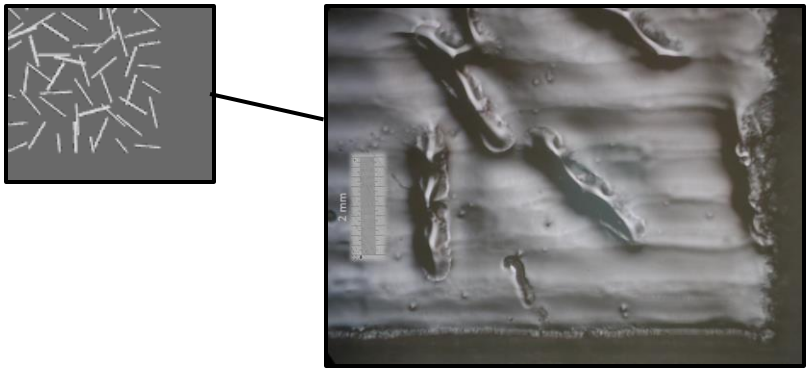

Figure A10. Optical image of a 3D printed fibre composite structure. Fibres were designed to be 2 mm long and 0.1 mm thick. The optical image testify for the material mixing ate the interface between fibres and matrix that lead to a deformation of the reinforcement due to physical limits of the multi material manufacturing system.

Appendix B – Limpet tooth modelling

'Engineering and bio-engineering approaches to manufacturing limpet tooth material.'

Introduction.

It has recently been shown that limpet tooth possesses unique and desirable mechanical properties that result from its specific structure and composition [34]. The overarching aim of this project is to generate limpet tooth material via engineering and bioinspired approaches. The radula, a tongue-like structure found in certain molluscs, was first identified in the mid-17th century by biologist and microscopist Jan Swammerdam whose work was translated into Latin and published posthumously some 50 years later in the *Biblia naturae* (Book of Nature). The teeth of the limpet radula were later described as 'infinitely small' by Michel Anderson in 1757 who observed 200 teeth in longitudinal rows in the land snails as well as the limpet genus *Patella*. The composition of limpet tooth aroused both interest and controversy in the scientific community with a division between those who thought the limpet radula was made of silica, and others who suggested that the radula was made primarily of the polysaccharide chitin. In 1856 two separate publications suggested that gastropod teeth contained both organic and inorganic components, or in other words it is a composite material. Most recently in 2015, Professor Asa Barber demonstrated that the tooth of the common limpet (*Patella vulgata*) has the highest recorded tensile strength and elastic modulus of any biologically occurring material (4.90+/-1.90 and 120+/-30 GPa respectively), stronger than spider silk and comparable to man-made carbon fibres [34]. The exceptional mechanical properties and unique structures of limpet tooth are evolutionarily

optimised for rasping algae from rock surfaces. A man-made material with similar mechanical properties would be desirable in many different applications. The information provided in previous studies on the composition, structure and developmental biology of limpet tooth are invaluable first steps in understanding how to generate limpet tooth in the laboratory. Observing high-magnification electron microscopy images portraying the tooth cusp of the limpet *Patella Vulgata* (Figure B1) was the first step to get inspired for after proceeding with a composite generative design idealization. The changing orientation of the nanofibrous goethite in the chitin matrix (Figure B2) is reported with a mineral fibre length of approximately 3µm and a fibre diameter of 20nm.

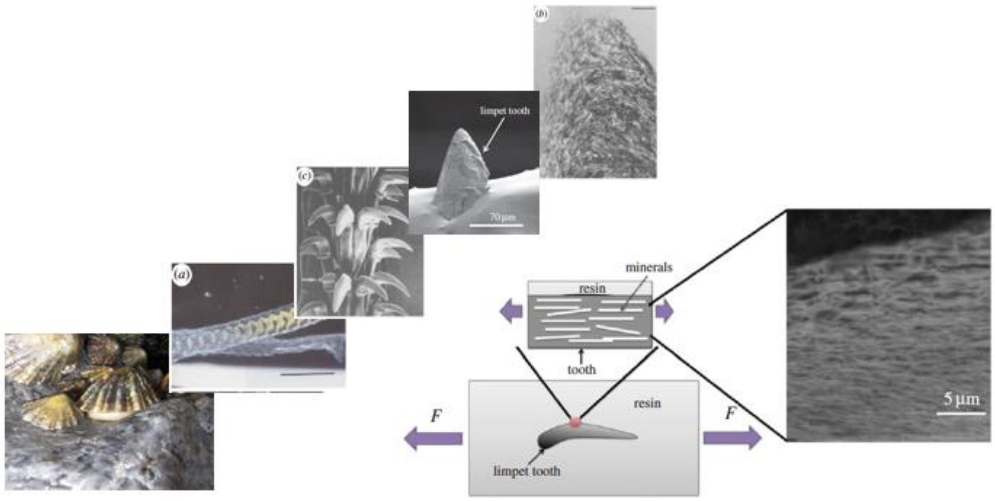

Figure B1. Hierarchical structures of the limper (Patella Vulgata). From the optical image of the tongue-like radula containing bands of teeth along a length of many centimetres to the high-magnification electron microscopy images of each tooth in which in contained an anisotropic composite structure made of the goethite reinforcement fibre and the chitin matrix highlighting the structural resemblance to a fibre-reinforced composite material.

This section provides information about the developed biomimetic design inspired by the ghoetite fibres and chitin matrix found in limpet tooth. A generative design work-flow is proposed with the aim to automatically build a bioinspired composite design

starting from a set of points distributed in the boundary of the limpet tooth cusp in input, modelled as a cone. This process results in a hybrid fibre composite while controlling the percentage of fibres, fibre geometry and aspect ratio of the desired design.

The idea was to distribute the reinforcement, defined by a predesigned geometry of interest (ellipsoidal, cylindrical and so on) inside the cusp (bulk) following SEM images of the natural limpet tooth design (Figure B2).

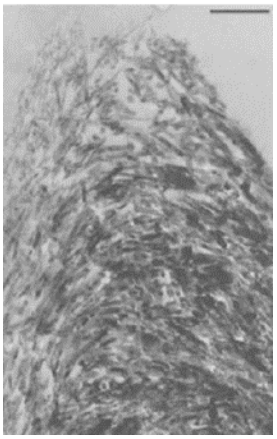

Figure B2. High-magnification electron microscopy images of the tooth cusp show the changing orientation of the nanofibrous goethite.

The graphical algorithm editor Grasshopper, integrated with Rhinoceros 3-D modelling tools (McNeel), was used for controlling the fibres distribution inside the bulk of the limpet tooth. Grasshopper is a suitable instrument for architects and designers to solve design issues using a parametric or associative method. The algorithm is a set of rules and instructions applied in a step by step procedure. The relevant information in input are analysed with the aim to produce significant and congruent results with the mimicked natural structure. All possible operations and commands in CAD become part of a code that can be applied to a large number of objects in the design field. A

visual approach (Figure B3) helps in the identification of different parts of the built circuit using different colours, each one applying a different implemented function.

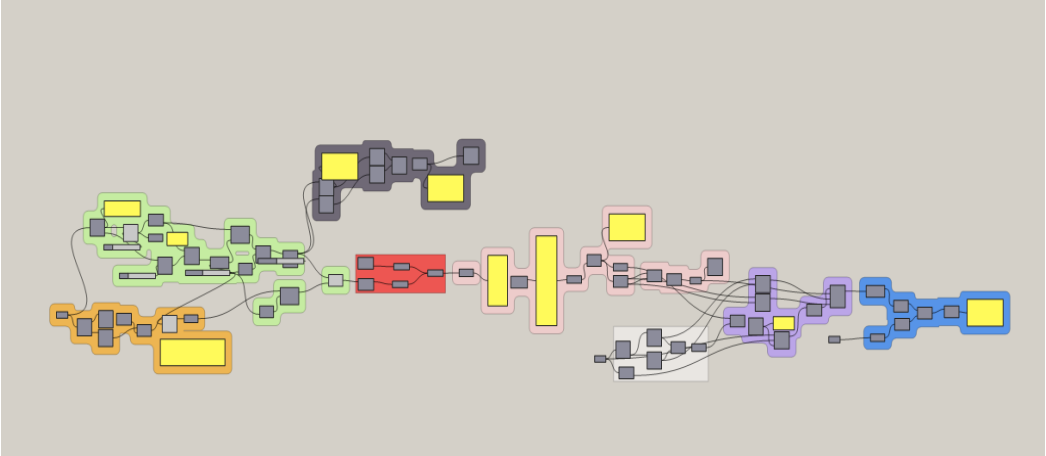

Figure B3. Main algorithm for the limpet tooth bio-inspired design assembly. Every colour groups the component assembled to reach a single function.

Direction and orientation of the fibres were assigned following directional axis traced between points on the bottom of the cusp and points placed on its longitudinal axes. In particular, the design generation starts with the green section that receives the cone geometry as an input after being deconstructed to a boundary representation by a *DeBrep* operation. The median axis of the cusp was evaluated by the orange sub circuit as the line connecting the centre of the base of the cone and the tip (Figure B4-a). The green section was designed to scale the curve circumscribing the cusp base in smaller circumferences through XY plane towards the base centre, depending on the desired number of circumferences given in input (Figure B4-b).

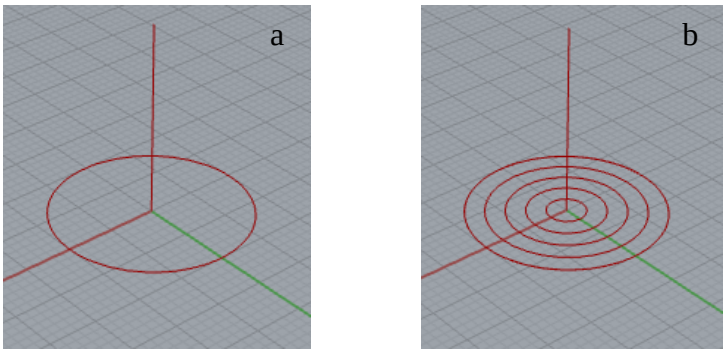

Figure B4. Representation of the modelled tooth cusp base inscribed by a circumference (a) gradually scaled (b) for generating the starting point of the guidelines giving in input n=5.

Points on the median axis and points on the circumferences were linked in order to define guidelines to direct the fibres, which are oriented according to guidelines normal vectors (Figure B5).

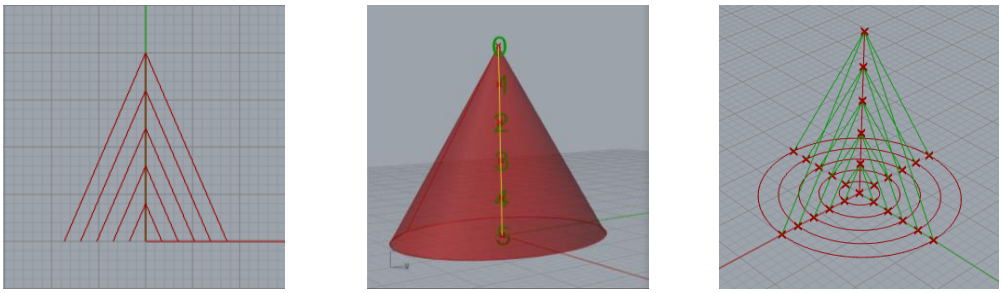

Figure B5. Guidelines generated after giving in n=5 for both circumferences and median line.

The directional lines were given as input to the red section, retrieving a dashed pattern where each dash represented the axis of each single fibre. In order to fill the bulk with as many fibres as possible, the already realized fibres orientations were duplicated in the black session and rotated half of the angle separating the original points on the circumferences (Figure B6). This saved computational time due to the eventual implementation of a second sub circuit equal to the one previously described.

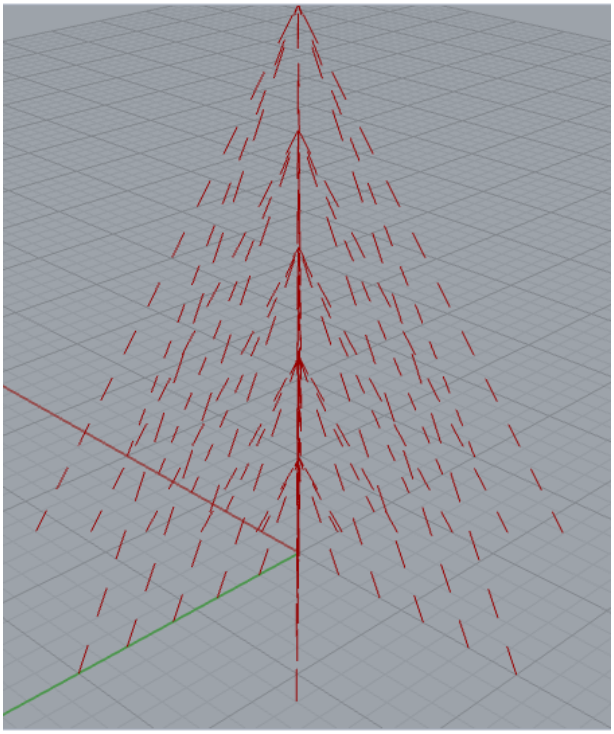

Figure B6. Dashed pattern resulting from an input number of seeds n=4 distributed on circumferences and median line. The dashed pattern is shifted among two adjacent guidelines along Z axis so that each gap becomes passing from a line to another. In order to save computational power the number of guidelines is doubled rotating the existing pattern.

Varying the number of seeds on both circumferences and longitudinal axis, controls the resulting composite reinforcement in terms of volume percentage (Figure B7).

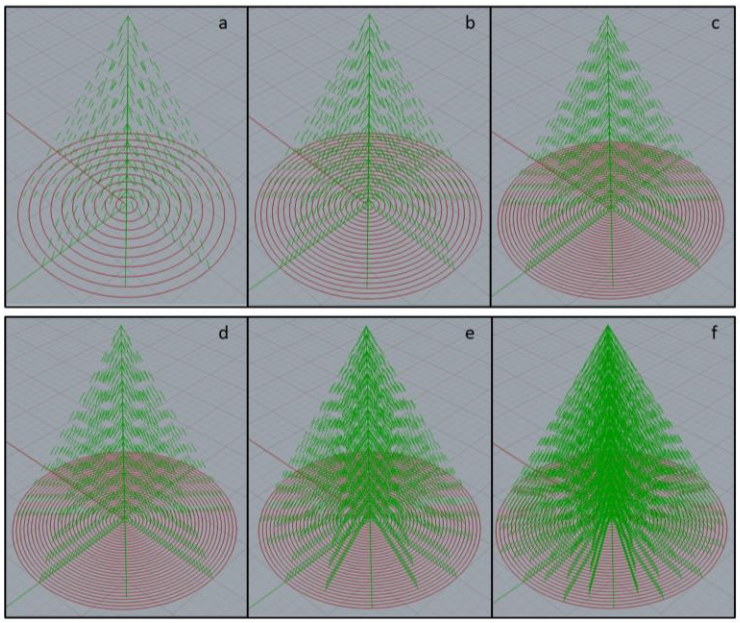

Figure B7. On The top an increasing percentage of fibres increasing the number of circumferences a seeds on the median line of the cusp with n ranging from 10 to 30 with a step size of 10. On the bottom two representation of the increasing percentage of reinforcement varying a second parameter Sc relative to the seeds distributed on 30 circumferences from 4 to 16 increasing with a step size of 4.

Recurrent segments under a certain threshold in length were excluded from the design by the pink section (Figure B8). The purple section evaluated the scaling factor comparing the longitudinal axes of dashes and designed fibre geometry input (Figure B3). The chosen fibre reinforcement geometry was then scaled in order to fit the remaining segments (Figure B9). The volume percentage of fibres referred to the whole bulk is retrieved in the blue step as the ratio between the reinforcement volume and the volume of the cusp. The resulting design is a watertight (closed) mesh ready to be 3D printed. Meshes were printed using a Multi material 3D printer Projet 5500X (3D system) with a layer resolution of 16μm.

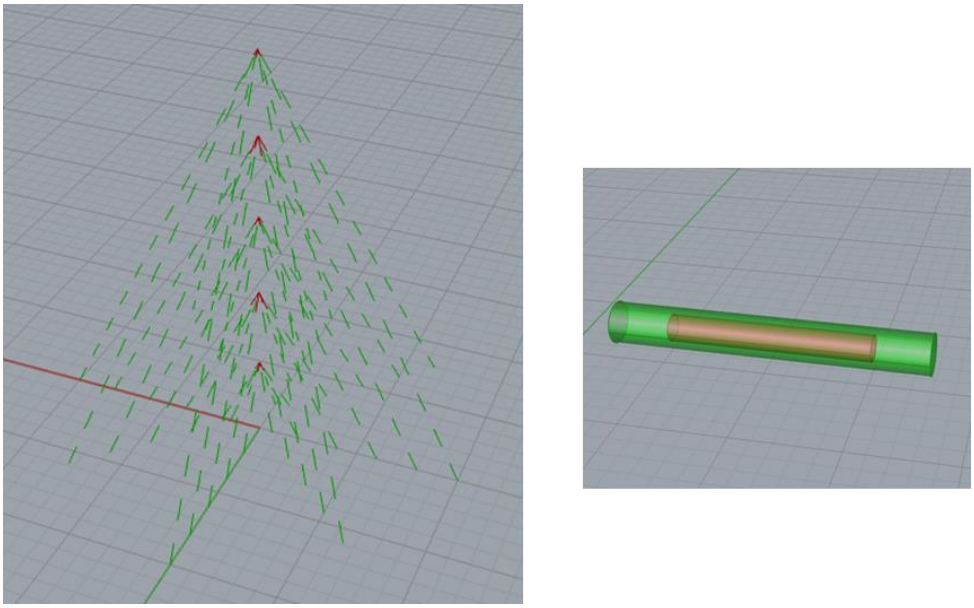

Figure B8. On the left the dashed patter is depicted highlighting in the excluded segments because shorter than a desired threshold. On the right a scaled representation of the fibre given in input, adapted to the dashes length.

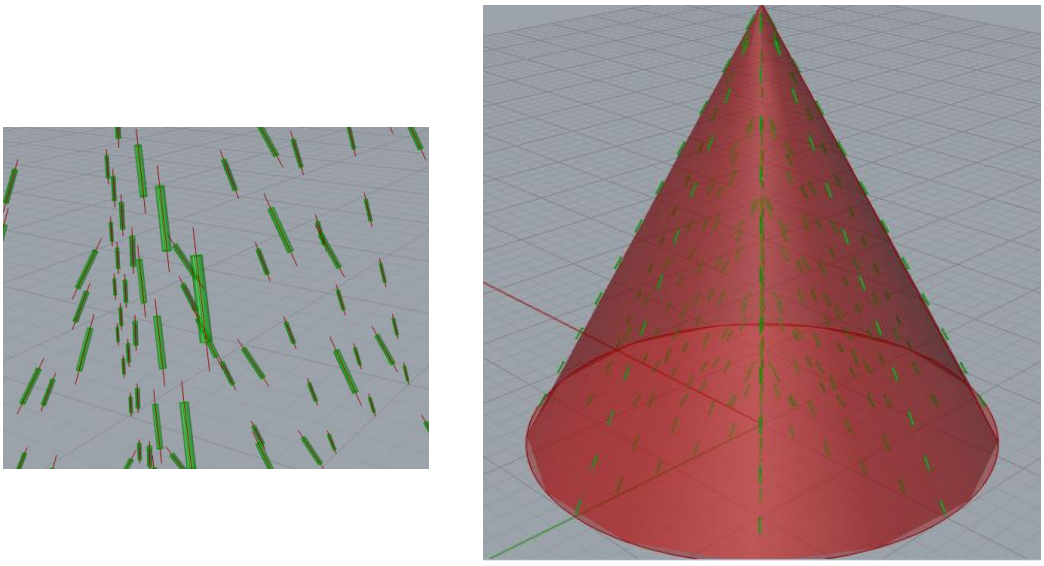

Figure B9. On the left an example of the fibres distribution among each dash fitted inside the bulk of the cusp given in input, representing the virtual version of the limpet tooth bio inspired composite

In order to control the final fibre composite design inspired by a limpet tooth cusp, we need to correlate the input parameters with the target ones.

The input parameters are:

- The number of circumferences concentric to the cusp base surface centroid C_S;
- The number of seeds along the longitudinal axis of the cusp S_L;
- The number of seeds on each circumference S_C.

The goal is to build a pattern of shifted fibres so that if a direction line has fibres placed on dashes, the nearby directions have fibre placed on the holes. This will allow a better shear strength transmission with a resulting stronger composite.

The target parameter are:

- The fibre aspect ratio depending on the chosen geometry;
- The volume fraction V_f of the fibre on the overall composite.

The volume fraction V_f can be easily computed as follows:

$$V_f = \frac{V_{fibers}}{V_{cusp}}$$

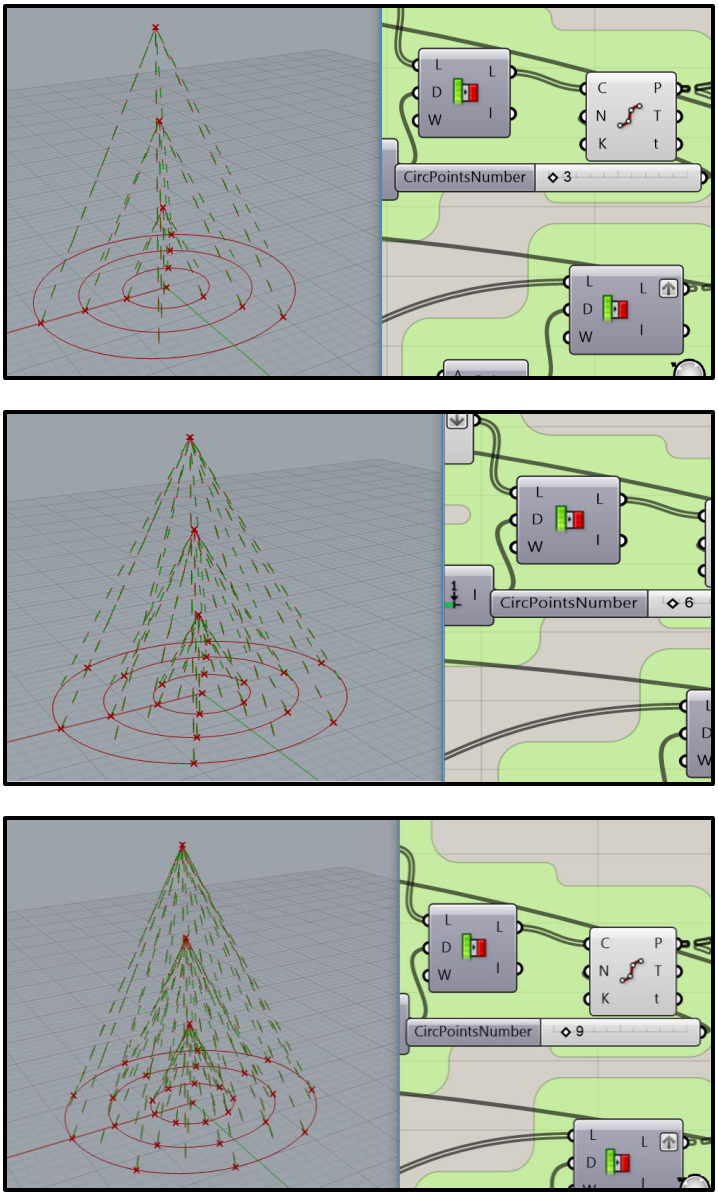

Figure B10. From the top to the bottom an increasing reinforcement volume fraction varying the number of seeds on the circumferences generating from three to nine planes on which the guidelines lie.

It can be shown how the total amount of number of seeds influence the volume fraction of the fibres on the overall composite (Figure B10) shows three snapshots of the modelled tooth cusp with the same number of circumferences C_S and seeds placed on the longitudinal axis S_L. The number of seeds distributed on the circumferences increased in order to strongly rise the reinforcement volume fraction V_f. The

reinforcement fibre diameter is highly dependent on the number of circumferences on the XY plane. The idea is to maintain the reinforcement fibre disconnected from each other so that shear force transfer from matrix to fibre and vice versa is possible once the model is printed and subjected to eventual mechanical tests.

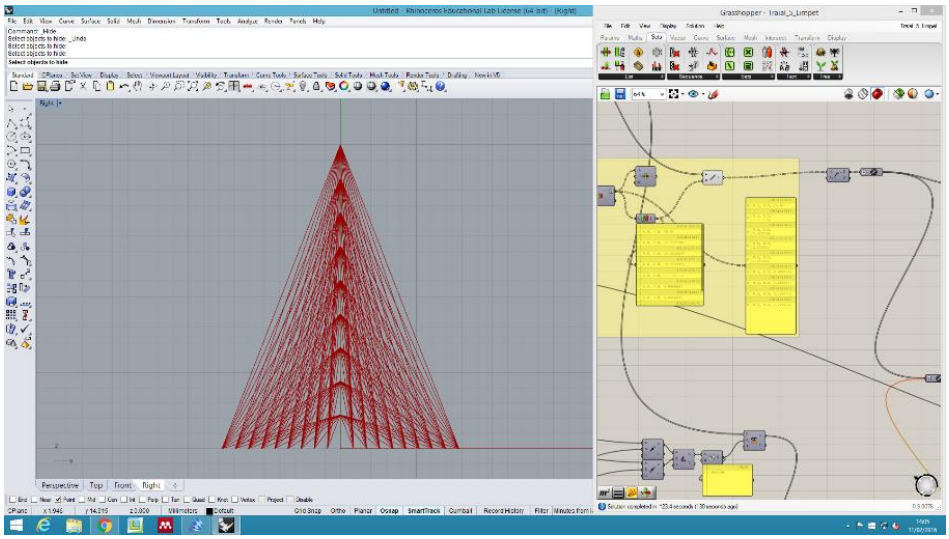

Figure B11. Guidelines generated considering S_L = 10 and Sc equal to 50. The output is a structure with overlapping guidelines that generate fibres mesh superimposition resulting in a not watertight mesh.

The choice of having the same number in input for both circumferences and seeds on the longitudinal axis the above mentioned parameters allowed a distribution of the fibres avoiding superimposition of the reinforcement features and consequential problem related to the meshing part (Figure B11) before printing.

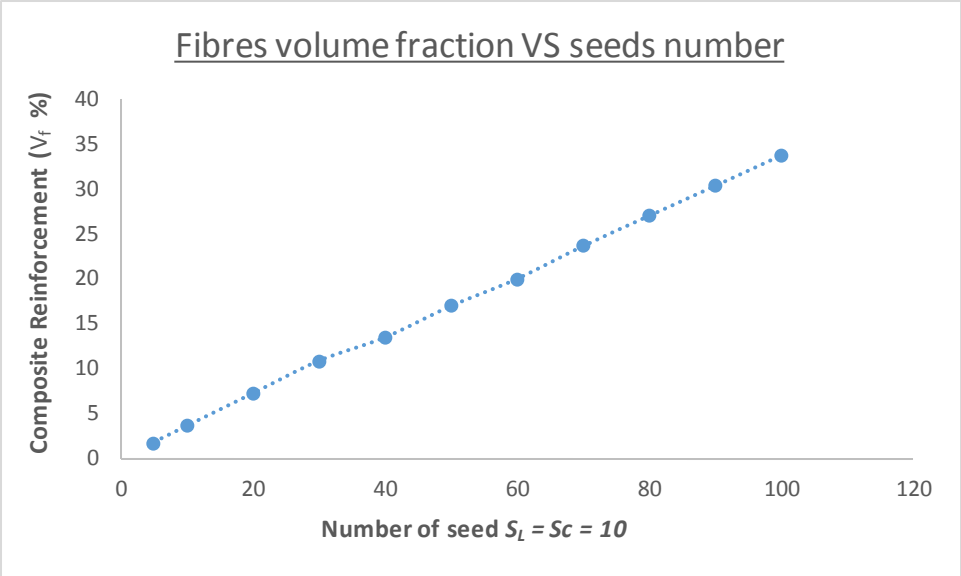

Figure B12. Effect of the number of seeds on the volume fraction of the reinforcement with S_L = Sc = 10

The purpose of this study was to reach values of V_f starting from a reasonable number of circumferences and relative seeds on the longitudinal axis of the cusp that could allow to reach at least 1% of the total volume of the composite. The first observation on these results concerned the impact of the number of seeds placed on the circumferences and related out coming directions of the fibres that allowed to reach values of V_f up to 34% (Figure B12). The second observation concerned the aspect ratio of the reinforcement that resulted completely manageable in CAD environment allowing a free design of the fibre according to the mimicked natural model. This study was limited to an idealized cylindrical fibre shape with a reasonable aspect ratio equal to 10. Therefore, the resulting composite design in terms of reinforcement volume fraction is very efficient since the generation of biomimetic structures is very intuitive and fast, with limits related only to the computational power of the work station used (Intel (R) Xeon(R) CPU E5-1620 v3 @ 3.50 GHz, RAM 16.0 GB, 64-bit Operating System, x64-based processor, AMD Radeon Graphics Processor SDI). The CAD

approach also resulted positive since a closed and watertight mesh of the samples was obtained in a short time. This allowed a direct interface between the generative module for the generation of the mimicked composite structure and the additive manufacturing system. Multi material 3D printer (3D System Projet 5500x) was employed to manufacture three different samples with an increasing percentage of reinforcement (Figure B13) stating the reproducibility of the designed structures also here highly dependent on the computational power of the workstation.

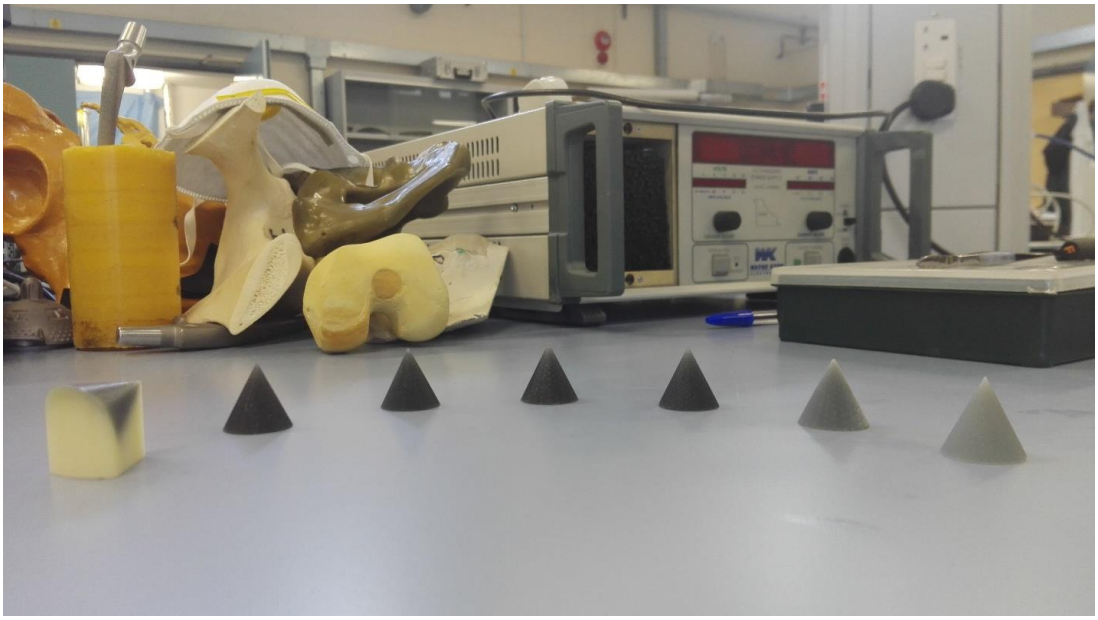

Figure B13. Manufactured bioinspired limpet teeth composites. Starting from the left-hand side we can observe the cone after being printed before wax supporting material removal. A bulk material cone sample was printed with an elastomeric black photopolymer, followed by three composite samples with increasing fibre volume fraction of respectively 1% , 3% , 6%. The last two cones were printed with bulk material and with fibre volume percentage of 3% and 0% respectively.

Appendix C – Ethic Review

FORM UPR16

Research Ethics Review Checklist

Please include this completed form as an appendix to your thesis (see the Research Degrees Operational Handbook for more information

UNIVERSITY OF PORTSMOUTH

Postgraduate Research Student (PGRS) Information				Student ID:	796509
PGRS Name:	Marco Curto				
Department:	S.M.D.E.	First Supervisor:	Dr. Gianluca Tozzi		
Start Date: (or progression date for Prof Doc students)	01/10/2015				
Study Mode and Route:	Part-time ☐ Full-time ☒	MPhil ☐ PhD ☒	MD ☐ Professional Doctorate ☐		

Title of Thesis:	Multi-material 3D Printing of Bioinspired Mechanical Architectures
Thesis Word Count: (excluding ancillary data)	~ 45000

If you are unsure about any of the following, please contact the local representative on your Faculty Ethics Committee for advice. Please note that it is your responsibility to follow the University's Ethics Policy and any relevant University, academic or professional guidelines in the conduct of your study

Although the Ethics Committee may have given your study a favourable opinion, the final responsibility for the ethical conduct of this work lies with the researcher(s).

UKRIO Finished Research Checklist:
(If you would like to know more about the checklist, please see your Faculty or Departmental Ethics Committee rep or see the online version of the full checklist at: http://www.ukrio.org/what-we-do/code-of-practice-for-research/)

a) Have all of your research and findings been reported accurately, honestly and within a reasonable time frame?	YES ☒ NO ☐
b) Have all contributions to knowledge been acknowledged?	YES ☒ NO ☐
c) Have you complied with all agreements relating to intellectual property, publication and authorship?	YES ☒ NO ☐
d) Has your research data been retained in a secure and accessible form and will it remain so for the required duration?	YES ☒ NO ☐
e) Does your research comply with all legal, ethical, and contractual requirements?	YES ☒ NO ☐

Candidate Statement:

I have considered the ethical dimensions of the above named research project, and have successfully obtained the necessary ethical approval(s)

Ethical review number(s) from Faculty Ethics Committee (or from NRES/SCREC):	ETHIC-2019-335

If you have *not* submitted your work for ethical review, and/or you have answered 'No' to one or more of questions a) to e), please explain below why this is so:

Signed *(PGRS)*:	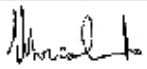	Date: 29/03/2019

UPR16 – April 2018

Certificate of Ethics Review

Project Title: Multi-material 3D Printing of Bioinspired Mechanical Architectures

Name: Marco Curto **User ID:** 796509 **Application Date:** 13-Mar-2019 16:36 **ER Number:** ETHIC-2019-335

You must download your certificate, print a copy and keep it as a record of this review.

It is your responsibility to adhere to the University Ethics Policy and any Department/School or professional guidelines in the conduct of your study including relevant guidelines regarding health and safety of researchers and University Health and Safety Policy.

It is also your responsibility to follow University guidance on Data Protection Policy:

- General guidance for all data protection issues
- University Data Protection Policy

You are reminded that as a University of Portsmouth Researcher you are bound by the UKRIO Code of Practice for Research; any breach of this code could lead to action being taken following the University's Procedure for the Investigation of Allegations of Misconduct in Research.

Any changes in the answers to the questions reflecting the design, management or conduct of the research over the course of the project must be notified to the Faculty Ethics Committee. Any changes that affect the answers given in the questionnaire, not reported to the Faculty Ethics Committee, will invalidate this certificate.

This ethical review should not be used to infer any comment on the academic merits or methodology of the project. If you have not already done so, you are advised to develop a clear protocol/proposal and ensure that it is independently reviewed by peers or others of appropriate standing. A favourable ethical opinion should not be perceived as permission to proceed with the research; there might be other matters of governance which require further consideration including the agreement of any organisation hosting the research.

(A1) Please briefly describe your project:: Evolution has long assisted natural kingdom creatures to optimise their architectures in terms of material distribution and mechanical performances. Species adaptation is a self-iterative process based on remodelling mechanisms where the rule is withstanding mechanical loads. Environmental inputs are gathered and digested by plants, animals or human hierarchical systems where tissues are grown in a bottom up fashion adding material where needed, saving energy and preventing material waste. Maintaining the same stunning mechanical performances is a hard challenge to achieve especially with man-made materials where final products are widely obtained with top down processes and material subtractions. Nature is a book to read, it dictates trajectories and key parameters by which materials are allocated within different living system parts. Remodelling activities has allowed various species to survive during their time preventing critical mechanical damages and preserving vital tissues. Bio- inspiration is a line of thought that follows tracks and blueprints provided by nature. A wide range of engineering problems can be solved with answers embedded in natural high- performance structural materials. Everyday living devices need to be improved by integrating comparable architectures and material distribution from the natural kingdom. Currently, transfer of information and concepts from biology to engineering is relatively lacking. Technology is consequently missing many advantages of biological design mostly because of big data handling information and absence in material manufacturing control at the small scales. Fidelity in translating mechanical function from biological structures to man-made devices can be found in Multi-Material 3D Printing (MM3DP). Manufacturing natural hybrid replicas represents the main goal of the project. The success of this study therefore lies in tuning into the key parameters via algorithm modelling and generative design based on parametric diagrams to produce suitable files for MM3DP. The potential is to create associative models that explore multiple configurations through control of the input parameters and proportion taken from nature. The study aims to compare mechanical answers between natural and bio-inspired 3D printed replicas and defining a trade-off between structural parameters belonging to the respective category.
(A2) What faculty do you belong to?: Technology
(A3) I am sure that my project requires ethical review by my Faculty Ethics Committee because it includes at least one material ethical issue.: No
(A5) Has your project already been externally reviewed?: No
(B1) Is the study likely to involve human participants?: No
(B2) Are you certain that your project will not involve human subjects or participants?: Yes
(B4) Will the study involve National Health Service patients or their relatives or carers?: No
(B5) Do human participants/subjects take part in studies without their knowledge/consent at the time, or will deception of any sort be involved? (e.g. covert observation of people, especially if in a non-public place): No
(B7) Does the study involve participants who are unable to give informed consent or in are in a dependent position (e.g. children, people with learning disabilities, unconscious patients, Portsmouth University students)?: No
(B9) Will financial inducements (other than reasonable expenses and compensation for time) be offered to participants?: No
(C1) Are drugs, placebos or other substances (e.g. food substances, vitamins) to be administered to the study participants?: No
(C2) Will human tissue (essentially anything with cells in it) be used in your project?: No
(C3) Is pain or more than mild discomfort likely to result from the study?: No
(C4) Could the study induce psychological stress or anxiety in participants or third parties?: No
(C5) Will the study involve prolonged or repetitive testing?: No
(C6) Is there any risk to the health & safety of the researcher or members of the research team beyond those that have already been risk assessed?: No
(D2) Are there risks of damage to physical and/or ecological environmental features?: No
(D4) Are there risks of damage to features of historical or cultural heritage (e.g. impacts of study techniques, taking of samples)?: No

(E1) Will the study involve the investigator and/or any participants in activities that could be considered contentious, unacceptable, or illegal, or in any other way harmful to the reputation of the University of Portsmouth?: **No**
(E2) Are there any potentially socially or culturally sensitive issues involved? (e.g. sexual, political, legal/criminal or financial): **No**
(F1) Does the project involve animals in any way?: **No**
(F2) Could the research outputs potentially be harmful to third parties?: **No**
(G1) Please confirm that you have read the University Ethics Policy and have considered the implications for your project.: **Confirmed**
(G2) Please confirm that you have read the UK RIO Code of Practice for Research and will conduct your project in accordance with it.: **Confirmed**
(G3) The University is committed to The Concordat to Support Research Integrity.: **Confirmed**
(G4) Submitting false or incorrect information is a breach of the University Ethics Policy and may be considered as misconduct and be subject to disciplinary action. Please confirm you understand this and agree that the information you have entered is correct.: **Confirmed**